

**Synthesis and Photophysics of Mn- and Yb-doped
CsPbX₃ (X = Cl, Br, I) Perovskite and Analogous
TlX Semiconductor Nanocrystals**

*A thesis
submitted in partial fulfilment
of the requirements for the*

Doctorate of Philosophy

By

Wasim Jeelani Mir

(20143342)



**Department of Chemistry,
Indian Institute of Science Education and Research (IISER)
Pune, India - 411008**

February 2019

DECLARATION

I declare that this written submission represents my ideas in my own words and wherever other's ideas have been included, I have adequately cited and referenced the original sources. I also declare that I have adhered to all principles of academic honesty and integrity and have not misrepresented or fabricated or falsified any idea / data / fact / source in my submission. I understand that violation of the above will cause for disciplinary action by the Institute and can also evoke penal action from the sources from whom proper permission has not been taken when needed.

Date:

Mr. Wasim Jeelani Mir

(ID: 20143342)

CERTIFICATE

This is to certify that this dissertation entitled “**Synthesis and Photophysics of Mn- and Yb-doped CsPbX₃ (X = Cl, Br, I) Perovskite and Analogous TIX Semiconductor Nanocrystals**” towards the partial fulfilment of the PhD degree at the Indian Institute of Science Education and Research (IISER) Pune. The dissertation represents original research carried out by Wasim Jeelani Mir at IISER Pune under my supervision. Part of the research given in appendix A was carried out by Wasim at Institute des Nanosciences Paris under the supervision of Dr. Emmanuel Lhuillier. The work presented here or any part of it has not been included in any other thesis submitted previously for the award of any degree or diploma from any other university or institution.

Date:

Dr. Angshuman Nag
(Research Supervisor)

Acknowledgements

I would like to acknowledge each and everyone who have contributed directly or indirectly in my PhD thesis work. Some of the noteworthy acknowledgements are mentioned below.

First of all, I would like to hearty acknowledge my Ph.D thesis supervisor Dr. Angshuman Nag for his utmost sincere support, guidance, and care throughout my PhD program. I am fascinated by his approach of dealing with problems which typically involves starting from a basic point known to me and then going step by step deep inside the fundamentals. It is difficult to express in words the kind of utmost character he is among scientific peers. His energy, cool temperament, friendly work culture enlightens me in a constructive way which makes him cool and smart professor before me.

I acknowledge constant support and patience from my parents and uncle without that this long journey of Ph.D would have been impossible for me. I dedicate my patience to my mother who is always behind me for good wishes and wanted me to become doctor. My uncle (chemistry lecturer) and his teaching especially on chemistry laid a strong foundation to pursue chemistry as an elective subject with confidence.

I would like to acknowledge all teachers who have taught me and made me what I am today. I heartily acknowledge faculties of chemistry department IISER Pune and Kashmir University especially those who taught me the chemistry subject.

I would like to acknowledge my research advisory committee members Dr. Pankaj, Dr. Angshuman and Dr. Arup for shaping me up in various RAC meetings throughout my Ph.D.

I acknowledge discussions with all my lab members both present and ex-members. Some of my lab members have directly contributed in my research work like Dr. Abhishek, Dr. Jagadeesh and BSMS students like Yogesh, Aditya, Ashutosh, and Sreejit.

I am grateful to acknowledge INSP-Paris team where I worked for six months under supervision of Dr. Emmanuel Lhuillier. I acknowledge Dr. Sandrine, PhD students Clement, and Baithe for their valuable discussions.

I acknowledge SAIF-IIT Mumbai and IIT-Chennai for measurements like EPR and ICP-AES.

Finally, I acknowledge council of scientific and industrial research (CSIR), India for Ph.D fellowship, Indo-French centre for promotion of advanced research (CEFIPRA) for six-months Raman-Charpak Fellowship 2016, IISER Pune for excellent infrastructure.

List of abbreviations

NCs: Nanocrystals

NPLs: Nanoplatelets

QDs: Quantum Dots

DMS: Dilute Magnetic Semiconductor

PL: Photoluminescence

PLQY: Photoluminescence Quantum Yield

EQE: External Quantum Efficiency

BET: Back Energy Transfer

ET: Electron Transfer

FWHM: Full Width Half Maximum

NIR: Near Infrared

CBM: Conduction Band Minimum

VBM: Valence Band Maximum

CB: Conduction Band

VB: Valence Band

LED: Light Emitting Diode

LSC: Luminescent Solar Concentrator

SAV: Surface Area to Volume

FESEM: Field Emission Scanning Electron Microscopy

ICP-AES: Inductively Coupled Plasma Atomic Emission Spectrometry

LSPR: Localized Surface Plasmon Resonance

XRD: X-ray Diffraction

TEM: Transmission Electron Microscopy

HRTEM: High Resolution Transmission Electron Microscopy

MeOAc: Methyl Acetate

OLAI: Oleylammonium Iodide

TBABr: Tetrabutylammonium Bromide

TBAI: Tetrabutylammonium Iodide

ODE: 1-Octadecene

OLA: Oleylamine

OA: Oleic Acid

Synopsis

CsPbX₃ (X = Cl, Br, I) perovskite nanocrystals (NCs) has emerged as unique semiconductors with efficient optoelectronic properties, in spite of having defects. Therefore, CsPbX₃ NCs are often termed as defect tolerant NCs. The major focus of this thesis is to dope these extraordinary NCs with optically active metal ions such as Mn²⁺ and Yb³⁺. These dopants give rise to luminescence that do not suffer from problems like self-absorption, and are useful in applications such as luminescent solar concentrators, light emitting diodes, and light harvesting for solar cell. In this thesis, we have developed synthesis methodologies to dope CsPbX₃ NCs and studied their optical properties. Importantly, lanthanide based Yb³⁺ doping is easily feasible in the octahedral site of Pb²⁺ in CsPbX₃ perovskite NCs, unlike the other semiconductors that offer tetrahedral coordination for lanthanides. In search of completely replacing lead, we have also prepared TIX (X = B, I) NCs and studied their defect tolerant behavior.

Chapter 1: Introduction

In the introduction chapter, I have introduced briefly topics related to my thesis work along with recent advancement in the field. Starting from bulk semiconductors to in-depth theory behind quantum confinement effect in semiconductor NCs is given. Dominance of surface related phenomena in NCs has been discussed. This is followed by an introduction to doping in semiconductors from bulk to NCs. Details of luminescence related properties of Mn-doped in II-VI semiconductors has been discussed. Then we start discussing about CsPbX₃ perovskites NCs which is the main material studied in this thesis. The recent evolution of Pb-halide perovskites as efficient optoelectronic material and their defect tolerant behavior has been discussed in detail. Then the challenges and opportunities of doping in CsPbX₃ perovskite NCs has been discussed. Particularly, recent advancement in Mn- and Yb-doping is thoroughly discussed. Final section is dedicated to designing analogous Pb-free metal halide semiconductors before pointing out the scope of the present thesis.

Chapter 2: Doping Mn in Colloidal Cesium Lead Chloride Perovskite Nanoplatelets

In this chapter, we develop one pot colloidal synthesis at room temperature to dope Mn²⁺ in CsPbCl₃ nanoplatelets (NPLs) with thickness ~2.3 nm exhibiting strong quantum confinement effect. Our report is the first report of Mn-doping in CsPbX₃ perovskite NPLs after two reports showed Mn-doping in CsPbCl₃ nanocubes. But those nanocubes fall in weaker confinement regime unlike our NPLs. Mn-doping introduces new emission channel

around 586 nm with long lifetime of 1.3 ms. This emission is characteristic of spin-forbidden d-d transition from ${}^4T_1 \rightarrow {}^6A_1$ of Mn^{2+} doped in $CsPbCl_3$ NPLs. By varying Mn-concentration, maximum photoluminescence quantum yield (PLQY) ~20% for Mn-emission is observed for 0.8% Mn-doped $CsPbCl_3$ NPLs and decreases with further increase in Mn-content. Attempts to dope Mn through one pot-synthesis in $CsPbBr_3$ NPLs or nanocubes remained challenging at that time. Anion exchange of Mn-doped $CsPbCl_3$ NPLs to Mn-doped $CsPbBr_3$ NPLs lead to limited success. Clearly, there was a need of novel synthesis strategy to dope Mn in $CsPbBr_3$ NCs which is addressed in chapter 3.

Chapter 3: Postsynthesis Doping of Mn and Yb into Colloidal $CsPbX_3$ (X= Cl, Br, I) Perovskite Nanocrystals

Our target was to achieve Mn-doping in narrower band gap $CsPbBr_3$ NCs compared to earlier success of Mn-doping in $CsPbCl_3$ NCs with band gaps in UV-blue region. We addressed this challenge by developing novel postsynthesis strategy in this chapter. In the postsynthesis doping, the host NCs were prepared first, and then different Mn precursors were added to host NCs. We find that Mn-oleate precursor does not lead to Mn-doping in $CsPbBr_3$ NCs, which explains the reason of unsuccessful doping of $CsPbBr_3$ NPLs and nanocubes. While Mn-doped $CsPbBr_3$ NPLs show intense PL at room temperature, Mn-emission is absent in the case of nanocubes. But Mn-emission appears when the PL is measured at lower temperature. We find that thermally driven back energy transfer from Mn-dopant to host quenches Mn-emission in Mn-doped $CsPbBr_3$ NCs. This back energy transfer can be suppressed either by increasing optical band gap of $CsPbBr_3$ NCs through quantum confinement effect or by decreasing PL measurement temperature. After Mn-doping, we extended the postsynthesis strategy for Yb^{3+} doping. Yb-emission emerges in near infrared (~1.2 eV) in all compositions of $CsPbX_3$ (X = Cl, Br, I) NCs including different shapes with long lifetime of the order of millisecond range. This Yb^{3+} doping in $CsPbX_3$ perovskite NCs has tremendous scope in near-infrared lasers, light emitting diodes, and sensors.

Chapter 4: Postsynthesis Mn-Doping in $CsPbI_3$ Nanocrystals to Stabilize Black Perovskite Phase

There is a big problem that $CsPbI_3$ do not stabilize in the optoelectronically active black perovskite phase at room temperature. In this chapter, the role of Mn-doping on structural stability of desired black phase of $CsPbI_3$ NCs at room temperature is addressed. Unlike bulk, $CsPbI_3$ NCs were reported to form in black perovskite phase at room temperature, but it transforms to the non-perovskite phase with time. High surface energy of NCs helps the

formation of black phase of CsPbI₃ NCs at room temperature. Subsequently, two reports were able to improve stability of black phase of CsPbI₃ NCs through Mn-doping by employing one pot synthesis. But it is unclear whether NCs alone stabilize black phase or Mn-doping has a role to play since synthesis of undoped and Mn-doped CsPbI₃ NCs were carried in two different batches. Unlike previous reports we studied more reliably the role of Mn-doping on black phase stability of CsPbI₃ NCs by employing our postsynthesis strategy. Reaction related inhomogeneity in size, structure and surface energy of host CsPbI₃ NCs can be neglected in our postsynthesis doping. We find that both lattice contraction and surface passivation upon Mn-doping in CsPbI₃ NCs is crucial to improve the stability of the desired black phase in ambient conditions. Thin film of Mn-doped CsPbI₃ NCs remained stable for about a month in ambient conditions with relative humidity ~30%. Similarly, Mn-doping improves PL stability of CsPbBr₃ NCs in ambient conditions where no phase transition is expected.

Chapter 5: Colloidal Thallium Halide Nanocrystals Analogous to CsPbX₃ Perovskites and their Defect Tolerance.

In this chapter, we studied TIX (X = Br, I) NCs which are analogous to CsPbX₃ perovskite NCs in terms of having similar defect tolerant valence electronic band structure, but, TIX do not exist in perovskite structure. Tl⁺ and Pb²⁺ are isoelectronic. We then addressed colloidal synthesis challenge of TIX NCs for the first time to examine their defect tolerance character. Interestingly, TIX NCs showed PL at room temperature unlike bulk TIX which was a good starting point for us. Nature of PL is broad compared to CsPbX₃ perovskite NCs but reasonable good PLQY ~6 to 10% is observed for TII and TIBr NCs respectively in UV-blue band gap materials. PL decay lifetimes are in the range of 4-12 ns and increases with emission wavelength. To examine further absence of deep defect states, we studied terahertz carrier dynamics in TIX NCs films. Interestingly, high THz carrier mobilities (~ 220 - 329 cm²V⁻¹S⁻¹) and long diffusion lengths (~ 0.25 - 0.98 μm) were observed in our TIX NCs suggesting defect tolerance nature of TIX NCs.

Appendices A and B:

The thesis also includes two appendices. Appendix A: Strategy to overcome recombination limited photocurrent in CsPb(Br_{1-x}I_x)₃ NCs arrays. This appendix is dedicated to fabrication of photodetector based on layer by layer growth of thin film of CsPb(Br,I)₃ NCs. We find that photocurrent increase by 10⁴ times compared to dark current but this photocurrent is limited by bimolecular recombination. By using nanotrench geometry of electrodes to apply high

electric fields, we were able to collect charge efficiently and photoconductivity enhances by a 1000 factor. Appendix B: Origin of excitonic absorption and emission from colloidal Ag₂S nanocrystals. In this appendix, the focus is to realize excitonic absorption and emission from Ag₂S NCs. Prior reports suggest broad featureless absorption of Ag₂S NCs. Our findings suggest contribution of mid-gap defect states along with band-edges, broaden the absorption spectra. Removing those defects lead to sharp excitonic absorption of Ag₂S NCs. Consequently, intense near infrared excitonic or band-edge emission with high PLQY ~20% and shorter PL decay lifetime ~11 ns is observed.

Table of Contents

1. Introduction

1.1 Introduction to Defect Tolerant Perovskite Semiconductors.....	2
1.2 Semiconductor Nanocrystals(NCs).....	3
1.2.1 Brief History.....	4
1.2.2 Quantum Confinement Effect in Semiconductors.....	5
1.2.3 Surface to Volume Ratio.....	8
1.3 Doping in Semiconductors.....	9
1.4 Doping in Semiconductor NCs.....	10
1.4.1 Fundamentals of Mn-emission.....	14
1.4.2 Yb-doped Semiconductor NCs.....	18
1.5 CsPbX₃ (X = Cl, Br, I) Perovskite Semiconductors.....	21
1.5.1 CsPbX ₃ Perovskite Structure	22
1.5.2 Evolution of Lead Halide Perovskite.....	23
1.5.3 CsPbX ₃ Perovskite NCs and Defect Tolerance.....	23
1.6 Ease and Challenges in Doping CsPbX₃ NCs.....	25
1.7 Doping for Stability of CsPbX₃ Perovskite NCs.....	27
1.8 Pb-Free Perovskites.....	27
1.9 Scope of This Thesis.....	29
1.10 References.....	31

2. Doping Mn in Colloidal Cesium Lead Chloride Perovskite Nanoplatelets (NPLs)

Abstract.....	42
Graphical Abstract.....	42
2.1 Introduction.....	43
2.2 Experimental Section.....	44
2.2.1 Preparation of Cs-oleate Stock Solution	44
2.2.2 Preparation of PbCl ₂ Solution With and Without Mn ²⁺ Molecular Precursor	44
2.2.3 Synthesis of Mn-doped CsPbCl ₃ NPLs.....	44
2.2.4 Anion Exchange.....	45
2.2.5 Characterization Methods.....	45

2.3 Results and Discussion.....	46
2.3.1 Synthesis Scheme of Colloidal Mn-doped CsPbCl ₃ NPLs	46
2.3.2 Morphology and Dimensional Analysis of Mn-doped NPLs.....	46
2.3.3 Structural Evidence of Mn-doping in CsPbCl ₃ NPL Lattice.....	48
2.3.4 Mn-doping introduces new emission channel at 586 nm.....	50
2.3.5 Excited state dynamics shows millisecond lifetime of Mn-emission.....	52
2.3.6 Anion exchange of Mn-doped CsPbCl ₃ to CsPbBr ₃ NPLs.....	53
2.5 Conclusions.....	54
2.6 References.....	55
3. Postsynthesis Doping of Mn and Yb into Colloidal CsPbX₃ (X = Cl, Br, I) Perovskite Nanocrystals (NCs)	
Abstract.....	61
Graphical Abstract.....	61
3.1 Introduction.....	62
3.2 Experimental Section.....	63
3.2.1 Cs-oleate Precursor Solution.....	63
3.2.2 CsPbBr ₃ NPLs.....	63
3.2.3 CsPbBr ₃ Nanocubes	64
3.2.4 CsPbCl ₃ Nanocubes	64
3.2.5 CsPbI ₃ Nanocubes.....	65
3.2.6 Doping Mn ²⁺ and Yb ³⁺ in CsPbX ₃ NCs (both Nanocubes and NPLs).....	65
3.2.7 Characterization Methods.....	65
3.3 Results and Discussion.....	66
3.3.1 Postsynthesis Mn-doping in CsPbX ₃ NCs.....	66
3.3.2 Morphology and Thickness of Mn-doped in CsPbBr ₃ NPLs.....	68
3.3.3 Evidence of Mn-doping in Lattice of CsPbBr ₃ NPLs.....	69
3.3.4 Mn-doping Improving Optical Absorption and Emission of 5 ML CsPbBr ₃ NPLs.....	69
3.3.5 Thickness Dependent Emission Color from Mn-doped CsPbBr ₃ NPLs.....	71
3.3.6 Mn-doping in CsPbBr ₃ Nanocubes.....	72
3.3.7 Mn-emission from 1.9% Mn-doped CsPbBr ₃ Nanocubes.....	74
3.3.8 Temperature Dependent PL and Barrier for Back Energy Transfer.....	75

3.3.9 Synthesis, Morphology and Structure of Yb-doped CsPbX ₃ Nanocubes and NPLs.....	77
3.3.10 Near IR Yb-Emission from Yb-doped CsPbX ₃ NCs.....	78
3.4 Conclusions.....	80
3.5 References.....	80
4. Postsynthesis Mn-Doping in CsPbI₃ Nanocrystals (NCs) to Stabilize Black Perovskite Phase	
Abstract.....	87
Graphical Abstract.....	87
4.1 Introduction.....	88
4.2 Experimental Section.....	90
4.2.1 Synthesis of Colloidal CsPbI ₃ and CsPbBr ₃ Nanocubes.....	90
4.2.2 Postsynthesis Mn Doping.....	91
4.2.3 OLAI Treatment.....	91
4.2.4 Characterization Methods.....	91
4.3 Results and Discussion	92
4.3.1 Synthesis and Characterization of Colloidal Mn-doped CsPbI ₃ NCs.....	92
4.3.2 Effect of Surface on Optical Properties and Stability of Colloidal NCs.....	94
4.3.3 Role of Lattice Doping in Stabilizing NCs Films.....	97
4.3.4 Role of Mn-doping in Stabilizing CsPbBr ₃ NCs Films.....	100
4.4 Conclusions.....	101
4.5 References.....	102
5. Colloidal Thallium Halide Nanocrystals (NCs) Analogous to CsPbX₃ Perovskites and their Defect Tolerance	
Abstract.....	109
Graphical Abstract.....	109
5.1 Introduction	110
5.2 Experimental Section	112
5.2.1 TII NCs.....	112
5.2.2 TIBr NCs.....	112
5.2.3 Characterization Methods.....	113
5.3 Results and Discussion	113

5.3.1 Synthesis.....	113
5.3.2 Morphology and Structure of TII NCs.....	114
5.3.3 Temperature Dependent Phase Transition in TII NCs.....	114
5.3.4 Optical Properties of TII NCs.....	116
5.3.5 Morphology and Structure of TIBr NCs.....	118
5.3.6 Optical Properties of TIBr NCs.....	119
5.3.7 Mobility and Diffusion Length.....	119
5.3.8 Comparison of TIX NCs with other Semiconductor NCs with Optical Band Gap >2.5 eV (< 500 nm).....	121
4.4 Conclusions.....	122
4.5 References.....	123
Appendix A: Strategy to Overcome Recombination Limited Photocurrent in CsPb(Br_{0.65}I_{0.35})₃ Nanocrystal Arrays.....	129
Appendix B: Origin of Excitonic Absorption and Emission from Colloidal Ag₂S Nanocrystals.....	141
Thesis Outlook and Future Directions	153
List of Publications.....	161

Chapter 1
Introduction

1.1 Introduction to defect tolerant perovskite semiconductors

Semiconductors are crystalline materials that does not conduct electricity at room temperature when unperturbed. But, a small perturbation in the form of (electrical bias, incident light, and doping) can lead to huge change in conductivity. This is due to the fact that semiconductors have a finite band gap between valence band (VB) and conduction band (CB). VB is fully occupied with electrons and CB is an empty band under no perturbation. Charge carriers in both VB and CB are delocalized on all the atoms that contribute in the formation of these two bands. Thus, if an electron is added to CB with the help of say an electrical bias, this electron is free to move in this CB without undergoing scattering with other electrons. This ideal scenario gives rise to good semiconductor properties. However, life is not so simple because of the presence of defect states in between VB and CB which are localized in nature. These defect states can trap the charge carrier with detrimental effects on semiconductor properties such as poor mobility of charge carriers and shorter carrier lifetime.

The traditional approach is removing these defect states by improving crystallinity of semiconductor. For this purpose often single crystal synthesis at high temperature $> 1000\text{ }^{\circ}\text{C}$ or highly sophisticated epitaxial growth is required to obtain a good quality semiconductor. On the other hand, lead halide perovskites have recently emerged as unique semiconductors wherein, in spite of the presence of defects, we get good semiconductor properties. Such materials which show good semiconductor properties despite having plethora of defects are termed as defect tolerant semiconductors.¹ Thus one can solution process these defect tolerant semiconductors in a cost-effective way, wherein, system is expected to have defects but still we get good optical and optoelectronic properties. For example, the present status of solar cell efficiency from MAPbI_3 is $\sim 23\%$ and is comparable to commercial Si solar cell efficiency $\sim 24\%$.²

From bulk to nanocrystals (NCs), apart from the lattice defects, role of surface defects also becomes critical. Interestingly, the surface defects in lead halide perovskite NCs are also less detrimental for optical and electronic properties. In fact, the first report on CsPbX_3 ($X = \text{Cl}, \text{Br}, \text{I}$) perovskite NCs showed 90% photoluminescence quantum yield (PLQY) without any surface modification and narrow emission linewidth ($\sim 85\text{ meV}$).³ Present status is like light emitting diodes (LEDs) from CsPbI_3 NCs have been reported with external quantum efficiency (EQE) exceeding 20% and is comparable to commercial LEDs.⁴ All these exciting properties suggest that lead halide perovskite NCs are also defect tolerant.

When I started my PhD, the evolution of CsPbX₃ perovskites NCs as defect tolerant materials was on cards. This motivated me to look into doping aspects in these unique semiconductor NCs. The broad idea behind this thesis is to combine novel semiconducting properties of CsPbX₃ perovskites NCs with dopant properties to introduce new optical functionality, and to improve stability.

1.2 Semiconductor nanocrystals:

The word “nano” prefix of NCs indicates that the size of object is in nanometer (nm) and $1\text{ nm} = 10^{-9}\text{ m}$. NCs are crystalline materials typically having size in the range of 1-100 nm. Like macroscopic or bulk materials, NCs can be semiconducting or metallic in nature but contain lesser number of atoms ranging from 100 to few thousands.⁵ To have a better feeling of nm scale, 1 nm long thread can clasp 10 hydrogen atom beads to form a nano-neckless of hydrogen atoms.

Why nano is so interesting in material science especially in semiconductors? The straight forward answer is in nano-regime, the intrinsic properties of semiconductors starts changing. This gives us an opportunity to design novel materials out of the existing macroscopic semiconductors. For example, color is an intrinsic property of CdSe which is a benchmark II-VI semiconductor well studied in literature.⁶ If we decrease the size of CdSe crystal below its excitonic Bohr diameter (characteristic of the material), the color of CdSe crystal starts changing.⁷⁻⁸ This change in color is due to change in optical band gap of CdSe semiconductor NCs upon decrease in size below its excitonic Bohr diameter though quantum confinement effect.⁸ Complete details of fundamental reason behind this quantum confinement effect driven change in band gap will be discussed later in this chapter. Through quantum confinement effect one can tune optical, and electronic properties at nanoscale by simply making NCs. These NCs show properties in between that of bulk and constituent atoms or molecules, and thus forms a bridge between atomic limit to bulk form. Understanding properties of NCs could help us to unveil the aspects of both atomic and bulk form and their transformation from one to another.

Another aspect of dealing with nano-regime is properties of NCs are mainly dominated by surface atoms. This is due to the high surface to volume ratio (SAV) of NCs unlike bulk crystals where surface has a negligible role. Thus, many exotic properties at the nanoscale arise from the combination of high SAV ratio of NCs and quantum confinement effect.

Furthermore, NCs self-assembly/super lattice/thin films opens up a new field of research where additional novel functionalities could be realized through NC to NC coupling.⁹

One striking aspects is that the NCs can be dispersed in desirable solvents by tuning the nature of surface passivation. Such a colloidal dispersion of NCs in a solvent should not be confused with solution which altogether has different meaning. When NCs are dispersed in solvents, they retain their individual property of a NC unlike solution of NaCl that dissociates into Na^+ and Cl^- . This colloidal dispersion of NCs can be used to make cost-effective thin films for device purpose. In addition, the dispersion phase allows one to functionalize these NCs on surface to carry out a specific function.

In spite of the fact that growth of NCs, characterization and assessment of its properties is a challenging task, research on NCs has remained one of the hot topics across globe since last three decades. Two important aspects of semiconductor NCs need to be understood more elaborately which will in turn help us to understand the research work carried out in this thesis. These are quantum confinement effect in NCs and high SAV ratio of NCs. After introducing these terms, this chapter introduces various topics studied in this thesis ranging from novel CsPbX_3 perovskite and their NCs, doping Mn and Yb in semiconductor NCs, ease and challenges of doping in CsPbX_3 perovskite NCs and their recent progress, and finally metal halides NCs analogous to CsPbX_3 perovskite NCs.

1.2.1 Brief history

In ancient times around 4th century, Romans were able to embed tiny gold crystals in glass for decoration purpose. The interesting specimen from Roman era is Lycurgus cup made up of glass embedded with tiny gold crystals. The Lycurgus cup has the ability to change the color when illuminated with light from outside and within the cup.¹⁰ Later, Michael Faraday in 1856 synthesized the first time colloidal gold solution of various colors while reducing gold chloride solution using phosphorus.¹¹ He attributed various colors to scattering of light by minute gold particles. More than a century passed, when Richard P. Feynman gave insightful lecture on December 29, 1959 at Caltech, USA which later developed a thought among scientists “*to control and manipulate things on small scale*”.¹² One of the famous saying by Feynman “*There’s is plenty of room at the bottom*” was an open invitation to a new field of science later termed as the ‘*Nanoscience*’. Although effect of quantum confinement in optical absorption spectra of excitons of transition metal dichalcogenide thin films were known in 1968.¹³⁻¹⁴ But the first experimental evidence for quantum size effects on exciton is reported

for tiny CuCl crystals dispersed in a silicate glass by Ekimov and co-workers in 1981.¹⁵ Soon after this in 1982, Al. F. Afros and A. L. Afros performed first theoretical calculation based on effective mass approximation (EMA) to explain these quantum size effects on excitons.¹⁶ It is to be noted that further improvements in EMA were made by Brus that led to famous Brus equation discussed later.¹⁷ Other notable early experimental reports of quantum size effects came from Henglein¹⁸ and Brus.¹⁹ In addition to quantum size effects, Brus in 1991 found quantum confinement of carriers also enhances the linear and non-linear optical properties, and formation of bi-excitons.²⁰ These pioneering works set up the tone for further research and development in nanoscience field from synthesis to applications. New tools were developed which are around us to understand and characterize these tiny nanomaterials.

1.2.2 Quantum confinement effect in semiconductors

Semiconductors possess a characteristic band structure comprising VB occupied with electrons and an empty CB. The two bands (VB and CB) are separated by forbidden energy gap known as the band gap. Upon absorption of photon with incident light energy $h\nu > \Delta E$ (band gap), electron in the CB and hole in the VB are created as shown in energy scale Figure 1.1a. This electron and hole being oppositely charged are held by electrostatic force of attraction in space and is given the special name ‘exciton’. The force of attraction between electron and hole is known as exciton binding energy. This coupled electron-hole or exciton can be thought of analogous to a hydrogen atom where, hole is a proton. In the hydrogen atom the distance between proton and electron is known as the Bohr radius, similarly, the distance between coupled electron-hole in a semiconductors is known as the exciton Bohr radius ‘ r_B ’. Exciton Bohr radius ‘ r_B ’ and its binding energy ‘ E_{ex} ’ are material specific and depends on the effective masses of electron and hole, dielectric constant of the material through following equation.²¹

$$r_B = \frac{\epsilon \hbar^2}{\mu e^2} \quad \text{and} \quad E_{ex} = \frac{\mu e^4}{2\epsilon^2 \hbar^2} \quad \dots\dots\dots (1)$$

Where μ is reduced mass given by $\mu = \frac{m_e^* m_h^*}{m_e^* + m_h^*}$, m_e^* and m_h^* are effective masses of electron and hole respectively, ‘ ϵ ’ is dielectric constant, $\hbar = \frac{h}{2\pi}$, ‘ h ’ is Plank’s constant, and ‘ e ’ is charge of an electron. It is to be noted that m_e^* and m_h^* in a good semiconductor are typically smaller than free electron mass ‘ m_0 ’, and ϵ is much larger than vacuum/air. Therefore, r_B of semiconductors is significantly larger and smaller E_{ex} when compared to the hydrogen atom. Typical values of r_B for common semiconductors fall in the range of 1-10 nm, while, E_{ex} in

case of bulk semiconductors falls in the range of 1-100 meV. We will see later that E_{ex} in quantum confinement regime depends on the size/shape of semiconductor NCs.

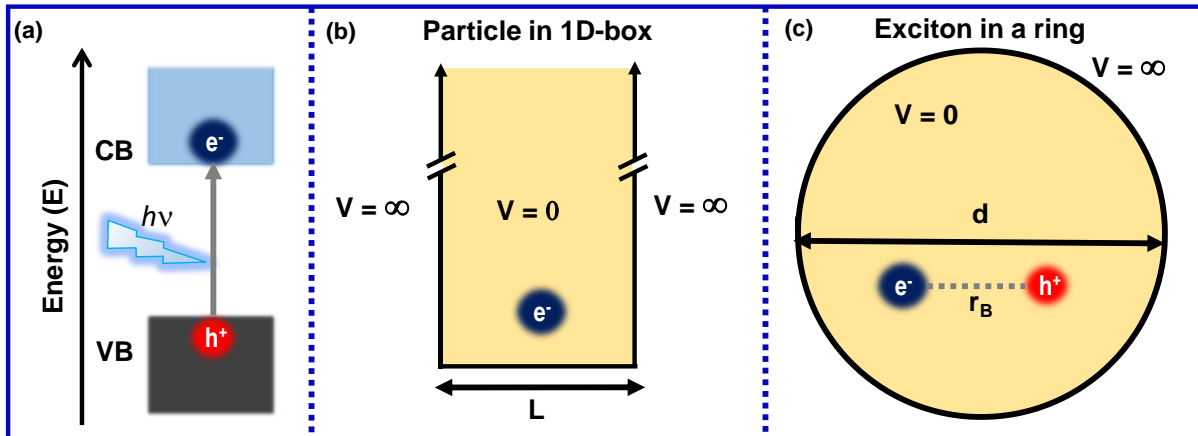


Figure 1.1: (a) Pictorial representation of electron (e^-) and hole (h^+) formation in CB and VB respectively upon absorption of light. The e^- and h^+ are held by columbic force of attraction and this electron-hole pair is termed as the exciton. (b) Schematics of particle (e^-) in 1D box of length ‘L’. (c) Schematics of particle (exciton) in a ring of diameter ‘d’. In both the schematics panel b-c, the particle is approximated to be present anywhere inside the box or ring but has infinite potential outside box/ring. Panel b is adapted following ref. 22.

In order to understand origin of quantum confinement, we refer to familiar solution of Schrodinger equation for a particle (electron) in a 1D-box (see Figure 1.1b) problem given below.²²

$$E = \frac{n^2 h^2}{8mL^2}$$

$$\Delta E_{n,n+1} = E_{n+1} - E_n = (2n + 1) \frac{h^2}{8mL^2}$$

$$\therefore \Delta E_{n,n+1} \propto \frac{1}{L^2} \dots\dots\dots (2)$$

Where ‘E’ is energy of a state and ‘ $\Delta E_{n,n+1}$ ’ is energy gap between ‘n’ and $(n + 1)^{th}$ state, ‘n’ is an integer ($n = 1, 2, 3, \dots$), ‘h’ is Plank’s constant, ‘m’ is the mass of particle and ‘L’ is the length of box. Equation (2) depicts that, if the length of box is decreased, the energy gap between levels increases and vice-versa. From here we saw that the energy gap between two levels varies with size (length) of 1D-box. Similarly, the energy expression for a particle in 3-D cubical box follows same proportionality of equation (2) as shown below.²²

$$E = (n_x^2 + n_y^2 + n_z^2) \frac{h^2}{8mL^2}$$

Where $n_x = 1, 2, 3, \dots$

$$\therefore \Delta E_{n,n+1} \propto \frac{1}{L^2} \dots\dots\dots (3)$$

Let's now take the case of ring, the simplest model to describe semiconductor NC of spherical shape. The potential for a particle (exciton) inside the ring/NC is zero and outside the ring, the potential is infinite as shown in Figure 1.1c. Now, if we extend the approach of particle in 1D and 3D box problem to this ring, qualitatively the following proportionally remains truly valid.²²

$$\Delta E_{n,n+1} \propto \frac{1}{d^2} \dots\dots\dots (4)$$

Where 'd' is the diameter of the ring. As per equation (4), we can qualitatively say that if we decrease the size of semiconductor NCs less than exciton Bohr diameter ($d = 2r_B$). The excitons get confined to smaller space than its bulk regime. As a result the band gap between the VB and CB increases. A modified Brus equation¹⁷ shown below based on effective mass approximation is used to calculate band gap of QDs.²³⁻²⁴

$$E_{g,QD} = E_{bulk} + \frac{h^2}{8R^2} \left[\frac{1}{m_e^*} + \frac{1}{m_h^*} \right] - \frac{1.786e^2}{4\pi\epsilon_o\epsilon_r R^2} - 0.248(E * Ry) \dots\dots\dots (5)$$

Where, $E_{g,QD}$ is predicted band gap energy of QD; R is radius of QD; m_e^* and m_h^* are effective mass of electron and hole respectively; h is Planck's constant; ϵ_o permittivity of vacuum; ϵ_r is dielectric constant; $E * Ry$ is Rydberg energy; and E_{bulk} is characteristic bulk band gap of a semiconductor. The second term in right hand side of equation (5) is $\frac{h^2}{8R^2} \left[\frac{1}{m_e^*} + \frac{1}{m_h^*} \right]$ corresponds to confinement energy and is inversely related to R^2 . The third term $\frac{1.786e^2}{4\pi\epsilon_o\epsilon_r R^2}$ is columbic binding energy of exciton and is inversely proportional to R (its contribution is very small due to high ϵ_r of semiconductor). The last term is $0.248(E * Ry)$ which takes care of electron-hole spatial correlation effect.

Generally, bulk semiconductor crystals have a fixed band gap, but beyond certain size less than the exciton Bohr diameter of a semiconductor, the band gap can be tuned see Figure 1.2a-b. This phenomenon of size dependent change in band gap is known as quantum confinement effect and such semiconductor NCs which exhibit quantum confinement effect are known as quantum dots (QDs). This quantum confinement effect differentiates semiconductor NCs from both its constituent atoms and bulk counterpart. Apart from size dependent change in band gap, QDs show increased oscillator strength for optical transition,

i.e transition probability increases. Also, confinement of electron and hole leads to atomic like quantized states see schematics in Figure 1.2a, unlike continuous bands in bulk semiconductor. The atomic like quantized states become more prominent with increase in strength of quantum confinement in smaller NCs in Figure 1.2a.²⁵

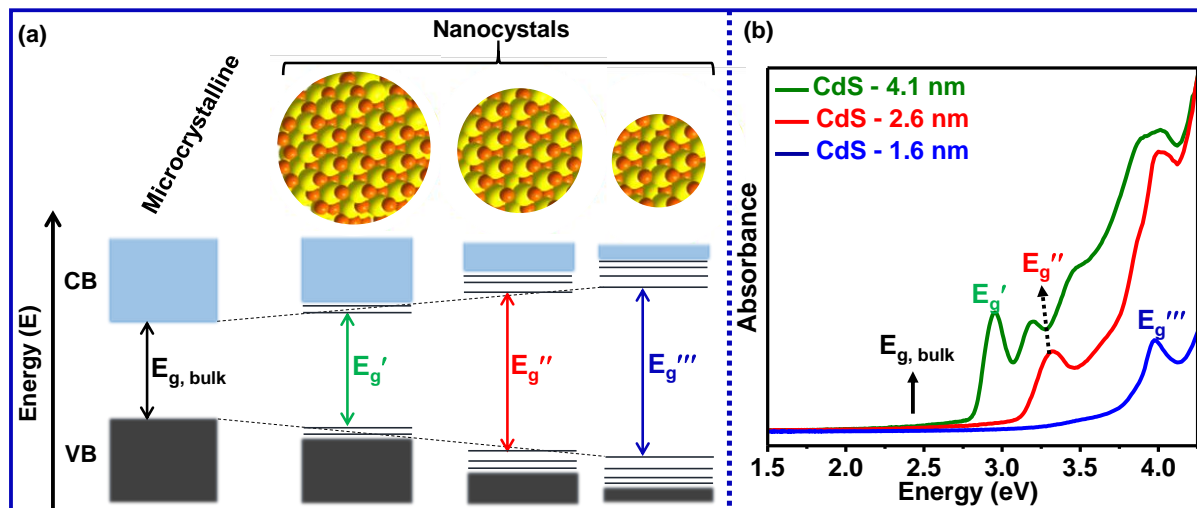


Figure 1.2: (a) Pictorial representation of valence band structure of bulk (microcrystalline) to NCs under quantum confinement regime. The decrease in size below exciton Bohr diameter increases the band gap between VB and CB through quantum confinement effect. Also, same quantum confinement leads to atomic like quantized states rather than continuous bands and is more prominent in smallest size NCs. (b) Steady state optical absorption spectra of three different sizes of CdS NCs showing optical band gaps at higher energy compared to bulk band gap due to quantum confinement effect. Panel a is adapted following ref. 8. Panel b is reprinted with permission from ref. 25. Copyright 2015 American Chemical Society.

1.2.3 Surface to Volume ratio

Another size dependent parameter which affects the properties at the nano-regime is the high SAV ratio. SAV is defined as the ratio of surface area to the volume of an object and is inversely proportional to radius ' R ' or diameter ' D ' of NCs. Due to high SAV ratio of NCs compared to bulk, properties at nanoscale have significant contribution from surface atoms, unlike macroscopic materials where surface atoms have negligible role. The fraction of atoms covering the surface to the total atoms present in a NC is termed as dispersion ' F '. For ' N ' spherical atoms of a cubic or spherical shaped NC, the dispersion follows $N^{-\frac{1}{3}}$ proportionality as shown in Figure 1.3 and inversely proportional to the radius ' R '.²⁶ To have a better feeling, spherical NC with 1 nm diameter typically has 70% of atoms present on the surface.²⁷ Thus, nanoscale material show different reactivity, melting points, vapour pressure etc compared to same material in the bulk form. For example, when the size of gold is reduced to few nm, the resulting gold nanoparticles show enhanced catalytic activity for driving CO oxidation.²⁸⁻²⁹ High surface area of gold nanoparticles leaves more surface atoms exposed and thus

increases the chances of reactivity. Similarly, other physical properties such as melting point, vapour pressure can also change when SAV ratio is high due to increases in surface energy. Surface energy is defined as energy required to put a dangling bond on surface and increases dramatically with increase in SAV ratio or with increase in the number of under coordinated bonds on surface. Thus surface atoms can easily escape in a nanoparticle due to the high surface energy and thus decrease in melting point of say Pt or Pd nanoparticles.³⁰ On the other hand, this high SAV ratio of nanoparticles increases biological toxicity concern.³¹

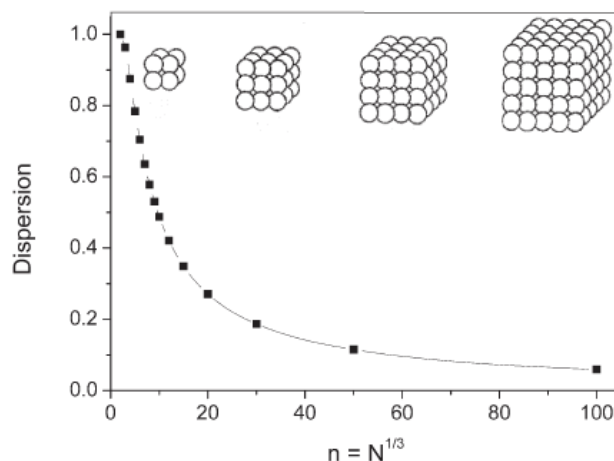


Figure 1.3: Dispersion or fraction of atoms covering surface of a NC is plotted as a function of $N^{-1/3}$, where N is number of spherical atoms in a NC with cubic morphology. Reprinted with permission from ref. 26. Copyright 2006 Royal Society of Chemistry.

Optical properties of semiconductor NCs are significantly affected due to the high SAV ratio of NCs. Large number of dangling bonds on surface of NCs often generates a non-bonding defect state in between VB and CB. Such defects are localised in nature and can trap electron and hole, detrimental to both the luminescence efficiency and transport of the charge carriers in semiconductor NCs. Tackling this large number of dangling bonds on surface in semiconductor NCs is challenging. Few strategies developed so far is passivation of surface bonds through forming a core-shell type heterostructure, and passivation with the help of long chain organic ligands. Throughout this thesis work, long chain organic ligands are used to passivate the surface of NCs.

1.3 Doping in semiconductors

Doping means intentional incorporation of extrinsic impurities in a crystalline host without changing the host electronic structure. Doping in semiconductors is a long-established successful strategy to control electronic, and optical properties of the semiconductors.³² This is due to the fact that in semiconductors, doping can significantly change number of conduction electrons or holes in CB or VB respectively. As a result, modulation of electronic

properties of semiconductors could be easily achieved. For example, doping Si semiconductor with pentavalent or trivalent impurity changes nature of conductivity to n-type or p-type respectively through modulation of carrier concentration. Doping magnetic impurity can introduce magnetic properties to non-magnetic host semiconductors. One classical example is Mn^{2+} ion when doped in GaAs (non-magnetic host) introduces ferromagnetism.³³ Extensive doping can also be used to introduce localized surface plasmon resonance (LSPR) in a wide band gap Sn-doped In_2O_3 NCs. Degenerate doping of Sn^{4+} in In_2O_3 NCs introduces free electron in CB of In_2O_3 . These doped conduction electrons can oscillate collectively in presence of electromagnetic radiations giving rise to LSPR in infrared region of Sn-doped In_2O_3 NCs.³⁴ Interestingly, by varying doping concentration of Sn, free electron concentration varies and thus tuning of LSPR band is achieved in Sn-doped In_2O_3 NCs.³⁵ Such LSPR bands have potential applications in the field of thermochromic windows,³⁶ and optical sensing.³⁷

Semiconductors are interesting hosts for optically active dopants and the combination of both (semiconductor + optically active dopant) is used to tailor optical functionality in a semiconductor. Such materials have huge influence in the field of light emitting diodes (LEDs), luminescent solar concentrators (LSCs), and optical thermometry.³² Following sections discuss in detail optically active dopants in semiconductor NCs

1.4 Doping in semiconductor NCs

Doping in bulk semiconductors is generally controlled by the thermodynamic solid solubility limit of dopant. Out of this solubility limit, 50% or more Mn-doping is achieved in II-VI semiconductors (ZnS/Se, CdS/Se) under thermal equilibrium condition.³⁸ However, same Mn-doping in II-VI semiconductor NCs is challenging, and often small percentage of dopants get incorporated in host NCs and in some host NCs, no doping has been achieved.³⁹ It is believed that these semiconductor NCs show self-annealing process wherein dopants are expelled from interior of NC to surface. Typical, doping in bulk semiconductor is usually achieved at very high temperature (> 1100 °C) whereas colloidal synthesis of semiconductor NCs is carried around 300 °C due to limitation from boiling point of organic solvents. At this temperature diffusion of impurity into host which requires thermal equilibrium is difficult to achieve, and thus small amounts of the dopant get introduced in NCs.⁴⁰ Despite these challenges, doping in semiconductor NCs is one of the top most active research from last two decades. One reason is size/shape dependent band gap tuning of semiconductor NCs gives wider flexibility to dope optically active dopants. Another important reason is that doping in

quantum confined semiconductor NCs increases dopant-carrier interactions. For example, doping a magnetic ion e.g. Mn^{2+} into a non-magnetic semiconductor NC can give rise to fascinating magnetic and magneto optical properties and are popularly known as dilute magnetic semiconductor (DMS) NCs.^{33, 41-42} Such DMS NCs benefit from interaction of dopant with charge carriers of host semiconductor NCs. One direct evidence of the dopant interaction with carrier is giant Zeeman splitting of excitonic PL observed at 4.2 K under zero magnetic fields for single Mn-doped CdSe NC, see schematics Figure 1.4a and experimental results in Figure 1.4b.⁴³ Since Mn^{2+} has a nuclear spin value of 5/2 and thus splits excitonic PL into 6 hyperfine lines due to six spin projection of Mn^{2+} spin ($\pm 5/2, \pm 3/2, \pm 1/2$) interacting with exciton. But, the single to noise ratio is poor. The improvements can be made by using lanthanide dopants which have higher magnetic moment compared to transition metals for same number of unpaired electrons. But, the same lanthanide doping in semiconductors or their NCs is difficult to achieve which is discussed later in this chapter.

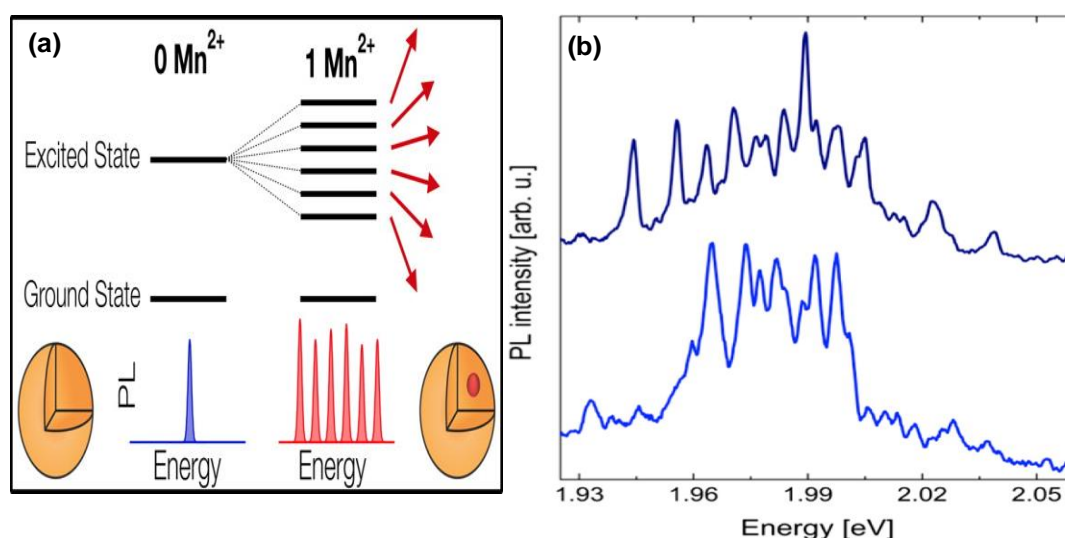


Figure 1.4: Pictorial representation of giant Zeeman splitting of excitonic PL in presence of magnetic dopant Mn^{2+} . Mn^{2+} has nuclear spin value of 5/2 and excitonic PL (carrier) can experience 6 different possible interaction with Mn-dopant. (b) PL spectra recorded at 4.2 K under zero magnetic fields for single particle Mn-doped $\text{Cd}_{0.9997}\text{Mn}_{0.0003}\text{Se}/\text{CdS}$ NC. Panel a-b reprinted with permission from ref. 43. Copyright 2016 American Chemical Society.

Moreover, stronger the quantum confinement in semiconductor NCs, greater will be the magnitude of giant the Zeeman splitting. Such materials once developed pave way towards future spintronics, solotronics and magneto-optical gating.⁴⁴

When dopants are optically active in nature such as Mn^{2+} or Yb^{3+} , a new emission channel is introduced in host semiconductor NCs and is characterized by long emission lifetimes. In strong confinement regime of NCs, efficient energy transfer from host to dopant is possible

due to increased probability of overlap of exciton-dopant wave function. Typically dopant emission in semiconductor NCs can originate in two forms. 1) Purely dopant emission appears with no sign of excitonic emission see Figure 1.5a, and 2) both dopant and excitonic emission emerges out as the dual emission color see Figure 1.5b.⁴⁵ Moreover, the tuning of dual (excitonic-dopant) emission color can be achieved by tuning the size/shape dependent host band gap, or by varying Mn-dopant concentration.

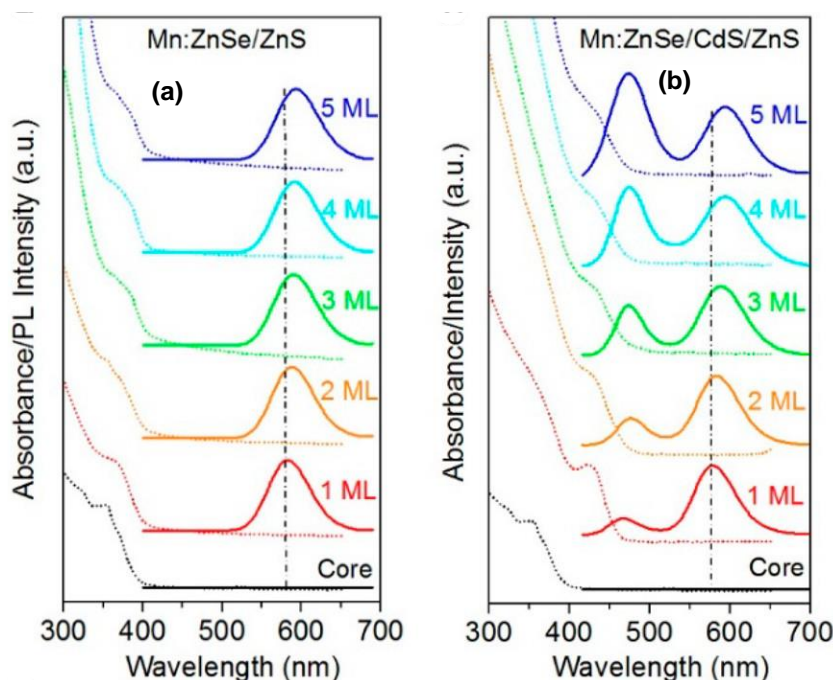


Figure 1.5: Optical absorption spectra (dotted line) and PL spectra (solid line) of Mn-doped ZnSe based core with different shell heterostructured NCs, (a) corresponds to ZnS shell, (b) CdS/ZnS shell. Panel (a) shows only dopant emission arises with no emission from host and in panel (b) both dopant and host emission arises. The black dashed line depicts slight tunability of Mn-emission is achieved upon change in thickness of shell/environment around Mn-dopant. Panel a-b reprinted with permission from ref. 45. Copyright 2017 American Chemical Society.

It is to be noted that dopant-emission energy typically emerges at a fixed energy which is dopant specific and shows slight dependence on environment but independent of band gap of host NCs. Limited tunability in dopant emission energy has been achieved in Mn-doped ZnSe/ZnS ensemble NCs by changing shell thickness (see Figure 1.5a-b). However, widely tunable Mn-emission in single NC host is reported and is discussed later in this section. In the case of Cu-doped ZnSe/CdSe core/shell NCs, the emission arises from transition involving one host state and one dopant state. In such cases, the size dependent tunability of dopant emission can be observed.⁴⁶ These doped semiconductor NCs can be used in simple and innovative ways from LEDs to harvesting solar energy benefitting from red shifted dopant emission compared to host absorption. This red shifted dopant emission ensures less or no re-

absorption of dopant emission by the host NCs, see red shaded Mn-emission in Figure 1.6a.⁴⁷ Inset of Figure 1.6a shows that negligible re-absorption of Mn-emission arises from ligands of NCs and weakly absorbing Mn levels lying in midgap of Mn-doped CsPbCl₃ NCs. Thus befitting from this re-absorption free dopant-emission, Mn-doped II-VI semiconductor NCs and recently Mn-doped CsPbCl₃ NCs have been used to fabricate LSC based solar cells.⁴⁷⁻⁴⁹ Ideally any material with emission energy red-shifted from absorption can be a suitable candidate for LSCs provided the PLQY of that emission is high enough. Mn-emission in CsPbCl₃ NCs satisfy both significant red-shift and high PLQY.

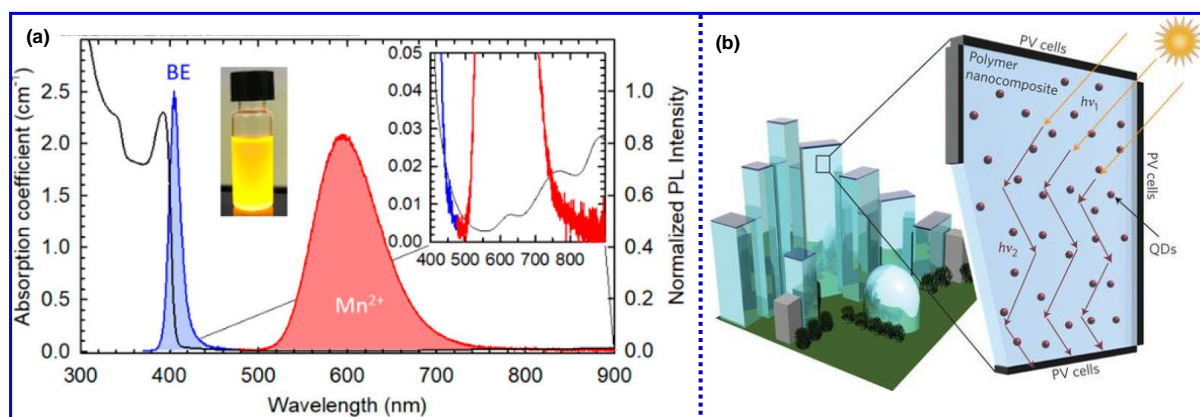


Figure 1.6: Optical absorption and PL spectra of Mn-doped CsPbCl₃ NCs in which band edge (BE) and Mn-emission are highlighted in blue and red shade respectively. BE emission spectra (blue shade) shows significant overlap with host absorption, but Mn-emission spectra shows zero overlapping with host absorption spectra. Inset of panel (a) shows zoomed view of Mn-emission spectra with slight absorption of Mn-emission energy arising due to ligands present on NCs and midgap Mn-levels. (b) Schematics of luminescent solar concentrator window of polymer waveguide matrix embedded with reabsorption free doped NCs as an alternative for solar powered urban building. Panel (a) is reprinted with permission from ref. 47. Copyright 2017 American Chemical Society, and panel b with permission from ref. 50. Copyright 2017 Nature Publishing Group.

LSCs are promising candidates for building-integrated photovoltaic (BIPV) semitransparent windows capable of harnessing solar energy into power as shown schematically in Figure 1.6b.⁵⁰ The idea is to create solar energy powered buildings feasible in urban areas. Typical LSC consists of polymer waveguide in which luminescent material with emission free from re-absorption is embedded, and at the edges Si solar modules are placed as shown pictorially in Figure 1.6b. The sunlight is captured by luminescent material which then re-emits in all directions and waveguide concentrates this emitted light at the edges where Si solar modules convert this light to power. Any re-absorption losses are detrimental to the efficiency and cannot be afforded in LSC based solar cells. Another way of exploiting this red shifted Mn-emission in CsPbCl₃ NCs is to enhance the weak EQE of Si-solar cells below 450 nm.⁵¹⁻⁵² A thin film of Mn-doped CsPbCl₃ NCs ~50 nm over Si solar cell shows nearly 100%

transparency to visible and near infrared (NIR) light. In this way light ≤ 400 nm is efficiently absorbed by Mn-doped CsPbCl₃ NCs and converts it into 586 Mn-emission which is then efficiently absorbed by the underneath Si solar cell. Similarly, thin film of Yb-doped CsPbCl₃ NCs is used recently over Si-solar cell for the same purpose and ~4% enhancement of Si-solar cell efficiency is realized.⁵³ Last but not the least, both Mn and Yb doped semiconductor NCs are suitable candidates for LEDs from visible to NIR region. Recently, PLQY ~130 % is reported for Yb-emission in case of Yb-doped CsPbCl₃ NCs through quantum cutting phenomenon.⁵⁴ Therefore, NIR LEDs and sensors based on Yb-doped CsPbCl₃ NCs are not far away from realization.

While all the above mentioned properties and applications of impurity doped semiconductors will be of greater significance if doping is carried out in the quantum confined semiconductor NCs. So, it is highly appealing and desirable to develop methods to achieve doping in the quantum confined semiconductor NCs. In this thesis, the second chapter is based on this novelty aspect wherein Mn is doped in strongly confined CsPbCl₃ nanoplatelets (NPLs). Also, major part of the thesis addresses the synthesis challenge of Mn- and Yb-doped CsPbX₃ perovskite NCs followed by the investigation of their optical properties.

1.4.1 Fundamentals of Mn-emission

Mn²⁺ doping is one of the most widely explored and versatile dopant for semiconductor hosts including NCs. This is because of the fact that Mn²⁺ prefers tetrahedral coordination (octahedral coordination is also possible) and most of semiconductors such as CdSe, CdS, GaAs, ZnS, Si etc have tetrahedral coordination environments. Upon doping Mn²⁺ in a suitable host of semiconductor NCs typically leads to bright luminescence in visible region ~2.12 eV (586 nm) due to ⁴T₁ → ⁶A₁ internal d-d transition of Mn²⁺. In addition, Mn²⁺ ion is magnetic in nature and also introduces magnetic character to host semiconductor NCs. Thus, Mn-doping can give rise to interesting magnetic and magneto-optical properties when doped in semiconductors NCs. This section will discuss in detail Mn-doping from its optical readout point and is directly concerned with the major part of this thesis.

PL spectroscopy is an excellent probe to study Mn-doping in semiconductor NCs. Interesting aspect of Mn-doping in semiconductor NCs comes into play when band gap of host is greater than Mn-emission energy gap. This requirement of suitable band gap motivated researchers to study Mn-doping extensively in II-VI semiconductor NCs.^{39, 55} Figure 1.7a shows size dependent PL spectra of Mn-doped CdSe NCs at 5 K, and in Figure 1.7b shows PL maximum

of both Mn-emission and excitonic emission plotted as a function of the NC diameter ranging from 2.3 to 5 nm.⁵⁵ Clearly, Mn-emission emerges when the optical band gap (~PL maximum energy) of host NCs is larger than the Mn-emission energy gap. As a result, only small sized CdSe NCs with diameter < 3 nm exhibit the Mn-emission. Large sized CdSe NCs have smaller optical band gaps than Mn-emission energy and thus no sensitization of Mn-dopant is possible.

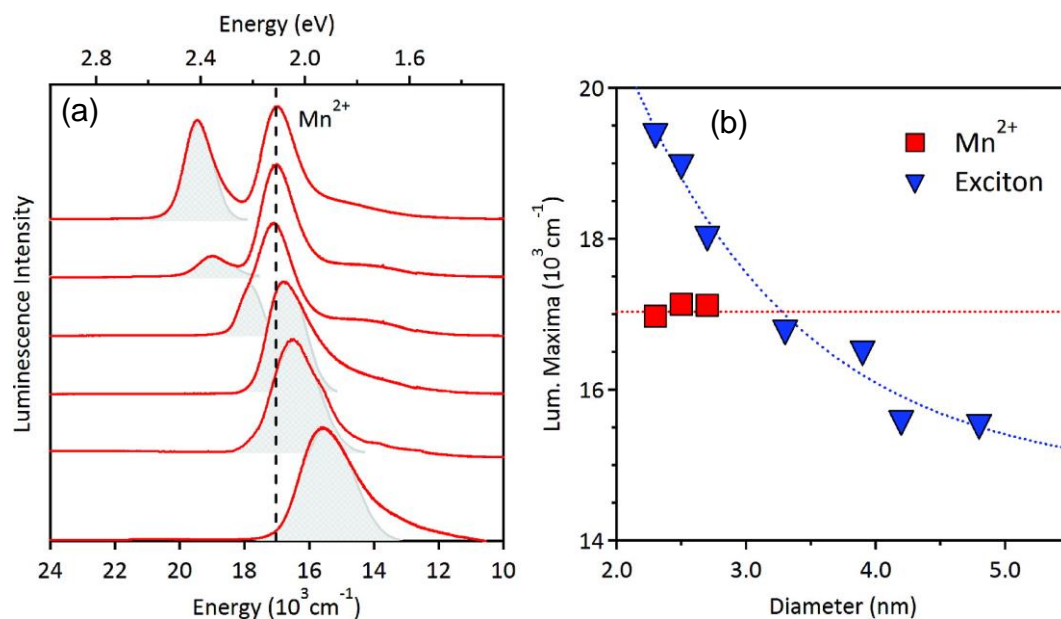


Figure 1.7: PL spectra of Mn-doped in different sized CdSe NCs ranging from 2 to 5 nm from top to bottom. (b) PL emission maximum energy as a function of CdSe NCs diameter. Clearly Mn-emission emerges when host emission energy is greater than Mn-emission energy. Panel a-b reprinted with permission from ref. 55. Copyright 2008 American Chemical Society.

Upon electron-hole excitation in CdSe semiconductor NCs, the excitonic energy is transferred non-radiatively to Mn-dopant thereby exciting Mn from ground state to excited state. The excited Mn then de-excites radiatively through ${}^4\text{T}_1$ - ${}^6\text{A}_1$ d-d atomic level transition giving rise to Mn-emission.⁵⁶ The mechanistic details of sensitization processes involved will be discussed later in this section, let's try to understand first the origin of ${}^4\text{T}_1$ to ${}^6\text{A}_1$ transition of Mn. Free Mn^{2+} ion possesses five unpaired electrons in the 5 fold degenerate 3d orbital. In presence of weak ligand field tetrahedral or octahedral geometry, the ground state retains 5 unpaired electrons in symmetric from (${}^6\text{A}_1$), but degeneracy of d orbital splits in t_2 and e sets in excited state see Figure 1.8.⁴⁴ Clearly, it can be seen from Figure 1.8 that spin state of ground state is different from that of all excited state configurations. As a result, all electronic transition from ground state are spin forbidden for Mn^{2+} , however, can feel some relaxation in presence of spin-orbit coupling or local strain in ligand field. Typical molar extinction

coefficients of these spin forbidden transitions are of the order of $1\text{-}10\text{ M}^{-1}\text{cm}^{-1}$ and are rarely observed. One way to efficiently excite weakly absorbing Mn^{2+} is to dope it in a direct band gap semiconductor NC which shows strong extinction coefficient typically $\sim 10^5\text{ M}^{-1}\text{cm}^{-1}$ for light absorption. Energy transfer from host to Mn-dopant can excite Mn to its excited state. Once Mn is excited, it emits light in visible region ($\sim 586\text{ nm}$) by undergoing radiative de-excitation from lowest excited state (${}^4\text{T}_1$) to ground state (${}^6\text{A}_1$) as depicted in Figure 1.8. Due to the spin forbidden nature of this ${}^4\text{T}_1\text{-}{}^6\text{A}_1$ transition, Mn-emission is characterized by long lifetime in millisecond range. Typically, Mn-emission shows high PLQY when doped in semiconductor NCs. PL efficiency of Mn-emission depends on rate of forward energy transfer from host to dopant, total rate of non-radiative processes or defect density and rate of backward energy transfer from dopant to host which requires thermal activation.

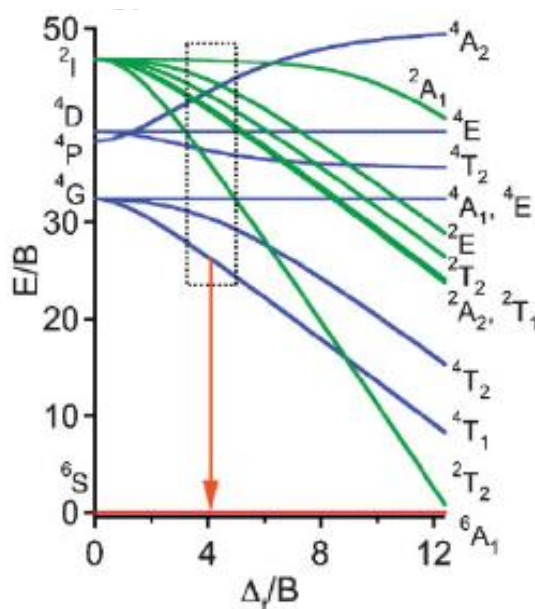


Figure 1.8: Tanabe-Sugano diagram of Mn^{2+} (d^5) system in a cubic field showing ${}^6\text{A}_1$ ground state and low lying spin-forbidden excited states. Clearly ${}^4\text{T}_1$ is low lying excited state energy level in weak ligand fields depicted by dotted rectangle. Commonly encountered Mn-emission energy in Mn-doped semiconductor NCs corresponds to ${}^4\text{T}_1\rightarrow{}^6\text{A}_1$ transition. Reprinted with permission from ref. 44. Copyright 2008 WILEY-VCH.

The probable mechanism of Mn-sensitization can be understood from three level system band diagram in energy scale in Figure 1.9. k_r^{QD} and k_r^{Mn} stands for radiative decay constant of quantum dot (QD) and Mn respectively, k_{nr}^{QD} and k_{nr}^{Mn} stands for total non-radiative decay constant of QD and Mn respectively, k_{ET} is the central parameter and stands for rate constant for energy transfer (ET). Ground state stands for all electrons in VB are filled and Mn is in electronic ground state (${}^6\text{A}_1$), while excitonic state is when electrons are promoted to CB forming excitons. ${}^4\text{T}_1$ is lowest lying excited state of Mn above this state, higher energy

excited state are lying depicted by $^{2,4}\Gamma$ gamma distribution. Based on sub-nanosecond energy transfer rates observed in colloidal semiconductor NCs,⁵⁷ most probably Dexter-type⁵⁸ exchange interaction are involved in sensitization of Mn involving transfer of excitonic energy non-radiatively to Mn-dopant. Another proposed theory of sensitization is electron transfer from CB to 4T_1 state of Mn. However, such transfer will change oxidation state of Mn^{2+} to Mn^+ which is proposed to form a short lived transient species. Although, both theories agree on fact that final Mn-emission arises from Mn^{2+} oxidation state involving radiative de-excitation from 4T_1 excited state to 6A_1 ground state.

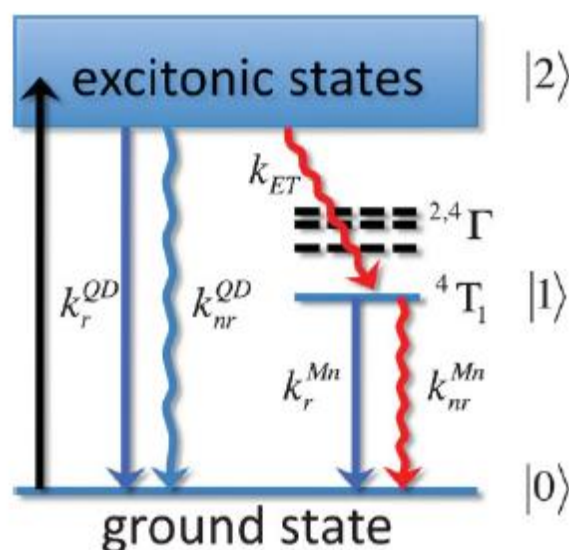


Figure 1.9: Pictorial representation of various radiative (straight lines) and non-radiative (curved lines) processes involved in Mn-doped semiconductors upon absorption of photon. Ground state corresponds to all electrons in VB and Mn has all electrons unpaired (ground state of Mn). Excitonic state corresponds to electrons promoted to CB. Mn-dopant is sensitized upon non-radiative energy transfer from excitonic state to Mn-dopant which then undergoes radiative and non-radiative transition from the low lying excited state energy level 4T_1 . Reprinted with permission from ref. 44. Copyright 2008 WILEY-VCH.

Mn-doped colloidal semiconductor NCs exhibit Mn-emission with three characteristics features, 1) limited spectral tunability, 2) broad spectral width, and 3) long lifetime of Mn-emission. Mn-emission arising from atomic d-d levels of Mn is primarily independent of size/shape and to some extent local environment of host and thus narrow tunability window is possible for Mn-emission. The maximum tunability of Mn-emission achieved from Mn-doped in II-VI semiconductor ensemble NCs is ≤ 150 meV ranging from orange to red region of visible spectrum. Hazarika et al.⁵⁹ reported spectral tunability of 370 meV of Mn-emission at single particle level in Mn-doped $Zn_{0.25}Cd_{0.75}S$ NCs covering green to red region of visible spectrum. Such a large spectral tunability of Mn-emission is attributed to asymmetry in ligand field environment of Mn in different NCs. Another characteristic feature of Mn-

emission from ensemble Mn-doped NCs is broad spectral width (≥ 180 meV). Such a broad spectral width questions the atomic level nature of Mn-emission. One of the reason attributed to this anomaly is coupling of vibrational structure of host NCs and Mn *d* levels. Interestingly, single particle level PL spectroscopy in Mn-doped Zn_{0.25}Cd_{0.75}S NCs by Hazarika et al. reports very narrow ~60 to 75 meV spectral width of Mn-emission and attributed this lower limit of spectral width to coupling of vibrational structure of host and Mn *d* levels.⁵⁹ Finally, long PL lifetime of Mn-emission of the order of milliseconds is due to spin forbidden nature of ⁴T₁-⁶A₁ transition. Such a long lifetime is an advantage for phosphor and sensors type applications.

1.4.2 Yb³⁺ doped semiconductor NCs

Lanthanide (Ln³⁺) doping including Yb³⁺ has been mostly carried out in insulators such as wide band gap oxides or fluoride lattice where lanthanides based emission are well reported and studied.⁶⁰⁻⁶¹ The same Ln³⁺ doping in semiconductors has remained a challenge.⁶² This is due to the fact that Ln³⁺ prefers octahedral or higher coordination and most common semiconductors such as Si, GaAs, CdSe, ZnS etc have tetrahedral coordination environments. Lanthanide doping in narrower band gap semiconductors absorbing in visible region is highly desired. On the other hand, CsPbX₃ perovskite are unique and novel semiconductor hosts where octahedral coordination environment is present for Pb²⁺ cation. One straight future outlook of this compatibility is to dope CsPbX₃ NCs with Ln³⁺ based magnetic dopant and to probe the magnetic-optical properties discussed in thesis outlook and future directions.

In case of Yb³⁺ and other trivalent lanthanides, the f-f optical transitions are atomically sharp but are parity forbidden in nature with poor extinction coefficient of light absorption.⁶³⁻⁶⁴ The atomically sharp nature of intra 4f transition in all Ln³⁺ including Yb³⁺ is due to fact that screening of 4f orbitals by outer 5s and 5p orbitals makes intra 4f-4f transition less sensitive to ligand fields.⁶⁴ Sensitization of trivalent lanthanides and resulting Ln³⁺ based emission is vastly explored in literature due to the potential scope in phosphors, sensors, imaging etc. However, for all these application high luminescence efficiency and long lifetime of intra 4f transition is desirable. In prior literature, sensitization of Ln³⁺ was achieved with the help of organic fluorophore molecules.⁶⁵⁻⁶⁶ But, such a combination resulted so far maximum PL efficiency of 63% and long lifetime of 712 μ s for Yb-emission.⁶⁷ On the other hand, Ln³⁺ dopants including Yb³⁺ have been incorporated in wide band gap fluoride, oxide lattice (commonly in NaYF₄, LaF₃, LuPO₄, Gd₂O) for up conversion anti-Stokes emission.⁶⁰⁻⁶¹ Interestingly, suitable combination of host and dopants has resulted into PL efficiencies

beyond 100% for Ln^{3+} emission through quantum cutting down conversion process.⁶⁸⁻⁶⁹ But, these hosts are insulators with wide band gap and require high energy UV excitation source. Subsequently, benefitting from high light absorption coefficient of direct band gap II-VI semiconductor NCs, efforts have been made to dope Ln^{3+} in visible band gap II-VI and III-V NCs such as CdS, CdSe, InP etc.^{62-63, 70-72} However, prior literature suggested difficulty to dope Ln^{3+} in these semiconductor hosts eventually suffering from poor sensitization/PLQY of dopant emission and small radiative lifetimes in μs range for Yb-emission.^{62-63, 73} The difficulty in doping Ln^{3+} in these semiconductor hosts is attributed to following two reasons. Ln^{3+} are generally hard acids and do not prefer soft bases like S^{2-} , Se^{2-} or P^{3-} . Secondly, Ln^{3+} prefer octahedral or higher coordination environment, thus making incorporation difficult at tetrahedral site of Cd^{2+} , Zn^{2+} , In^{3+} commonly encountered in II-VI and III-V semiconductor NCs. Therefore Ln^{3+} doping in narrow band gap semiconductors is highly challenging.

Recently, Yb-doping in CsPbCl_3 NCs is reported exhibiting longer lifetime ~ 2 ms for Yb-emission.^{53-54, 74} CsPbX_3 NCs with band gaps in the visible region are desirable candidates for doping lanthanides, where, Ln^{3+} or Yb^{3+} replaces Pb^{2+} from its octahedral site in CsPbX_3 perovskite structure. Also, high molar extinction coefficient of CsPbX_3 NCs can sensitize efficiently Yb^{3+} which then shows emission in NIR region.⁷⁵ Figure 1.10a shows that indeed most of the trivalent lanthanides were successfully doped in CsPbCl_3 NCs exhibiting sharp emission from visible to NIR region in same host.⁷⁴ As expected all Ln^{3+} emissions are red-shifted from excitonic emission of host. For a specific case, optical absorption and PL spectra is shown in Figure 1.10b for Yb-doped CsPbCl_3 NCs.⁵⁴ Clearly, Figure 1.10b shows Yb-emission emerges in NIR region around 990 nm, with no absorption feature corresponding to this Yb-emission. The Yb-emission arises due to energy transfer from excitonic states of host CsPbCl_3 NCs to Yb-dopant thereby exciting Yb^{3+} to higher energy state ($^2\text{F}_{5/2}$). The excited Yb^{3+} then emits through intra f-f transition from $^2\text{F}_{5/2} \rightarrow ^2\text{F}_{7/2}$ level falling in NIR region 1.25 eV (~ 990 nm). It is to be noted that Yb-emission is spin allowed transition unlike Mn-emission but remains parity forbidden. The overall process of sensitization and energy transfer is qualitatively similar as depicted for Mn-dopant see schematics in Figure 1.9. Interestingly, NIR PLQY of Yb-emission increases from 10 to 130% upon increase in Yb-dopant concentration from 0.2 to 7.4% respectively see Figure 1.10c. High PL efficiency for Yb-emission exceeding 100% is attributed to quantum cutting phenomenon where one high energy photon excites two Yb-dopants.⁵⁴ Interestingly, Yb^{3+} ($4f^{13}$) exhibits clean energy level structure involving only two states, ground state $^2\text{F}_{7/2}$ and single excited state $^2\text{F}_{5/2}$ compared

to other Ln^{3+} ions such as Ce^{3+} , Eu^{3+} , Gd^{3+} wherein multiple f-states are present as shown in Figure 1.11.⁷⁶

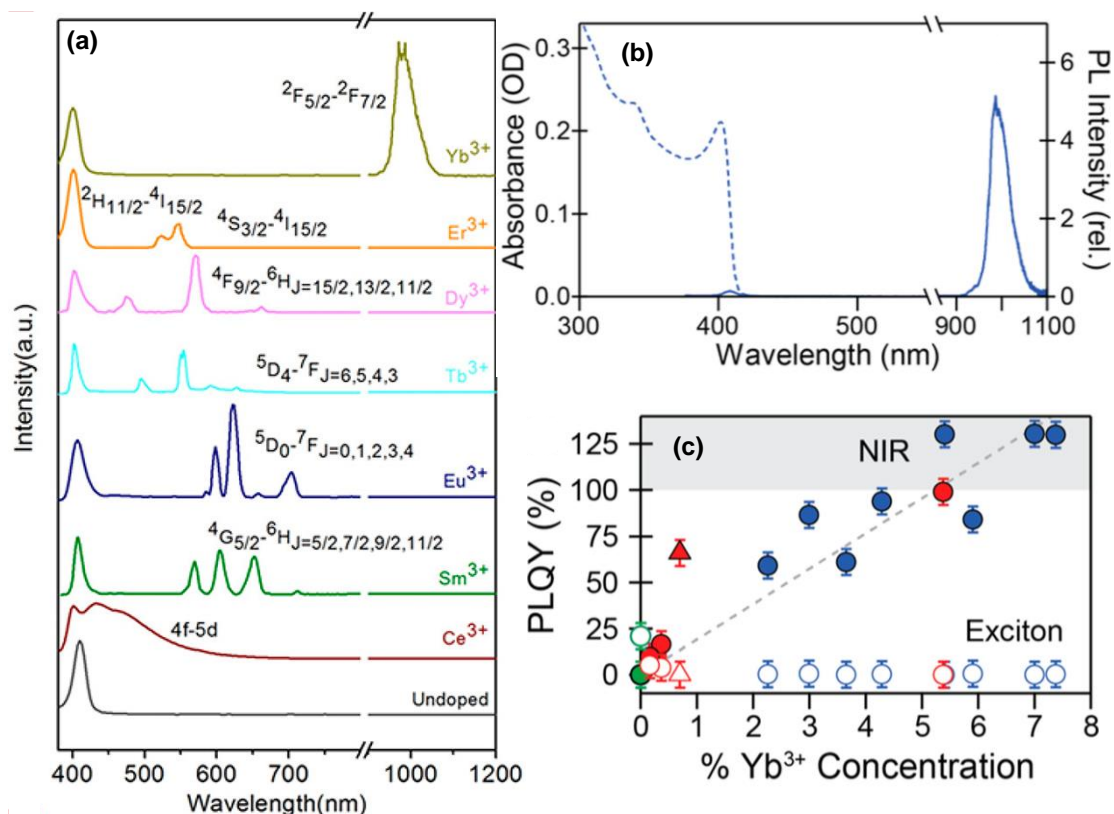


Figure 1.10: (a) PL spectra of lanthanides (Ln^{3+}) doped CsPbCl_3 NCs. (b) Optical absorption and PL spectra of Yb-doped CsPbCl_3 NCs exhibiting NIR Yb-emission at lower energy from host absorption (downconversion emission). (c) Estimated PLQY of excitonic emission and NIR Yb-emission as a function of Yb-concentration. More than 100% PLQY of NIR Yb-emission is due to quantum cutting of higher energy photon into two low energy photons. Panel (a) is reprinted with permission from ref. 74. and panel b-c is from ref. 54. Copyright 2017 and Copyright 2018 American Chemical Society.

This clean energy level structure of Yb^{3+} involving only two energy levels makes it one of the popular lanthanide dopant for introducing optical functionality to semiconductor NCs. This is driven by the fact that non-radiative process increases with increase in number of energy levels and are expected to be lesser for the case of Yb^{3+} compared to many other lanthanides. On the other hand narrower emission energy of Yb^{3+} emission (1.25 eV , 10000 cm^{-1}) is sensitive to quenching environments detrimental to luminescence efficiency and radiative lifetime.⁷⁷⁻⁷⁸ Three to four quanta of N-H stretching or O-H stretching vibrations ($\sim 3500 \text{ cm}^{-1}$) from ligands quenches the Yb-emission.⁷⁷⁻⁷⁸ Similar to Mn-emission, Yb-emission energy is insensitive to size/shape/composition dependent band gap of host semiconductor NCs. Finally, significant red-shifted Yb-emission from host absorption in Yb-doped CsPbCl_3 NCs is innovatively used to increase the overall Si solar cell efficiency by $\sim 4\%$.⁵³ But same Yb^{3+}

doping in narrower band gap CsPbBr₃ and CsPbI₃ NCs has remained challenging. Chapter 3 in this thesis addresses this issue by developing novel postsynthesis strategy to achieve Yb-doping in CsPbX₃ (X = Cl, Br, I) perovskites NCs of various compositions and shapes.

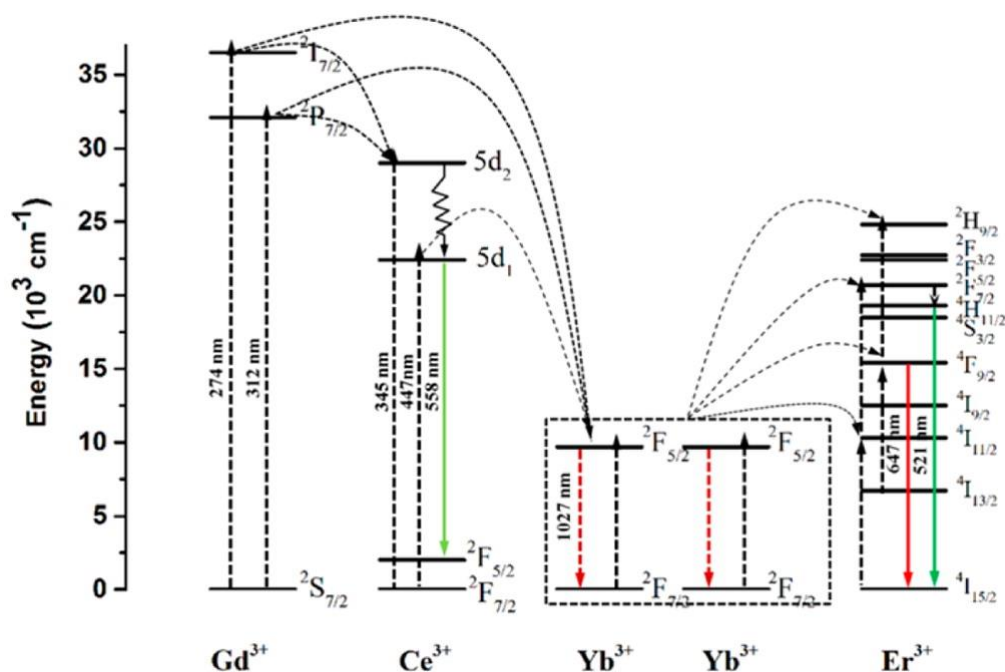


Figure 1.11: Schematics of energy levels diagrams of Yb³⁺, Gd³⁺, Ce³⁺, and Er³⁺. Among all lanthanides Yb³⁺ possesses clean valence energy level structure involving only two states. Reprinted with permission from ref. 76. Copyright 2016 American Chemical Society.

1.5 CsPbX₃ (X = Cl, Br, I) perovskite semiconductors.

Both charge carrier mobility and carrier lifetime of semiconductors are strongly dependent on interference of trap states (deep defect states). To get high quality semiconductor, one way is to get rid of trap states. Typically, high synthesis temperature >1000 °C is a way although costly to obtain high quality Si semiconductor used in solar panels or epitaxial growth of GaAs is another way but even more expensive. A different approach is to design defect tolerant novel semiconductors. For example, CsPbX₃ perovskites show good semiconducting properties despite having defects as discussed in section 1.1. Thus, one can solution processes these lead halide perovskite in a cheaper way while retaining good semiconductor properties. As a result, these lead halides perovskite have recently dominated in photovoltaic's research and an increase in solar cell efficiency from ~4% to ~23% is achieved within six years.² The superior optoelectronic performance of lead halide perovskite despite having defects arises due to its defect-tolerant band structure wherein defect states do not fall deep within the midgap.^{1, 79} This breakthrough in lead halide perovskite has changed the way of our thinking to design novel semiconductor materials and is the central material studied in this thesis.

1.5.1 CsPbX₃ perovskite structure

CsPbX₃ perovskites show temperature or pressure dependent structural polymorphic transitions and commonly encountered phases are cubic, tetragonal, and orthorhombic phases.⁸⁰ Cubic CsPbX₃ (X= Cl, Br, I) has crystal structure same as that of CaTiO₃ mineral which is named perovskite after Russian mineralogist Lev Perovski.⁸¹ This cubic perovskite structure has the highest symmetry compared to other polymorphs and is the simplest structure discussed in detail in this section.

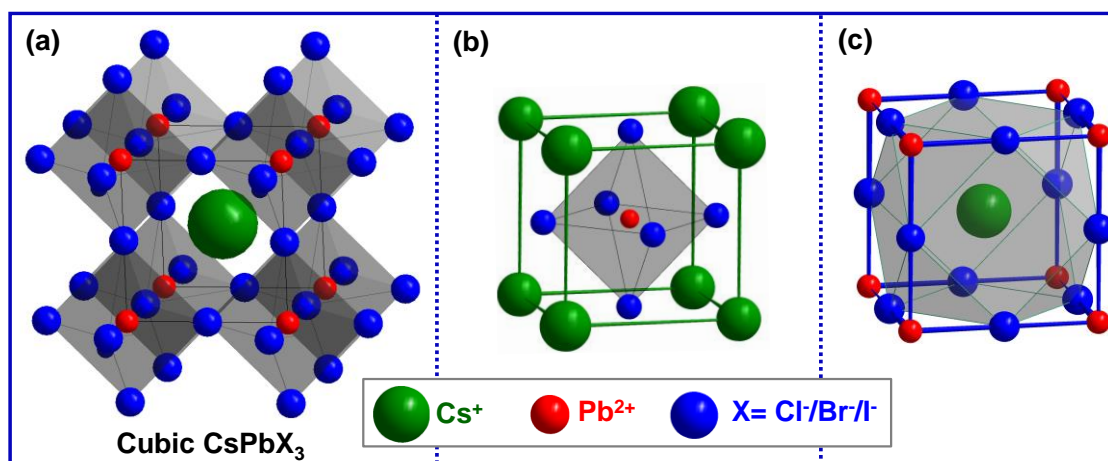


Figure 1.12: Schematics of cubic perovskite structure of CsPbX₃ similar to structure CaTiO₃ mineral. Unit cell of CsPbX₃ perovskite showing (b) six-fold coordination environment of Pb²⁺ cation, and (c) 12-fold coordination environment of Cs⁺ cation.

Simple cubic perovskite structure has three types of lattice positions popularly known as A-site, B-site and X-site for ABX₃ perovskite. A-site is occupied by large sized cation (Cs⁺), B-site is occupied by smaller cation (Pb²⁺) and anion occupies X-site. The total charge on A and B cation is neutralized by total anion charge in its empirical formulae. Simple cubic perovskite structure is shown in Figure 1.12a and corresponding unit cell shown in Figure 1.12b-c in two different ways. The B-site (Pb²⁺) has a coordination number 6 (see octahedral arrangement of X⁻ around Pb²⁺ in Figure 1.12b) while A-site has 12-fold coordination environment (see cuboctahedral arrangement of X⁻ around Cs⁺ in Figure 1.12c). Thus overall cubic perovskite structure has three dimensional arrangement of corner shared {PbX₆}⁴⁻ octahedra (see Figure 1.12a) and the voids created in this arrangement are occupied by A-site (Cs⁺) cation. Similar corner shared {PbX₆}⁴⁻ octahedra are present in orthorhombic or tetragonal phases but differ in bond angle between Pb-X-Pb and arrangement of A-site (Cs⁺) cation. In case of CsPbX₃ perovskites, both Pb and X orbitals contribute in the formation CB minimum (CBM) and VB maximum (VBM) which are responsible for transport of charge carriers. So this connectivity of {PbX₆}⁴⁻ octahedra in perovskite structure is crucial to

achieve efficient transport of charge carriers. A-site cation (Cs^+) doesn't contribute directly to VBM or CBM and role of Cs^+ is to maintain charge neutrality and to stabilize the 3D structure of $\{\text{PbX}_6\}^{4-}$ octahedra. Although other cations such as CH_3NH_3^+ with different size than Cs^+ can indirectly influence the band gap of APbX_3 perovskite through lattice expansion or contraction.

1.5.2 Evolution of lead halide perovskites

Long back in 1958, Moller reported that CsPbX_3 crystals are intensely colored and exists in the perovskite structure.⁸² Later, in 1999 Kagan et al reported thin film field effect transistor from organic-inorganic Sn based perovskite.⁸³ At that time reasonably good field effect mobility was reported ($\sim 0.6 \text{ cm}^2\text{V}^{-1}\text{s}^{-1}$). After nearly one decade in 2009, Kojima et al. reported solar cell based on organic-inorganic ($\text{CH}_3\text{NH}_3\text{PbI}_3$) perovskite photoactive material with 3.8% efficiency and interestingly an open circuit voltage (V_{oc}) $\sim 0.96 \text{ V}$.⁸⁴ Soon after this in 2012, two reports appeared with solar cell efficiency around 10% based on same $\text{CH}_3\text{NH}_3\text{PbI}_3$ perovskite as the photoactive material.⁸⁵⁻⁸⁶ Subsequently, first high efficiency solar cell based on $\text{CH}_3\text{NH}_3\text{PbI}_3$ with efficiency more than 18% was reported in 2015 by Jeon et al.⁸⁷ Presently, certified solar cell efficiency $\sim 23.3\%$ is reported in $\text{CH}_3\text{NH}_3\text{PbI}_3$ perovskite based solar cell.² This unprecedented increase in solar cell efficiency in $\text{CH}_3\text{NH}_3\text{PbI}_3$ perovskite within short span of time is a breakthrough in photovoltaic industry. But, organic-inorganic lead halide perovskite suffer from poor thermal stability due to the presence of volatile organic component (CH_3NH_3^+).⁸⁸ Replacing organic cation (CH_3NH_3^+) with Cs^+ improves thermal stability and also retains the defect tolerance character because both VBM and CBM are responsible for optical and transport properties are contributed by lead and halide orbitals only.⁸⁹ In 2015, Protesescu et al. reported colloidal CsPbX_3 NCs for the first time.³ At present, many other optical and optoelectronic properties including LEDs, lasing and photodetector are being studied extensively.

1.5.3 CsPbX_3 perovskite nanocrystals and defect tolerance

The first report on CsPbX_3 perovskite NCs showed narrow emission spectral width (12 - 42 nm) and high PLQY $\sim 90\%$ from these NCs.³ Although organic-inorganic lead halide perovskite NCs were reported one year before in 2014 but lesser PLQY $\sim 20\%$ was reported at that time.⁹⁰ The later report where CsPbX_3 perovskite NCs show $\sim 90\%$ PLQY despite having high SAV ratio and without any core-shell type surface modification is indeed remarkable. Therefore, surface defects also show minimal interference in optical properties. This triggered prompt reaction among researchers across globe and during last three years

countless research articles have been published on these CsPbX_3 perovskite NCs.^{3, 91} Recently, CsPbX_3 perovskite NCs exhibit EQE beyond 20% matching with commercial LEDs,⁴ solar cells beyond 16% efficiency mark,⁹²⁻⁹³ reduced PL blinking,⁹¹ and low threshold for lasing.⁹⁴ Another advantage of CsPbX_3 perovskite NCs is that the composition can be tuned with wider flexibility allowing tuning of optical band gap in the entire visible region as shown in Figure 1.13a-b.³ The photographs in Figure 1.13a show intense emission color under UV-lamp. The tuning of optical properties through size/shape dependent quantum confinement adds more flavour in exploration of CsPbX_3 NCs. It is to be noted that the first report suggested cubic perovskite structure adopted by these CsPbX_3 NCs.³ Shortly, Swarnkar et al. showed that CsPbBr_3 NCs exist in orthorhombic perovskite phase similar to bulk CsPbBr_3 .⁵³ Interestingly, they compared narrow emission line width (~ 85 meV) in CsPbBr_3 NCs with other benchmark CdSe, core-shell type CdSe/CdS-ZnS or organic rhodamine-6G dye (see Figure 1.13c). Clearly, the emission color purity of CsPbBr_3 NCs is far better than other two categories of materials.

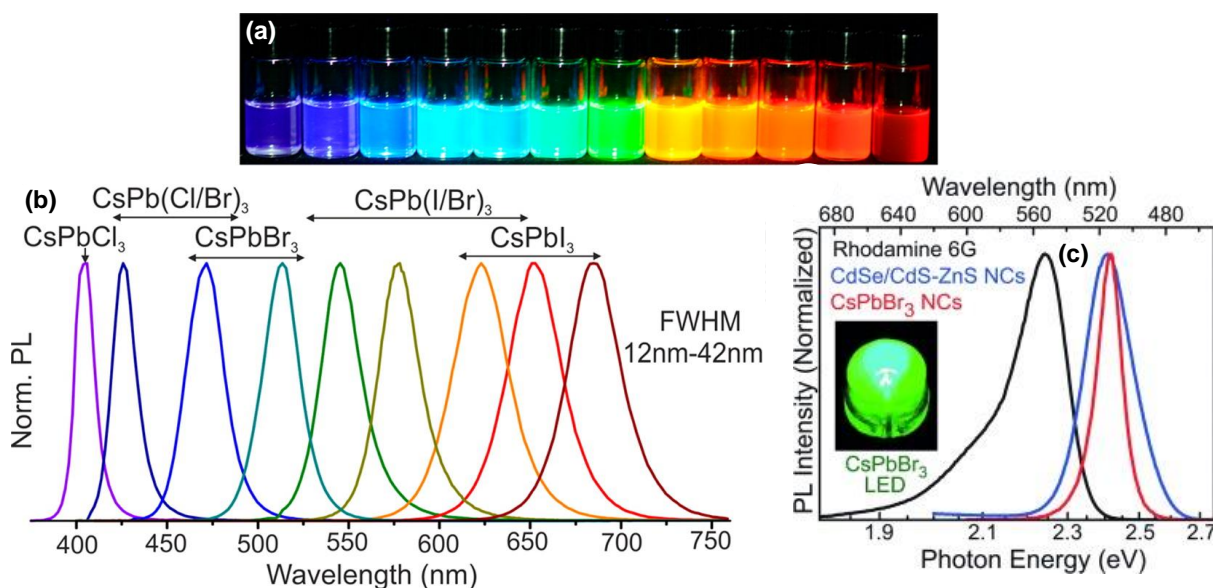


Figure 1.13: (a) Photographs of colloidal CsPbX_3 NCs dispersions under UV light showing bright luminescence colors depending upon compositions. (b) PL spectra of CsPbX_3 perovskite NCs with tunable emission in the entire visible region depending on halide composition. (c) PL spectra of CsPbBr_3 NCs compared with CdSe/CdS-ZnS core-shell type heterostructured NCs and organic fluorophore rhodamine 6G. Panel a-b is reprinted from ref. 41 which is an open access article under ACS Editor's Choice category. Panel c is reprinted with permission from ref. 91. Copyright 2015 Wiley-VCH.

The origin of novel PL properties in CsPbX_3 perovskite NCs is attributed to its unique electronic band structure.^{79, 95} Figure 1.14 compares schematics of valence orbital band diagram of CsPbX_3 and II-VI (CdSe) or III-V (GaAs) semiconductors.¹ Due to the filled outer valence shell inert pair $6s^2$ present on Pb^{2+} , VBM in CsPbX_3 is antibonding in nature

whereas, in the case of CdSe or GaAs, the VBM has bonding contribution. Moreover in CsPbX₃ band structure, CBM is stabilized by spin-orbit coupling unlike the case of II-VI, and III-V semiconductors. Thus, the combination of antibonding nature of VBM and stabilization of CBM through spin orbit coupling is rare and distinctive in CsPbX₃ perovskite. In this unique band structure, any non-bonding defect state from dangling bonds are expected to either resonate within bands or forms shallow levels near VBM or CBM.⁹⁶ Such materials are termed as defect-tolerant semiconductors while traditional CdSe NCs are termed as defect-intolerant semiconductors. Eventually, a defect tolerant CsPbX₃ perovskite NCs are ideal host to dope optically active metal ions such as Mn and Yb. In this thesis we combine novel defect tolerant CsPbX₃ perovskite NCs and dopants (Mn or Yb) to tailor optical functionality of doped CsPbX₃ NCs.

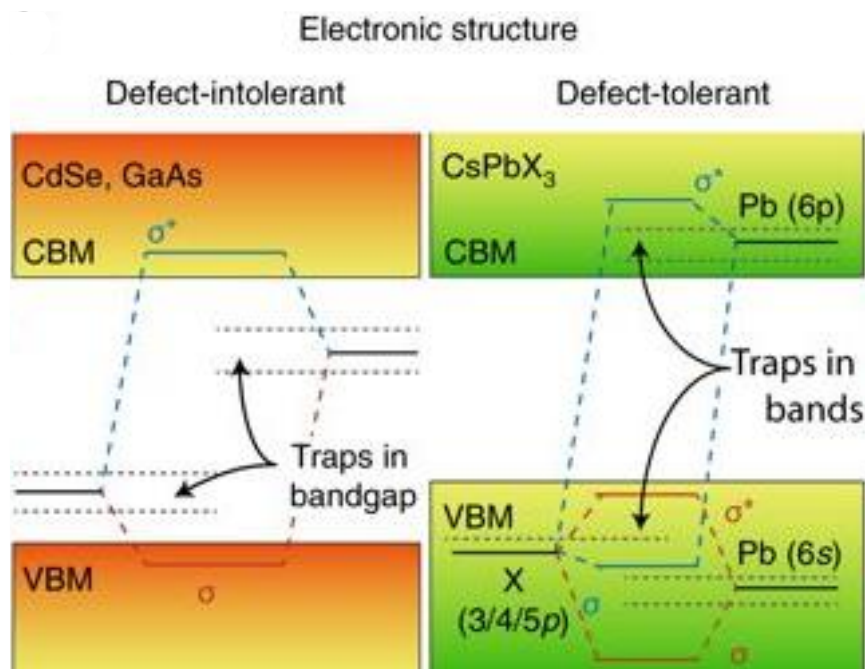


Figure 1.14: Schematics of valence band structure of II-VI or III-V semiconductors (CdSe or GaAs) in comparison with defect tolerant band structure of CsPbX₃ perovskite semiconductors. Reprinted with permission from ref. 1. Copyright 2018 Nature Publishing Group.

1.6 Ease and challenges in doping CsPbX₃ NCs

So far, two major strategies have been developed to dope CsPbX₃ perovskite NCs, 1) one pot synthesis where lead and dopant precursor are added together and reaction is carried out leading to simultaneous nucleation and doping,⁹⁷ 2) postsynthesis strategy involving either substitution of Pb by dopant metal aided by anion exchange⁹⁸⁻⁹⁹ or anion exchange of pre-doped CsPbCl₃ NCs to other compositions of doped-CsPbX₃ host NCs.¹⁰⁰ The widely explored approach of doping in CsPbX₃ perovskite NCs is one pot strategy or co-nucleation

doping see schematics in Figure 1.15a.³² In this co-nucleation doping, the doping and nucleation occur simultaneously and cannot be decoupled unlike growth doping or dopant-nucleation doping see schematics in Figure 1.15b-c. The latter two strategies namely growth doping and dopant-nucleation doping are widely explored strategies to dope II-VI semiconductor NCs but not yet successfully demonstrated to dope CsPbX₃ NCs.

One pot synthesis of doping in CsPbX₃ perovskite NCs is widely successful to dope Mn and Yb in CsPbCl₃ NCs, but faces challenges to dope CsPbBr₃ or CsPbI₃ NCs.¹⁰⁰ This is probably due to fact that Mn or Yb precursor dissolve as oleate precursor in organic solvents containing strong Mn-O (402 KJ mol⁻¹) or Yb-O (387 KJ mol⁻¹) bonds.¹⁰¹ On the other hand strength of Pb-X bonds decreases from Pb-Cl (301 KJ mol⁻¹) to Pb-Br (248 KJ mol⁻¹) and Pb-I (194 KJ mol⁻¹).¹⁰¹ As a result, the weaker Pb-Br and Pb-I bonds in CsPbBr₃ and CsPbI₃ NCs create problem in co-nucleation step of doping in presence of strong Mn-O or Yb-O bond. Recently, one pot colloidal synthesis of Mn-doping in CsPbBr₃ NCs is achieved in presence of HBr which reduces strong Mn-O bonds to weaker Mn-Br bonds thus favouring co-nucleation step.¹⁰²

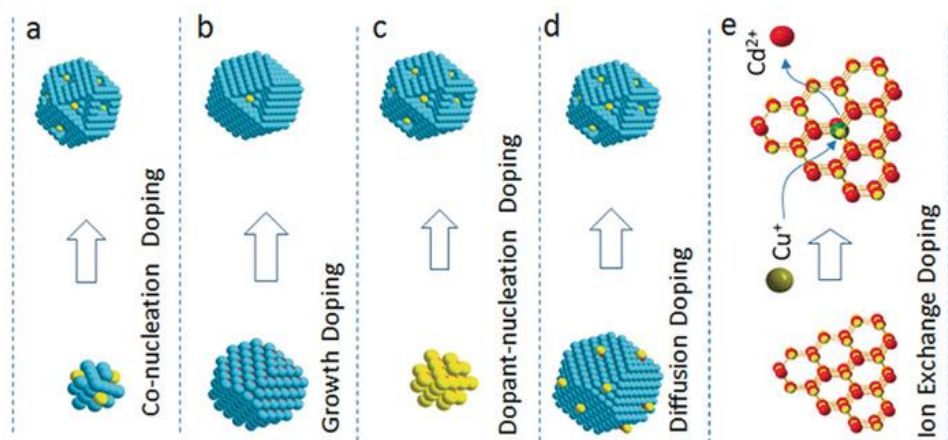


Figure 1.15: Schematics of vastly explored doping strategies to dope II-VI semiconductor NCs, (a) co-nucleation doping, (b) growth doping, (c) dopant-nucleation doping, (d) diffusion doping and (e) ion exchange doping. Co-nucleation doping and ion-exchange processes are widely adapted strategies to dope CsPbX₃ perovskite NCs. Panel a-e is reprinted with permission from ref. 32. Copyright 2017 Wiley-VCH.

Another approach to address doping challenge is diffusion doping or ion-exchange doping see schematics in Figure 1.15d-e.³² In diffusion controlled doping, the insertion of dopants into crystal lattice NCs is achieved through diffusion process often aided with annealing in II-VI semiconductor NCs. This type of strategy again if tried in a conventional way involving use of oleate precursors dissolved in organic solvents fails to dope CsPbBr₃ or CsPbI₃ NCs.

Chapter 3 and 4 in this thesis discusses novel postsynthesis strategy to achieve Mn and Yb doping in CsPbBr₃ and CsPbI₃ NCs at room temperature. On the other hand, ion-exchange doping where typically cation is exchanged is well known for II-VI semiconductor NCs, but CsPbX₃ NCs show reluctance towards cation exchange processes. There are few reports where cation exchange of Pb with Mn aided by anion exchange process is claimed but leads to increases in band gap by forming mixed halide Mn-doped CsPb(Br,Cl)₃ NCs.⁹⁸⁻⁹⁹ However, benefitting from fast anion exchange processes in CsPbX₃ NCs. Pre-doped CsPbCl₃ NCs can be used as templates for synthesizing other doped compositions as well.¹⁰⁰ This anion exchange is a newer strategy to dope all compositions of CsPbX₃ but in traditional II-VI semiconductor NCs favourable cation exchange is used to dope metal ions.

Doping can be substitutional where dopant replaces the native atom from its lattice position or interstitial where dopant sits in the interstitial site of host lattice. In both the cases doping metal ion in semiconductor NCs including CsPbX₃ perovskite NCs is often associated with strain affecting quality of crystals. Annealing at high temperature improves quality of crystals by kicking out these defects. In order to minimize this strain and to achieve successful doping in II-VI semiconductor NCs, often dopants with ionic radii similar to the substituted host ion is chosen.

1.7 Doping for stability of CsPbX₃ perovskite NCs

Till now we discussed doping with the idea of tailoring properties. But in recent time, a new direction has been introduced. It has been reported that Mn-doping can improve stability of CsPbX₃ perovskite NCs.¹⁰³⁻¹⁰⁴ Importantly, there is an outstanding problem, that the optoelectronically active black perovskite phase of CsPbI₃ NCs has limited stability in ambient conditions at room temperature. The black phase transforms to the optoelectronically inactive yellow phase with time.¹⁰⁴ It has been proposed that doping Mn improve the stability of the black phase of CsPbI₃ NCs, without deteriorating the optoelectronic properties of the host.¹⁰⁴ This interesting observation has motivated us to understand the mechanistic insights behind improved stability of Mn-doped CsPbI₃ NCs. Chapter 4 of this thesis discusses the issue in details.

1.8 Pb-free perovskites

Toxicity and instability of Pb-halide perovskite, along with scientific curiosity lead to extensive search for Pb-free perovskites. In order to look for possible replacements for Pb²⁺, one way is to look for metal halides exhibiting defect tolerant electronic band structure

similar to CsPbX₃ perovskite. Two major aspects wherein metal ions possess nS^2 electrons in outermost S orbital giving rise to antibonding VBM and stabilization of CBM through spin orbit coupling are considered to be prerequisite for such defect tolerant band structure. Table 1.1 highlights possible replacements of Pb²⁺ with other ions having same valence electronic configuration and thus outermost nS^2 electrons. Replacement of Pb²⁺ by these cations thus expected to retain the antibonding nature of VBM.

	Ge ²⁺	
In ⁺	Sn ²⁺	Sb ³⁺
Tl ⁺	Pb ²⁺	Bi ³⁺

Table 1.1: P-block elements having same valence electronic configuration as that of Pb²⁺ and thus outermost valence shell nS^2 inert pair of electrons. Ge²⁺, Sn²⁺, and In⁺ shown in red are unstable oxidation states.

Replacing Pb²⁺ with Sn²⁺ or Ge²⁺ from same group of periodic table see Table 1.1 are ideal choices since the charge of B-site cation remains +2, that is required to retain 3D perovskite structure. However, Sn based analogue CsSnX₃ perovskite NCs have been reported but exhibit poor PLQY (< 1%) probably due to weak spin orbit coupling of CBM.¹⁰⁵ More importantly, Sn²⁺/Sn⁴⁺ oxidation potential is -0.15 V compared to oxidation potential of Pb²⁺/Pb⁴⁺ (-1.67 V) and suggests Sn²⁺ is prone to oxidation.¹⁰⁶ Ge in +2 oxidation state is even more unstable and readily oxidizes to Ge⁴⁺ (Ge²⁺/Ge⁴⁺ = 0 V).¹⁰⁶ These instabilities of Sn and Ge in +2 oxidation state is not serving the purpose and control over such parameters is difficult to achieve. Although, Sn⁴⁺ based Cs₂SnI₆ having vacancy ordered double perovskite structure have been reported in bulk and NCs of various shapes.¹⁰⁷⁻¹⁰⁸ But again PLQY reported is < 1% not expected from a defect tolerant system. Replacing Pb²⁺ with Sb³⁺ creates charge imbalance in perovskite structure and thus leads to decrease in structural dimensionality to a 2D layered perovskite.¹⁰⁹ Nevertheless, Cs₃Sb₂I₉ and Rb₃Sb₂I₉ 2D layered perovskites NCs also showed poor PLQY (~6.7%).¹⁰⁹⁻¹¹⁰ Also reduction in dimensionality decreases band dispersion and thus increase in effective masses, which is detrimental for carrier mobilities. Similarly, Cs₃Bi₂X₉ NCs were also reported in low dimensional structures with poor PLQY (< 1%).¹¹⁰ On the other hand replacing Pb²⁺ with Tl⁺ retains both outermost nS^2 inert pair and strong spin orbit coupling of CBM in TlX. We note that Pb²⁺ and Tl⁺ are isoelectronic However, TlX doesn't exist in perovskite structure. But electronic band

structure of TIX is very similar to that of CsPbX₃ perovskite. This motivated us to explore synthesis and photophysics of TIX (X = Br, I) NCs discussed in detail in chapter 5 of this thesis.

Another strategy to design Pb-free metal halide perovskites is 3D double halide perovskites. Two divalent Pb²⁺ cations when replaced with one monovalent (M⁺) and other with trivalent (M³⁺) cation forms Cs₂M⁺M³⁺X₆ double perovskite structure see Figure 1.16.¹¹¹ M³⁺ are mostly Bi³⁺ and Sb³⁺ retaining outermost s orbital inert pair, while M⁺ cations are Cu⁺, Ag⁺, Tl⁺, Au⁺ and In⁺. The major advantage for double perovskite is that the charge neutrality can be maintained by two different kinds of cations, which lead to the formation of desired 3D perovskite phase. A total of 11 compounds were predicted to be both stable with suitable band gaps using first-principle calculations.¹¹¹ However, later it was reported that most of these double perovskites have large and indirect band gaps see ref.¹¹²⁻¹¹³

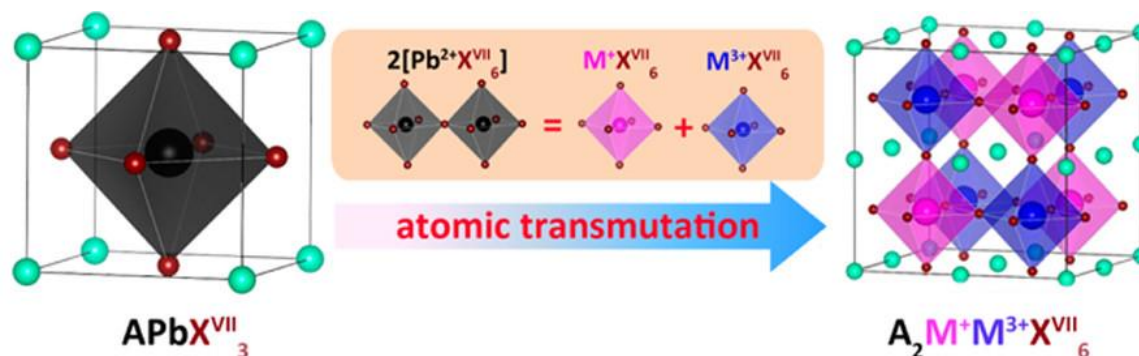


Figure 1.16: Transmutation of two Pb²⁺ cation in APbX₃ (CsPbX₃) perovskite structure by one monovalent (M⁺) and one trivalent (M³⁺) cations forms metal halide double perovskite structure with general formulae A₂M⁺M³⁺X₆. Reprinted with permission from ref. 111. Copyright 2017 American Chemical Society.

Overall, different Pb-free metal halides perovskite are still being explored. But unfortunately, optoelectronic performance of Pb-free perovskite are still inferior compared to Pb-based perovskite.

1.9 Scope of this thesis

In 2015, CsPbX₃ (X = Cl, Br, I) perovskite NCs emerged as novel defect tolerant semiconductor NCs exhibiting 90% PLQY with narrow emission linewidth.³ There was a need to combine the defect tolerant CsPbX₃ host perovskites with the dopant properties to tailor optical functionality and to enhance the stability of host perovskite structure.

When I started my PhD, no synthesis protocols were reported to dope these newly emerged defect tolerant CsPbX₃ hosts. Consequently, a major scope of my thesis became the synthesis

of Mn- and Yb-doped CsPbX₃ perovskite NCs. We reported Mn-doping in CsPbCl₃ NPLs for the first time exhibiting Mn-emission employing one pot synthesis at room temperature discussed in chapter 2. But the same Mn-doping in narrower band gap CsPbBr₃ host NCs through one pot synthesis did not work well. Also, the role of Mn-doping on optical properties of Mn-doped CsPbCl₃ NCs showed inconsistency in three reports including ours at that time.^{97, 100, 114} There was then need of novel strategy to dope narrower band gap CsPbBr₃ perovskite NCs and to study in a controlled way, the role of dopants on optical properties of host NCs. We then addressed this challenge in chapter 3 employing novel postsynthesis strategy, first to achieve Mn-doping in narrower band gap CsPbBr₃ NCs, and then the role of Mn-doping on optical properties of host is studied more reliably. On the other hand, lanthanide (Ln³⁺) doping in semiconductor hosts was challenging due to unfavourable tetrahedral coordination environment in semiconductors such as CdSe, Si, GaAs etc. Interestingly, Pb²⁺ in CsPbX₃ perovskite structure has octahedral coordination environment and are narrower band gap semiconductor host for Ln³⁺ doping. We, therefore dope Yb³⁺ dopant, the one with the simplest f-orbital valence energy structure among all Ln³⁺ dopants by simply extending our postsynthesis strategy for Yb-doping. Subsequently, we report Yb-doping in all composition of CsPbX₃ (X = Cl, Br, I) perovskite NCs including various shapes. Yb-doping in narrower band gap CsPbBr₃ and CsPbI₃ NCs is observed for the first time employing our postsynthesis strategy unlike prior reports of Yb-doping in wider band gap CsPbCl₃ or CsPbCl_{3-x}Br_x NCs.^{53, 74}

So far, we employed doping to tailor optical properties but a new direction was reported that, doping Mn²⁺ can improve structural stability of host CsPbX₃ perovskite NCs.¹⁰³⁻¹⁰⁴ But, one genuine concern is that undoped and Mn-doped CsPbX₃ NCs were obtained in two different batches of reactions.¹⁰³⁻¹⁰⁴ Thus synthesis related inhomogeneity of host NCs could overestimate the role of Mn-dopant. Consequently, there was need of controlled experiments to examine stability aspect of CsPbX₃ perovskite NCs upon doping Mn. We, therefore employed our postsynthesis strategy to understand more reliably the role of Mn-doping on structural stability of host CsPbX₃ NCs in chapter 4. Synthesis related inhomogeneity of size, shape, and structure of host CsPbX₃ NCs can be neglected in our postsynthesis. In addition, postsynthesis doping allows us to study surface vs lattice contribution stabilizing doped CsPbX₃ NCs. Our key finding is that lattice contraction and surface passivation of Mn-doped CsPbI₃ NCs improves black phase stability compared to undoped CsPbI₃ NCs.

Finally, metal halides analogous to CsPbX₃ perovskite need to be explored to design Pb-free defect tolerant semiconductor NCs. We find that Tl⁺ is ideal choice for replacing Pb²⁺ because both Pb²⁺ and Tl⁺ are isoelectronic species. Also, TlX show strong spin orbit coupling of CBM similar to the case of CsPbX₃ perovskites. Thus, TlX and CsPbX₃ perovskite have similar valence electronic band structure. We, therefore, explored Pb-free TlX (X = Br, I) NCs synthesis for the first time which exist in non-perovskite structure but with a scope of defect tolerant nature in chapter 5. PL spectroscopy along with THz spectroscopy were employed to see interference of traps in optical and optoelectronic properties of TlX NCs discussed in chapter 5.

1.10 References

1. Akkerman, Q. A.; Rainò, G.; Kovalenko, M. V.; Manna, L. Genesis, Challenges and Opportunities for Colloidal Lead Halide Perovskite Nanocrystals. *Nat. Mater.* **2018**, *17*, 394-405.
2. NREL Best Research Solar Cell Efficiencies (<https://www.nrel.gov/pv/assets/pdfs/pv-efficiencies-07-17-2018.pdf>), (accessed, 30 January 2019).
3. Protesescu, L.; Yakunin, S.; Bodnarchuk, M. I.; Krieg, F.; Caputo, R.; Hendon, C. H.; Yang, R. X.; Walsh, A.; Kovalenko, M. V. Nanocrystals of Cesium Lead Halide Perovskites (CsPbX₃, X = Cl, Br, and I): Novel Optoelectronic Materials Showing Bright Emission with Wide Color Gamut. *Nano Lett.* **2015**, *15*, 3692-3696.
4. Chiba, T.; Hayashi, Y.; Ebe, H.; Hoshi, K.; Sato, J.; Sato, S.; Pu, Y.-J.; Ohisa, S.; Kido, J. Anion-Exchange Red Perovskite Quantum Dots with Ammonium Iodine Salts for Highly Efficient Light-Emitting Devices. *Nat. Photonics* **2018**, *12*, 681-687.
5. Talapin, D. V.; Lee, J.-S.; Kovalenko, M. V.; Shevchenko, E. V. Prospects of Colloidal Nanocrystals for Electronic and Optoelectronic Applications. *Chem. Rev.* **2010**, *110*, 389-458.
6. Yu, W. W.; Qu, L.; Guo, W.; Peng, X. Experimental Determination of the Extinction Coefficient of CdTe, CdSe, and CdS Nanocrystals. *Chem. Mater.* **2003**, *15*, 2854-2860.
7. Alivisatos, A. P. Semiconductor Clusters, Nanocrystals, and Quantum Dots. *Science* **1996**, *271*, 933-937.
8. Donegá, C. d. M. Synthesis and Properties of Colloidal Heteronanocrystals. *Chem. Soc. Rev.* **2011**, *40*, 1512-1546.
9. Boles, M. A.; Engel, M.; Talapin, D. V. Self-Assembly of Colloidal Nanocrystals: From Intricate Structures to Functional Materials. *Chem. Rev.* **2016**, *116*, 11220-11289.

10. Ashby, M. F.; Ferreira, P. J.; Schodek, D. L. Chapter 2 - An Evolutionary Perspective. In *Nanomaterials, Nanotechnologies and Design*, 1st Edition, Butterworth-Heinemann: Boston, 2009, 17-39.
11. Faraday, M. X. The Bakerian Lecture: Experimental Relations of Gold (and Other Metals) to Light. *Philosophical Transactions of the Royal Society London*. **1857**, 147, 145-181.
12. Goddard III, A. W.; Brenner, D.; Lyshevski, E. S.; Iafrate, J. G. *Handbook of Nanoscience, Engineering, and Technology*, 3rd Edition, CRC press.
13. Evans, B. L.; Young, P. A. Delocalized Excitons in Thin Anisotropic Crystals. *Phys. Status Solidi B* **1968**, 25, 417-425.
14. Yoffe, A. D. Low-Dimensional Systems: Quantum Size Effects and Electronic Properties of Semiconductor Microcrystallites (Zero-Dimensional Systems) and Some Quasi-Two-Dimensional Systems. *Adv. Phys.* **1993**, 42, 173-262.
15. Ekimov, A.; Onuschenko, A.; Tsekhomskii, V. Exciton Light Absorption by CuCl Microcrystals in Glass Matrix. *Sov. Glass Phys. Chem.* **1980**, 6, 511-512.
16. Efros, A. L.; Efros, A. L. Interband Absorption of Light in a Semiconductor Sphere. *Sov. Phys. Semicond.* **1982**, 16, 772-775.
17. Brus, L. E. Electron–Electron and Electron-Hole Interactions in Small Semiconductor Crystallites: The Size Dependence of the Lowest Excited Electronic State. *J. Chem. Phys.* **1984**, 80, 4403-4409.
18. Henglein, A. Photo-Degradation and Fluorescence of Colloidal-Cadmium Sulfide in Aqueous Solution. *Berichte der Bunsengesellschaft für physikalische Chemie* **1982**, 86, 301-305.
19. Brus, L. E. A Simple Model for the Ionization Potential, Electron Affinity, and Aqueous Redox Potentials of Small Semiconductor Crystallites. *J. Chem. Phys.* **1983**, 79, 5566-5571.
20. Brus, L. Quantum Crystallites and Nonlinear Optics. *Appl. Phys. A* **1991**, 53, 465-474.
21. Gaponenko, S. V. *Optical Properties of Semiconductor Nanocrystals*. Cambridge University Press: Cambridge, 1998.
22. Castellan, G. W. *Physical Chemistry*. Addison-Wesley, 1973.
23. Chukwuocha, E. O.; Onyeaju, M. C.; Harry, T. S. T. Theoretical Studies on the Effect of Confinement on Quantum Dots Using the Brus Equation. *World J. Condens. Matter Phys.* **2012**, 2, 5.
24. Kayanuma, Y. Quantum-Size Effects of Interacting Electrons and Holes in Semiconductor Microcrystals with Spherical Shape. *Phys. Rev. B* **1988**, 38, 9797-9805.

25. Mir, W. J.; Swarnkar, A.; Sharma, R.; Katti, A.; Adarsh, K. V.; Nag, A. Origin of Unusual Excitonic Absorption and Emission from Colloidal Ag₂S Nanocrystals: Ultrafast Photophysics and Solar Cell. *J. Phys. Chem. Lett.* **2015**, *6*, 3915-3922.
26. Roduner, E. Size Matters: Why Nanomaterials Are Different. *Chem. Soc. Rev.* **2006**, *35*, 583-592.
27. Rotello, V. M. *Nanoparticles: Building Blocks for Nanotechnology*. Springer, **2004**.
28. Zeng, J.; Zhang, Q.; Chen, J.; Xia, Y. A Comparison Study of the Catalytic Properties of Au-Based Nanocages, Nanoboxes, and Nanoparticles. *Nano Lett.* **2010**, *10*, 30-35.
29. Haruta, M.; Daté, M. Advances in the Catalysis of Au Nanoparticles. *Appl. Catal., A* **2001**, *222*, 427-437.
30. Guisbiers, G.; Abudukelimu, G.; Hourlier, D. Size-Dependent Catalytic and Melting Properties of Platinum-Palladium Nanoparticles. *Nanoscale Res. Lett.* **2011**, *6*, 396.
31. Nel, A.; Xia, T.; Mädler, L.; Li, N. Toxic Potential of Materials at the Nanolevel. *Science* **2006**, *311*, 622-627.
32. Pradhan, N.; Das Adhikari, S.; Nag, A.; Sarma, D. D. Luminescence, Plasmonic, and Magnetic Properties of Doped Semiconductor Nanocrystals. *Angew. Chem., Int. Ed.* **2017**, *56*, 7038-7054.
33. Ohno, H. Making Nonmagnetic Semiconductors Ferromagnetic. *Science* **1998**, *281*, 951-956.
34. Gilstrap Jr., R. A.; Capozzi, C. J.; Carson, C. G.; Gerhardt, R. A.; Summers, C. J. Synthesis of a Nonagglomerated Indium Tin Oxide Nanoparticle Dispersion. *Adv. Mater.* **2008**, *20*, 4163-4166.
35. Tandon, B.; Shanker, G. S.; Nag, A. Multifunctional Sn- and Fe-Codoped In₂O₃ Colloidal Nanocrystals: Plasmonics and Magnetism. *J. Phys. Chem. Lett.* **2014**, *5*, 2306-2311.
36. Kim, J.; Ong, G. K.; Wang, Y.; LeBlanc, G.; Williams, T. E.; Mattox, T. M.; Helms, B. A.; Milliron, D. J. Nanocomposite Architecture for Rapid, Spectrally-Selective Electrochromic Modulation of Solar Transmittance. *Nano Lett.* **2015**, *15*, 5574-5579.
37. Mendelsberg, R. J.; McBride, P. M.; Duong, J. T.; Bailey, M. J.; Llordes, A.; Milliron, D. J.; Helms, B. A. Dispersible Plasmonic Doped Metal Oxide Nanocrystal Sensors That Optically Track Redox Reactions in Aqueous Media with Single-Electron Sensitivity. *Adv. Opt. Mater.* **2015**, *3*, 1293-1300.
38. Hwang, I.; Kim, H.; Kim, J.-E.; Park, H. Y.; Lim, H. Solid Solubilities of Magnetic Ions in Diluted Magnetic Semiconductors Grown under Equilibrium Conditions. *Phys. Rev. B* **1994**, *50*, 8849-8852.

39. Nag, A.; Chakraborty, S.; Sarma, D. D. To Dope Mn^{2+} in a Semiconducting Nanocrystal. *J. Am. Chem. Soc.* **2008**, *130*, 10605-10611.
40. Erwin, S. C.; Zu, L.; Haftel, M. I.; Efros, A. L.; Kennedy, T. A.; Norris, D. J. Doping Semiconductor Nanocrystals. *Nature* **2005**, *436*, 91.
41. Yu, J. H., et al. Giant Zeeman Splitting in Nucleation-Controlled Doped $CdSe:Mn^{2+}$ Quantum Nanoribbons. *Nat. Mater.* **2009**, *9*, 47.
42. Bussian, D. A.; Crooker, S. A.; Yin, M.; Brynda, M.; Efros, A. L.; Klimov, V. I. Tunable Magnetic Exchange Interactions in Manganese-Doped Inverted Core–Shell $ZnSe-CdSe$ nanocrystals. *Nat. Mater.* **2008**, *8*, 35.
43. Fainblat, R.; Barrows, C. J.; Hopmann, E.; Siebeneicher, S.; Vlaskin, V. A.; Gamelin, D. R.; Bacher, G. Giant Excitonic Exchange Splittings at Zero Field in Single Colloidal $CdSe$ Quantum Dots Doped with Individual Mn^{2+} Impurities. *Nano Lett.* **2016**, *16*, 6371-6377.
44. Beaulac, R.; Archer, P. I.; Ochsenein, S. T.; Gamelin, D. R. Mn^{2+} -Doped $CdSe$ Quantum Dots: New Inorganic Materials for Spin-Electronics and Spin-Photonics. *Adv. Funct. Mater.* **2008**, *18*, 3873-3891.
45. Li, Z.-J.; Hofman, E.; Blaker, A.; Davis, A. H.; Dzikovski, B.; Ma, D.-K.; Zheng, W. Interface Engineering of Mn-Doped $ZnSe$ -Based Core/Shell Nanowires for Tunable Host–Dopant Coupling. *ACS Nano* **2017**, *11*, 12591-12600.
46. Brovelli, S.; Galland, C.; Viswanatha, R.; Klimov, V. I. Tuning Radiative Recombination in Cu-Doped Nanocrystals Via Electrochemical Control of Surface Trapping. *Nano Lett.* **2012**, *12*, 4372-4379.
47. Meinardi, F.; Akkerman, Q. A.; Bruni, F.; Park, S.; Mauri, M.; Dang, Z.; Manna, L.; Brovelli, S. Doped Halide Perovskite Nanocrystals for Reabsorption-Free Luminescent Solar Concentrators. *ACS Energy Lett.* **2017**, *2*, 2368-2377.
48. Erickson, C. S.; Bradshaw, L. R.; McDowall, S.; Gilbertson, J. D.; Gamelin, D. R.; Patrick, D. L. Zero-Reabsorption Doped-Nanocrystal Luminescent Solar Concentrators. *ACS Nano* **2014**, *8*, 3461-3467.
49. Bradshaw, L. R.; Knowles, K. E.; McDowall, S.; Gamelin, D. R. Nanocrystals for Luminescent Solar Concentrators. *Nano Lett.* **2015**, *15*, 1315-1323.
50. Meinardi, F.; Ehrenberg, S.; Dharmo, L.; Carulli, F.; Mauri, M.; Bruni, F.; Simonutti, R.; Kortshagen, U.; Brovelli, S. Highly Efficient Luminescent Solar Concentrators Based on Earth-Abundant Indirect-Bandgap Silicon Quantum Dots. *Nat. Photonics* **2017**, *11*, 177.

51. Wang, F.; Yang, M.; Ji, S.; Yang, L.; Zhao, J.; Liu, H.; Sui, Y.; Sun, Y.; Yang, J.; Zhang, X. Boosting Spectral Response of Multi-Crystalline Si Solar Cells with Mn²⁺ Doped CsPbCl₃ Quantum Dots Downconverter. *J. Power Sources* **2018**, *395*, 85-91.
52. Wang, Q.; Zhang, X.; Jin, Z.; Zhang, J.; Gao, Z.; Li, Y.; Liu, S. F. Energy-Down-Shift CsPbCl₃:Mn Quantum Dots for Boosting the Efficiency and Stability of Perovskite Solar Cells. *ACS Energy Lett.* **2017**, *2*, 1479-1486.
53. Zhou, D.; Liu, D.; Pan, G.; Chen, X.; Li, D.; Xu, W.; Bai, X.; Song, H. Cerium and Ytterbium Codoped Halide Perovskite Quantum Dots: A Novel and Efficient Downconverter for Improving the Performance of Silicon Solar Cells. *Adv. Mater.* **2017**, *29*, 1704149.
54. Milstein, T. J.; Kroupa, D. M.; Gamelin, D. R. Picosecond Quantum Cutting Generates Photoluminescence Quantum Yields over 100% in Ytterbium-Doped CsPbCl₃ Nanocrystals. *Nano Lett.* **2018**, *18*, 3792-3799.
55. Beaulac, R.; Archer, P. I.; Liu, X.; Lee, S.; Salley, G. M.; Dobrowolska, M.; Furdyna, J. K.; Gamelin, D. R. Spin-Polarizable Excitonic Luminescence in Colloidal Mn²⁺-Doped CdSe Quantum Dots. *Nano Lett.* **2008**, *8*, 1197-1201.
56. Bhargava, R. N.; Gallagher, D.; Hong, X.; Nurmikko, A. Optical Properties of Manganese-Doped Nanocrystals of ZnS. *Phys. Rev. Lett.* **1994**, *72*, 416-419.
57. Seufert, J.; Bacher, G.; Scheibner, M.; Forchel, A.; Lee, S.; Dobrowolska, M.; Furdyna, J. K. Dynamical Spin Response in Semimagnetic Quantum Dots. *Phys. Rev. Lett.* **2001**, *88*, 027402.
58. Dexter, D. L. A Theory of Sensitized Luminescence in Solids. *J. Chem. Phys.* **1953**, *21*, 836-850.
59. Hazarika, A.; Layek, A.; De, S.; Nag, A.; Debnath, S.; Mahadevan, P.; Chowdhury, A.; Sarma, D. D. Ultranarrow and Widely Tunable Mn²⁺-Induced Photoluminescence from Single Mn-Doped Nanocrystals of ZnS-CdS Alloys. *Phys. Rev. Lett.* **2013**, *110*, 267401.
60. Heer, S.; Kömpe, K.; Güdel, H.-U.; Haase, M. Highly Efficient Multicolour Upconversion Emission in Transparent Colloids of Lanthanide-Doped NaYF₄ Nanocrystals. *Adv. Mater.* **2004**, *16*, 2102-2105.
61. Wang, F.; Liu, X. Recent Advances in the Chemistry of Lanthanide-Doped Upconversion Nanocrystals. *Chem. Soc. Rev.* **2009**, *38*, 976-989.
62. Martín-Rodríguez, R.; Geitenbeek, R.; Meijerink, A. Incorporation and Luminescence of Yb³⁺ in CdSe Nanocrystals. *J. Am. Chem. Soc.* **2013**, *135*, 13668-13671.
63. Creutz, S. E.; Fainblat, R.; Kim, Y.; De Siena, M. C.; Gamelin, D. R. A Selective Cation Exchange Strategy for the Synthesis of Colloidal Yb³⁺-Doped Chalcogenide Nanocrystals

with Strong Broadband Visible Absorption and Long-Lived near-Infrared Emission. *J. Am. Chem. Soc.* **2017**, *139*, 11814-11824.

64. Mahalingam, V.; Vetrone, F.; Naccache, R.; Speghini, A.; Capobianco, J. A. Colloidal $\text{Tm}^{3+}/\text{Yb}^{3+}$ -Doped LiYF_4 Nanocrystals: Multiple Luminescence Spanning the UV to NIR Regions Via Low-Energy Excitation. *Adv. Mater.* **2009**, *21*, 4025-4028.

65. Moore, E. G.; Samuel, A. P. S.; Raymond, K. N. From Antenna to Assay: Lessons Learned in Lanthanide Luminescence. *Acc. Chem. Res.* **2009**, *42*, 542-552.

66. Agbo, P.; Abergel, R. J. Ligand-Sensitized Lanthanide Nanocrystals: Merging Solid-State Photophysics and Molecular Solution Chemistry. *Inorg. Chem.* **2016**, *55*, 9973-9980.

67. Hu, J.-Y.; Ning, Y.; Meng, Y.-S.; Zhang, J.; Wu, Z.-Y.; Gao, S.; Zhang, J.-L. Highly near-IR Emissive Ytterbium(III) Complexes with Unprecedented Quantum Yields. *Chem. Sci.* **2017**, *8*, 2702-2709.

68. Wegh, R. T.; Donker, H.; Oskam, K. D.; Meijerink, A. Visible Quantum Cutting in $\text{LiGdF}_4:\text{Eu}^{3+}$ through Downconversion. *Science* **1999**, *283*, 663-666.

69. Eilers, J. J.; Biner, D.; Wijngaarden, J. T. v.; Krämer, K.; Güdel, H.-U.; Meijerink, A. Efficient Visible to Infrared Quantum Cutting through Downconversion with the $\text{Er}^{3+}-\text{Yb}^{3+}$ Couple in $\text{Cs}_3\text{Y}_2\text{Br}_9$. *Appl. Phys. Lett.* **2010**, *96*, 151106.

70. Bol, A. A.; van Beek, R.; Meijerink, A. On the Incorporation of Trivalent Rare Earth Ions in II–VI Semiconductor Nanocrystals. *Chem. Mater.* **2002**, *14*, 1121-1126.

71. Raola, O. E.; Strouse, G. F. Synthesis and Characterization of Eu-Doped Cadmium Selenide Nanocrystals. *Nano Lett.* **2002**, *2*, 1443-1447.

72. Chengelis, D. A.; Yingling, A. M.; Badger, P. D.; Shade, C. M.; Petoud, S. Incorporating Lanthanide Cations with Cadmium Selenide Nanocrystals: A Strategy to Sensitize and Protect Tb(III). *J. Am. Chem. Soc.* **2005**, *127*, 16752-16753.

73. Dethlefsen, J. R.; Mikhailovsky, A. A.; Burks, P. T.; Døssing, A.; Ford, P. C. Lanthanide Modification of CdSe/ZnS Core/Shell Quantum Dots. *J. Phys. Chem. C* **2012**, *116*, 23713-23720.

74. Pan, G., et al. Doping Lanthanide into Perovskite Nanocrystals: Highly Improved and Expanded Optical Properties. *Nano Lett.* **2017**, *17*, 8005-8011.

75. Ravi, V. K.; Markad, G. B.; Nag, A. Band Edge Energies and Excitonic Transition Probabilities of Colloidal CsPbX_3 (X = Cl, Br, I) Perovskite Nanocrystals. *ACS Energy Lett.* **2016**, *1*, 665-671.

76. Luo, Z.-H.; Liu, Y.-F.; Zhang, C.-H.; Zhang, J.-X.; Qin, H.-M.; Jiang, H.-C.; Jiang, J. Effect of Yb³⁺ on the Crystal Structural Modification and Photoluminescence Properties of GGAG:Ce³⁺. *Inorg. Chem.* **2016**, *55*, 3040-3046.
77. Rabouw, F. T.; Prins, P. T.; Villanueva-Delgado, P.; Castelijns, M.; Geitenbeek, R. G.; Meijerink, A. Quenching Pathways in NaYF₄:Er³⁺,Yb³⁺ Upconversion Nanocrystals. *ACS Nano* **2018**, *12*, 4812-4823.
78. Shavaleev, N. M.; Scopelliti, R.; Gummy, F.; Bünzli, J.-C. G. Surprisingly Bright near-Infrared Luminescence and Short Radiative Lifetimes of Ytterbium in Hetero-Binuclear Yb–Na Chelates. *Inorg. Chem.* **2009**, *48*, 7937-7946.
79. Brandt, R. E.; Stevanović, V.; Ginley, D. S.; Buonassisi, T. Identifying Defect-Tolerant Semiconductors with High Minority-Carrier Lifetimes: Beyond Hybrid Lead Halide Perovskites. *MRS Commun.* **2015**, *5*, 265-275.
80. Stoumpos, C. C.; Kanatzidis, M. G. The Renaissance of Halide Perovskites and Their Evolution as Emerging Semiconductors. *Acc. Chem. Res.* **2015**, *48*, 2791-2802.
81. Kay, H. F.; Bailey, P. C. Structure and Properties of CaTiO₃. *Acta Crystallogr.* **1957**, *10*, 219-226.
82. Moller, C. K. Crystal Structure and Photoconductivity of Cæsium Plumbahalides. *Nature* **1958**, *182*, 1436.
83. Kagan, C. R.; Mitzi, D. B.; Dimitrakopoulos, C. D. Organic-Inorganic Hybrid Materials as Semiconducting Channels in Thin-Film Field-Effect Transistors. *Science* **1999**, *286*, 945-947.
84. Kojima, A.; Teshima, K.; Shirai, Y.; Miyasaka, T. Organometal Halide Perovskites as Visible-Light Sensitizers for Photovoltaic Cells. *J. Am. Chem. Soc.* **2009**, *131*, 6050-6051.
85. Kim, H.-S., et al. Lead Iodide Perovskite Sensitized All-Solid-State Submicron Thin Film Mesoscopic Solar Cell with Efficiency Exceeding 9%. *Sci. Rep.* **2012**, *2*, 591.
86. Lee, M. M.; Teuscher, J.; Miyasaka, T.; Murakami, T. N.; Snaith, H. J. Efficient Hybrid Solar Cells Based on Meso-Superstructured Organometal Halide Perovskites. *Science* **2012**, *338*, 643-647.
87. Jeon, N. J.; Noh, J. H.; Yang, W. S.; Kim, Y. C.; Ryu, S.; Seo, J.; Seok, S. I. Compositional Engineering of Perovskite Materials for High-Performance Solar Cells. *Nature* **2015**, *517*, 476.
88. Juarez-Perez, E. J.; Hawash, Z.; Raga, S. R.; Ono, L. K.; Qi, Y. Thermal Degradation of CH₃NH₃PbI₃ Perovskite into NH₃ and CH₃I Gases Observed by Coupled Thermogravimetry–Mass Spectrometry Analysis. *Energy Environ. Sci.* **2016**, *9*, 3406-3410.

89. Kulbak, M.; Gupta, S.; Kedem, N.; Levine, I.; Bendikov, T.; Hodes, G.; Cahen, D. Cesium Enhances Long-Term Stability of Lead Bromide Perovskite-Based Solar Cells. *J. Phys. Chem. Lett.* **2016**, *7*, 167-172.
90. Schmidt, L. C.; Pertegás, A.; González-Carrero, S.; Malinkiewicz, O.; Agouram, S.; Mínguez Espallargas, G.; Bolink, H. J.; Galian, R. E.; Pérez-Prieto, J. Nontemplate Synthesis of CH₃NH₃PbBr₃ Perovskite Nanoparticles. *J. Am. Chem. Soc.* **2014**, *136*, 850-853.
91. Swarnkar, A.; Chulliyil, R.; Ravi, V. K.; Irfanullah, M.; Chowdhury, A.; Nag, A. Colloidal CsPbBr₃ Perovskite Nanocrystals: Luminescence Beyond Traditional Quantum Dots. *Angew. Chem., Int. Ed.* **2015**, *54*, 15424-15428.
92. Han, J.; Luo, S.; Yin, X.; Zhou, Y.; Nan, H.; Li, J.; Li, X.; Oron, D.; Shen, H.; Lin, H. Hybrid PbS Quantum-Dot-in-Perovskite for High-Efficiency Perovskite Solar Cell. *Small* **2018**, *14*, 1801016.
93. Swarnkar, A.; Marshall, A. R.; Sanhira, E. M.; Chernomordik, B. D.; Moore, D. T.; Christians, J. A.; Chakrabarti, T.; Luther, J. M. Quantum Dot-Induced Phase Stabilization of α -CsPbI₃ Perovskite for High-Efficiency Photovoltaics. *Science* **2016**, *354*, 92-95.
94. Yakunin, S.; Protesescu, L.; Krieg, F.; Bodnarchuk, M. I.; Nedelcu, G.; Humer, M.; De Luca, G.; Fiebig, M.; Heiss, W.; Kovalenko, M. V. Low-Threshold Amplified Spontaneous Emission and Lasing from Colloidal Nanocrystals of Caesium Lead Halide Perovskites. *Nat. Commun.* **2015**, *6*, 8056.
95. Filippetti, A.; Mattoni, A. Hybrid Perovskites for Photovoltaics: Insights from First Principles. *Phys. Rev. B* **2014**, *89*, 125203.
96. Kang, J.; Wang, L.-W. High Defect Tolerance in Lead Halide Perovskite CsPbBr₃. *J. Phys. Chem. Lett.* **2017**, *8*, 489-493.
97. Parobek, D.; Roman, B. J.; Dong, Y.; Jin, H.; Lee, E.; Sheldon, M.; Son, D. H. Exciton-to-Dopant Energy Transfer in Mn-Doped Cesium Lead Halide Perovskite Nanocrystals. *Nano Lett.* **2016**, *16*, 7376-7380.
98. Huang, G.; Wang, C.; Xu, S.; Zong, S.; Lu, J.; Wang, Z.; Lu, C.; Cui, Y. Postsynthetic Doping of MnCl₂ Molecules into Preformed CsPbBr₃ Perovskite Nanocrystals Via a Halide Exchange-Driven Cation Exchange. *Adv. Mater.* **2017**, *29*, 1700095.
99. Chen, D.; Zhou, S.; Fang, G.; Chen, X.; Zhong, J. Fast Room-Temperature Cation Exchange Synthesis of Mn-Doped CsPbCl₃ Nanocrystals Driven by Dynamic Halogen Exchange. *ACS Appl. Mater. Interfaces* **2018**, *10*, 39872-39878.

100. Liu, W.; Lin, Q.; Li, H.; Wu, K.; Robel, I.; Pietryga, J. M.; Klimov, V. I. Mn²⁺-Doped Lead Halide Perovskite Nanocrystals with Dual-Color Emission Controlled by Halide Content. *J. Am. Chem. Soc.* **2016**, *138*, 14954-14961.
101. Luo, Y. R. Bond Dissociation Energies in Diatomic molecules. <https://notendur.hi.is/agust/rannsoknir/papers/2010-91-CRC-BDEs-Tables.pdf>.
102. Parobek, D.; Dong, Y.; Qiao, T.; Son, D. H. Direct Hot-Injection Synthesis of Mn-Doped CsPbBr₃ Nanocrystals. *Chem. Mater.* **2018**, *30*, 2939-2944.
103. Zou, S., et al. Stabilizing Cesium Lead Halide Perovskite Lattice through Mn(II) Substitution for Air-Stable Light-Emitting Diodes. *J. Am. Chem. Soc.* **2017**, *139*, 11443-11450.
104. Akkerman, Q. A.; Meggiolaro, D.; Dang, Z.; De Angelis, F.; Manna, L. Fluorescent Alloy CsPb_xMn_{1-x}I₃ Perovskite Nanocrystals with High Structural and Optical Stability. *ACS Energy Lett.* **2017**, *2*, 2183-2186.
105. Jellicoe, T. C., et al. Synthesis and Optical Properties of Lead-Free Cesium Tin Halide Perovskite Nanocrystals. *J. Am. Chem. Soc.* **2016**, *138*, 2941-2944.
106. Atkins, P.; Atkins, P. W.; de Paula, J. *Atkin's Physical Chemistry*, OUP Oxford, 2014.
107. Maughan, A. E.; Ganose, A. M.; Bordelon, M. M.; Miller, E. M.; Scanlon, D. O.; Neilson, J. R. Defect Tolerance to Intolerance in the Vacancy-Ordered Double Perovskite Semiconductors Cs₂SnI₆ and Cs₂TeI₆. *J. Am. Chem. Soc.* **2016**, *138*, 8453-8464.
108. Wang, A.; Yan, X.; Zhang, M.; Sun, S.; Yang, M.; Shen, W.; Pan, X.; Wang, P.; Deng, Z. Controlled Synthesis of Lead-Free and Stable Perovskite Derivative Cs₂SnI₆ Nanocrystals Via a Facile Hot-Injection Process. *Chem. Mater.* **2016**, *28*, 8132-8140.
109. Pal, J.; Manna, S.; Mondal, A.; Das, S.; Adarsh, K. V.; Nag, A. Colloidal Synthesis and Photophysics of M₃Sb₂I₉ (M = Cs and Rb) Nanocrystals: Lead-Free Perovskites. *Angew. Chem., Int. Ed.* **2017**, *56*, 14187-14191.
110. Yang, B.; Chen, J.; Yang, S.; Hong, F.; Sun, L.; Han, P.; Pullerits, T.; Deng, W.; Han, K. Lead-Free Silver-Bismuth Halide Double Perovskite Nanocrystals. *Angew. Chem., Int. Ed.* **2018**, *57*, 5359-5363.
111. Zhao, X.-G.; Yang, J.-H.; Fu, Y.; Yang, D.; Xu, Q.; Yu, L.; Wei, S.-H.; Zhang, L. Design of Lead-Free Inorganic Halide Perovskites for Solar Cells Via Cation-Transmutation. *J. Am. Chem. Soc.* **2017**, *139*, 2630-2638.
112. Meng, W.; Wang, X.; Xiao, Z.; Wang, J.; Mitzi, D. B.; Yan, Y. Parity-Forbidden Transitions and Their Impact on the Optical Absorption Properties of Lead-Free Metal Halide Perovskites and Double Perovskites. *J. Phys. Chem. Lett.* **2017**, *8*, 2999-3007.

113. Xiao, Z.; Du, K.-Z.; Meng, W.; Wang, J.; Mitzi, D. B.; Yan, Y. Intrinsic Instability of $\text{Cs}_2\text{In(I)M(III)X}_6$ (M = Bi, Sb; X = Halogen) Double Perovskites: A Combined Density Functional Theory and Experimental Study. *J. Am. Chem. Soc.* **2017**, *139*, 6054-6057.

114. Mir, W. J.; Jagadeeswararao, M.; Das, S.; Nag, A. Colloidal Mn-Doped Cesium Lead Halide Perovskite Nanoplatelets. *ACS Energy Lett.* **2017**, *2*, 537-543.

Chapter 2

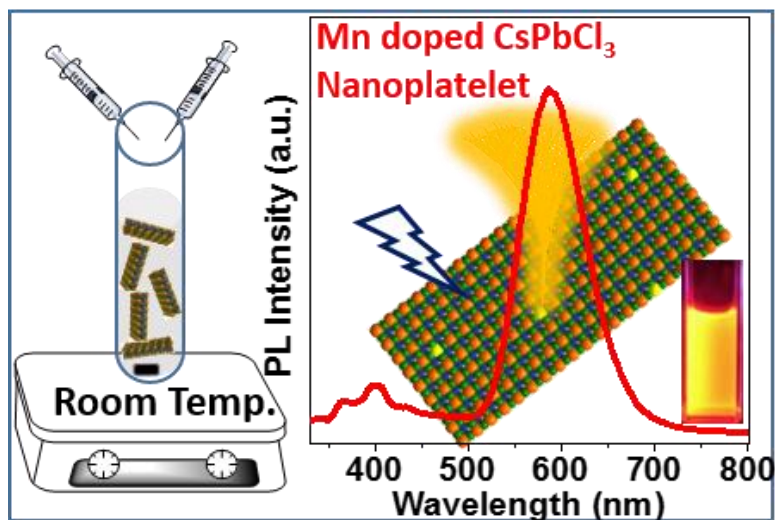
Doping Mn in Colloidal Cesium Lead Chloride Perovskite Nanoplatelets

.....
The work presented in this chapter is published under following details. Mir, J. W.; Jagadeeswararao, M.; Das, S.; Nag, A. *ACS Energy Lett.* **2017**, *2*, 537–543. This is an open access article under the ACS AuthorChoice category.

Abstract

Strong quantum confinement in Mn-doped semiconductor nanocrystals enhances dopant-carrier exchange interactions. Here, we report the synthesis and optical properties of strongly quantum confined, quasi two-dimensional, Mn-doped CsPbCl₃ nanoplatelets. A room-temperature synthesis was employed to prepare the platelets with thickness 2.3 nm (4 monolayers), which is significantly smaller than the Bohr excitonic diameter (5 nm) of CsPbCl₃. Efficient transfer of excitonic energy of the host to the Mn²⁺ dopant ions lead to a spin-forbidden $^4T_1 \rightarrow ^6A_1$ Mn *d*-electron emission with the highest quantum yield ~20%, and exhibit a long lifetime of 1.6 ms. Anion exchange reactions at room temperature lead to the formation of Mn-doped CsPbBr₃ nanoplatelets, with weak Mn-emission. These newly developed Mn-doped cesium lead halide nanoplatelets are suitable candidates to explore the manifestation of quantum confinement on dopant-carrier exchange interaction, exhibiting interesting magneto-optical properties.

Graphical abstract



2.1 Introduction

Doping Mn^{2+} ions in a low-dimensional semiconductor nanocrystal (NC) in the quantum confinement regime provides fascinating optical,¹⁻³ magneto-optical,⁴⁻⁷ and light harvesting,⁸⁻¹⁰ properties mainly because of the interaction of quantum confined charge carriers of the host with the dopant ions. A defect-free semiconductor host NC will be ideal to realize the efficacy of such phenomena. In this regard, colloidal cesium lead halide (CsPbX_3 , X = Cl, Br, I) perovskite NCs have been recently proven to be a better defect-tolerant material compared to traditional CdSe based NCs.^{11-15,16} Therefore, developing synthetic methodologies for Mn-doping in low-dimensional CsPbX_3 NCs is naturally desired. Very recently (in October 2016), two reports appeared almost simultaneously demonstrating Mn-doping in CsPbX_3 nanocubes,¹⁷⁻¹⁸ but in both the cases, size of nanocubes were too big to exhibit strong quantum confinement effect. Here we report Mn-doping in CsPbCl_3 nanoplatelets (NPLs), exhibiting strong quantum confinement.

CsPbX_3 NCs exhibited a plethora of interesting properties including, ~90% photoluminescence (PL) quantum efficiency with narrow spectral width (FWHM = 85 meV),¹¹ reduced PL blinking,¹² low threshold for lasing,¹⁹ and a high carrier mobility within a NC measured using terahertz photoconductivity¹⁴. These intrinsic properties have also been culminated into optoelectronic devices such as efficient light emitting diodes (LEDs),^{13, 15, 20} solar cells,²¹ and photodetectors²². Better control of the synthesis of NCs and their surface chemistry is the key to realize the above mentioned properties and applications. Protesescu *et al* reported the first reliable synthesis of all-inorganic CsPbX_3 (X = Cl, Br, I) perovskite nanocubes.¹¹ Subsequently, Bekenstein *et al*²³ and Akkerman *et al*²⁴ reported the synthesis of CsPbX_3 NPLs employing different routes. There are other reports on controlling the shape and compositions of Pb-halide based perovskite NCs.^{25-27,28,29} Though a significant improvement has been made in the synthesis of these NCs including nanocubes, NPLs, and nanowires, still synthesizing stable nanocubes with edge-length smaller than 7 nm, and stable NPLs less than 2 nm thick, are challenging.³⁰ One unique advantage of all these NCs is the postsynthetic anion exchange among Cl, Br, and I achieving a desired composition with bandgap across the UV-visible region.^{31-33,34} Furthermore, growth of Au NCs on the corners of pre-synthesized CsPbX_3 nanocubes has been reported recently employing a simple route.³⁵

Development of synthetic chemistry of CsPbX_3 NCs is progressing in a rapid pace, and got further enriched by the recent reports of colloidal Mn-doped CsPbX_3 nanocubes.¹⁷⁻¹⁸ In both these reports, sizes of NCs were slightly bigger than the Bohr excitonic diameters, and

therefore, the host NC do not exhibit strong quantum confinement effect. However, quantum confinement of charge carriers (conduction band electron or valence band hole) of the host is known to enhance the *sp-d* interaction between charge carriers and Mn dopants resulting into giant Zeeman splitting of electronic states,⁵⁻⁶ which in turn exhibits interesting magneto-optic, and even futuristic solotronic-optoelectronic properties⁷ in Mn-doped CdSe NCs. Therefore, developing synthetic protocol of Mn doping in a quantum confined low-dimensional CsPbX₃ NC is an important step for future exploration of diluted magnetic semiconductor properties of such perovskite NCs. Here we report doping of Mn in a quasi two-dimensional CsPbX₃ NPLs exhibiting strong quantum confinement effect, and study the effect of excitonic energy transfer from the host to the dopant using PL.

2.2 Experimental Section

2.2.1 Preparation of Cs-oleate stock solution

CsCO₃ (1 mmol, 350 mg) was loaded in three neck round bottom flask (RB) along with 20 mL 1-octadecene (ODE) and 1.25 mL oleic acid (OA) following ref.²⁴ The reaction mixture was degassed minimum three time at 100 °C and then temperature is raised to 150 °C for complete dissolution of CsCO₃ in ODE. As prepared Cs-oleate solution is stored at room temperature.

2.2.2 Preparation of PbCl₂ solution with and without Mn²⁺ molecular precursor

PbCl₂ (2 mmol, 556.22 mg) was dissolved at room temperature in mixture of solvents containing 2 mL dimethyl sulfoxide (DMSO), 3 mL dimethylformamide (DMF), 0.25 mL HCl and 0.25 mL HNO₃. Total volume of solution is 5.5 mL. As obtained solution is divided into five parts with 1.0 mL PbCl₂ solution in each part. For doping Mn²⁺ in CsPbCl₃ NPLs, additionally x mol% MnCl₂.4H₂O with respect to Pb²⁺ was added and dissolved in 1.0 mL PbCl₂ solution. For (0 , 0.5 , 1 , 5 and 10 mol% Mn²⁺ with respect to Pb²⁺), a calculated amount of (0 mg, 0.39 mg, 0.79 mg, 4.15 mg, 7.91 mg) of MnCl₂ . 4H₂O was taken respectively for undoped and x mol% Mn-doped.

2.2.3 Synthesis of Mn-doped CsPbCl₃ nanoplatelets

All synthesis were carried out at room temperature under ambient atmosphere without extra purification or drying of chemicals and solvents used in this work. CsPbCl₃ NPLs were synthesized after modifying the reported synthesis described by Akkerman *et al.*²⁴ To a solution of 1.25 mL of ODE, 0.125 mL OA, 0.125 mL oleylamine (OLA) in a test tube at room temperature under vigorous stirring, 0.1 mL already prepared Cs-oleate stock solution

preheated to 100 °C was added and then 0.2 mL PbCl₂ with or without Mn²⁺ precursor solution prepared as mentioned above is swiftly injected followed by quick addition of 5 mL acetone. The immediate appearance of white precipitate upon addition of acetone as antisolvent signifies the formation of CsPbCl₃ NPLs. The supernatant is carefully thrown out and white precipitate of CsPbCl₃ NPLs is dispersed in hexane or toluene. Further washing is carried out carefully by using ethyl acetate as antisolvent and centrifuged at 4000 rpm followed by redispersion of precipitate in hexane. These colloidal CsPbCl₃ NPLs show natural tendency to aggregate within few days, however colloidal dispersion of CsPbCl₃ NPLs in hexane show prolonged colloidal stability upto a week under refrigeration.

2.2.4 Anion exchange

The anion exchange reaction in case of undoped and Mn-doped CsPbCl₃ to CsPbBr₃ NPLs was performed at room temperature. Typically 0.2 mL crude solution of CsPbCl₃ NPLs was diluted by adding 1 mL hexane in a glass vial under vigorous stirring and to this diluted solution 1mL PbBr₂ stock solution (PbBr₂ 261 mg dissolved in 1 mL OA, 1 mL OLA and 8 mL ODE at 130 °C) was swiftly injected. As obtained CsPbBr₃ NPLs were washed once using ethyl acetate and centrifuged at 6000 rpm followed by redispersing precipitate in hexane.

2.2.5 Characterization methods

Transmission electron microscopy (TEM) images and high resolution TEM (HRTEM) images were collected on a UHR FEG-TEM, JEOL JEM-2100F electron microscope using a 200 kV electron source. Atomic force microscopy (AFM) data were collected using Keysight atomic force microscope (model: AFM 5500) by using tapping mode technique. The sample for AFM measurement were prepared by drop casting dilute dispersion of CsPbCl₃ NPLs in hexane on a silicon wafer followed by flushing with nitrogen and then further drying under vacuum for about 6 hours. Powder X-ray diffraction (XRD) pattern were recorded for powder samples using a Bruker D8 Advance x-ray diffractometer using Cu K α radiation (1.54 Å). X-band electron paramagnetic resonance (EPR) measurements were performed on JEOL JES-FA200 ESR spectrometer at room temperature. Inductively coupled plasma optical emission spectroscopy (ICP-OES) data was obtained by employing ARCOS M/s. Spectro, Germany. Thermo scientific (Evolution 300) UV/Vis spectrometer was used for UV-visible absorption measurements. Steady state PL and PL decay dynamics were recorded on FLS 980 (Edinburgh Instruments) using microsecond flash lamp with power 100W and nano-second LED laser. For excitonic emission PL decay dynamics, 340 nm LED laser was used as

excitation source and PL decay dynamics of Mn-emission at 586 nm were recorded using microsecond flash lamp with 300 nm excitation. Photoluminescence quantum yield figures were obtained for fresh samples. For excitonic emission quinine sulfate dye solution in 0.5 M HCL was used as reference standard and for Mn-emission rhodamine 6G dye in distilled water was used as reference standard.

2.3 Results and Discussion

2.3.1 Synthesis of colloidal Mn-doped CsPbCl₃ NPLs

Colloidal Mn-doped CsPbCl₃ NPLs were prepared at room temperature under ambient atmosphere after modifying the method reported to prepare undoped CsPbBr₃ NPLs.²⁴ Schematic in Figure 2.1 shows the simple synthetic protocol. Colloidal stability of these NCs is for about 4-5 days, however, most of data presented here were measured using freshly prepared samples for a better comparative study. Elemental analysis using ICP-AES of the product show 0.1, 0.2, 0.8, and 2% Mn, for the added precursor concentration of 0.5, 1, 5, and 10 % Mn respectively, with respect to the Pb content. Clearly, only a small fraction of the added Mn was present in the final product, suggesting difficulty in Mn doping into CsPbCl₃ NPLs, similar to other reported^{36,37} semiconductor NCs. This Mn concentration of the product NC will be used as the dopant percentage throughout this chapter.

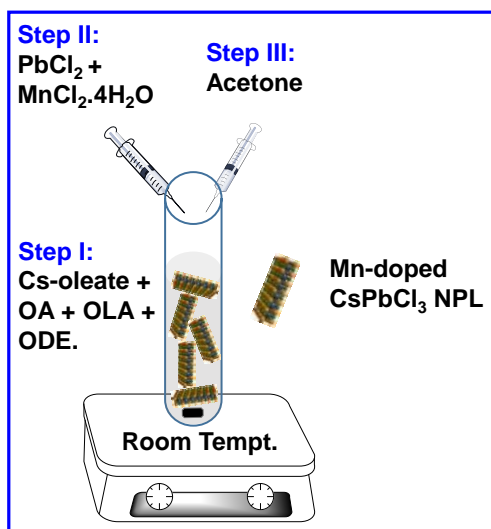


Figure 2.1: Schematics of synthesis of Mn-doped CsPbCl₃ NPLs carried out at room temperature and ambient conditions. OA, OLA and ODE are short notations for oleic acid, oleylamine and 1-octadecene respectively.

2.3.2 Morphology and dimensional analysis of Mn-doped NPLs

Morphological aspects of all undoped and Mn-doped samples are similar. We discuss here the morphology of 0.8% Mn doped CsPbCl₃ NPLs, as a representative case. Schematics in Figure 2.2a and recorded TEM image in Figure 2.2b show NPLs lying flat on TEM grid.

Inset of Figure 2.2b shows a magnified view of such NPLs. A concentrated solution of the sample often leads to face-to-face self-assembly of NPLs, and such self-assembled NPLs lies perpendicular on TEM grid, similar to prior reports^{23, 36} of CsPbBr₃ NPLs. Schematics in Figure 2.2c and recorded TEM image in Figure 2.2d show self-assembled region.

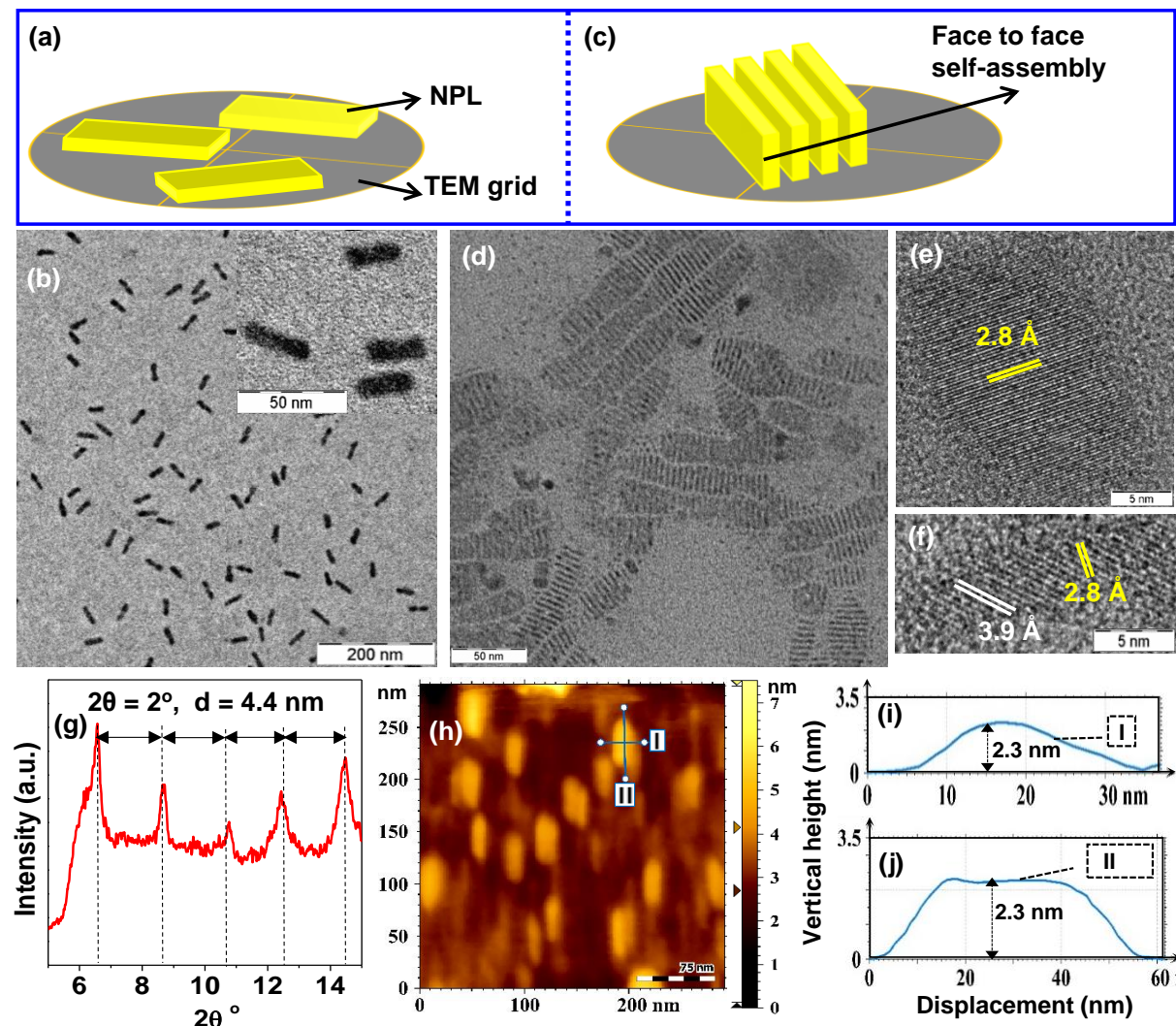


Figure 2.2: Morphology of 0.8% Mn-doped CsPbCl₃ NPLs. (a) Schematics of NPLs lying flat on TEM grid, and (b) TEM image of NPLs lying flat on the TEM grid; inset shows a magnified view. (c) Schematics of face to face self-assembly of NPLs and lying perpendicular on TEM grid. (d) TEM image of self-assembled NPLs lying perpendicular on TEM grid. HRTEM images showing lattice fringes for NPLS (e) lying flat, and (f) lying perpendicular on TEM grid. (g) Shows low-angle XRD data signifying the superstructure formation by the self-assembled NPLs. (h) AFM image of NPLs and corresponding height profiles (i and j) obtained from a NPL of the AFM image. Height profiles I (i) and II (j) represent the heights along the lines I and II in the AFM image, after considering the background height as zero.

These self-assembled NPLs in Figure 2.2d allow us to determine the thickness of our NPLs as 2.2 ± 0.3 nm. HRTEM image (Figure 2.2e) of a NPL lying flat on TEM grid shows the single crystalline nature of the NPL. The observed lattice planes can be assigned to both (200) plane

of cubic and (200) plane of tetragonal CsPbCl_3 . Likewise, the HRTEM image (Figure 2.2f) of the NPL lying perpendicular on TEM grid can be assigned to both (110) and (200) lattice planes for cubic and (101) and (200) and (002) plane of tetragonal phase. So the HRTEM images are not sufficient enough to distinguish between cubic and tetragonal phase of CsPbCl_3 NPLs, and the issue will be discussed later using powder XRD data. Low-angle XRD pattern of the sample shown in Figure 2.2g exhibits systematic diffraction peaks originating from the self-assembled superstructure of the NPLs. The hierarchical structure obtained by self-assembled stacking of NPLs is termed as superstructure. The interplanar distance of the superstructure obtained from such diffraction peaks correspond to 4.4 nm, which accounts for thickness of the NPL along with the capping layer. Furthermore, AFM image in Figure 2.2h and corresponding height profiles in Figure 2.2i and 2.2j, reveals the thickness of the NPLs as 2.3 nm. This 2.3 nm thickness corresponds to 4 monolayer (ML) of CsPbCl_3 NPL assuming cubic or tetragonal crystal phase.

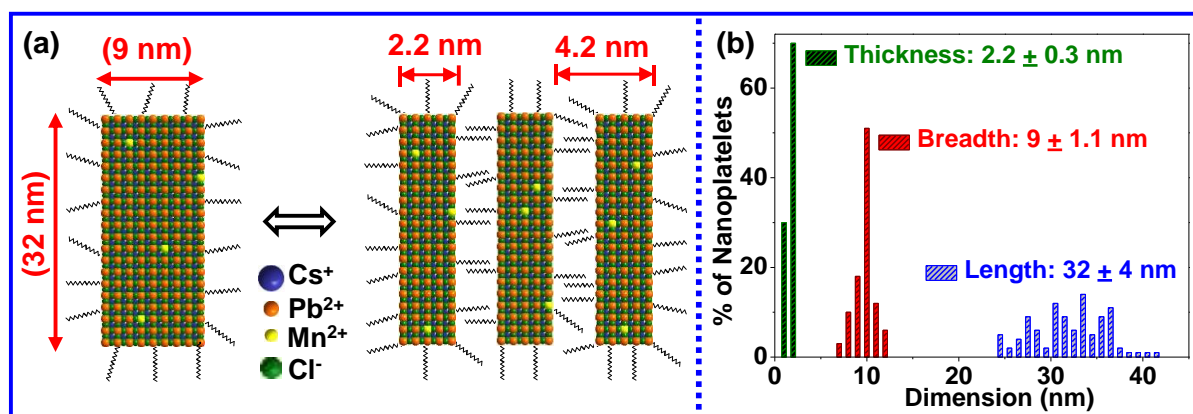


Figure 2.3: (a) Schematic representations of Mn-doped CsPbCl_3 NPL and their lateral dimensions, right side of panel (a) shows face-to-face self-assembly of 4 monolayer NPLs and the spacing in between NPLs. (b) Size-distribution plots of NPLs obtained from TEM images in Figure 2.2.

The obtained average dimensions and the self-assembly of Mn-doped CsPbCl_3 4 ML NPLs are schematically shown in the Figure 2.3a. The self-assembled NPLs are 2 nm apart which corresponds to the organic capping layer thickness as schematically shown in the right side panel of Figure 2.3a. Size distribution plots (Figure 2.3b) obtained from TEM images summarizes the morphology of CsPbCl_3 NPLs. These NPLs exhibit homogeneity in dimensions with length = 32 ± 4 nm, breadth = 9 ± 1.1 nm, and thickness = 2.2 ± 0.3 nm.

2.3.3 Structural evidence of Mn-doping in CsPbCl_3 NPL lattice

Bulk CsPbCl_3 are known to exhibit structural polymorphs around room temperature. XRD studies on bulk CsPbCl_3 by Moller suggested cubic is stable phase above 47 °C, which

undergoes a tetragonal distortion below 47 °C.³⁹ However the extent of tetragonal distortion is very small which is evident from a very small c/a ratio (1.007) at room temperature see Figure 2.4a. Clearly, there is no major difference between the cubic and tetragonal phase of bulk CsPbCl_3 . Later, electron paramagnetic resonance (EPR) studies suggested more polymorphs within a narrow temperature window between 25 and 47 °C.⁴⁰ The energy differences between these different structures are very small, and therefore, predicting the expected crystal structure for CsPbCl_3 NPLs at room temperature is challenging, because of the significant but unknown energy contributions arising from organic-capped surfaces of NPLs.

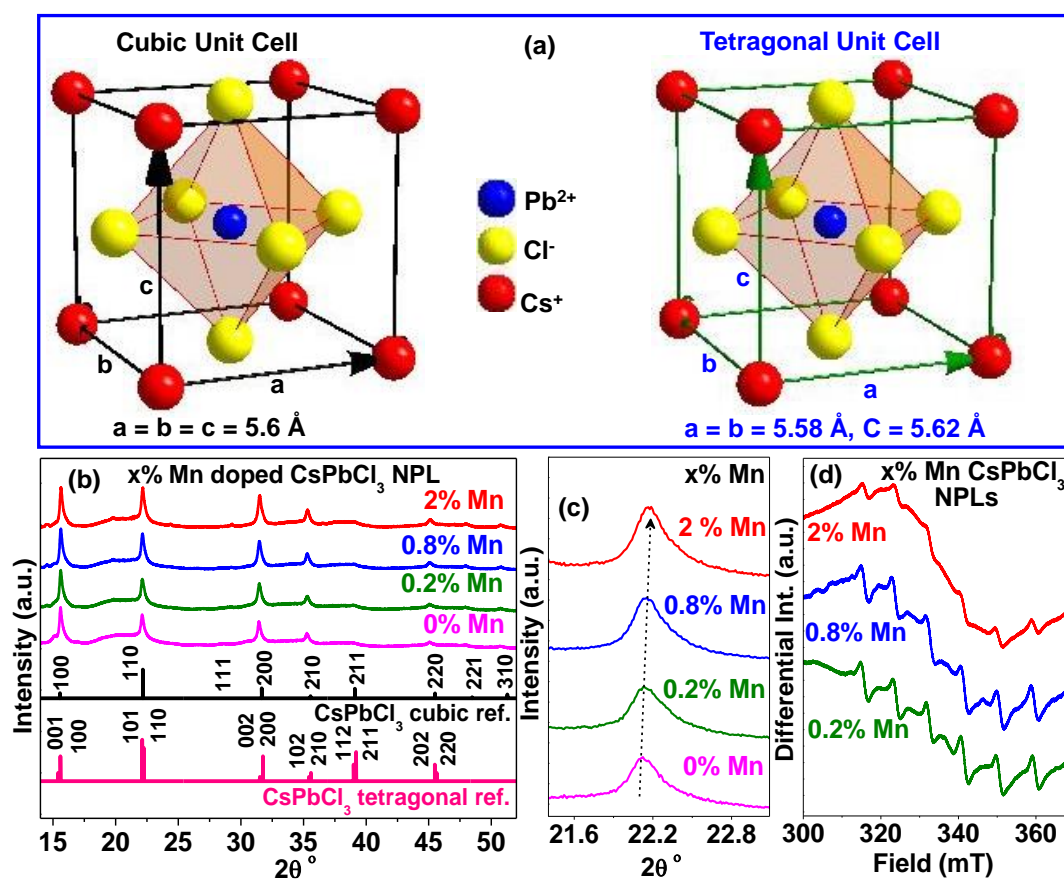


Figure 2.4: Crystal structure and evidence of Mn-doping in CsPbCl_3 NPLs. (a) Schematics of unit cell for cubic and tetragonal phase of CsPbCl_3 . Both cubic and tetragonal unit cell are having similar lattice parameter with c/a ratio of 1.007. (b) Comparison of XRD data of NPLs having different Mn contents with reference data for cubic and tetragonal phase of bulk CsPbCl_3 . (c) Magnified view of the XRD data showing a systematic shift in peak position with Mn-doping. (d) X-band EPR data showing hyperfine splitting of Mn^{2+} ions incorporated in the lattice of CsPbCl_3 NPLs. XRD patterns in panel (b-c), EPR (d) were shifted vertically for a better presentation. Schematics in panel (a) is made following ref.³⁹

A comparison of XRD patterns of Mn-doped CsPbCl_3 NPLs with standard bulk patterns, shown in Figure 2.4b, cannot distinguish between cubic and tetragonal phase of NPLs. Apart from the similarity in the different structures, the analysis becomes more complicated

because of the broadening of XRD peaks of NPLs. In fact, such complexity of analysis has probably lead to different assignments of XRD patterns of CsPbCl₃ NPLs in prior literature. For example, ref¹⁸ assigned orthorhombic structure, ref¹⁷ assigned cubic structure, and ref⁴¹ assigned tetragonal structure of CsPbCl₃ NPLs. We do not observe the splitting of XRD peaks at $2\theta \sim 32^\circ$, suggesting possibility of cubic structure of CsPbCl₃ NPLs over tetragonal structure, but such assignment is not unambiguous because broadening of XRD pattern can blur such splitting. Therefore, the exact assignment of the crystal structure of our Mn-doped CsPbCl₃ is not possible at present. However, all these concerned structures are very similar to each other with three dimensional framework of corner shared PbCl₆ octahedrons, where Cs reside in the voids of the framework (Figure 2.4a). We mention here that further detail about the crystal structure is not required to support the conclusions of this paper.

No impurity peak is observed in the XRD patterns of Mn-doped CsPbCl₃ NPLs in Figure 2.4b suggesting the absence of any crystalline impurities. Interestingly, magnified view (Figure 2.4c) of the XRD peak at $2\theta \sim 22^\circ$ shows a small but systematic shift in the peak towards higher 2θ values with an increase in Mn doping. This shift gives the indication of Mn incorporation in the lattice of CsPbCl₃ NPLs, where Mn²⁺ replaces Pb²⁺. Ionic radius of Mn²⁺ in an octahedral coordination is 0.97 Å which significantly smaller than that for Pb²⁺ (1.33 Å).⁴² This decrease in average cation size with an increase in Mn content shifts the XRD pattern towards higher 2θ values.

X-band EPR spectra of Mn-doped CsPbCl₃ NPLs in Figure 2.4d shows sextet hyperfine splitting patterns confirming isolated Mn centers with +2 oxidation state. It is to be noted that interactions between Mn²⁺ ions are known to broaden the EPR spectrum very efficiently, and overlaps with sharp hyperfine patterns.⁴³ The fact that the EPR spectra of our Mn-doped CsPbCl₃ NPLs clearly exhibit the sharp hyperfine splitting without much interference from any broad EPR signals, rules out the possibility of unwanted clustering of Mn²⁺ ions forming a phase segregated state. The obtained hyperfine splitting energy is 8.6 mT (86 Gauss) for our Mn-doped CsPbCl₃ NPLs, which is very much similar to the hyperfine splitting energy (87 Gauss) observed in bulk Mn-doped CsPbCl₃. This observed value of hyperfine splitting strongly corroborates the fact that Mn²⁺ ions replaces the octahedrally coordinated Pb²⁺ ions in the lattice of CsPbCl₃ NPLs.

2.3.4 Mn-doping introduces new emission channel at 586 nm

A comparison of UV-visible absorption and PL data of undoped and 0.8 % Mn-doped CsPbCl₃ NPLs is presented in Figure 2.5a. Absorption spectra of both samples are similar

with lowest energy excitonic transitions at 355 nm (3.5 eV), which is significantly blue shifted compared to the bandgap of bulk (420 nm, 2.96 eV)²⁴ CsPbCl₃. This blue shift along with the sharp excitonic features in the absorption spectra is a clear evidence of strong quantum confinement of charge carriers in our CsPbCl₃ NPLs. Since the lateral dimensions (length = 32 nm, breadth = 9 nm) are larger than the Bohr excitonic diameter¹¹ (5 nm) of CsPbCl₃, the observed quantum confinement is because of small thicknesses (2.3 nm) of the NPLs, resulting into a quasi two-dimensional colloidal quantum-well⁴⁴ kind of structure experienced by the charge carriers.

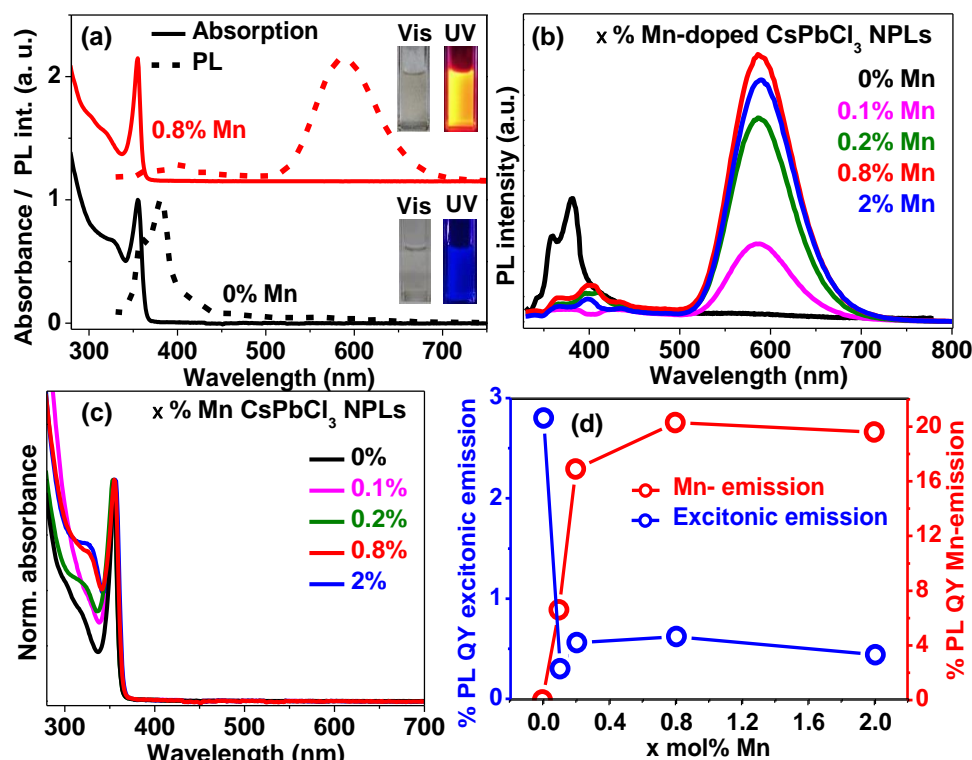


Figure 2.5: (a) UV-visible absorption and PL data showing that the 0.8% Mn-doped sample exhibit a new emission corresponding to the Mn d-d transition; insets show photographs of colloidal undoped and 0.8% Mn doped sample under visible (Vis) and UV light (UV). Variation of (b) PL spectra, (c) absorbance spectra, and (d) PL quantum yield for excitonic and Mn emission, as a function of Mn doping concentration. In (d), open circles are data point and solid lines are just guide to eye. In panel (a) UV-visible absorption and PL spectra for 0.8% Mn doped sample were shifted up by adding 1.15 to y-axis data for a better presentation.

Unlike absorption spectra, PL spectra of undoped and doped samples are distinctly different. The undoped sample shows excitonic emissions in the UV region, whereas the 0.8 % Mn-doped sample shows a strong emission at 586 nm along with suppression of the excitonic emission. Photographs of colloidal NCs in the inset of Figure 2.5a shows both samples are colorless under the visible light, however under UV-irradiation, the undoped sample show faint bluish color, and in contrast the doped sample shows an intense orange color. This

orange emission with peak maximum at 586 nm can be attributed to ${}^4T_1 \rightarrow {}^6A_1$ Mn *d-d* transition.^{2,17-18} This combination of XRD shift, EPR hyperfine splitting, and Mn *d*-electron emission, together confirms successful doping of Mn²⁺ ions into the lattice of CsPbCl₃ NPLs.

Variation in steady state PL intensity with Mn concentration from Mn-doped CsPbCl₃ NPLs is shown in Figure 2.5b. As the doping concentration increases, Figure 2.5b shows the intensity of excitonic emission decreases sharply, and intensity of Mn-emission increases till 0.8 % Mn doping, above which, the intensity decreases for 2% doping. Similar results were also obtained for Mn-doped in II-VI semiconductors, where the best PL efficiency was observed for about 1% Mn doping, and further increase in Mn content increases the interactions between neighboring Mn²⁺ ions decreasing the PL efficiency.³⁷ The dopant incorporation from 0% to 2% Mn does not change the optical band gap of CsPbCl₃ NPLs as shown in Figure 2.5c. Variation in reference quantum yields of both Mn-emission and excitonic emission with doping concentration is shown in Figure 2.5d. The highest quantum yield for Mn emission obtained from a freshly prepared 0.8% Mn-doped sample is 20.3 %. Undoped CsPbCl₃ NPLs shows only 2.8 % total PL QY arising only from excitonic emission. Similar low PL QY of CsPbCl₃ NCs has been observed in most prior literature, unlike ~90% QY for CsPbBr₃ NCs. Interestingly, after 0.8% Mn-doping, the total PL QY increases by an order of magnitude to ~20 %. This increase in PL intensity after doping suggest that the undoped CsPbCl₃ might also exhibit a defect-tolerant nature like CsPbBr₃, but it shows lower PL QY owing to its wider bandgap in the UV region. In a wider bandgap semiconductor, the probability for forming deep mid-gap state arising from capping molecule or through collision with surrounding molecule is more, and such mid-gap states are typically non-radiative in nature and quenching the PL. In the case of Mn-doped samples, new mid-gap levels are created within the NC lattice by Mn *d* states, which quench the excitonic PL more efficiently, compared to surface related defects. Interestingly, these inner-core mid-gap Mn *d* states are less sensitive to the surface/surrounding related non-radiative channels, and therefore, emit light with enhanced PL QY.

2.3.5 Excited state dynamics shows millisecond lifetime of Mn-emission

PL decay profile (Figure 2.6a) of the excitonic emission (emission at 360 nm) of the undoped CsPbCl₃ NPLs can be fitted with a bi-exponential decay with lifetimes 2.4 ns (77% contribution) and 6.6 ns (23% contribution). These results are similar to the lifetimes of cesium lead halide NCs reported earlier.^{11-12, 30} PL decay of the orange emission shown in Figure 2.6b for 0.8% Mn-doped sample exhibits a very long lifetime of 1.6 ms, because of the

spin-forbidden nature of the 4T_1 to 6A_1 transition. Changing the Mn concentration in the range of 0.1 to 2 % does not have a significant influence on the lifetime of this Mn d -electron emission.

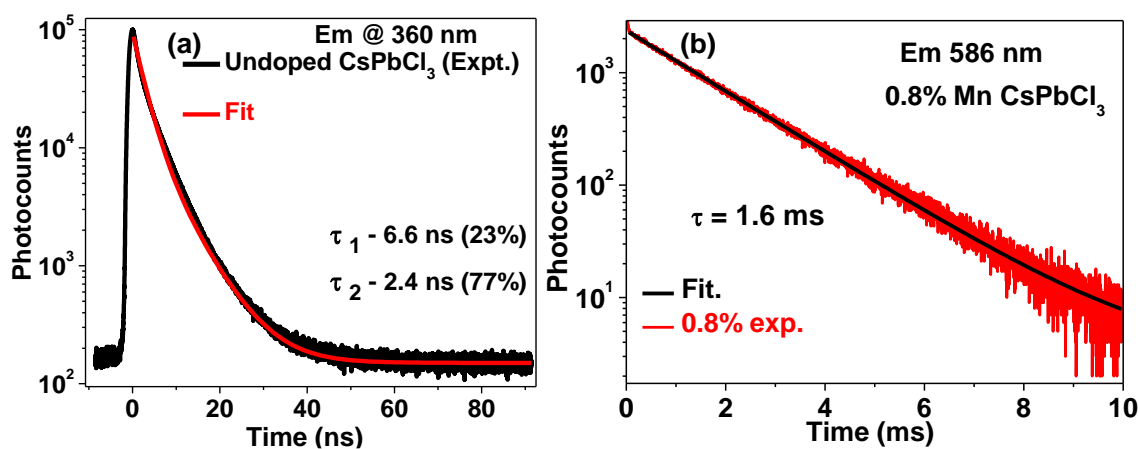


Figure 2.6: PL decay dynamics of CsPbCl₃ and Mn-doped CsPbCl₃ NPLs. (a) Decay of excitonic emission with emission at 360 nm after excitation with picosecond pulse LED source at 340 nm. (b) Mn d -emission with emission at 586 nm after excitation with microsecond flash lamp at 300 nm. In both figures, “Expt.” implies experimental data, and “Fit” implies a bi-exponential fit in (a) and a single-exponential fit in (b).

2.3.6 Anion exchange of Mn-doped CsPbCl₃ to CsPbBr₃ NPLs

After preparing Mn-doped CsPbCl₃ NPLs, we attempted to achieve Mn emission by directly synthesizing Mn-doped CsPbBr₃ NPLs, but the results were not encouraging. It appears that Mn doping in CsPbBr₃ NPLs is more difficult compared to Mn-doping in CsPbCl₃ NPLs. Similar preference of Mn doping in CsPbCl₃ nanocubes was also reported by Liu *et al* and they suggested that the similarity in bond energies between Mn-Cl and Pb-Cl helps Mn-doping in CsPbCl₃ NCs.¹⁷ The reasons behind such selective Mn-doping in CsPbCl₃ NCs, and difficulty in Mn-doping during the nucleation and growth of CsPbBr₃ and CsPbI₃ NCs need to be studied further. We will address this issue in next chapter of this thesis. Therefore, to achieve Mn-doped CsPbBr₃ NPLs for curiosity purpose, we employed an alternative route here, namely postsynthetic anion exchange reaction. Mn-doped CsPbCl₃ NPLs were treated with PbBr₂ solution to achieve Mn-doped CsPbBr₃ NPLs. This strategy of anion exchange was adapted following the prior report of Liu *et al*.¹⁷

UV-visible absorption and PL spectra of undoped CsPbCl₃ NPLs to undoped CsPbBr₃ NPLs is shown in Figure 2.7a, and Mn-doped CsPbCl₃ NPLs to Mn-doped CsPbBr₃ NPLs is shown in Figure 2.7b. Red shift in optical band gap shows the success of the employed anion exchange methodology. Both the doped and undoped samples of CsPbBr₃ NPLs show PL

peaks at ~ 440 and ~ 495 nm, probably arising from excitonic emission of CsPbBr_3 NPLs of different thicknesses. However, PL arising due to Mn d-emission has been observed for Mn-doped CsPbBr_3 NPLs (Figure 2.7b), but with weak intensity. XRD patterns in Figure 2.7c suggest the success of anion exchange reaction converting CsPbCl_3 NPLs to CsPbBr_3 NPLs. Furthermore, PL decay dynamics (Figure 2.7d) with emission at 585 nm exhibit a millisecond scale lifetime, agreeing with the spin forbidden Mn d–d transition. All these results suggest the success of Mn doping in CsPbBr_3 NPLs through anion exchange starting from Mn-doped CsPbCl_3 NPLs. However, further details regarding the difficulty in Mn doping into the CsPbBr_3 lattice and poor intensity of Mn emission will be addressed in next chapter.

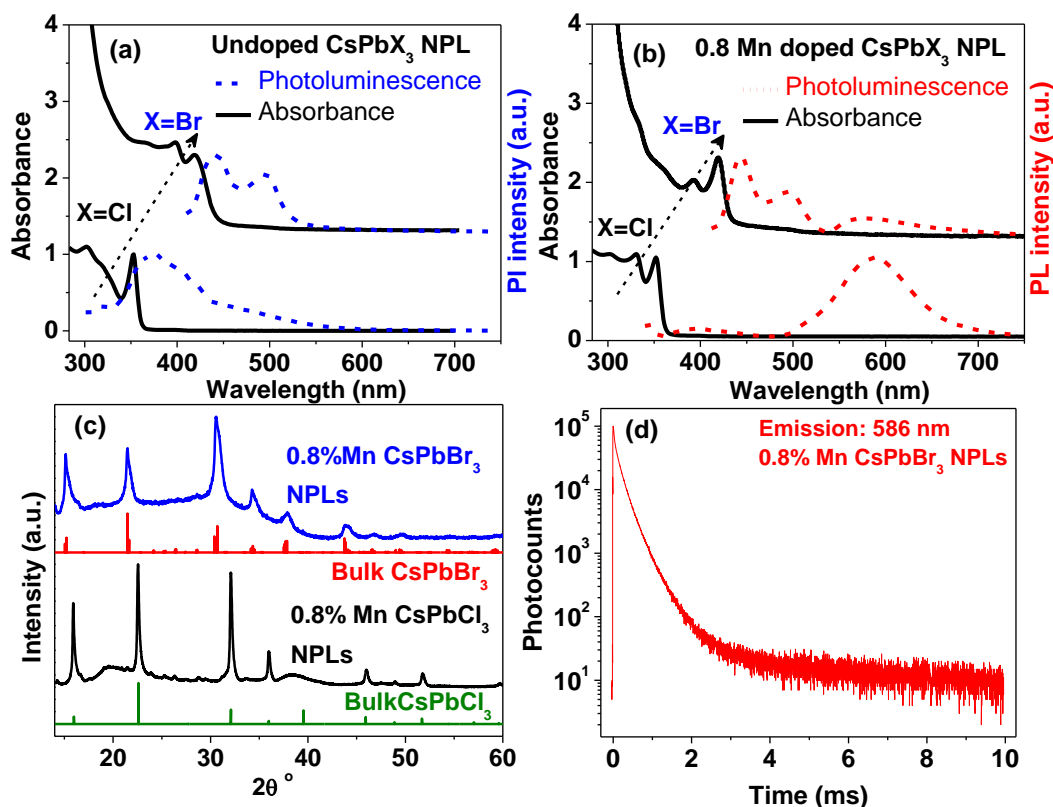


Figure 2.7: Optical absorption and PL spectra of (a) undoped CsPbCl_3 NPLs anion exchanged to CsPbBr_3 NPLs, (b) Mn-doped CsPbCl_3 NPLs anion exchanged to Mn-doped CsPbBr_3 NPLs. (c) Powder XRD patterns of 0.8% Mn-doped CsPbCl_3 NPLs anion exchanged to Mn-doped CsPbBr_3 NPLs along with their bulk references. (d) PL decay dynamics of Mn-doped CsPbBr_3 NPLs at emission 586 nm after excitation with a microsecond flash lamp at 300 nm.

2.4 Conclusions

Mn-doped CsPbCl_3 NPLs with thickness 2.3 nm (4 ML), length 32 nm and breadth 9 nm were prepared. Incorporation of Mn^{2+} ion in the lattice of CsPbCl_3 NPLs were unambiguously characterized using XRD, EPR and PL. These Mn-doped samples show efficient transfer of excitonic energy from the host to dopant, finally yielding orange colored

emission from the Mn d-electrons. PL lifetime of the Mn emission was as long as 1.6 ms, owing to the spin-forbidden 4T_1 to 6A_1 transition of Mn *d*-electron. Anion exchange reactions can convert Mn-doped CsPbCl₃ NPLs to Mn-doped CsPbBr₃ NPLs. A weak Mn emission was observed in Mn-doped CsPbBr₃ NPLs. To the best of our knowledge, these Mn-doped CsPbX₃ (X = Cl, Br) NPLs are the first report of Mn doping in CsPbX₃ host exhibiting strong quantum confinement of charge carriers. Such quantum confinement of charge carriers is expected to enhance the *sp-d* exchange interaction between the host and dopant ion providing interesting magneto-optic properties in future.

2.5 References

1. Norris, D. J.; Yao, N.; Charnock, F. T.; Kennedy, T. A. High-Quality Manganese-Doped ZnSe Nanocrystals. *Nano Lett.* **2001**, *1*, 3-7.
2. Pradhan, N.; Sarma, D. D. Advances in Light-Emitting Doped Semiconductor Nanocrystals. *J. Phys. Chem. Lett.* **2011**, *2*, 2818-2826.
3. Pradhan, N.; Goorskey, D.; Thessing, J.; Peng, X. G. An Alternative of CdSe Nanocrystal Emitters: Pure and Tunable Impurity Emissions in ZnSe Nanocrystals. *J. Am. Chem. Soc.* **2005**, *127*, 17586-17587.
4. Beaulac, R.; Archer, P. I.; Ochsenein, S. T.; Gamelin, D. R. Mn²⁺-Doped CdSe Quantum Dots: New Inorganic Materials for Spin-Electronics and Spin-Photonics. *Adv. Funct. Mater.* **2008**, *18*, 3873-3891.
5. Yu, J. H.; Liu, X. Y.; Kweon, K. E.; Joo, J.; Park, J.; Ko, K. T.; Lee, D.; Shen, S. P.; Tivakornsasithorn, K.; Son, J. S.; Park, J. H.; Kim, Y. W.; Hwang, G. S.; Dobrowolska, M.; Furdyna, J. K.; Hyeon, T. Giant Zeeman Splitting in Nucleation-Controlled Doped CdSe:Mn²⁺ Quantum Nanoribbons. *Nat. Mater.* **2010**, *9*, 47-53.
6. Rice, W. D.; Liu, W. Y.; Baker, T. A.; Sinitsyn, N. A.; Klimov, V. I.; Crooker, S. A. Revealing Giant Internal Magnetic Fields Due to Spin Fluctuations in Magnetically Doped Colloidal Nanocrystals. *Nat. Nanotech.* **2016**, *11*, 137-142.
7. Fainblat, R.; Barrows, C. J.; Hopmann, E.; Siebeneicher, S.; Vlaskin, V. A.; Gamelin, D. R.; Bacher, G. Giant Excitonic Exchange Splittings at Zero Field in Single Colloidal CdSe Quantum Dots Doped with Individual Mn²⁺ Impurities. *Nano Lett.* **2016**, *16*, 6371-6377.
8. Santra, P. K.; Kamat, P. V. Mn-Doped Quantum Dot Sensitized Solar Cells: A Strategy to Boost Efficiency Over 5%. *J. Am. Chem. Soc.* **2012**, *134*, 2508-2511.

9. Debnath, T.; Maity, P.; Maiti, S.; Ghosh, H. N. Electron Trap to Electron Storage Center in Specially Aligned Mn-Doped CdSe Q-Dot: A Step Forward in the Design of Higher Efficient Quantum-Dot Solar Cell. *J. Phys. Chem. Lett.* **2014**, *5*, 2836-2842.
10. Wang, J.; Li, Y.; Shen, Q.; Izuishi, T.; Pan, Z. X.; Zhao, K.; Zhong, X. H. Mn Doped Quantum Dot Sensitized Solar Cells with Power Conversion Efficiency Exceeding 9%. *J. Mater. Chem. A* **2016**, *4*, 877-886.
11. Protesescu, L.; Yakunin, S.; Bodnarchuk, M. I.; Krieg, F.; Caputo, R.; Hendon, C. H.; Yang, R. X.; Walsh, A.; Kovalenko, M. V. Nanocrystals of Cesium Lead Halide Perovskites (CsPbX₃, X = Cl, Br, and I): Novel Optoelectronic Materials Showing Bright Emission with Wide Color Gamut. *Nano Lett.* **2015**, *15*, 3692-3696.
12. Swarnkar, A.; Chulliyil, R.; Ravi, V. K.; Irfanullah, M.; Chowdhury, A.; Nag, A. Colloidal CsPbBr₃ Perovskite Nanocrystals: Luminescence Beyond Traditional Quantum Dots. *Angew. Chem. Int. Ed.* **2015**, *54*, 15424-15428.
13. Song, J. Z.; Li, J. H.; Li, X. M.; Xu, L. M.; Dong, Y. H.; Zeng, H. B. Quantum Dot Light-Emitting Diodes Based on Inorganic Perovskite Cesium Lead Halides (CsPbX₃). *Adv. Mater.* **2015**, *27* (44), 7162-+.
14. Yettapu, G. R.; Talukdar, D.; Sarkar, S.; Swarnkar, A.; Nag, A.; Ghosh, P.; Mandal, P. Terahertz Conductivity within Colloidal CsPbBr₃ Perovskite Nanocrystals: Remarkably High Carrier Mobilities and Large Diffusion Lengths. *Nano Lett.* **2016**, *16*, 4838-4848.
15. Pan, J.; Quan, L. N.; Zhao, Y. B.; Peng, W.; Murali, B.; Sarmah, S. P.; Yuan, M. J.; Sinatra, L.; Alyami, N. M.; Liu, J. K.; Yassitepe, E.; Yang, Z. Y.; Voznyy, O.; Comin, R.; Hedhili, M. N.; Mohammed, O. F.; Lu, Z. H.; Kim, D. H.; Sargent, E. H.; Bakr, O. M. Highly Efficient Perovskite-Quantum-Dot Light-Emitting Diodes by Surface Engineering. *Adv. Mater.* **2016**, *28*, 8718-8725.
16. Brinck S. T.; Infante, I. Surface Termination, Morphology, and Bright Photoluminescence of Cesium Lead Halide Perovskite Nanocrystals. *ACS Energy Lett.* **2016**, *1*, 1266-1272
17. Liu, W.; Lin, Q.; Li, H.; Wu, K.; Robel, I.; Pietryga, J. M.; Klimov, V. I. Mn²⁺-Doped Lead Halide Perovskite Nanocrystals with Dual-Color Emission Controlled by Halide Content. *J. Am. Chem. Soc.* **2016**, *138*, 14954-14961.
18. Parobek, D.; Roman, B. J.; Dong, Y.; Jin, H.; Lee, E.; Sheldon, M.; Son, D. H. Exciton-to-Dopant Energy Transfer in Mn-Doped Cesium Lead Halide Perovskite Nanocrystals. *Nano Lett.* **2016**, *16*, 7376-7380.
19. Yakunin, S.; Protesescu, L.; Krieg, F.; Bodnarchuk, M. I.; Nedelcu, G.; Humer, M.; De Luca, G.; Fiebig, M.; Heiss, W.; Kovalenko, M. V. Low-Threshold Amplified Spontaneous

Emission and Lasing from Colloidal Nanocrystals of Caesium Lead Halide Perovskites. *Nat. Commun.* **2015**, *6*.

20. Zhang, X. Y.; Lin, H.; Huang, H.; Reckmeier, C.; Zhang, Y.; Choy, W. C. H.; Rogach, A. L. Enhancing the Brightness of Cesium Lead Halide Perovskite Nanocrystal Based Green Light-Emitting Devices through the Interface Engineering with Perfluorinated Ionomer. *Nano Lett.* **2016**, *16*, 1415-1420.

21. Swarnkar, A.; Marshall, A. R.; Sanhira, E. M.; Chernomordik, B. D.; Moore, D. T.; Christians, J. A.; Chakrabarti, T.; Luther, J. M. Quantum Dot-Induced Phase Stabilization of α -CsPbI₃ Perovskite for High-Efficiency Photovoltaics. *Science* **2016**, *354*, 92-95.

22. Ramasamy, P.; Lim, D.-H.; Kim, B.; Lee, S.-H.; Lee, M.-S.; Lee, J.-S. All-inorganic Cesium Lead Halide Perovskite Nanocrystals for Photodetector Applications. *Chem. Commun.* **2016**, *52*, 2067-70.

23. Bekenstein, Y.; Koscher, B. A.; Eaton, S. W.; Yang, P. D.; Alivisatos, A. P. Highly Luminescent Colloidal Nanoplates of Perovskite Cesium Lead Halide and Their Oriented Assemblies. *J. Am. Chem. Soc.* **2015**, *137*, 16008-16011.

24. Akkerman, Q. A.; Motti, S. G.; Srimath Kandada, A. R.; Mosconi, E.; D'Innocenzo, V.; Bertoni, G.; Marras, S.; Kamino, B. A.; Miranda, L.; De Angelis, F.; Petrozza, A.; Prato, M.; Manna, L. Solution Synthesis Approach to Colloidal Cesium Lead Halide Perovskite Nanoplatelets with Monolayer-Level Thickness Control. *J. Am. Chem. Soc.* **2016**, *138*, 1010-1016.

25. Sichert, J. A.; Tong, Y.; Mutz, N.; Vollmer, M.; Fischer, S.; Milowska, K. Z.; Cortadella, R. G.; Nickel, B.; Cardenas-Daw, C.; Stolarczyk, J. K.; Urban, A. S.; Feldmann, J. Quantum Size Effect in Organometal Halide Perovskite Nanoplatelets. *Nano Lett.* **2015**, *15*, 6521-6527.

26. Shamsi, J.; Dang, Z. Y.; Bianchini, P.; Canale, C.; Di Stasio, F.; Brescia, R.; Prato, M.; Manna, L. Colloidal Synthesis of Quantum Confined Single Crystal CsPbBr₃ Nanosheets with Lateral Size Control up to the Micrometer Range. *J. Am. Chem. Soc.* **2016**, *138*, 7240-7243.

27. Zhang, D. D.; Yu, Y.; Bekenstein, Y.; Wong, A. B.; Alivisatos, A. P.; Yang, P. D. Ultrathin Colloidal Cesium Lead Halide Perovskite Nanowires. *J. Am. Chem. Soc.* **2016**, *138*, 13155-13158.

28. Tong, Y.; Ehrat, F.; Vanderlinden, W.; Cardenas-Daw, C.; Stolarczyk, J. K.; Polavarapu, L.; Urban, A. S. Dilution-Induced Formation of Hybrid Perovskite Nanoplatelets. *ACS Nano* **2016**, *10*, 10936-10944.

29. Saidaminov, M. I.; Almutlaq, J.; Sarmah, S.; Dursun, I.; Zhumekenov, A. A.; Begum, R.; Pan, J.; Cho, N.; Mohammed, O. F.; Bakr, O. M. Pure Cs₄PbBr₆: Highly Luminescent Zero-Dimensional Perovskite Solids. *ACS Energy Lett.* **2016**, *1*, 840–845
30. Ravi, V. K.; Swarnkar, A.; Chakraborty, R.; Nag, A. Excellent green but less impressive blue luminescence from CsPbBr₃ Perovskite Nanocubes and Nanoplatelets. *Nanotech.* **2016**, *27*.
31. Nedelcu, G.; Protesescu, L.; Yakunin, S.; Bodnarchuk, M. I.; Grotevent, M. J.; Kovalenko, M. V. Fast Anion-Exchange in Highly Luminescent Nanocrystals of Cesium Lead Halide Perovskites (CsPbX₃, X = Cl, Br, I). *Nano Lett.* **2015**, *15*, 5635-5640.
32. Akkerman, Q. A.; D'Innocenzo, V.; Accornero, S.; Scarpellini, A.; Petrozza, A.; Prato, M.; Manna, L. Tuning the Optical Properties of Cesium Lead Halide Perovskite Nanocrystals by Anion Exchange Reactions. *J. Am. Chem. Soc.* **2015**, *137*, 10276-10281.
33. Hoffman, J. B.; Schleper, A. L.; Kamat, P. V. Transformation of Sintered CsPbBr₃ Nanocrystals to Cubic CsPbI₃ and Gradient CsPbBr_xI_{3-x} through Halide Exchange. *J. Am. Chem. Soc.* **2016**, *138*, 8603-8611.
34. Ravi, V. K.; Markad, G. B.; Nag, A. Band Edge Energies and Excitonic Transition Probabilities of Colloidal CsPbX₃ (X = Cl, Br, I) Perovskite Nanocrystals. *ACS Energy Lett.* **2016**, *1*, 665-671.
35. Balakrishnan, S. K.; Kamat, P. V. Au–CsPbBr₃ Hybrid Architecture: Anchoring Gold Nanoparticles on Cubic Perovskite Nanocrystals. *ACS Energy Lett.* **2016**, 88-93.
36. Erwin, S. C.; Zu, L.; Haftel, M. I.; Efros, A. L.; Kennedy, T. A.; Norris, D. J. Doping Semiconductor Nanocrystals. *Nature* **2005**, *436*, 91-94.
37. Nag, A.; Chakraborty, S.; Sarma, D. D. To dope Mn²⁺ in a Semiconducting Nanocrystal. *J. Am. Chem. Soc.* **2008**, *130*, 10605-10611.
38. Kulbak, M.; Gupta, S.; Kedem, N.; Levine, I.; Bendikov, T.; Hodes, G.; Cahen, D. Cesium Enhances Long-Term Stability of Lead Bromide Perovskite-Based Solar Cells. *J. Phys. Chem. Lett.* **2016**, *7*, 167-172.
39. C. K. Møller Crystal Structure and Photoconductivity of Cæsium Plumbohalides. *Nature*, **1958**, *182*, 1436–1436
40. J. A. Cape, R. L. White, R. S. Feigelson. EPR Study of the Structure of CsPbCl₃. *J. App. Phys.* **1969**, *40*, 5001
41. Lv, L. F.; Xu, Y. B.; Fang, H. H.; Luo, W. J.; Xu, F. J.; Liu, L. M.; Wang, B. W.; Zhang, X. F.; Yang, D.; Hu, W. D.; Dong, A. G. Generalized Colloidal Synthesis of High-Quality,

Two-Dimensional Cesium Lead Halide Perovskite Nanosheets and Their Applications in Photodetectors. *Nanoscale* **2016**, *8*, 13589-13596.

42. Shannon, R. D., Revised Effective Ionic-Radii and Systematic Studies of Interatomic Distances in Halides and Chalcogenides. *Acta Crystallogr. Sect. A* **1976**, *32* (SEP1), 751-767.

43. Nag, A.; Sapra, S.; Nagamani, C.; Sharma, A.; Pradhan, N.; Bhat, S. V.; Sarma, D. D. A Study of Mn²⁺ Doping in CdS Nanocrystals. *Chem. Mater.* **2007**, *19*, 3252-3259.

44. Nasilowski, M.; Mahler, B.; Lhuillier, E.; Ithurria, S.; Dubertret, B. Two-Dimensional Colloidal Nanocrystals. *Chem. Rev.* **2016**, *116*, 10934-10982.

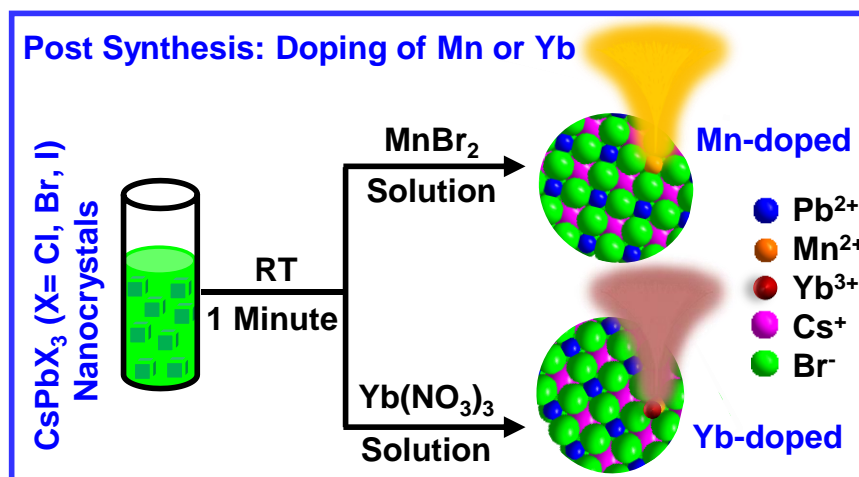
Chapter 3

Postsynthesis Doping of Mn and Yb into Colloidal CsPbX₃ (X = Cl, Br, I) Perovskite Nanocrystals

.....
The work presented in this chapter is already published under following details. Mir, J. W.; Mahor, Y.; Lohar, A.; Jagadeeswararao, M.; Das, S.; Mahamuni, S.; Nag A. *Chem. Mater.* **2018**, *30*, 8170–8178. Permission is taken for the whole article. Copyright 2018 American Chemical Society.

Abstract

Doping Mn and Yb into CsPbX₃ (X = Cl, Br, I) nanocrystals (NCs) yields luminescence due to de-excitation through d-d (yellow-red emission) and f-f transitions (near infrared emission), respectively. However, till date, both the Mn- and Yb-emission are obtained from perovskite NCs with wider band gap (<480 nm). To overcome this problem, we have developed a post-synthesis doping method, where Mn and Yb can be easily doped into pre-formed CsPbX₃ NCs with band gaps in the entire visible region. Different morphologies like nanoplatelets and nanocubes are doped. Since we dope pre-formed host NCs, the effect of dopants on optical properties can be studied more reliably using the same batch of host NCs for both undoped and doped samples. We find that the problem of absence of Mn-emission from Mn-doped CsPbBr₃ NCs can be overcome by suppressing back energy transfer from Mn to host NCs, either by increasing the band gap of host by quantum confinement or by measuring photoluminescence at lower temperatures. Interestingly, dopants are found to enhance the excitonic emission intensities and reduce the Urbach absorption tail, suggesting reduced defect density compared to undoped NCs. These added functionalities and capability to dope lower band gap materials can be explored further for near infrared light emitting diodes, sensing and luminescent solar concentrators of desired colors.

Graphical abstract

3.1 Introduction

Colloidal cesium lead halide (CsPbX₃ where X = Cl, Br, I) perovskite nanocrystals (NCs) are now established as an interesting class of optical and optoelectronic materials.¹⁻⁹ It is thus intriguing to dope optically active metal ions such as Mn²⁺ or Yb³⁺ in CsPbX₃ NCs to impart new functionalities for both fundamental curiosity and potential applications. Reports of Mn doping¹⁰⁻¹² and Yb doping¹³⁻¹⁵ appeared in recent times, but choice of host largely remained CsPbCl₃, CsPb(Cl/Br)₃, and quantum confined CsPbBr₃ NCs with wider (> 2.58 eV) band gaps absorbing only UV-to-blue light. Doping in narrower band gap hosts like CsPbBr₃ and CsPbI₃ NCs that can absorb the wide range of UV-visible light has not been explored. In this manuscript, we dope Mn and Yb into such narrower band gap perovskite hosts by developing a generic postsynthesis doping strategy. We also provide insights about dopant emission by employing temperature-dependent photoluminescence (PL) spectroscopy.

Mn and Yb dopants emit intense light via inner core d-d and f-f de-excitation transitions at ~600 nm (2.06 eV) and ~990 nm (1.25 eV), respectively. But in both the cases d-d and f-f transitions are forbidden, so the dopants get excited via absorption of light by the host NCs. This decoupling of absorption and emission processes leads to a large energy difference between absorption from host and emission from dopant. For example, the dopant emissions are ~1.07 eV and ~1.85 eV lower in energy compared to their absorption edge of host for Mn and Yb-doped in CsPbCl₃ NCs respectively.^{10, 14} Relying on this large energy difference and high PL quantum yield (PLQY) of Mn-emission (QY 58 %) ^{10, 16} and Yb-emission (QY 130 %),¹⁴ simple but innovative ways of boosting solar cell efficiencies,^{15, 17} including luminescent solar concentrators (LSCs)^{18, 19} can be designed.

Although, both CsPbBr₃ and CsPbI₃ NCs have suitable band gaps to sensitize Yb-emission, doping Yb in these NCs has remained a challenge so far. On the other hand, CsPbI₃ NCs have band gap lower than Mn-emission energy, so sensitization of Mn-emission via host absorption is unlikely. Consequently, Mn-doped CsPbI₃ NCs is not a good option for Mn-emission, however, it should be noted that there is another research direction where such doping is now being explored to increase the stability of the host for solar cell applications.^{20, 21} Unlike CsPbI₃, the typical band gap of CsPbBr₃ nanocubes is sufficiently wide (~2.48 eV, 500 nm) to sensitize Mn-emission. But often, Mn doping into CsPbBr₃ nanocubes do not exhibit Mn-emission.^{11, 21} Introduction of Mn dopants through direct colloidal synthesis in CsPbBr₃ nanocubes is difficult to achieve using MnBr₂ precursor which solubilizes in the reaction mixture as Mn-oleate complex containing Mn-O bond.¹¹ This difficulty is due to the

higher bond dissociation energy of Mn-O (402 KJ/mol) compared to Pb-Br (248.5 KJ/mol).¹¹ In other words, strong driving force is required to incorporate Mn from Mn-oleate precursor to form CsPb_{1-x}Mn_xBr₃ product. Recently, Mn-doped CsPbBr₃ NCs were reported through similar hot injection method²² but by using an additional entity, namely, HBr. This HBr converts Mn-oleate to Mn-Br which drives Mn doping inside CsPbBr₃ NCs. Mn-emission is observed from these Mn-doped CsPbBr₃ NCs with optical band gap ≥ 2.58 eV (≤ 480 nm).²² But the QY for Mn emission decreases systematically from 27% to 1.6%, by decreasing the band gap from 2.72 eV to 2.58 eV with increasing size of CsPbBr₃ NCs. Mn emission has not been reported yet using CsPbBr₃ NC host with narrower (< 2.58 eV) band gap. Also, to the best of our knowledge, Yb-doping has been reported only for CsPbCl₃ and CsPb(Cl/Br)₃ NCs.¹³⁻¹⁵ Clearly, doping both Mn and Yb into CsPbX₃ NCs with narrower band gap still remains a challenge.

Here, we have designed a simple postsynthesis strategy to dope Mn in CsPbBr₃ nanoplatelets (NPLs) and nanocubes. The nature of Mn-Br bond between introduced precursor and bond required to form in Mn-doped CsPbBr₃ lattice remained same for all these samples, but the optical band gap of the host varied from 2.92 to 2.53 eV by controlling the size and shape of the host. A detailed characterization shows the presence of dopant in all the samples, but the intensity of Mn-emission decreases systematically with decreasing the band gap of the host. We find that the back energy transfer from Mn to host is the dominant mechanism for quenching the Mn emission with decreasing band gap. Our postsynthesis doping strategy can successfully dope all compositions of CsPbX₃ (X = Cl, Br, I) nanocubes and NPLs yielding near infrared (NIR) Yb-emission.

3.2 Experimental Section

3.2.1 Cs-oleate precursor solution

Prepared by dissolving 350 mg of Cs₂CO₃ in 20 mL 1-octadecen (ODE) and 1.25 mL oleic acid (OA) in inert atmosphere at 150 °C and stored for further use.²³

3.2.2 CsPbBr₃ NPLs

Synthesis of CsPbBr₃ NPLs is carried out at room temperature under ambient atmosphere following ref.²³ But reactions are scaled up by 4 times. Typically 5 mL ODE, 0.5 mL OA and 0.5 mL oleylamine (OLA) are taken into a 50 mL centrifuge tube followed by addition of 0.5 mL Cs-oleate precursor solution (0.1 M, preheated at 100 °C) under vigorous stirring. After that, 0.8 mL PbBr₂ precursor solution prepared by dissolving 2 mmol (735 mg) PbBr₂ in

5 mL DMF is injected to the reaction mixture. Within ~10 s, slight white turbidity appears and 20 mL acetone is swiftly injected into reaction mixture to quench the reaction. Then the reaction mixture is centrifuged at 6000 rpm (1-2 mL hexane is added to this crude solution to prevent immiscibility with excess acetone) for 5 minutes. The wet pellet obtained is redispersed in 2-3 mL hexane and washed again by adding methyl acetate (MeOAc) as antisolvent (typically 1 : 2 v/v ratio of hexane : methyl acetate). The resulting turbid solution is centrifuged at 6000 rpm for 5 minutes and pellet obtained is redispersed in hexane for postsynthesis doping and characterization. The above procedure results into 5 monolayer (ML) CsPbBr₃ NPLs as desired product. To control thickness of CsPbBr₃ NPLs to 4 ML and 3 ML 20 μ L and 40 μ L HBr is added to the 0.8 mL PbBr₂ precursor solution, respectively. The remaining procedure is same as described for 5 ML NPLs.

3.2.3 CsPbBr₃ nanocubes

Colloidal CsPbBr₃ nanocubes were synthesized through hot injection synthesis after minor modifications of the protocols reported in ref.¹⁻² PbBr₂ (0.5 mmol, 183.5 mg) and 12 mL ODE are loaded into three neck round bottom flask (RB) connected to schlenk line apparatus. The reaction mixture under continuous stirring was degassed in alternating vacuum and nitrogen at ~100 °C for 30-45 minutes. Then, 1.5 mL OA and 1.5 mL OLA are injected into the reaction mixture under N₂ flow. Again the reaction mixture is degassed in alternating vacuum and nitrogen for next half an hour. The temperature of reaction mixture is set to 130 °C under continuous N₂ flow. Once the reaction mixture becomes clear at set temperature 130 °C, 1 mL Cs-oleate from stock solution (0.1 M, pre-heated at ~100 °C) is quickly injected into the reaction mixture. A light green color appears within ~5 s and the reaction is quenched immediately by immersing the flask into liquid nitrogen bath. CsPbBr₃ nanocubes are then precipitated at room temperature by addition of excess methyl acetate to crude solution of nanocubes till turbidity appears and centrifuged at 6000 rpm for 5 minutes. The obtained pellet is redispersed in 2-3 mL hexane after discarding supernatant. The 2nd washing is carried out by adding methyl acetate (~1 : 2 v/v ratio of hexane : methyl acetate) and centrifuging again at 6000 rpm or 5 minutes. The obtained pellet is finally redispersed in hexane and stored for postsynthesis doping and further studies.

3.2.4 CsPbCl₃ nanocubes

CsPbCl₃ nanocubes are synthesized following same procedure as adapted for CsPbBr₃ nanocubes but with following differences in precursor concentration. For synthesizing CsPbCl₃ nanocubes PbCl₂ (0.752 mmol, 209 mg), 20 mL ODE were initially taken in RB and

then 2 mL OA, 2 mL OLA, 2 mL TOP are injected at 100 °C after degassing. The reaction in this case is carried out at 160 °C by injecting Cs-oleate 1.4 mL (0.1 M) followed by immediate quenching.

3.2.5 CsPbI₃ nanocubes

Synthesis and washing procedure are similar for both CsPbI₃ and CsPbBr₃ nanocubes. For synthesis of CsPbI₃ nanocubes, PbI₂ (1 mmol, 461 mg), 20 mL ODE, 2.5 mL OA, 2.5 mL OLA followed by injection of preheated Cs-oleate solution 2 mL (0.1 M) at reaction temperature 120 °C gives desired product.

3.2.6 Doping Mn²⁺ and Yb³⁺ in CsPbX₃ NCs (both nanocubes and NPLs)

For efficient and facile postsynthesis doping, the desired CsPbX₃ NCs are washed minimum two times as described above in synthesis procedure of NCs. Our postsynthesis doping is carried out at room temperature and ambient atmosphere. Initially, freshly prepared Mn precursor solution is obtained by dissolving MnBr₂ salt in a mixture of acetone : toluene solvents in the volume ratio of 1 : 3 respectively with the help of sonication. The volume ratio has been optimized to minimize the polarity of precursor solution detrimental for colloidal stability of CsPbX₃ NCs. Similarly, Yb precursor solution is obtained by dissolving Yb(NO₃).5HO in a mixture of methyl acetate : toluene in the same volume ratio of 1 : 3 respectively. Next undoped NCs dispersion obtained after synthesis and washing are divided equally in different vials. Different amounts of dopant precursor solution are then added to the NCs dispersion under continuous stirring for 1 minute to achieve different dopant concentrations. Once Mn or Yb is doped, the product NCs are then washed using MeOAc as anti-solvent to precipitate the NCs. The wet pellet obtained after centrifugation is redispersed in hexane. In case of Mn doped CsPbBr₃ NPLs, additional level of purification is achieved by refrigerating the dispersion of Mn doped NPLs in hexane for 2-3 hours to remove unreacted precursors that precipitates out at low temperature. The supernatant is decanted and stored for further studies after discarding any precipitate obtained.

3.2.7 Characterization methods

Structural analysis is carried out using a Bruker D8 Advance X-ray diffraction (XRD) diffractometer using Cu K α (1.54 Å) radiation. XRD patterns are recorded after drop casting colloidal NCs on glass slides. Transmission electron microscopy (TEM) and high-resolution TEM (HRTEM) images are collected by using a 200 kV UHR FEG-TEM, JEOL JEM 2100F field emission transmission electron microscope. Atomic force microscopy (AFM) images

are captured using Key sight atomic force microscope (AFM 5500) employing tapping mode technique. Dilute dispersions of NCs are drop casted over Si substrate for AFM analysis. Inductively coupled plasma atomic emission spectroscopy (ICP-AES) analysis is carried out using ARCOS simultaneous ICP spectrometer, Analytical Instruments GmbH, Germany. Electron Paramagnetic Resonance (EPR) spectra are collected using a JES- FA200 ESR spectrometer (JEOL, Japan) in X-band frequency range at room temperature and measurements were carried out with powder samples. UV-visible-NIR absorption spectra are recorded using a Perkin Elmer and Lambda-45 UV/Vis/NIR spectrometer. PL, PL excitation (PLE) spectra and PL decay dynamics (time-correlated single photon counting) are recorded using FLS 980 spectrophotometer (Edinburgh Instruments). For Mn and Yb PL decay dynamics, microsecond flash lamp is used as excitation source. For excitonic PL decay dynamics, picosecond pulsed diode laser (405 nm) is used as excitation source. Low-temperature PL studies are carried out for NCs films on quartz substrates using a closed cycle cryostat. Reference PLQY of Mn emission were calculated using rhodamine-6G dye dissolved in ethanol as reference standard ($\Phi = 0.96$).

3.3 Results and Discussion

3.3.1 Postsynthesis Mn-doping in CsPbX₃ NCs

We developed a postsynthesis strategy to dope Mn and Yb in colloidal CsPbX₃ NCs. Undoped CsPbX₃ NCs with desired compositions, size and shape are first prepared following reported protocols.^{7, 23} In the second step, postsynthesis doping methodology is employed to dope a host either with Mn or Yb of desired concentrations, by employing a one-minute reaction at room temperature. The schematic representation of Mn doping in CsPbBr₃ NPLs is depicted in Figure 3.1a. When the postsynthesis doping reaction is carried out by dissolving MnBr₂ into oleic acid forming Mn-oleate complex, the reaction fails to dope Mn in CsPbBr₃ NPLs as evident from absence of Mn emission (~596 nm) in corresponding PL spectra in Figure 3.1b. Interestingly, addition of small amounts of HBr to Mn-oleate complex dopes Mn into CsPbBr₃ NPLs with emergence of Mn emission (Figure 3.1b). However, use of HBr during the postsynthesis doping degrades the quality of NPLs in terms of poor colloidal stability and low PL QY. Based on these results, we developed a new precursor for the postsynthesis Mn doping, avoiding both Mn-oleate and HBr. The new precursor is MnBr₂ dissolved in a mixture of acetone : toluene = 1:3 (by volume) solvents. This mixture optimizes the polarity of the medium in such a way that MnBr₂ get dissolved but the NPLs still remain stable. Use of toluene alone could not dissolve the MnBr₂, and higher

concentrations of acetone destabilize the NPLs. As shown in Figure 3.1, the postsynthesis doping using MnBr_2 solution yields clear Mn emission at 596 nm, without destabilizing the NPLs. Therefore, this MnBr_2 solution precursor is used to achieve Mn doping into CsPbBr_3 NCs throughout in this chapter.

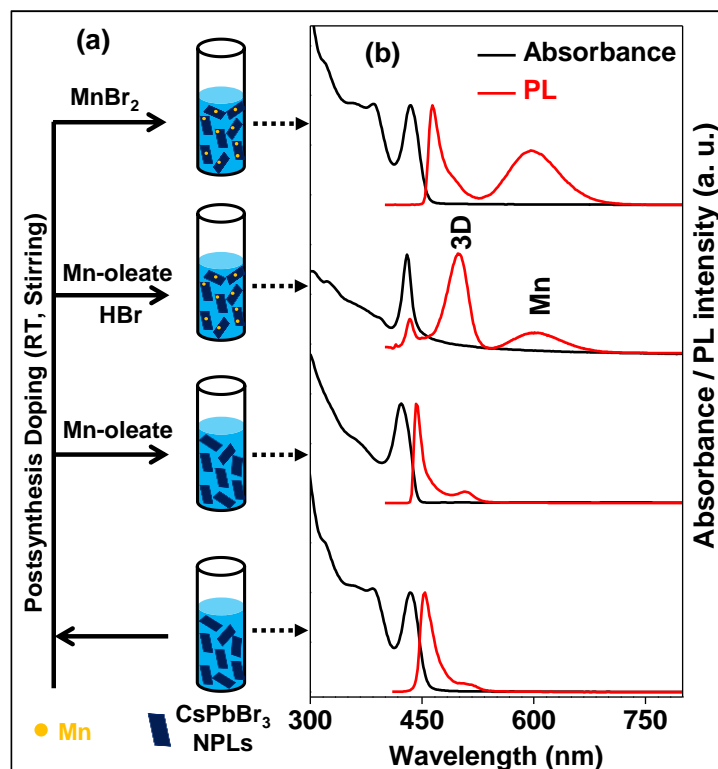


Figure 3.1: (a) Schematics showing postsynthesis doping of Mn in CsPbBr_3 NPLs, using different precursor solutions. (b) Comparison of UV-visible absorption and PL spectra of the products obtained after doping, with the starting undoped sample. Dotted arrows connect the spectra in (b) with corresponding sample in (a). PL peaks ~ 500 nm is from 3D bulk-like CsPbBr_3 and that ~ 596 nm originate from Mn emission.

The postsynthesis Mn doping strategy discussed for NPLs can be easily extended to dope CsPbBr_3 nanocubes as well. It is important to note that our postsynthesis doping strategy does not require a change in halide composition, in sharp difference with the reported²⁴ halide-exchange driven postsynthesis Mn doping. In that reported approach, MnCl_2 molecules are reacted with CsPbBr_3 nanocubes yielding Mn-doped $\text{CsPb}(\text{Cl}/\text{Br})_3$ mixed halide NCs with a wider band gap.²⁴ Therefore, the halide-exchange driven doping method using MnCl_2 precursor is not suitable to dope narrower band gap compositions of CsPbX_3 NCs, unlike our doping strategy. The complete mechanistic insights of the postsynthesis doping reaction are not yet understood. But we believe that the doping strategy benefits from the dynamic nature of ligand binding to adsorb dopants on the surface of NCs,²⁵ and fast halide migration to incorporate dopants into the CsPbX_3 perovskite NCs.^{26, 27} The doping concentrations of the

product NCs are determined by inductively coupled plasma atomic emission spectroscopy (ICP-AES). All the dopant percentages mentioned in this chapter are the ones obtained from product NCs employing ICP-AES spectroscopy, and are not the nominal precursor concentrations.

3.3.2 Morphology and thickness of Mn-doped in CsPbBr₃ NPLs

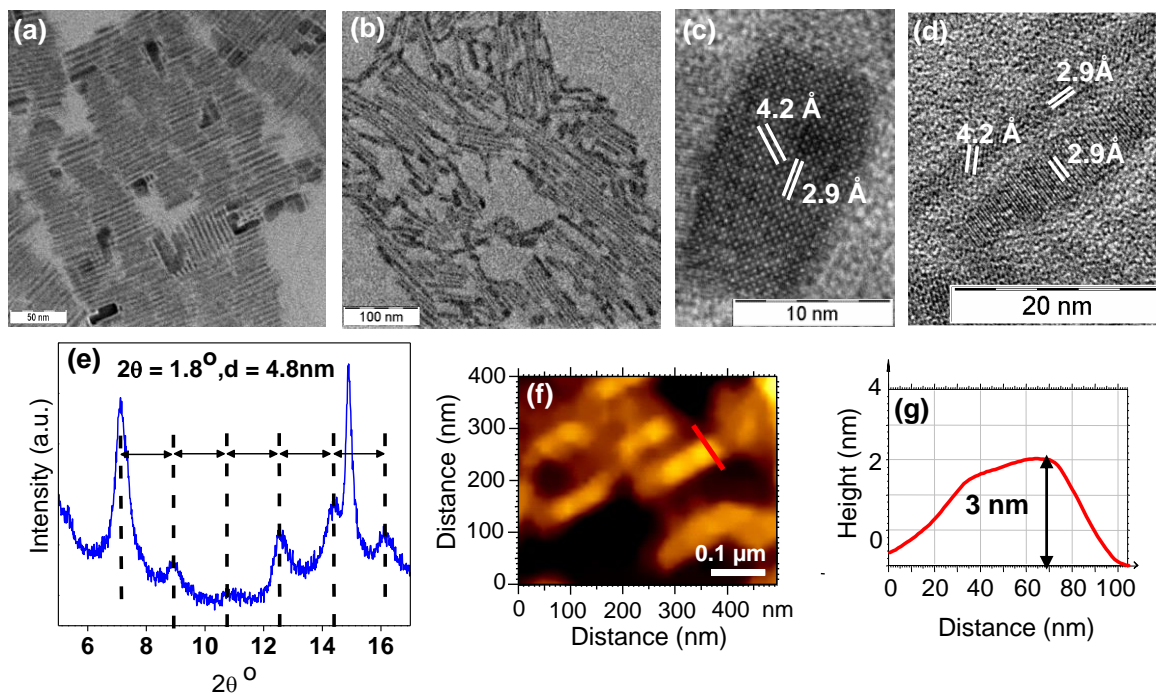


Figure 3.2: TEM image of (a) undoped and (b) 4.3% Mn-doped 5 ML NPLs. HRTEM image: (c) one NPL lying flat on TEM grid and (d) NPLs stacked face-to-face lying perpendicular on TEM grid. (e) Shows low angle XRD of self-assembled NPLs with an interlayer spacing of 4.8 nm. AFM image (f) and corresponding height profile (g) of 4.3% Mn-doped 5ML NPLs.

Figure 3.2a shows the TEM image of 5 monolayer (ML) thick CsPbBr₃ NPLs. In accordance with previous reports^{23, 28} these NPLs have tendency to stack with each other laterally allowing us to determine the thickness of NPLs ~3 nm. The lateral dimension of these NPLs is $8.6 \pm 1.3 \text{ nm} \times 45.7 \pm 8.2 \text{ nm}$. TEM image in Figure 3.2b shows that the morphology and dimensions of NPLs remain similar for 4.3% Mn doping. High resolution (HR) TEM image (Figure 3.2c) of Mn-doped 5 ML NPL lying flat on TEM grid displays highly crystalline nature of NPL. Figure 3.2d shows the HRTEM image of 5 ML Mn-doped NPLs stacked face-to-face and lying perpendicular to the TEM grid. The interplanar distances correspond to CsPbBr₃ NPLs similar to prior report.²⁹ The self-assembled NPLs correspond to interlayer spacing of 4.8 nm (see low angle XRD in Figure 3.2e, whereas, 3 nm corresponds to 5 ML and 1.8 nm to organic ligands) similar to previous report.²³ AFM image and corresponding

height profile plot of Mn-doped 5 ML NPLs in Figure 3.2f-g confirms that the thickness of these NPLs is 3 nm. Overall, the microscopic analysis confirms that the size and morphology of NPLs remain similar before and after our postsynthesis Mn doping reaction.

3.3.3 Evidence of Mn-doping in lattice of CsPbBr₃ NPLs

To verify whether our postsynthesis doping method can incorporate Mn into the lattice of CsPbBr₃ NPLs or not, we employed XRD and electron paramagnetic resonance (EPR) spectroscopy. Figure 3.3a shows absence of additional impurity peak for the doped sample. A magnified view of the XRD peaks in Figure 3.3b suggests that the peak for doped samples slightly shifts to higher 2θ values, suggesting substitution of Pb²⁺ in the lattice with smaller sized Mn²⁺. X-band EPR spectra (Figure 3.3c) recorded at room temperature for both 4.3% and 1.6% doped samples show sextet hyperfine splitting patterns corresponding to Mn²⁺ ions isolated from each other. The hyperfine splitting energy of 9.1 mT is similar to previous reports²¹ of Mn-doped CsPbX₃ samples, suggesting incorporation of Mn²⁺ into the lattice of CsPbBr₃ NPLs. As Mn concentration increases from 1.6% to 4.3%, the exchange interaction between neighboring Mn²⁺ ions increases, giving rise to a broad signal overlapping with the sextet hyperfine pattern.

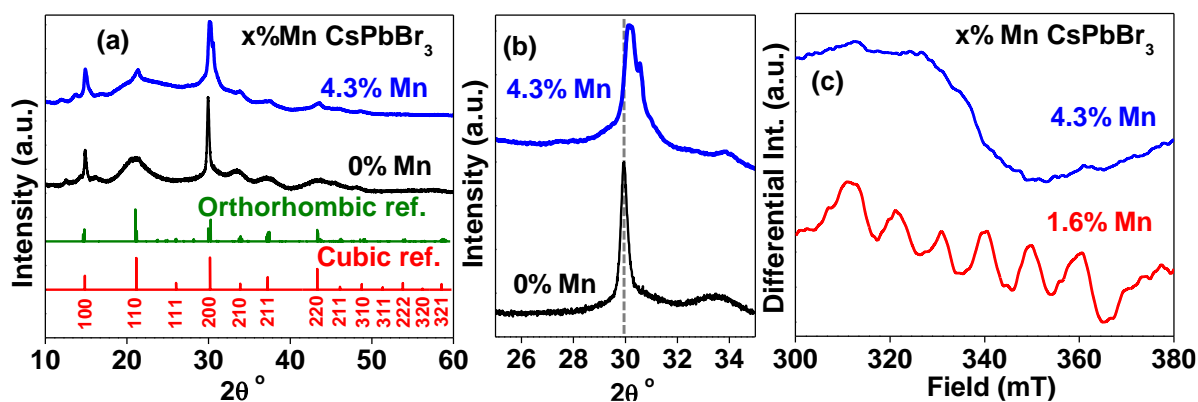


Figure 3.3: (a) XRD patterns of undoped and 4.3% Mn doped samples, along with reference XRD patterns for cubic and orthorhombic phase of CsPbBr₃. (b) Magnified view of XRD peak at $2\theta = 29.9^\circ$. (c) Room temperature X-band EPR of 1.6% and 4.3% Mn doped CsPbBr₃ NPLs.

3.3.4 Mn-doping improving optical absorption and emission of 5 ML CsPbBr₃ NPLs

The new PL peak in Figure 3.4a after Mn-doping arises from de-excitation of Mn *d*-electrons through spin forbidden $^4T_1 \rightarrow ^6A_1$ transition.³⁰ The intensity of Mn-emission initially increases with Mn content reaching a maximum for 4.3% Mn doping for 5 ML CsPbBr₃ NPLs and then decreases upon further increase in Mn concentration. Similar dependence of Mn-emission is usually observed^{12, 31-33} for different hosts, where intensity increases initially

because of the increase in emitting dopant centers, but the increase in dopant concentration increases exchange interactions between neighboring Mn, decreasing the emission efficiency per dopant ion.³¹ An opposing interplay between both processes gives the maximum Mn-emission at an intermediate dopant concentration. There are differences in prior reports on how the intensity of excitonic PL varies with Mn doping concentrations in perovskite NCs. Some reports^{10, 34, 35} showed increase in excitonic PL intensity with Mn doping, another set of reports^{12, 16, 32, 36-38} suggested a decrease in excitonic PL intensity with Mn doping. There are differences in synthesis protocols between different reports, and even within the same synthesis protocols, presence and absence of dopant (Mn precursor) may also influence the growth, influencing size and shape of NC and intrinsic defect levels in the host.^{37, 39} These possible differences in synthesis of undoped and doped samples might be the reasons behind the different results reported in literature.

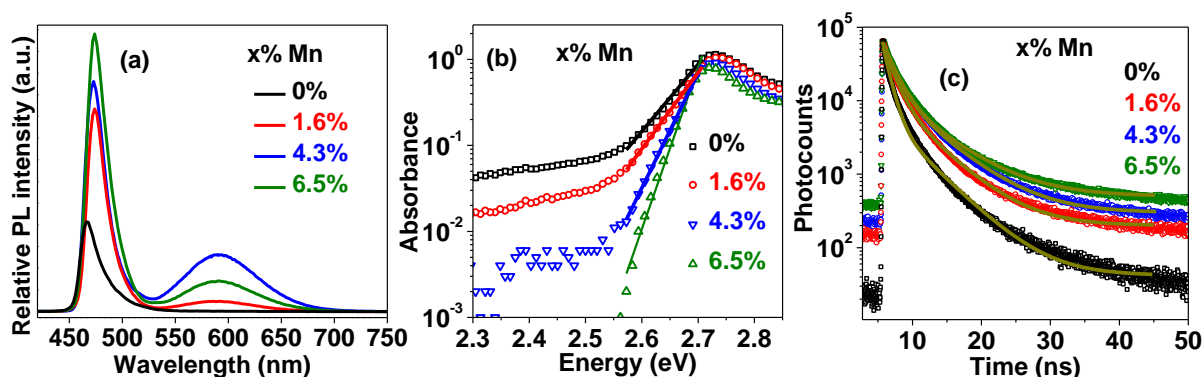


Figure 3.4: (a) PL spectra with intensity normalized by absorbance at excitation wavelength. (b) Absorbance in logarithmic scale, where symbols are experimental data and straight solid lines are guide to eye. (c) PL decay dynamics of excitonic emission (~464 nm), where symbols are experimental data and solid lines are corresponding fit using a bi-exponential decay function.

Our postsynthesis doping protocol provides a unique opportunity to achieve different dopant concentrations starting from the same batch of undoped NCs. This methodology eliminates most of the synthesis related inhomogeneity, to make the study of effect of dopant concentration more reliable. Interestingly, Figure 3.4a shows that the intensity of excitonic PL increases systematically with an increase in dopant concentration. Some prior reports suggested that dopant ions probably passivate defect such as halide vacancies.^{10, 34, 35} To further check such possibility, Figure 3.4b shows optical absorption spectra in logarithmic scale highlighting that the Urbach tail^{40, 41} below the excitonic or band gap transition decreases with Mn doping. This decrease in Urbach tail infers decrease in disorder or defects in the system, which agrees with the increase in excitonic PL intensity with Mn doping.

Figure 3.4c along with Table 3.1 show that the average lifetime of PL decay for excitonic emission (~464 nm) increases systematically with Mn doping, again suggesting the decrease in non-radiative (faster decay) trap states.

Table 3.1: Best fit parameters of excitonic PL decay of Mn-doped 5 ML CsPbBr₃ NPLs, corresponding to data shown in Figure 3.4c. The experimental data are fitted using bi-exponential decay fit: $I(t) = I(0) + (a_1 \exp^{-\frac{t}{\tau_1}} + a_2 \exp^{-\frac{t}{\tau_2}})$, where $I(t)$ and $I(0)$ are PL intensities at time 't' and t = 0 s respectively, a_1 and a_2 are amplitudes of lifetime components τ_1 and τ_2 respectively.

x% Mn-doped CsPbBr ₃ NPLs	τ_1 (ns)	τ_2 (ns)	a_1 (%)	a_2 (%)
0	1.0	4.7	99	1
1.5	1.4	4.9	98.5	1.4
4.3	1.5	5.5	98	2
6.5	1.6	6.0	98	2

3.3.5 Thickness dependent emission color from Mn-doped CsPbBr₃ NPLs

After dopant concentration, now we will discuss how thickness of CsPbBr₃ NPLs can tailor the optical properties. PL spectra of undoped 3 ML, 4 ML and 5 ML NPLs are shown in Figure 3.5a. In Figure 3.5b PL spectra are compared for three representative samples one for each 3 ML, 4 ML and 5 ML category, with optimized Mn content showing the most intense Mn-emission in each category. For 3ML sample, the optimized dopant concentration happens to be 2.8% Mn, for 4 ML 3.2% Mn, whereas, for 5 ML sample 4.3% Mn gives the most intense Mn-emission. All three doped samples exhibit dual emissions. Inset of Figure 3.5b shows the different colors coming out of the three samples upon irradiation with UV light ($\lambda = 365$ nm).

Importantly, the relative intensity of Mn-emission systematically increases with decreasing thickness of NPLs. PL decay dynamics of Mn-emission (Figure 3.5c) in 3 ML sample were fitted using a single-exponential decay function with lifetime of 222 μ s arising from majority of Mn on surface/sub-surface region. However, Mn-emissions from 4 ML and 5 ML samples exhibit a bi-exponential decay. There is a systematic increase in longer lifetime (510 to 550 μ s) component with increasing NPL thickness. This longer lifetime has been attributed to Mn

doped in the interior of NPLs. Mn dopant at the surface might experience some distortion in the octahedral local structure,⁴² influencing both the lifetime and peak energy of Mn-emission.

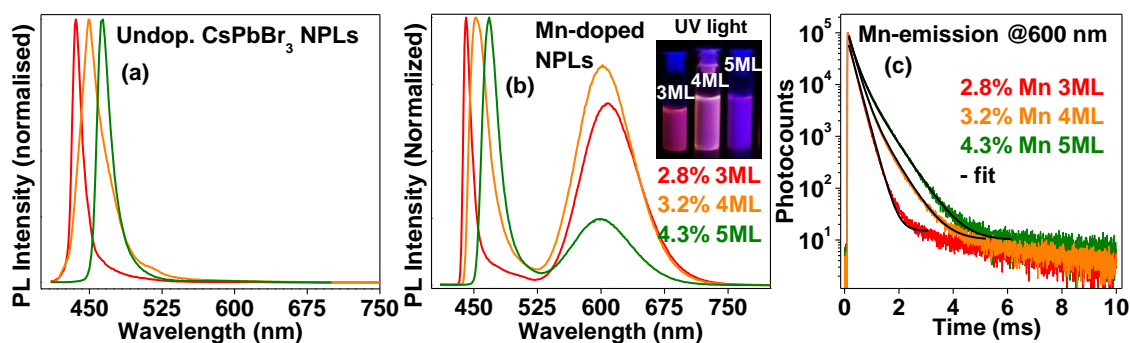


Figure 3.5: (a) PL spectra of undoped 3 ML, 4 ML and 5 ML CsPbBr₃ NPLs. (b) Optimized Mn-doped 3 ML, 4 ML and 5 ML NPLs exhibiting the most intense Mn-emission for each thickness categories, inset shows photographs of dual color emission under UV-light source. (c) PL decay dynamics of Mn-emission for Mn-doped in each thickness of CsPbBr₃ NPLs.

3.3.6 Mn-doping in CsPbBr₃ nanocubes

Now we will explore the efficacy of our postsynthesis Mn-doping protocol for doping CsPbBr₃ nanocubes. Note that the synthesis procedure for undoped NPLs and nanocubes are very much different, and therefore, expected to be somewhat different in terms of ligand binding and related surface chemistry. TEM image in Figure 3.6a shows 1.9% Mn-doped CsPbBr₃ nanocubes with edge length 8.4 ± 1.2 nm. The highly crystalline nature of nanocubes can be seen from lattice fringes displaying interplanar distance of 4.1 Å and 2.8 Å corresponding to (020) or (112) and (004) or (220) planes of orthorhombic CsPbBr₃ respectively. Optical absorption of both doped and undoped samples shown in Figure 3.6b are similar. PL spectra (Figure 3.6b) of both the samples recorded at room temperature are also similar showing only the excitonic emission and no emergence of Mn-emission in doped sample. Similar to NPLs, an increase in excitonic PL intensity is also observed for nanocubes after Mn doping. We note that a similar PL intensity is also observed when tetrabutylammonium bromide (TBAB) is added to CsPbBr₃ nanocubes (data not shown here), probably passivating the surface defects. But absence of Mn-emission from the Mn-doped CsPbBr₃ nanocubes raise doubt about the success of the employed doping methodology. XRD patterns in Figure 3.6c shows that both the undoped and 1.9% Mn doped CsPbBr₃ nanocubes are in orthorhombic phase similar to prior literature.² A magnified view of XRD peak at $2\theta = 29.9^\circ$ in Figure 3.6d suggests small shift towards higher 2θ upon Mn-doping. In order to further confirm whether Mn is doped or not, EPR is excellent tool to probe whether Mn is doped in lattice or not. Interestingly, EPR spectra (Figure 3.6d) of Mn-doped CsPbBr₃

nanocubes show clear sextet hyperfine splitting lines with splitting energy of 9.1 mT, suggesting (refer to earlier discussion corresponding to Figure 3.3c) the doping of Mn^{2+} into the lattice of CsPbBr_3 nanocubes.

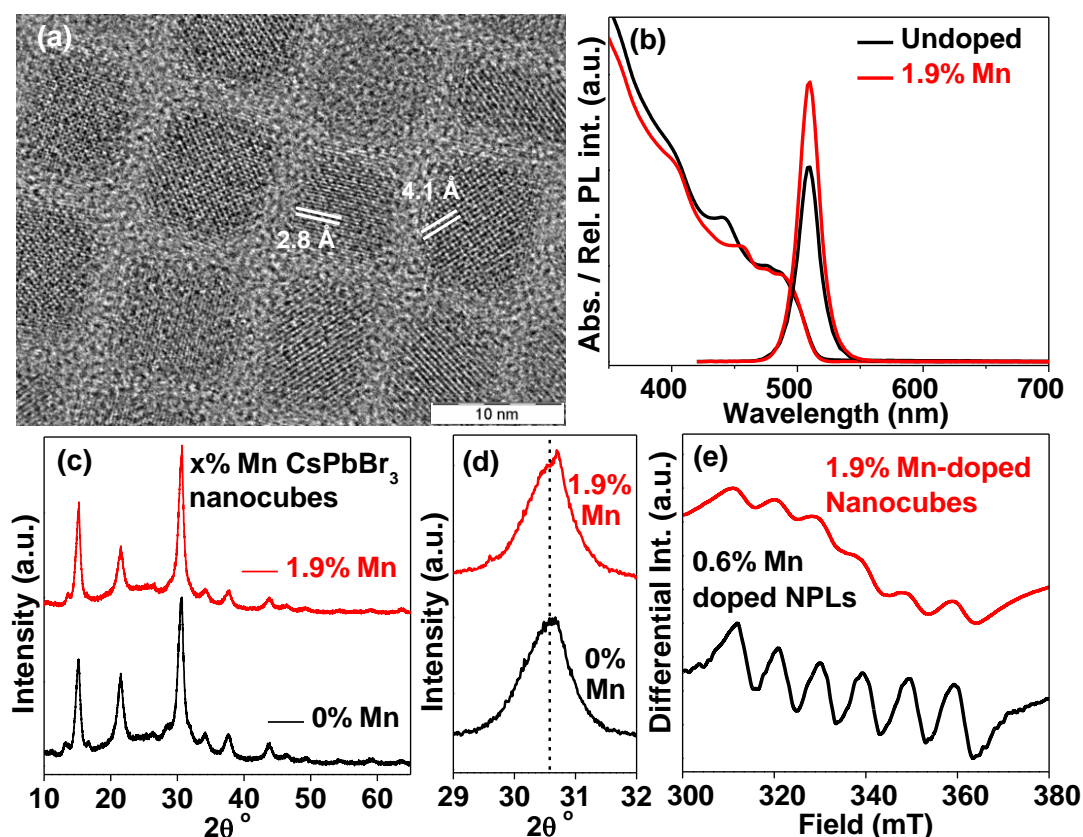


Figure 3.6: (a) TEM image of 1.9% Mn doped nanocubes. (b) Comparison of optical absorption, and PL spectra for undoped and 1.9% Mn-doped nanocubes. (c) Comparison of XRD pattern of undoped and Mn-doped nanocubes. (d) Magnified view of XRD peak at $2\theta = 30.5^\circ$. (e) X-band EPR of 1.9% Mn-doped nanocubes is similar to that of 0.6% Mn-doped NPLs.

So, EPR suggests Mn-doping but no Mn-emission is observed at room temperature for Mn-doped CsPbBr_3 nanocubes. We have varied the Mn doping concentration in the range of 1.9% to 3.9%, but none of the samples show Mn-emission at room temperature. The possible reasons behind this absence of Mn-emission could be (i) slower transfer of excitonic energy from host to dopant compared to excitonic recombination lifetime, (ii) high level of defect density quenching the Mn emission, and/or (iii) back energy transfer from dopant to host quenching Mn-emission. Lifetime for energy transfer from CsPbCl_3 to Mn dopants have been recently reported as ~ 380 ps.^{34, 43} Detailed analysis of energy transfer lifetime for Mn-doped CsPbBr_3 nanocubes is not yet available. But Figure 3.5b shows intense Mn-emission from CsPbBr_3 NPLs. Also, the energy transfer lifetimes of Mn-doped in II-VI semiconductors falls in picoseconds scale.^{44, 45} All these data suggest that the energy transfer lifetime from

CsPbBr₃ nanocubes to Mn is expected to be lower than a few nanoseconds lifetime of excitonic emission from the host. It is to be noted that the rate of excitonic recombination in CsPbBr₃ nanocubes is slower compared to CsPbCl₃ nanocubes.¹ These results suggest that slower energy transfer from CsPbBr₃ nanocube host to Mn dopants is unlikely to be the reason behind the absence of Mn emission. The second possibility of high level of defect density in CsPbBr₃ nanocubes is also unlikely, since CsPbBr₃ nanocubes exhibit significantly higher excitonic PL QY compared to both CsPbBr₃ NPLs and CsPbCl₃ nanocubes which exhibit strong Mn emission. Therefore, we investigate the third possibility, namely, back energy transfer from dopant Mn to host as the probable reason for quenching Mn-emission from Mn-doped CsPbBr₃ nanocubes.

3.3.7 Mn-emission from 1.9% Mn-doped CsPbBr₃ nanocubes

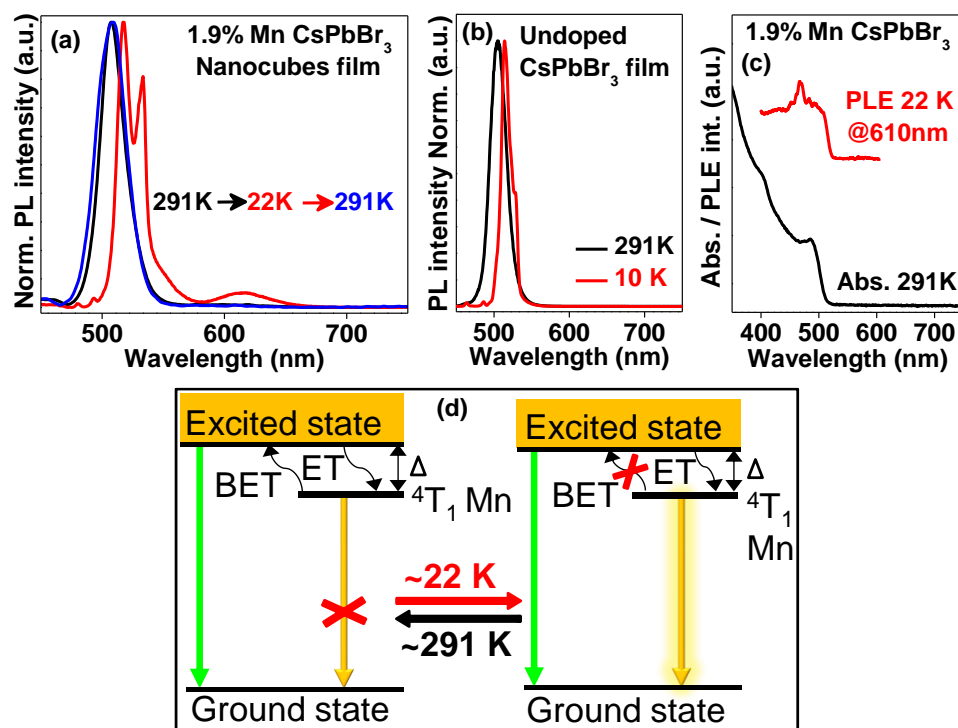


Figure 3.7: (a) Temperature dependent PL spectra recorded reversibly at 291 K, 22 K and back at 291 K for 1.9% Mn doped nanocubes film. (b) Temperature dependent PL spectra of undoped CsPbBr₃ nanocubes. (c) Absorbance at 291 K and PL excitation (PLE) recorded at 22 K for emission at 610 nm. (d) Schematics depicting the Mn-emission emerging at 22 K which otherwise remains quenched at 291 K due to back energy transfer from Mn to CsPbBr₃ nanocube host. Straight arrows indicate radiative transitions and curved arrows are for non-radiative transitions, namely, energy transfer (ET) and back energy transfer (BET).

Prior studies on Mn-doped CdSe NCs have shown similar back energy transfer quenching the Mn PL QY.⁴⁶⁻⁴⁸ Since the optical band gap of host is slightly larger than the Mn-emission energy, such back energy transfer will require thermal activation. This motivated us to study PL at low temperatures. Interestingly, Figure 3.7a shows the Mn-emission (610 nm) from

1.9% Mn-doped CsPbBr₃ nanocubes at 22 K and the emission vanishes at 291 K in a reversible manner during both heating and cooling process. Control experiments for undoped CsPbBr₃ nanocubes do not exhibit the 610 nm emission at low temperatures, as shown in Figure 3.7b. PL excitation (PLE) spectrum (Figure 3.7c) at 22 K shows that the 610 nm emission originates through excitation of CsPbBr₃ nanocubes. Since the Mn-emission lifetime is very long in sub-ms scale compared to a few ns lifetime of excitonic emission, even a relatively inefficient back energy transfer process can quench the Mn-emission. For this back energy transfer, an energy barrier Δ , defined as the difference between peak energies of excitonic emission and Mn-emission needs to be overcome. The process is schematically shown in Figure 3.7d, wherein, energy transfer (ET) from host to dopant and back energy transfer (BET) are depicted by curly solid line arrows. At low temperature BET is significantly reduced allowing Mn-emission to occur.

3.3.8 Temperature dependent PL and barrier for back energy transfer

To understand the back energy transfer better, we have studied temperature-dependent PL of both Mn-doped nanocubes and NPLs. Figure 3.8a shows that the excitonic PL of 1.9% Mn-doped CsPbBr₃ nanocubes undergoes a red-shift with decreasing temperature, along with a splitting of peak below 45 K, similar to prior reports^{16, 21, 49} of undoped CsPbBr₃ nanocubes. Figure 3.8b show the Mn emission starts appearing at \sim 225 K and systematically increases with decreasing temperature. Also, Mn-emission shows consistent systematic red-shift upon decreasing the measurement temperature. The red-shift is attributed to contraction of lattice that increases the ligand field strength around Mn²⁺ ions at lower temperature, decreasing energy gap between ⁴T_{1g} and ⁶A_{1g} states.⁵⁰ Figure 3.8d shows temperature dependent PL spectra of 2.8% Mn doped CsPbBr₃ NPLs with 3 ML thickness. Figure 3.8e highlights the increase in Mn emission intensity with decrease in temperature. In contrast to nanocubes (Figure 3.8a), the excitonic PL undergoes blue shift with decreasing temperature for Mn-doped NPLs. Since the temperature dependence of excitonic PL on shape of CsPbBr₃ NCs is not the focus of our present study, mechanistic insights behind this contrasting observation will be discussed elsewhere. Figure 3.8c shows the ratio ($I_{\text{Mn}}/I_{\text{exc}}$) of integrated intensity for Mn-emission (I_{Mn}) to excitonic emission (I_{exc}) increases with decreasing temperatures for both the samples. In the case of 3 ML sample, Δ is the largest as shown schematically in Figure 3.9. At lower temperatures, Δ increases further for NPLs as evident from the blue-shift in excitonic PL (Figure 3.8d). Both this increase in Δ and decrease in temperature is expected to suppress the back energy transfer from Mn to host, therefore, monotonically increasing

$I_{\text{Mn}}/I_{\text{exc}}$ with decreasing temperature. In the case of Mn-doped CsPbBr₃ nanocubes a minor abnormality in $I_{\text{Mn}}/I_{\text{exc}}$ is observed between 150 – 50 K region where the $I_{\text{Mn}}/I_{\text{exc}}$ slightly decreases with temperature. This abnormal trend might be because of the fact that excitonic PL peak for nanocubes red-shifts (Figure 3.8a) with decreasing temperature, therefore decreasing Δ which may slightly favor the back energy transfer.

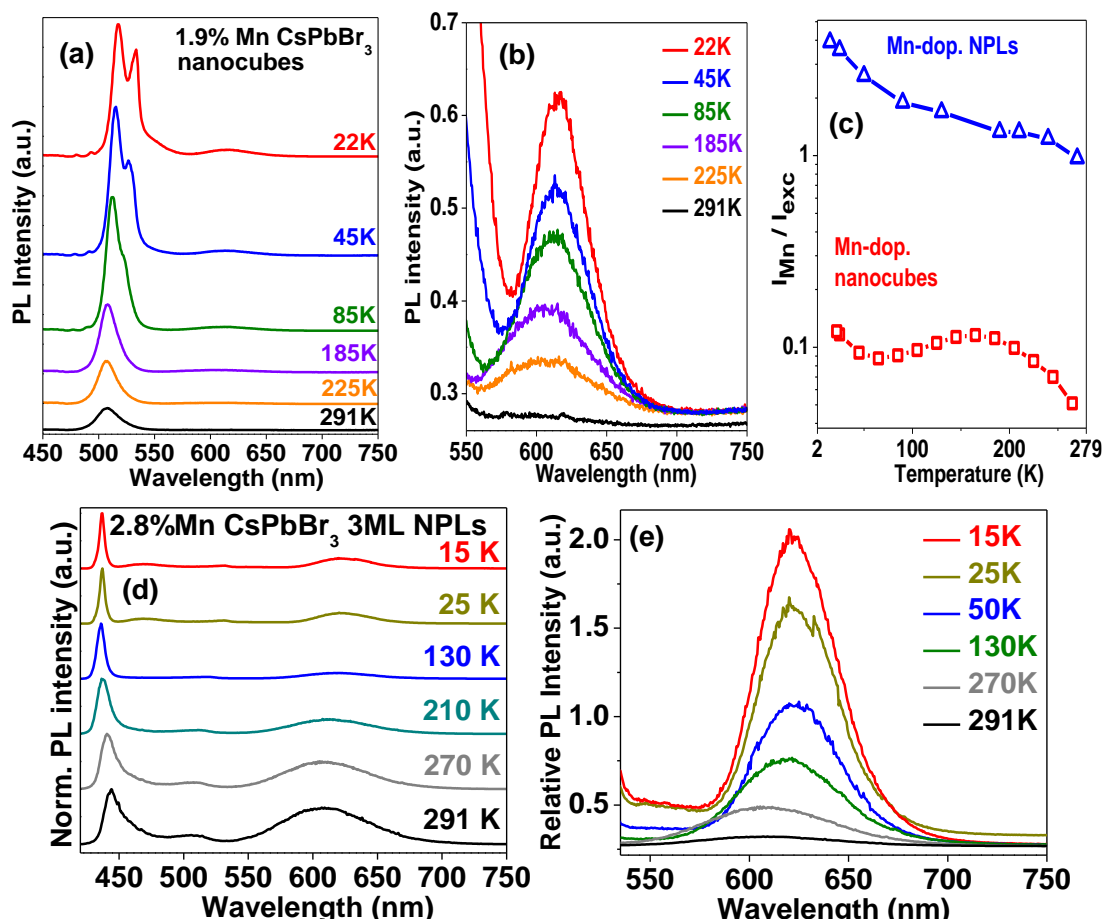


Figure 3.8: (a) Temperature dependent PL spectra and (b) spectral region from 550 to 750 nm highlighting the increase in Mn emission intensity upon decrease in temperature for 1.9% Mn-doped CsPbBr₃ nanocubes. (c) Ratio of integrated intensity of Mn-emission (I_{Mn}) to that of excitonic emission (I_{exc}) for 1.9% Mn-doped nanocubes and 2.8% Mn-doped 3 ML NPLs. The symbols denote experimental data and solid lines are guidance to observed trend. (d) Temperature dependent PL spectra and (e) spectral region from 540 to 750 nm for 2.8% Mn-doped CsPbBr₃ NPLs. Spectra in panel (a) and (d) have been shifted upwards for clarity in presentation.

Overall, the experimental results suggest Δ and temperature has opposing effect on back energy transfer. If temperature is constant, then increase in Δ should suppress the back energy transfer, thus resulting into higher intensity of Mn-emission. This is precisely what we observe (Figure 3.9), Δ is the smallest for CsPbBr₃ nanocubes resulting into absence of Mn-emission at room temperature (Figure 3.6b). In the case of NPLs, Δ increases with decreasing thickness of NPLs showing most intense Mn-emission for 3 ML sample (Figure 3.5b). This

requirement of larger Δ for efficient Mn-emission in perovskite NCs can also explain previous reports. For example, (i) Parobek et al²² showed PL QY for Mn emission increases with decreasing size of CsPbBr₃ nanocubes increasing the Δ , and (ii) stronger Mn-emission is observed from Mn-doped CsPbCl₃ with higher Δ compared to CsPb(Cl/Br)₃ nanocubes. We note that different systems and Δ also might influence the energy transfer rate from host to dopant, influencing the PL QY of Mn emission. But energy transfer lifetimes are expected (sub-ns) to be an order of magnitude faster compared to the excitonic lifetime,^{34, 43} whereas back energy transfer competes with extremely slow sub-ms Mn emission lifetimes. So we expect that the back energy transfer is dominant quenching mechanism of Mn emission in Mn-doped CsPbBr₃ nanocubes.

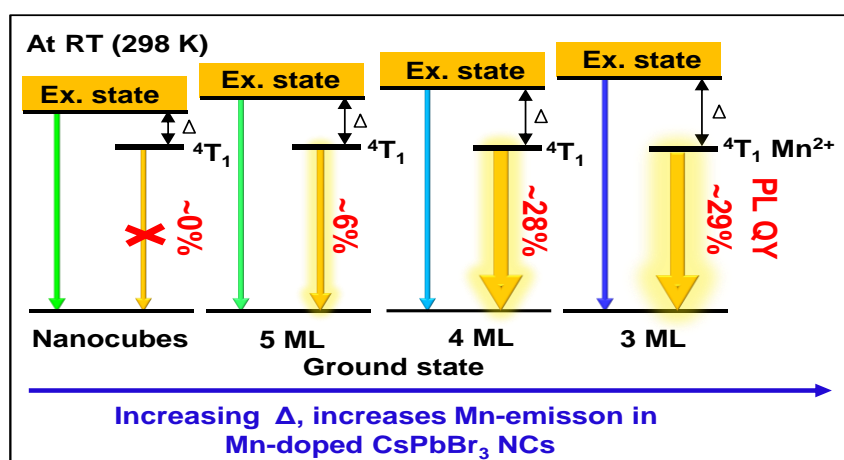


Figure 3.9: Schematics summarizing the fate of excited state at 298 K, upon changing the barrier (Δ) for back energy transfer in CsPbBr₃ NCs.

3.3.9 Synthesis, morphology and structure of Yb-doped CsPbX₃ nanocubes and NPLs

Final section of this manuscript is dedicated to adapt our postsynthesis methodology to dope Yb in all compositions of CsPbX₃ nanocubes. Precursor solution of Yb(NO₃)₃ in acetone : toluene mixture with volume ratio 1 : 3 (similar to Mn-doping case) works well for the postsynthesis Yb-doping in CsPbCl₃ and CsPbBr₃ NCs. But presence of acetone destabilizes the cubic phase of CsPbI₃ nanocubes. Therefore, postsynthesis Yb-doping in all compositions of CsPbX₃ NCs is carried out by replacing acetone with methyl acetate.⁷ So our final Yb-precursor is Yb(NO₃)₃ dissolved into the mixture of methyl acetate : toluene with volume ratio 1 : 3, for all Yb-doped samples reported in this paper. The resultant doped NCs are washed carefully without addition of excess polar solvents and optimized conditions are mentioned in the SI. We have also demonstrated Yb-doping in CsPbBr₃ NPLs. Within our knowledge, there is no prior report of Yb doping in CsPbBr₃ or CsPbI₃ NCs. Optical band gap of CsPbBr₃ nanocubes is 2.53 eV (490 nm) and that of CsPbI₃ nanocubes is 1.96 eV

(630 nm). Band gaps of both samples are sufficiently large compared to energy gap $^2F_{5/2} \rightarrow ^2F_{7/2}$ of Yb emission (~990 nm, 1.25 eV). So, one would expect Yb-emission from all halide compositions of CsPbX₃ NCs. Also, barrier for the vexing problem of back energy transfer from Yb to CsPbX₃ host should be high. This motivated us to dope Yb in all compositions of CsPbX₃ NCs.

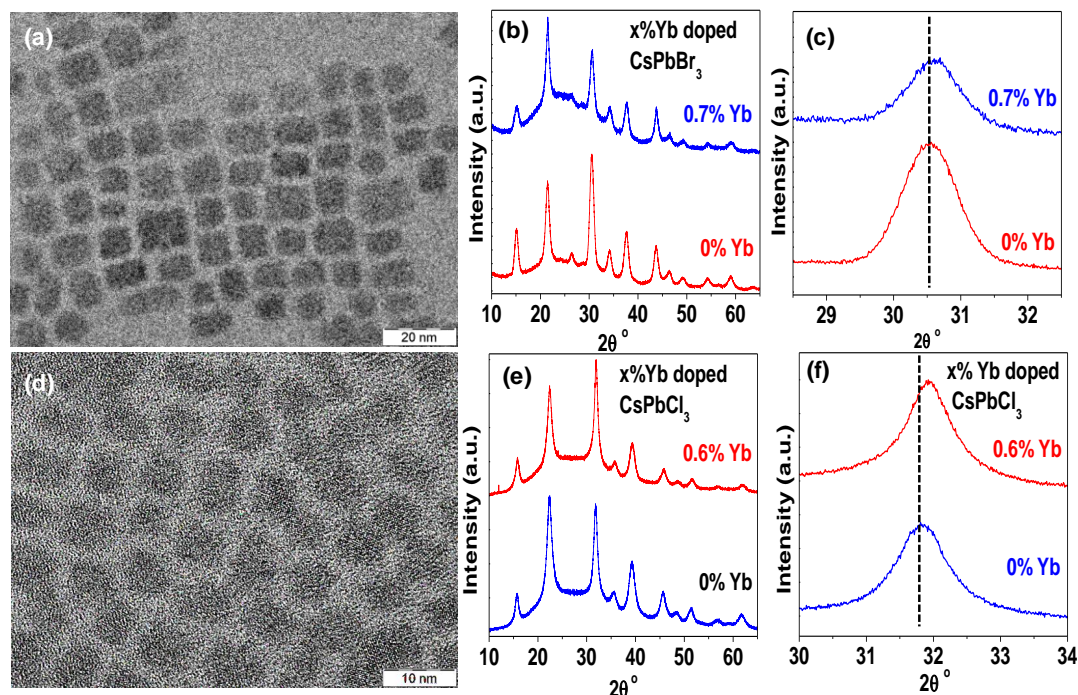


Figure 3.10: (a) TEM image of 0.7% Yb-doped CsPbBr₃ nanocubes. Comparison of (b) XRD pattern and (c) magnified view of XRD peak at $2\theta = 30.55^\circ$ for undoped and 0.7% Yb doped CsPbBr₃ nanocubes. (d) TEM image of 0.6% Yb-doped CsPbCl₃ nanocubes. XRD pattern (e) and (f) magnified view of XRD peak at $2\theta = 30.8^\circ$ for undoped and 0.6% Yb doped CsPbCl₃ nanocubes.

Figure 3.10a shows a representative TEM image of 0.7% Yb-doped CsPbBr₃ with cubic morphology. Figure 3.10b shows both undoped and Yb-doped CsPbBr₃ exist in orthorhombic phase. Figure 3.10c suggest lattice doping of Yb in CsPbBr₃ nanocubes upon shift of XRD peak at $2\theta = 30.55^\circ$ towards higher 2θ values in Yb-doped CsPbBr₃ nanocubes. Similarly, cubic morphology and Yb doping is confirmed in CsPbCl₃ nanocubes see detailed characterization using TEM and XRD in Figure 3.10d-f. Overall, postsynthesis doping of Yb in CsPbX₃ nanocubes preserves morphology, size and structure of nanocubes before and after Yb-doping.

3.3.10 Near IR Yb-emission from Yb-doped CsPbX₃ NCs

Figure 3.11a shows PL spectra of undoped (dashed lines) and Yb-doped (solid lines) CsPbX₃ NCs. The intensity of excitonic PL increases after Yb-doping for all compositions, similar to

the case of Mn-doping discussed above. The relative intensity of Yb-emission measured using NIR detector should not be correlated with excitonic emission of host that has been measured with a different detector in the visible region. But the intensity of NIR Yb-emission can be compared for different hosts. 0.6% Yb-doped CsPbCl₃ nanocubes with the highest band gap yield the highest intensity for Yb-emission compared to 0.7% Yb-doped CsPbBr₃ nanocubes. Previous literature suggests Yb-emission is somewhat sensitive to local environment in the host.^{51, 52} In Figure 3.11a, peak position of the Yb-emission shows a small blue-shift of ~20 nm as the host changes from CsPbCl₃ to CsPbI₃ nanocubes.

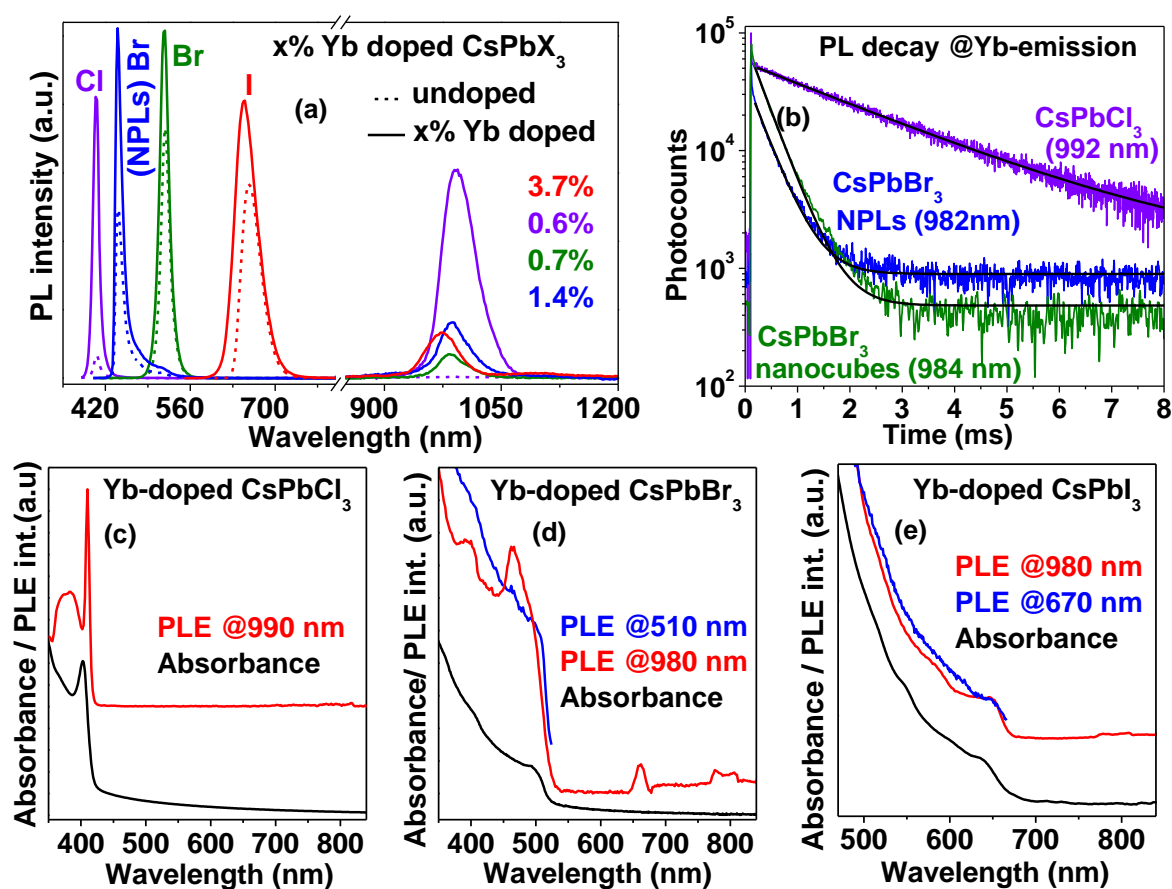


Figure 3.11: (a) PL spectra of undoped and Yb-doped CsPbX₃ nanocubes and CsPbBr₃ NPLs. Dotted lines are for undoped samples, and solid lines of same color are for Yb-doped samples. The relative PL intensity of excitonic emission of host in visible region should not be compared with the NIR Yb-emission since the detectors for visible and NIR region are different. (b) PL decay dynamics of Yb-emission from CsPbX₃ nanocubes and NPLs are fitted with single exponential decay function. Comparison of UV-visible-NIR absorption and PLE spectra of (c) Yb-doped CsPbCl₃, (d) Yb-doped CsPbBr₃, and (e) Yb-doped CsPbI₃ nanocubes.

PL decay dynamics of Yb-emission shown in Figure 3.11b are fitted with a single-exponential decay function. A long lifetime ~0.4 ms is observed for Yb-doped CsPbBr₃ NPLs and nanocubes, and further longer lifetime ~2.4 ms is observed for Yb-doped CsPbCl₃

nanocubes. PL excitation (PLE) data for all the Yb-doped samples are shown in Figure 3.11c-e. The similarity of PLE data with absorption spectra of host NCs confirms that the host NCs absorb the excitation light. This excited host then excites the Yb-dopants, which then emit light during the de-excitation process. Both longer lifetimes (Figure 3.11b), along with the PLE data (Figure 3.11c-e) suggest doping of Yb into the lattice of NCs, similar to prior reports.^{13, 15} Prior literature suggested quantum cutting, where one high energy photon absorbed by the host can excite two Yb-dopants.¹⁴ We have not made such quantitative estimation in the present study, and therefore, do not comment on the exact mechanism of downconversion of Yb-emission.

3.4 Conclusions

We have developed a generic postsynthesis strategy to dope Mn²⁺ and Yb³⁺ in the family of CsPbX₃ perovskite NCs of various compositions and shapes. The host NCs are pre-formed from a single synthesis and remains the same for different dopant concentrations, allowing us to study the effect of doping on optical properties more systematically and reliably. These Mn-doped and Yb-doped CsPbX₃ NCs exhibit dopant emission along with excitonic emission from host. Mn-doped CsPbBr₃ nanocubes (optical gap 490 nm) do not exhibit Mn-emission at room temperature. We find that the BET from dopant to host quenches the Mn-emission in these nanocubes. This BET can be suppressed either by decreasing the temperature, or by increasing Δ . Therefore, Mn-doped CsPbBr₃ nanocubes exhibit Mn-emission at temperatures below 225 K. On the other hand, Mn-doped CsPbBr₃ NPLs can exhibit intense Mn-emission at room temperature because of large Δ . We then extended our postsynthesis doping approach to Yb-doped CsPbX₃ NCs of all halide compositions. NIR Yb-emission from Yb-doped CsPbBr₃ and CsPbI₃ NCs are reported here for the first time. We hope that this 1-minute postsynthesis doping procedure can be extended to other sets of dopants and perovskites NCs, in near future.

3.5 References

1. Protesescu, L.; Yakunin, S.; Bodnarchuk, M. I.; Krieg, F.; Caputo, R.; Hendon, C. H.; Yang, R. X.; Walsh, A.; Kovalenko, M. V. Nanocrystals of Cesium Lead Halide Perovskites (CsPbX₃, X = Cl, Br, and I): Novel Optoelectronic Materials Showing Bright Emission with Wide Color Gamut. *Nano Lett.* **2015**, *15*, 3692-3696.

2. Swarnkar, A.; Chulliyil, R.; Ravi, V. K.; Irfanullah, M.; Chowdhury, A.; Nag, A. Colloidal CsPbBr₃ Perovskite Nanocrystals: Luminescence beyond Traditional Quantum Dots. *Angew. Chem., Int. Ed.* **2015**, *54*, 15424-15428.
3. Jizhong, S.; Jianhai, L.; Xiaoming, L.; Leimeng, X.; Yuhui, D.; Haibo, Z. Quantum Dot Light-Emitting Diodes Based on Inorganic Perovskite Cesium Lead Halides (CsPbX₃). *Adv. Mater.* **2015**, *27*, 7162-7167.
4. Sichert, J. A.; Tong, Y.; Mutz, N.; Vollmer, M.; Fischer, S.; Milowska, K. Z.; García Cortadella, R.; Nickel, B.; Cardenas-Daw, C.; Stolarczyk, J. K.; Urban, A. S.; Feldmann, J. Quantum Size Effect in Organometal Halide Perovskite Nanoplatelets. *Nano Lett.* **2015**, *15*, 6521-6527.
5. Zhang, X.; Lin, H.; Huang, H.; Reckmeier, C.; Zhang, Y.; Choy, W. C. H.; Rogach, A. L. Enhancing the Brightness of Cesium Lead Halide Perovskite Nanocrystal Based Green Light-Emitting Devices through the Interface Engineering with Perfluorinated Ionomer. *Nano Lett.* **2016**, *16*, 1415-1420.
6. Zhang, D.; Yu, Y.; Bekenstein, Y.; Wong, A. B.; Alivisatos, A. P.; Yang, P. Ultrathin Colloidal Cesium Lead Halide Perovskite Nanowires. *J. Am. Chem. Soc.* **2016**, *138*, 13155-13158.
7. Swarnkar, A.; Marshall, A. R.; Sanehira, E. M.; Chernomordik, B. D.; Moore, D. T.; Christians, J. A.; Chakrabarti, T.; Luther, J. M. Quantum Dot-Induced Phase Stabilization of α -CsPbI₃ Perovskite for High-Efficiency Photovoltaics. *Science* **2016**, *354*, 92-95.
8. Zhi-Jun, L.; Elan, H.; Jian, L.; Hunter, D. A.; Chen-Ho, T.; Li-Zhu, W.; Weiwei, Z. Photoelectrochemically Active and Environmentally Stable CsPbBr₃/TiO₂ Core/Shell Nanocrystals. *Adv. Funct. Mater.* **2018**, *28*, 1704288.
9. Akkerman, Q. A.; Rainò, G.; Kovalenko, M. V.; Manna, L. Genesis, Challenges and Opportunities for Colloidal Lead Halide Perovskite Nanocrystals. *Nat. Mater.* **2018**, *17*, 394-405.
10. Parobek, D.; Roman, B. J.; Dong, Y.; Jin, H.; Lee, E.; Sheldon, M.; Son, D. H. Exciton-to-Dopant Energy Transfer in Mn-Doped Cesium Lead Halide Perovskite Nanocrystals. *Nano Lett.* **2016**, *16*, 7376-7380.
11. Liu, W.; Lin, Q.; Li, H.; Wu, K.; Robel, I.; Pietryga, J. M.; Klimov, V. I. Mn²⁺-Doped Lead Halide Perovskite Nanocrystals with Dual-Color Emission Controlled by Halide Content. *J. Am. Chem. Soc.* **2016**, *138*, 14954-14961.
12. Mir, W. J.; Jagadeeswararao, M.; Das, S.; Nag, A. Colloidal Mn-Doped Cesium Lead Halide Perovskite Nanoplatelets. *ACS Energy Lett.* **2017**, *2*, 537-543.

13. Pan, G.; Bai, X.; Yang, D.; Chen, X.; Jing, P.; Qu, S.; Zhang, L.; Zhou, D.; Zhu, J.; Xu, W.; Dong, B.; Song, H. Doping Lanthanide into Perovskite Nanocrystals: Highly Improved and Expanded Optical Properties. *Nano Lett.* **2017**, *17*, 8005-8011.
14. Milstein, T. J.; Kroupa, D. M.; Gamelin, D. R. Picosecond Quantum Cutting Generates Photoluminescence Quantum Yields Over 100% in Ytterbium-Doped CsPbCl₃ Nanocrystals. *Nano Lett.* **2018**, *18*, 3792-3799.
15. Donglei, Z.; Dali, L.; Gencai, P.; Xu, C.; Dongyu, L.; Wen, X.; Xue, B.; Hongwei, S. Cerium and Ytterbium Codoped Halide Perovskite Quantum Dots: A Novel and Efficient Downconverter for Improving the Performance of Silicon Solar Cells. *Adv. Mater.* **2017**, *29*, 1704149.
16. Yuan, X.; Ji, S.; De Siena, M. C.; Fei, L.; Zhao, Z.; Wang, Y.; Li, H.; Zhao, J.; Gamelin, D. R. Photoluminescence Temperature Dependence, Dynamics, and Quantum Efficiencies in Mn²⁺-Doped CsPbCl₃ Perovskite Nanocrystals with Varied Dopant Concentration. *Chem. Mater.* **2017**, *29*, 8003-8011.
17. Wang, F.; Yang, M.; Ji, S.; Yang, L.; Zhao, J.; Liu, H.; Sui, Y.; Sun, Y.; Yang, J.; Zhang, X. Boosting Spectral Response of Multi-Crystalline Si Solar Cells with Mn²⁺ Doped CsPbCl₃ Quantum Dots Downconverter. *J. Power Sources* **2018**, *395*, 85-91.
18. Bradshaw, L. R.; Knowles, K. E.; McDowall, S.; Gamelin, D. R. Nanocrystals for Luminescent Solar Concentrators. *Nano Lett.* **2015**, *15*, 1315-1323.
19. Meinardi, F.; Akkerman, Q. A.; Bruni, F.; Park, S.; Mauri, M.; Dang, Z.; Manna, L.; Brovelli, S. Doped Halide Perovskite Nanocrystals for Reabsorption-Free Luminescent Solar Concentrators. *ACS Energy Lett.* **2017**, *2*, 2368-2377.
20. Swarnkar, A.; Mir, W. J.; Nag, A. Can B-Site Doping or Alloying Improve Thermal- and Phase-Stability of All-Inorganic CsPbX₃ (X = Cl, Br, I) Perovskites? *ACS Energy Lett.* **2018**, *3*, 286-289.
21. Zou, S.; Liu, Y.; Li, J.; Liu, C.; Feng, R.; Jiang, F.; Li, Y.; Song, J.; Zeng, H.; Hong, M.; Chen, X. Stabilizing Cesium Lead Halide Perovskite Lattice through Mn(II) Substitution for Air-Stable Light-Emitting Diodes. *J. Am. Chem. Soc.* **2017**, *139*, 11443-11450.
22. Parobek, D.; Dong, Y.; Qiao, T.; Son, D. H. Direct Hot-Injection Synthesis of Mn-Doped CsPbBr₃ Nanocrystals. *Chem. Mater.* **2018**, *30*, 2939-2944.
23. Akkerman, Q. A.; Motti, S. G.; Srimath Kandada, A. R.; Mosconi, E.; D'Innocenzo, V.; Bertoni, G.; Marras, S.; Kamino, B. A.; Miranda, L.; De Angelis, F.; Petrozza, A.; Prato, M.; Manna, L. Solution Synthesis Approach to Colloidal Cesium Lead Halide Perovskite

- Nanoplatelets with Monolayer-Level Thickness Control. *J. Am. Chem. Soc.* **2016**, *138*, 1010-1016.
24. Guangguang, H.; Chunlei, W.; Shuhong, X.; Shenfei, Z.; Ju, L.; Zhuyuan, W.; Changgui, L.; Yiping, C. Postsynthetic Doping of MnCl₂ Molecules into Preformed CsPbBr₃ Perovskite Nanocrystals via a Halide Exchange- Driven Cation Exchange. *Adv. Mater.* **2017**, *29*, 1700095.
25. De Roo, J.; Ibáñez, M.; Geiregat, P.; Nedelcu, G.; Walravens, W.; Maes, J.; Martins, J. C.; Van Driessche, I.; Kovalenko, M. V.; Hens, Z. Highly Dynamic Ligand Binding and Light Absorption Coefficient of Cesium Lead Bromide Perovskite Nanocrystals. *ACS Nano* **2016**, *10*, 2071-2081.
26. Nedelcu, G.; Protesescu, L.; Yakunin, S.; Bodnarchuk, M. I.; Grotevent, M. J.; Kovalenko, M. V. Fast Anion-Exchange in Highly Luminescent Nanocrystals of Cesium Lead Halide Perovskites (CsPbX₃, X = Cl, Br, I). *Nano Lett.* **2015**, *15*, 5635-5640.
27. Akkerman, Q. A.; D’Innocenzo, V.; Accornero, S.; Scarpellini, A.; Petrozza, A.; Prato, M.; Manna, L. Tuning the Optical Properties of Cesium Lead Halide Perovskite Nanocrystals by Anion Exchange Reactions. *J. Am. Chem. Soc.* **2015**, *137*, 10276-10281.
28. Bekenstein, Y.; Koscher, B. A.; Eaton, S. W.; Yang, P.; Alivisatos, A. P. Highly Luminescent Colloidal Nanoplates of Perovskite Cesium Lead Halide and Their Oriented Assemblies. *J. Am. Chem. Soc.* **2015**, *137*, 16008-16011.
29. Huimei, H.; Bing, T.; Ying, M. Controlled Synthesis of Quantum Confined CsPbBr₃ Perovskite Nanocrystals under Ambient Conditions. *Nanotechnology* **2018**, *29*, 055601.
30. Narayan, P.; Samrat, D. A.; Angshuman, N.; D., S. D. Luminescence, Plasmonic, and Magnetic Properties of Doped Semiconductor Nanocrystals. *Angew. Chem., Int. Ed.* **2017**, *56*, 7038-7054.
31. Nag, A.; Chakraborty, S.; Sarma, D. D. To Dope Mn²⁺ in a Semiconducting Nanocrystal. *J. Am. Chem. Soc.* **2008**, *130*, 10605-10611.
32. Biswas, A.; Bakthavatsalam, R.; Kundu, J. Efficient Exciton to Dopant Energy Transfer in Mn²⁺-Doped (C₄H₉NH₃)₂PbBr₄ Two-Dimensional (2D) Layered Perovskites. *Chem. Mater.* **2017**, *29*, 7816-7825.
33. Lin, J.; Hu, D.-D.; Zhang, Q.; Li, D.-S.; Wu, T.; Bu, X.; Feng, P. Improving Photoluminescence Emission Efficiency of Nanocluster-Based Materials by in Situ Doping Synthetic Strategy. *J. Phys. Chem. C* **2016**, *120*, 29390-29396.
34. Rossi, D.; Parobek, D.; Dong, Y.; Son, D. H. Dynamics of Exciton–Mn Energy Transfer in Mn-Doped CsPbCl₃ Perovskite Nanocrystals. *J. Phys. Chem. C* **2017**, *121*, 17143-17149.

35. Gao, D.; Qiao, B.; Xu, Z.; Song, D.; Song, P.; Liang, Z.; Shen, Z.; Cao, J.; Zhang, J.; Zhao, S. Postsynthetic, Reversible Cation Exchange between Pb²⁺ and Mn²⁺ in Cesium Lead Chloride Perovskite Nanocrystals. *J. Phys. Chem. C* **2017**, *121*, 20387-20395.
36. Das Adhikari, S.; Dutta, S. K.; Dutta, A.; Guria, A. K.; Pradhan, N. Chemically Tailoring the Dopant Emission in Manganese- Doped CsPbCl₃ Perovskite Nanocrystals. *Angew. Chem.* **2017**, *129*, 8872-8876.
37. Das Adhikari, S.; Dutta, A.; Dutta, S. K.; Pradhan, N. Layered Perovskites L₂(Pb_{1-x}Mn_x)Cl₄ to Mn-Doped CsPbCl₃ Perovskite Platelets. *ACS Energy Lett.* **2018**, *3*, 1247-1253.
38. Chen, D.; Fang, G.; Chen, X. Silica-Coated Mn-Doped CsPb(Cl/Br)₃ Inorganic Perovskite Quantum Dots: Exciton-to-Mn Energy Transfer and Blue-Excitable Solid-State Lighting. *ACS Appl. Mater. Interfaces* **2017**, *9*, 40477-40487.
39. Tandon, B.; Yadav, A.; Khurana, D.; Reddy, P.; Santra, P. K.; Nag, A. Size-Induced Enhancement of Carrier Density, LSPR Quality Factor, and Carrier Mobility in Cr–Sn Doped In₂O₃ Nanocrystals. *Chem. Mater.* **2017**, *29*, 9360-9368.
40. Guyot-Sionnest, P.; Lhuillier, E.; Liu, H. A Mirage Study of CdSe Colloidal Quantum Dot Films, Urbach Tail, and Surface States. *J. Chem. Phys.* **2012**, *137*, 154704.
41. Pal, J.; Bhunia, A.; Chakraborty, S.; Manna, S.; Das, S.; Dewan, A.; Datta, S.; Nag, A. Synthesis and Optical Properties of Colloidal M₃Bi₂I₉ (M = Cs, Rb) Perovskite Nanocrystals. *J. Phys. Chem. C* **2018**, *122*, 10643-10649.
42. Nag, A.; Cherian, R.; Mahadevan, P.; Gopal, A. V.; Hazarika, A.; Mohan, A.; Vengurlekar, A. S.; Sarma, D. D. Size-Dependent Tuning of Mn²⁺ d Emission in Mn²⁺-Doped CdS Nanocrystals: Bulk vs Surface. *J. Phys. Chem. C* **2010**, *114*, 18323-18329.
43. Xu, K.; Meijerink, A. Tuning Exciton–Mn²⁺ Energy Transfer in Mixed Halide Perovskite Nanocrystals. *Chem. Mater.* **2018**, *30*, 5346-5352.
44. Chen, H. Y.; Chen, T. Y.; Son, D. H. Measurement of Energy Transfer Time in Colloidal Mn-Doped Semiconductor Nanocrystals. *J. Phys. Chem. C* **2010**, *114*, 4418-4423.
45. Chen, H. Y.; Maiti, S.; Son, D. H. Doping Location-Dependent Energy Transfer Dynamics in Mn-Doped CdS/ZnS Nanocrystals. *ACS Nano* **2012**, *6*, 583-591.
46. Beaulac, R.; Archer, P. I.; van Rijssel, J.; Meijerink, A.; Gamelin, D. R. Exciton Storage by Mn²⁺ in Colloidal Mn²⁺-Doped CdSe Quantum Dots. *Nano Lett.* **2008**, *8*, 2949-2953.
47. Beaulac, R.; Archer, P. I.; Ochsenein, S. T.; Gamelin, D. R. Mn²⁺-Doped CdSe Quantum Dots: New Inorganic Materials for Spin-Electronics and Spin-Photonics. *Adv. Funct. Mater.* **2008**, *18*, 3873-3891.

48. Vlaskin, V. A.; Janssen, N.; van Rijssel, J.; Beaulac, R.; Gamelin, D. R. Tunable Dual Emission in Doped Semiconductor Nanocrystals. *Nano Lett.* **2010**, *10*, 3670-3674.
49. Shinde, A.; Gahlaut, R.; Mahamuni, S. Low-Temperature Photoluminescence Studies of CsPbBr₃ Quantum Dots. *J. Phys. Chem. C* **2017**, *121*, 14872-14878.
50. Chen, W.; Su, F.; Li, G.; Joly, A. G.; Malm, J.-O.; Bovin, J. O. Temperature and Pressure Dependences of the Mn²⁺ and Donor–Acceptor Emissions in ZnS:Mn²⁺ Nanoparticles. *J. Appl. Phys.* **2002**, *92*, 1950-1955.
51. Creutz, S. E.; Fainblat, R.; Kim, Y.; De Siena, M. C.; Gamelin, D. R. Selective Cation Exchange Strategy for the Synthesis of Colloidal Yb³⁺-Doped Chalcogenide Nanocrystals with Strong Broadband Visible Absorption and Long-Lived Near-Infrared Emission. *J. Am. Chem. Soc.* **2017**, *139*, 11814-11824.
52. Martín-Rodríguez, R.; Geitenbeek, R.; Meijerink, A. Incorporation and Luminescence of Yb³⁺ in CdSe Nanocrystals. *J. Am. Chem. Soc.* **2013**, *135*, 13668-13671.

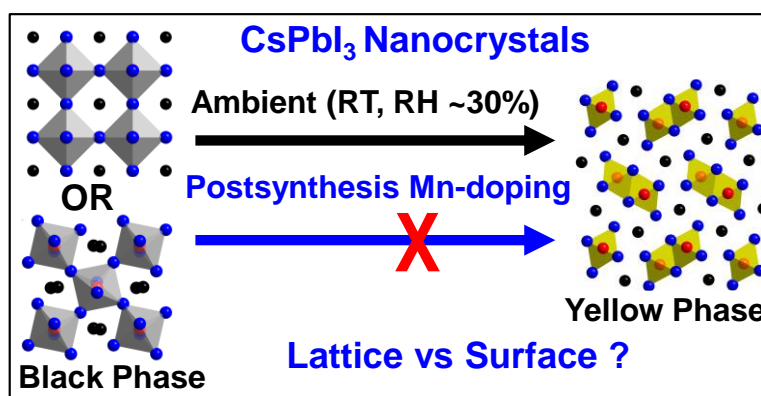
Chapter 4

Postsynthesis Mn-Doping in CsPbI₃ Nanocrystals to Stabilize Black Perovskite Phase

.....
The work presented in this chapter is published online under following details. Mir, J. W.; Swarnkar, A.; Nag, A. *Nanoscale* **2019**, *11*, 4278-4286. Copyright 2019 Royal Society of Chemistry.

Abstract

Long term stability of black perovskite phase of CsPbI₃ in ambient conditions is an important challenge for their optoelectronic applications in real life. Nanocrystalline size is found to improve the stability of the black phase at room temperature. Furthermore, doping Mn is proposed to improve the stability of black perovskite phase of CsPbI₃ nanocrystals (NCs). However, the undoped and Mn-doped CsPbI₃ NCs are prepared in different batches with somewhat different synthesis conditions thus obliterating the role of Mn on stability of black phase of CsPbI₃ NCs. Here, we elucidate the effect of Mn doping on the surface and lattice energy of CsPbI₃ NCs, stabilizing the black phase. For this purpose, we employ a postsynthesis doping strategy which has an advantage that the initial host remains the same for both undoped and Mn-doped samples. Uncertainties of size/shape, surface energy, and structure through direct synthesis of undoped and Mn-doped NCs in different batches can be neglected in our postsynthesis doping strategy, allowing us to study effect of dopant in a more controlled manner. Our postsynthesis Mn-doping in CsPbI₃ NCs shows that the black phase stability in ambient conditions improves from few days for undoped sample to nearly a month's time for Mn-doped sample. We find that though surface passivation with dopant precursor improve both colloidal and phase stability of black CsPbI₃ NCs, it is the contraction of lattice upon Mn-doping that mainly stabilize the films of black phase CsPbI₃ NCs. Similarly, we find that Mn-doped CsPbBr₃ NCs show improved ambient stability of photoluminescence compared to the undoped sample.

Graphical abstract

4.1 Introduction

Superior thermal stability of CsPbI₃ makes it more desirable over organic-inorganic hybrid perovskites like MAPbI₃ (MA⁺ = CH₃NH₃⁺) for optoelectronic applications including solar cells.¹ But the optoelectronically active black perovskite phase of CsPbI₃ is thermodynamically not stable at room temperature, instead an optoelectronically inactive yellow non-perovskite phase of CsPbI₃ forms at room temperature. Therefore, efforts are on to employ various material design tricks to stabilize the black perovskite phase of CsPbI₃ at room temperature. One of the most promising strategies to stabilize the black phase is by doping Mn into CsPbI₃ nanocrystals (NCs).²⁻⁴ But addition of Mn precursor during the synthesis of NCs can lead to different surface energy, NC size, and even different crystal structures namely α - and γ -phase (discussed later), compared to the synthesis of undoped NCs. Simultaneous change of multiple parameters makes it difficult to understand the role of Mn in stabilizing the black phase. Here, we develop a postsynthesis doping strategy to get more insights on the role Mn and thereby stabilizing the black phase of CsPbI₃ NCs in ambient conditions for a month or above.

All inorganic CsPbI₃ perovskite were proposed as thermally stable perovskite with solar cell efficiency already reaching to ~17%.⁵⁻⁷ Light emitting diodes⁸⁻⁹ (LEDs) and photodetectors¹⁰⁻¹¹ are also being made with black phase of CsPbI₃. It is noteworthy here that all inorganic perovskite CsPbBr₃ and anion exchanged CsPbI₃ exhibit commercially relevant external quantum efficiency (EQE) exceeding 20%.¹²⁻¹³ While the optoelectronically active perovskite structure of CsPbBr₃ is stable at room temperature, CsPbI₃ easily forms (or converts into) optoelectronically inactive non-perovskite yellow phase at room temperature.¹⁴⁻¹⁵ This instability of black perovskite phase of CsPbI₃ in ambient condition is a roadblock for its commercial applications. Swarnkar et al⁵ reported that the black phase is achieved by making colloidal NCs of CsPbI₃ NCs, and attributed it to surface energy of NCs.⁵ Subsequent to that, there are other reports as well suggesting small crystallite size helping the formation of black phase of CsPbI₃.¹⁶⁻¹⁷ There are also reports of formation of black phase of bulk CsPbI₃, by controlling reaction parameters such as rapid cooling of black CsPbI₃ from high (>310 °C) temperature to room temperature.¹⁸ It is important to note here that while Swarnkar et al. assigned the room temperature black phase of CsPbI₃ NCs as the cubic α -phase,⁵ Sutton et al. suggest the same room temperature black phase as orthorhombic γ -phase for their bulk CsPbI₃.¹⁸ Other recent reports also suggested room temperature black phase as the orthorhombic γ -phase of CsPbI₃ thin films.¹⁹⁻²⁰ Importantly, both the α - and γ -phase have the

three dimensional network of $\{\text{PbI}_6\}^{4-}$ octahedra, and termed as perovskite phase, unlike the yellow δ -phase where the 3D network is lost and termed as non-perovskite phase (see Figure 4.1). Both the α - and γ -phase exhibit very similar optoelectronic properties.^{18, 20} Therefore, the black phase irrespective of α or γ are optoelectronically active and desired at ambient condition.

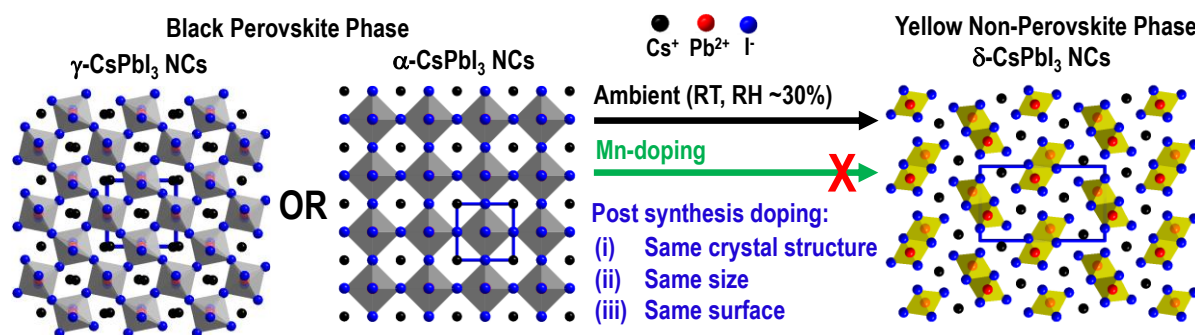


Figure 4.1: Schematics of CsPbI₃ black perovskite phase (α -CsPbI₃ or γ -CsPbI₃) which is unstable at room temperature (RT ~293 K) in relative humidity (RH ~30%) conditions and transforms to yellow non-perovskite phase (δ -CsPbI₃). Postsynthesis Mn doping stops the transformation by stabilizing the black phase for about a month in ambient conditions. This postsynthesis doping provides more controlled experimental conditions to understand role of Mn on structural stability of CsPbI₃ NCs wherein the initial host NCs remains the same (obtained from the same reaction) for both the doped and undoped sample.

There are other strategies to improve stability of CsPbX₃ perovskite NCs such as encapsulation (surface modification) of NCs into moisture-free matrix.^{6, 9, 21-31} In this approach, the improved stability is achieved at the cost of additional interface/shell/encapsulating material which often inhibits charge transfer/transport. A different approach to stability is by optimizing the structural parameters by doping or alloying at A³²⁻³³ or B^{2, 4, 34} or X³⁵⁻³⁶ site ions where A = Cs, formamidinium, B = Pb, different metal ions, and X = Cl, Br, I, in ABX₃ perovskite structure. Alloying at the X-site increases the band gap, which is not desired for solar cell and therefore, preferred X-site compositions are largely I with minor contribution from other halides. The present manuscript is on doping a few % Mn at B-site of CsPbI₃, such that the band gap and other optoelectronic properties of host remain unchanged, but doping improves the stability. Doping of Mn in CsPbX₃ perovskite NCs was initially motivated to impart new optical properties arising from Mn d-d atomic level transition.³⁷⁻³⁹ Soon after, Zou et al. suggested improved stability of CsPbBr₃ NC lattice by incorporation of Mn.² Later, Akkerman et al. showed that black phase of CsPbI₃ nanocubes could be made stable under ambient conditions for 30 days by alloying with Mn at B-site.³ Subsequently, partial replacement of Pb(II) with different metal ions such as Mn(II),^{2-3, 34, 40} Sn(II)⁴¹, Ge(II)⁴², Bi(III)⁴³, Sr(II)⁴⁴, Er(III)⁴⁵ in

CsPbX₃ have been reported to improve the stability of perovskite structure. In these prior reports, undoped and Mn-doped CsPbX₃ NCs are prepared in two different synthesis. As a result, in the presence and absence of Mn or other dopant precursors, or in other words a small change in reaction conditions, can modify the surface energy, NC size and/or structure of the host.^{7, 14, 20, 29, 46} As discussed above, all these parameters can influence the stability of black phase of CsPbI₃ NCs at room temperature.

To understand the role of Mn doping in stabilizing the black phase, we employed postsynthesis Mn doping. CsPbI₃ NCs prepared from one single reaction are divided into two fractions, and Mn is added only in one fraction and compared with the other undoped fraction. We studied structure and optical properties of NCs in both the forms, colloidal dispersions and films to understand surface and lattice contribution on the stabilization process. Finally, the stability of Mn-doped CsPbI₃ NCs films has been increased from few days to a month under ambient condition by this postsynthesis Mn doping.

4.2 Experimental Section

4.2.1 Synthesis of colloidal CsPbI₃ and CsPbBr₃ nanocubes

Cs-oleate precursor is prepared first by taking 0.5 g of Cs₂CO₃, 100 mL octadecene (ODE) and 3 mL oleic acid (OA) in three neck round bottom flask (RB) and then dissolved at 150 °C in inert atmosphere.⁵ The clear solution obtained is stored for further use. Colloidal CsPbI₃ nanocubes are then prepared through minor modification of reported procedure.⁵ PbI₂ (2.16 mmol, 1 g) and 50 mL ODE are taken in a three neck 500 mL RB connected to Schlenk line. The contents inside RB are degassed at 100 °C overnight (~12 hours) to remove moisture content. Then 5 mL OA and 5 mL oleylamine (OLA) are injected into the reaction mixture followed by 2nd round of degassing for 1 hour. The temperature is set to 180 °C under continuous N₂ flow. After clear solution is obtained at the set temperature, 18 mL Cs-oleate is injected quickly followed by dipping the flask immediately in ice-water bath mixture to quench the reaction. The obtained bright red colored solution (78 mL) is then washed carefully as mentioned here. The whole crude solution is taken and anhydrous methyl acetate (MeOAc) is added to this crude solution in 1:3 volume ratio respectively and then centrifuged at 8000 rpm for 30 sec. The obtained precipitate is dispersed in ~5 mL anhydrous hexane. Second washing is carried out in the same way by adding 15 mL MeOAc and again centrifuged at 8000 rpm for 30 sec. The wet pellet is finally dispersed in 20 mL anhydrous hexane or toluene for postsynthesis doping and characterization.

CsPbBr₃ nanocubes are prepared by modifying prior report.⁴⁷ Typically, PbBr₂ (0.5 mmol, 183.5 mg) and 12 mL ODE are loaded into 50 mL RB followed by degassing at 100 °C for 1 hour. In next step, 1.5 mL OA and 1.5 mL OLA are injected under N₂ flow. Second round of degassing is then carried out for half an hour. The reaction temperature is set to 130 °C under continuous N₂ flow. Once solution becomes clear at 130 °C, 2 mL Cs-oleate from stock solution (0.1 M, pre-heated at ~100 °C) is injected followed by quenching the reaction immediately by dipping flask in ice water bath. The crude solution is then washed twice using MeOAc, and final pellet obtained is dispersed in 5 mL anhydrous hexane which is then stored for postsynthesis doping.

4.2.2 Postsynthesis Mn doping

Postsynthesis doping of Mn in CsPbI₃ nanocubes is carried out at room temperature and under ambient conditions extending our prior report⁴⁸ (chapter 3) of Mn doping in CsPbCl₃ and CsPbBr₃. Typically, Mn precursor solution is prepared by dissolving ~ 29 mg (0.093 mmol) of MnI₂ in 2 mL MeOAc. Undoped CsPbI₃ NCs dispersion (from the above stock) is taken in two vials each containing 1 mL. In one vial containing CsPbI₃ NCs, 20 µL MnI₂ precursor solution is added under continuous stirring and kept on stirring for 1 minute to prepare 4.8% Mn-doped CsPbI₃ NCs. The second vial containing 1 mL undoped CsPbI₃ NCs is left as such without any doping and taken as control undoped CsPbI₃ NCs. Similarly, Mn-doping in CsPbBr₃ nanocubes is achieved in the same way with only difference that MnBr₂ (~20 mg in 2 mL MeOAc) is used as Mn precursor.

4.2.3 OLAI treatment

First OLAI is prepared by reacting OLA and HI as mentioned in prior report.⁴⁹ OLAI precursor solution is then made by taking ~30 mg OLAI (0.093 mmol) in 2 mL toluene. For OLAI-treatment, 40 µL of this OLAI precursor solution is added to undoped CsPbI₃ NCs under stirring for 1-minute at room temperature similar to postsynthesis doping strategy.

4.2.4 Characterization methods

Bruker D8 Advance X-ray diffractometer with Cu K α (1.54 Å) radiation is used to measure powder X-ray diffraction (XRD) patterns of NCs. Transmission electron microscopy (TEM) and high resolution TEM (HRTEM) images are captured using 200 kV UHR FEG-TEM, JEOL JEM 2100F field emission transmission electron microscope. Inductively coupled plasma atomic emission spectroscopy (ICP-AES) measurements are carried out using ARCOS simultaneous ICP spectrometer, Analytical Instruments GmbH, Germany. UV-visible

absorption spectra are recorded using Cary series UV Visible Spectrophotometers. Steady-state photoluminescence (PL) spectra and PL decay dynamics using time-correlated single photon counting technique are recorded using Edinburgh Instruments FLS 980 spectrophotometer. The samples are excited at 400 nm for recording steady state PL and 405 nm picosecond pulsed diode laser excitation is used for recording PL decay dynamics.

4.3 Results and Discussions

4.3.1 Synthesis and characterization of colloidal Mn-doped CsPbI₃ NCs

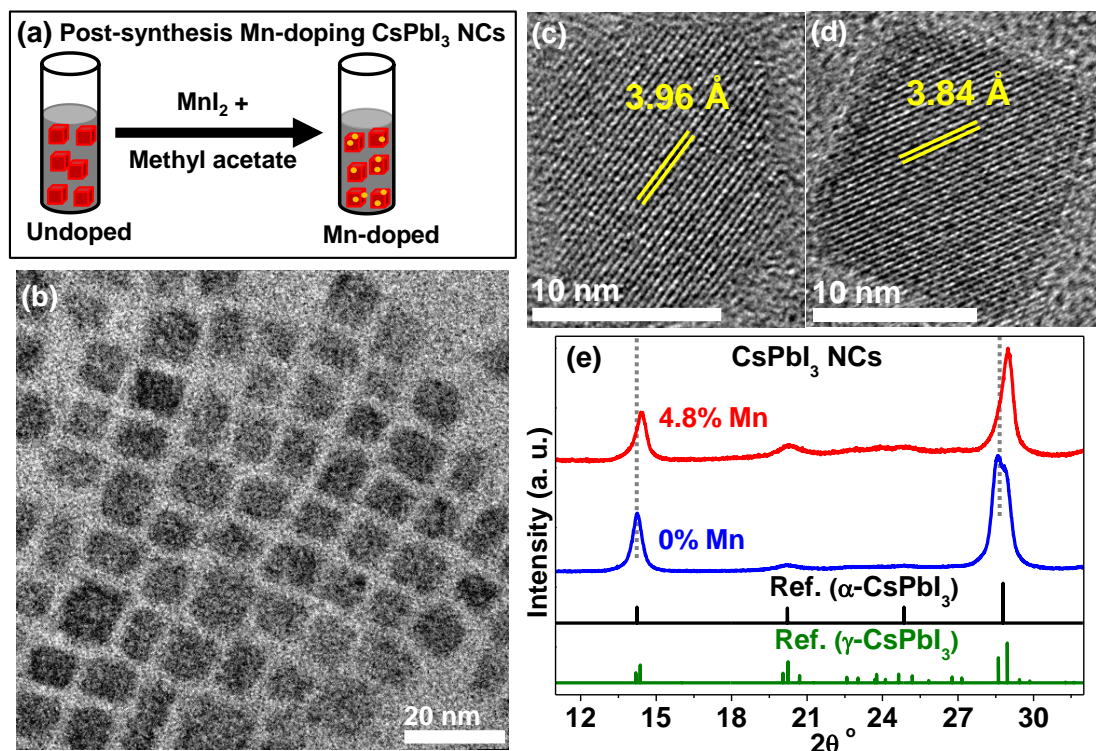


Figure 4.2: Postsynthesis Mn-doping in colloidal CsPbI₃ NCs. All the results are obtained within 24 hours (day 1) from the preparation of samples. (a) Schematics showing postsynthesis Mn-doping in CsPbI₃ NCs using MnI₂ solution as Mn precursor. (b) TEM image of Mn-doped CsPbI₃ NCs. HRTEM images of (c) undoped and (d) Mn-doped NCs showing interplanar distances. (e) Comparison of powder XRD patterns of undoped and Mn-doped CsPbI₃ NCs film with reference data for cubic α -CsPbI₃ and orthorhombic γ -CsPbI₃ black perovskite phases. Dashed vertical lines indicate the shift in XRD peaks upon doping Mn.

Postsynthesis doping of Mn in CsPbI₃ NCs is carried out in two steps by extending the methodology for the synthesis of Mn-doped CsPbCl₃ NCs reported in chapter 3. At first, black perovskite phase of colloidal CsPbI₃ NCs are prepared through hot injection method and washing is carried out with MeOAc following ref.⁵ The purified colloidal CsPbI₃ NCs are then doped with Mn in the second step. Figure 4.2a shows schematics of postsynthesis Mn-doping of CsPbI₃ NCs using MnI₂ precursor dissolved in MeOAc. Importantly, both undoped

and Mn-doped samples in our postsynthesis doping method are derivatives of the same batch (one reaction) of colloidal CsPbI₃ NCs. When a pot-synthesis of Mn-doped CsPbI₃ NCs are carried out, and then compared with undoped NCs prepared by a separate synthesis, then the presence and absence of dopants ions can influence the nucleation, growth, structure and surface properties of the host NCs. Therefore, in our postsynthesis doping, there is no difference in initial host NCs for both undoped and doped samples, which makes the comparison between Mn-doped and undoped samples more reliable.

ICP-AES shows 4.8% Mn with respect to Pb in our product Mn-doped CsPbI₃ NCs. Figure 4.2b shows representative TEM image of Mn-doped CsPbI₃ displaying the cubic morphology. The average size of nanocubes ~12 nm, and both morphology and size remained unchanged before and after postsynthesis Mn-doping, when measurements are done within a day from preparing the samples. Figure 4.2c-d shows HRTEM images of undoped and Mn-doped CsPbI₃ nanocubes respectively showing lattice fringes confirming high crystalline nature of both the samples. Interestingly, interplanar distance of 3.96 Å for undoped CsPbI₃ NC, reduces to 3.84 Å in the case of Mn-doped CsPbI₃ NC. These results suggest postsynthesis Mn-doping is accompanied by lattice compression of host CsPbI₃ lattice. This lattice compression is possible if Mn²⁺ is replacing Pb²⁺ from its octahedral lattice site since Mn²⁺ is smaller than Pb²⁺. In order to ensure further whether Mn is really doped in CsPbI₃ NCs lattice, XRD patterns from the ensemble of NCs are compared before and after Mn-doping in Figure 4.2e. XRD patterns also show peaks shift towards higher 2θ° upon doping Mn as indicated by dashed lines in Figure 4.2e. This result confirms that Mn doping in CsPbI₃ NCs is accompanied with lattice contraction of host NCs, in agreement with HRTEM results.

In literature, there is a debate regarding the crystal structure of the black phase of CsPbI₃ at room temperature. Possibility of both α- and γ-phase for the black colored CsPbI₃ at room temperature has been discussed.^{5, 18} The obtained phase can also depend on the reaction conditions and surface energy of CsPbI₃ crystallites. A comparison of our experimental data for CsPbI₃ NCs with reference data for both α- and γ-phase of bulk CsPbI₃ in Figure 4.2e is not conclusive. Broadening of XRD peaks in NCs blurs the differences between the two phases. Similar confusion between cubic and orthorhombic structure also existed for CsPbBr₃ NCs in earlier literature.^{47, 50} Interestingly, both α- and γ-phase of CsPbI₃ have very similar optoelectronic properties, therefore, any one of the two phases at room temperature is of

interest for real life applications. In the present manuscript, we term it as black perovskite phase of CsPbI₃ NCs, without assigning to any one of the two α - or γ -phases.

4.3.2 Effect of surface on optical properties and stability of colloidal NCs

After postsynthesis doping of Mn into colloidal CsPbI₃ NCs, we store the samples in an ambient condition containing moisture with relative humidity value of ~30%. To monitor any change in the sample, we measure the optical absorption and emission spectra over several days of storing. Figure 4.3a compares UV-visible absorption and photoluminescence (PL) spectra recorded on day 1 and day 3 for undoped (0% Mn) CsPbI₃ NCs. The energies of the excitonic absorption and PL reconfirm the formation of black phase of CsPbI₃ NCs. In the case of undoped CsPbI₃ NCs, the lowest energy excitonic absorption maximum is at 643 nm on day 1, which red shifts to 664 nm on day 3 and respective PL peak maximum also shift by ~10 nm. Interestingly, the Mn-doped sample in Figure 4.3b does not show such red shift in absorbance and PL on day 3 compared to the spectra of day 1. These results suggest undoped CsPbI₃ NCs may undergo Ostwald type⁵¹ growth of colloidal NCs in the toluene dispersion. In difference, Mn-doped sample retain the size of NCs and thus no shift in excitonic absorption or PL peak position with time.

This is the first difference between undoped and Mn-doped samples that could be clearly observed in our postsynthesis doping strategy. Doping can influence both the lattice and surface energies influencing the NC size.⁵² To examine whether passivation of dangling surface bonds stabilizing the colloidal NCs, control experiments with oleylammonium iodide (OLAI) are carried out. Unlike Mn²⁺ ions, OLA⁺ is too large a cation to be incorporated in the CsPbI₃ NC lattice, so any influence of OLAI will be restricted to surface of NCs alone. Postsynthesis OLAI treatment is done by addition of OLAI solution in undoped colloidal CsPbI₃ NCs. Figure 4.3c shows absorbance and PL spectra of OLAI treated CsPbI₃ NCs on day 1 and day 3. These OLAI treated NCs also retain the excitonic absorption maximum and PL peak position from day 1 through day 3 similar to Mn-doped sample, in sharp difference to untreated undoped sample. This improved stability of CsPbI₃ NCs by addition of OLAI may be attributed to effective passivation of surface restricting colloidal growth of NCs. These results suggest that the addition of Mn precursor (MnI₂ dissolved in MeOAc) is also playing a similar role of surface passivation and restricting the growth of colloidal Mn-doped NCs compared to undoped CsPbI₃ NCs. Prior studies also suggest that treatment of CsPbX₃ NCs with different metal-halide salts improves the surface passivation and thus huge enhancement in PLQY.⁵³⁻⁵⁶ The comparison of the OLAI treatment and Mn-doping data is

possible beyond experimental uncertainties, only because of the employed postsynthesis doping strategy. It has to be noted that the black phase of CsPbI₃ NCs converts to the yellow phase as the size of NCs increases.⁵ Therefore, restricting the growth of NCs by surface passivation during Mn-doping can also lead to stabilization of the black phase of CsPbI₃ NCs at room temperature. In addition to this surface passivation, the role of lattice energy upon Mn-doping to stabilize the black phase of CsPbI₃ NCs will be discussed later using NC films.

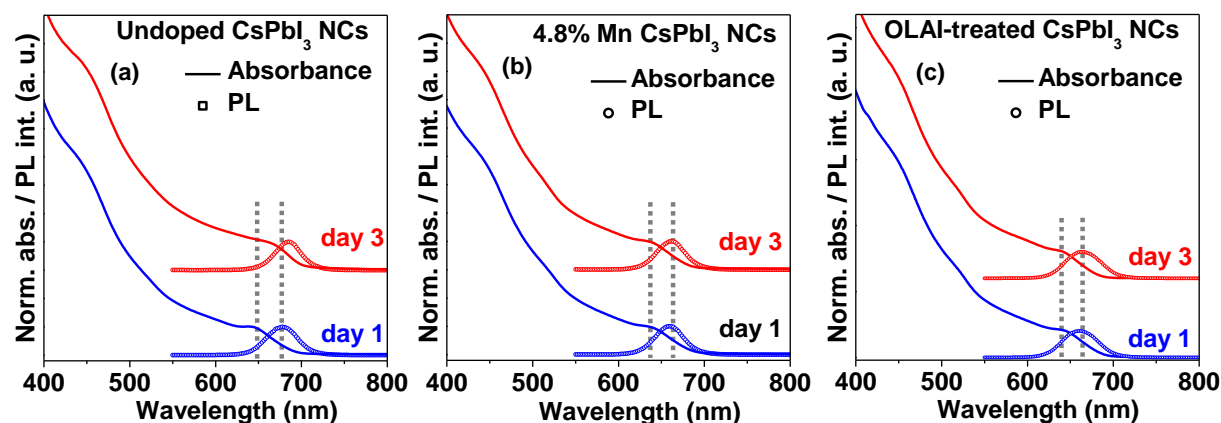


Figure 4.3: Comparison of steady state UV-visible absorption and PL spectra of (a) undoped colloidal CsPbI₃ NCs, (b) Mn-doped CsPbI₃ NCs, and (c) oleylammonium iodide (OLAI) treated undoped CsPbI₃ NCs on day 1 and day 3. Vertical dashed lines are guidance to any shift observed in excitonic features from day 1 to day 3.

Along with the red-shift of PL peak maximum in undoped CsPbI₃ NCs dispersion, a significant decrease in excitonic PL intensity within 10 days is observed as shown in Figure 4.4a. In this process CsPbI₃ NCs starts precipitating out of the colloidal dispersion, yielding yellow colored precipitates after about 10 days in relative humidity ~30%. So the increase in NC size leads to both precipitation and formation of yellow phase. On the other hand, Figure 4.4b shows PL spectra from day 1 to day 17 of Mn-doped colloidal CsPbI₃ NCs with insignificant shift in peak position. Though the PL intensity gradually decreased with time, but significant luminescence is retained even after 17 days, which is again in sharp contrast to the undoped sample. Colloidal stability also improves upon doping Mn in CsPbI₃ NCs. This improvement in both colloidal and PL stability with Mn doping again agrees with our previous inference that the addition of MnI₂ during postsynthesis doping passivates NC surface hindering the detrimental increase in NC size and thereby suppressing the conversion of black to yellow phase.

To get more insights, PL decay dynamics were recorded at the respective PL peak positions for both undoped and Mn-doped colloidal CsPbI₃ NCs (see Figure 4.4c-d) at different time intervals from the synthesis of NCs. PL decay dynamics on day 1 are fitted with single

exponential decay function for both undoped and Mn-doped sample giving a radiative lifetime of 17.1 ns and 18 ns respectively. This suggests our postsynthesis Mn-doping is not introducing any additional non-radiative decay channel to host CsPbI₃ NCs.

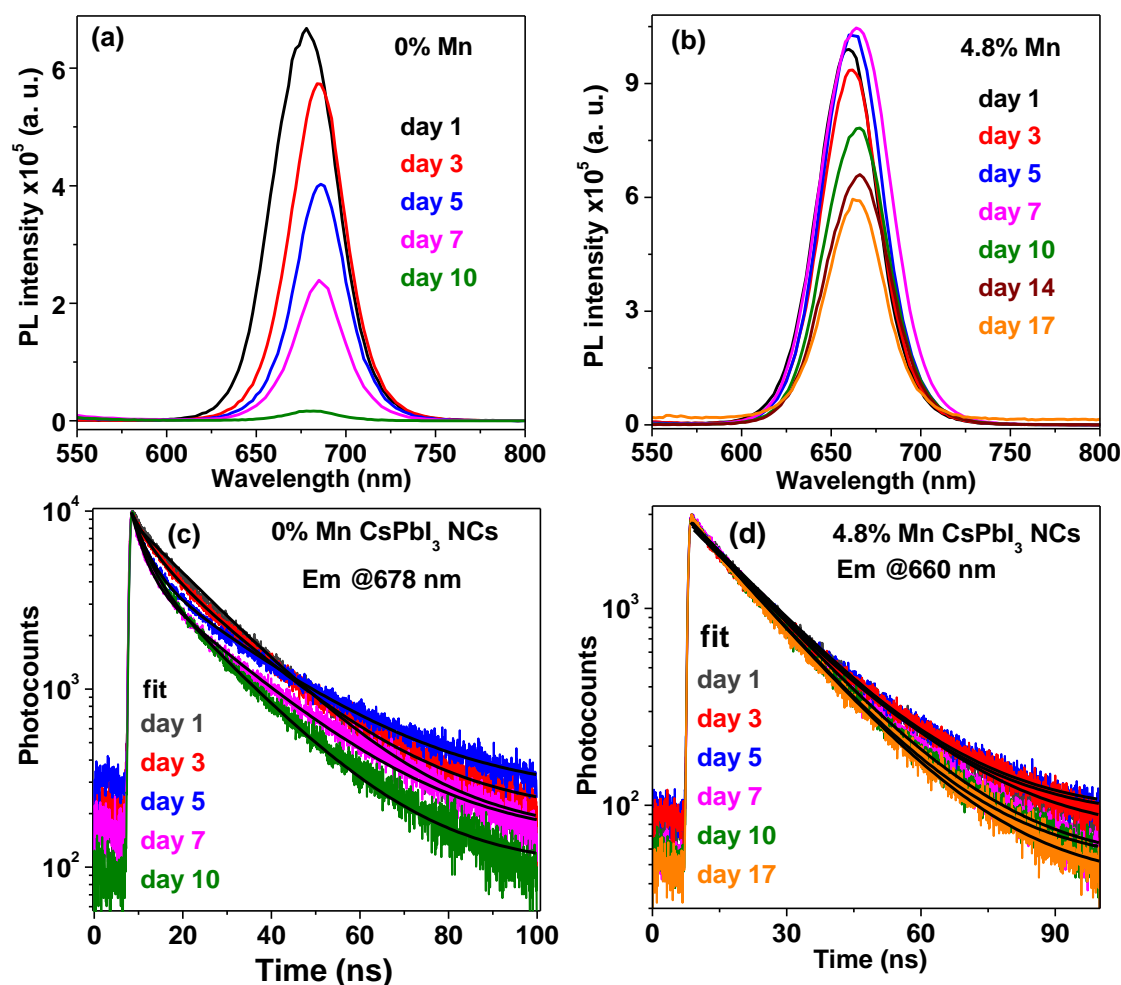


Figure 4.4: UV-visible absorption and PL spectra of (a) undoped and (b) 4.8% Mn-doped CsPbI₃ NCs dispersed in toluene at different time intervals from the preparation of NCs. PL decay dynamics recorded at emission peak maximum of (c) undoped CsPbI₃ NCs, and (d) 4.8% Mn-doped CsPbI₃ NCs after excitation with 405 nm picosecond pulsed diode laser.

Note that the Mn d-d transition energy (~586 nm) higher than the excitonic bandgap of CsPbI₃ NCs,⁵⁷⁻⁵⁹ therefore, excitonic energy does not get transferred to Mn states giving rise to similar PL decay dynamics for both the doped and undoped samples. However, the difference in PL decay between the two samples starts appearing on day 3 onwards. In the case of undoped CsPbI₃ NCs PL decay dynamics recorded on day 3 onwards are fitted with bi-exponential decay function. On the other hand, Mn-doped CsPbI₃ NCs retained single exponential decay dynamics from day 1 to day 17. The best fit parameters are given in Table 4.1. These PL decay dynamics results suggest the improvement of surface passivation during Mn-doping improves the stability of PL for a longer duration.

Table 4.1: Best fit parameters of PL decay dynamics for undoped and 4.8% Mn-doped CsPbI₃ NCs dispersed in toluene corresponding to the data given in Figure 4.4c-d.

0% Mn CsPbI ₃ nanocrystals	$y = a_1 * \exp\left(-\frac{t}{\tau_1}\right) + a_2 * \exp\left(-\frac{t}{\tau_2}\right) + y_0$			
	a ₁ (%)	τ ₁ (ns)	a ₂ (%)	τ ₂ (ns)
day 1		17.1	-	-
day 3	30	19.2	70	4.5
day 5	10	22.5	90	3.4
day 7	5	19.9	95	2.8
day 10	20	16.5	80	7.0
4.8% Mn CsPbI ₃ nanocrystals	$y = a * \exp\left(-\frac{x}{\tau}\right) + y_0$			
	τ (ns)			
day 1	18.0			
day 3	17.4			
day 5	18.2			
day 7	18.2			
day 10	16.7			
day 17	16.7			

4.3.3 Role of lattice doping in stabilizing NCs films

Now we will discuss the effect of postsynthesis doping of Mn or OLAI treatment on the stability of black perovskite phase of CsPbI₃ NCs films in the ambient conditions. The films are prepared by simple drop casting of the colloidal NCs on glass substrate and stored in the ambient conditions. Compared to colloidal dispersion of NCs in a non-polar hydrophobic medium, films of NCs are more exposed to moisture and oxygen present in the environment. Figure 4.5a shows photographs of undoped CsPbI₃ NCs film captured on day 1, day 5 and day 7. During this period in relative humidity ~30%, the color of film changes from dark red (termed as black phase) on day 1 to light yellow color (termed as yellow phase) on day 7, indicating change in optical band gap of the film. This transformation of color when monitored through optical absorption results into Figure 4.5b. Clearly, diminishing of excitonic feature centered at 650 nm is observed from day 1 to day 5 and vanishes on day 7 along with emergence of new absorption feature at 422 nm. This disappearing of 650 nm peak and emergence of new 422 nm peak explains the observed color change in film from day 1 to day 7 (Figure 4.5a).

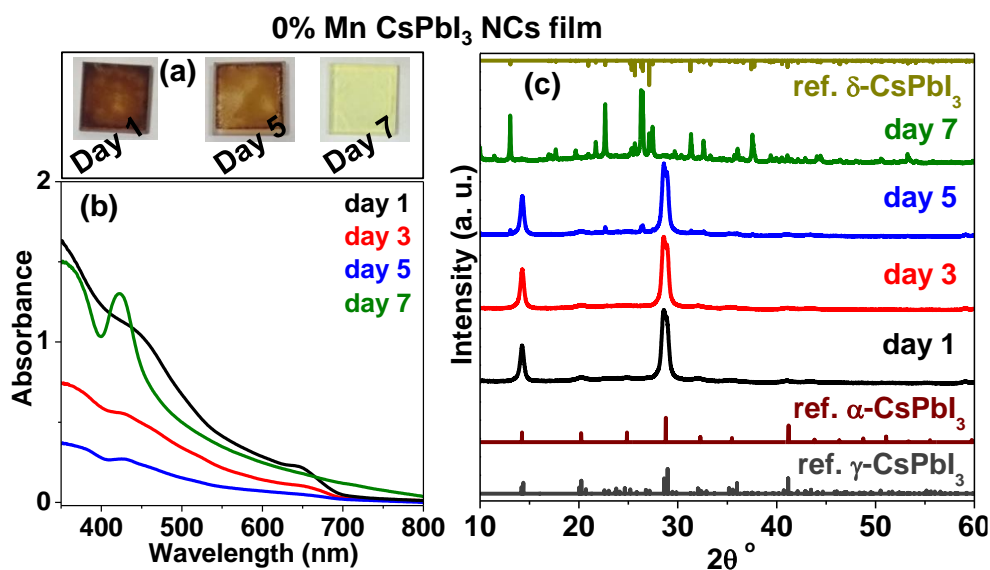


Figure 4.5: (a) Photographs of undoped CsPbI₃ NCs film captured in visible light at different time intervals while the film was stored in ambient conditions. (b) Steady state optical absorption spectra and corresponding (c) XRD patterns of same film at different time intervals starting from day 1.

To understand the reason behind the color change, we measured powder XRD patterns. Figure 4.5c shows the film of undoped CsPbI₃ NCs on day 1 exhibits black perovskite phase (α or γ). On day 5, new impurity peaks corresponding to yellow phase (non-perovskite δ phase) appears along with the original black phase. This process of conversion of black to yellow phase completes on day 7 when all peaks corresponding to the black phase disappear and the XRD pattern matches with yellow δ -phase of CsPbI₃ (Figure 4.5c). From above studies we understand that the undoped CsPbI₃ film undergoes phase transformation from black perovskite to yellow non-perovskite phase within a weak under ambient conditions and is accompanied by change in optical band gap. This transition is detrimental for optoelectronic applications, and therefore, Mn-doping is attempted to increase the stability of black phase at room temperature.

Unlike the case of undoped CsPbI₃ NCs, Mn-doped CsPbI₃ NCs film showed significantly improved stability of the black phase when stored under the same ambient conditions. Figure 4.6a shows the photographs of film captured on day 1, day 7 and day 28 suggesting no color change. Optical absorption spectra monitored with time in Figure 4.6b reveals improved stability of 650 nm excitonic absorption. The excitonic absorbance remains almost unchanged for a long duration and begins to decrease from day 21 onwards. The absorption spectrum is dominated by excitonic absorbance of black phase till monitored up to day 28. Although weak feature starts emerging at 422 nm after day 21 but very slow transformation till day 28 is observed. The contribution of yellow phase increases with times beyond day 28, but we

could observe the presence of black phase as a minor component even after 2 months. XRD patterns of the films recorded at different time intervals are plotted in Figure 4.6c. Clearly, no significant phase change of Mn-doped CsPbI₃ NCs is observed from day 1 to day 28. XRD pattern recorded on day 28 shows dominant black perovskite phase of CsPbI₃ NCs along with weak impurity peaks. These optical properties and XRD data confirm the stability of black phase of Mn-doped CsPbI₃ NCs films for about a month. Such improvement in the stability of black phase at room temperature is of significant importance for optoelectronic applications including solar cell. At least in the laboratory scale, one can fabricate and characterize a device in ambient conditions using these Mn-doped CsPbI₃ NCs.

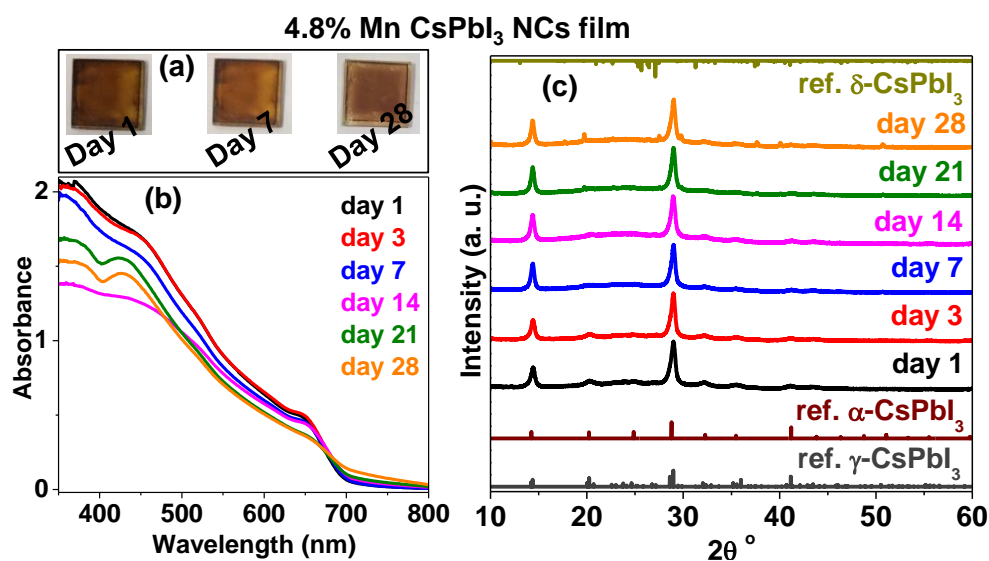


Figure 4.6: (a) Photographs of 4.8% Mn-doped CsPbI₃ NCs film captured in visible light at different time intervals when stored in ambient condition. (b) Optical absorption spectra and (c) XRD patterns of same film from day 1 to day 28.

While studying the colloidal dispersion (Figure 4.3), we observed similar improvement of colloidal stability and phase stability by both Mn-doping and OLAI treatment in undoped CsPbI₃ NCs. We extend this comparison to NCs film as well. In contrast to Mn-doped samples, OLAI-treated undoped CsPbI₃ NCs showed complete phase change from black perovskite phase to non-perovskite yellow phase within 10 days as shown by photographs (Figure 4.7a), absorption spectra (Figure 4.7b) and XRD patterns (Figure 4.7c). We discussed earlier that the same OLAI treated colloidal dispersion of CsPbI₃ NCs retained initial size (band gap and PL maximum) similar to Mn-doped NCs, when monitored with time. This stability is attributed to improved surface passivation. However, structural and optical studies on films show that the surface passivation is not enough to stabilize the black perovskite phase of CsPbI₃ NCs films. In difference to OLAI treated NCs films, Mn doping leads to contraction of CsPbI₃ NCs lattice. Overall, the comparison of OLAI treated undoped CsPbI₃

NCs and Mn-doped samples suggest that both surface passivation (mainly colloidal dispersion) and lattice doping helps to stabilize the black perovskite phase of CsPbI₃ NCs.

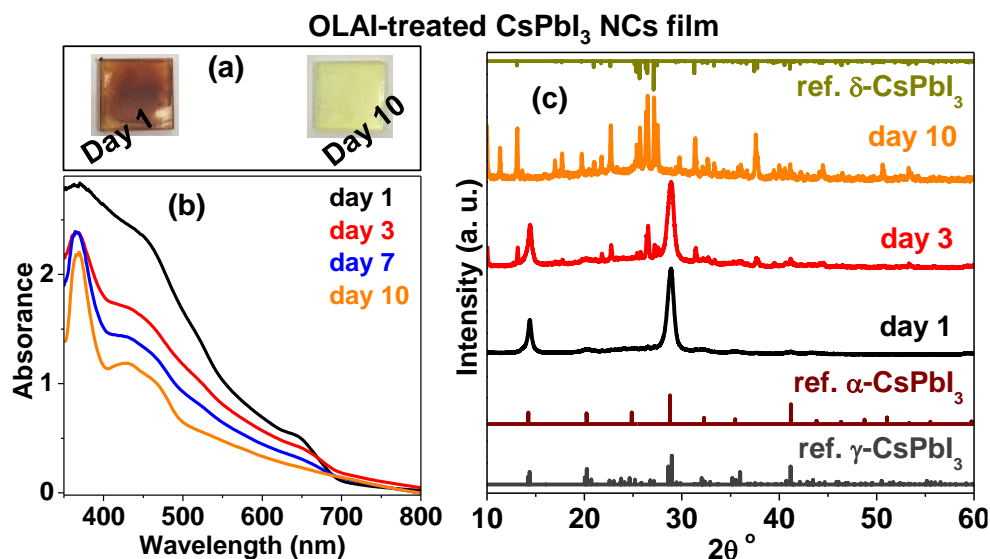


Figure 4.7: (a) Photographs of oleylammonium iodide (OLAI) treated undoped CsPbI₃ NCs film captured in visible light at different time intervals when stored under ambient conditions. (b) Steady state optical absorption spectra and (c) XRD patterns of same film from day 1 to day 10.

Prior literature suggests that the stability of black perovskite phase of CsPbI₃ upon doping/alloying with Mn originates from small increase in the tolerance factor accompanied with lattice contraction and overall enhancement of the cohesion energy of CsPbI₃ lattice.³ Theoretical studies carried out on cubic phase polymorph suggest that doping Mn enhances formation energy of CsPbI₃ lattice.² Lattice contraction is evident from our postsynthesis Mn doping in CsPbI₃ NCs see HRTEM images and XRD pattern in Figure 4.2c-e. Also, Mn-I bond has significantly higher bond dissociation energy (283 KJmol⁻¹) compared to Pb-I bond (194 KJmol⁻¹).⁶⁰ As a result, both lattice contraction together with higher bond dissociation energy of Mn-I stabilizes lattice and surface of Mn-doped NCs compared to undoped CsPbI₃ NCs of same size/shape. Furthermore, we note here that the same undoped CsPbI₃ NCs film converts to yellow phase in ambient conditions, relative humidity ~30%, but can retain black perovskite phase for more than a month when stored inside N₂ filled glove box.

4.3.4 Role of Mn-doping in stabilizing CsPbBr₃ NCs films

Unlike black phase of CsPbI₃ NCs, optoelectronically active orthorhombic phase of CsPbBr₃ NCs is significantly stable at room temperature.⁵⁰ Though the phase of CsPbBr₃ NCs does not change drastically with time, a decrease in PL intensity is often observed with time when stored in ambient conditions. Figure 4.8a-b shows PL spectra of undoped and Mn-doped CsPbBr₃ NCs films with storing time in ambient conditions. Mn-doped CsPbBr₃ NCs film

retains nearly 33% of its original PL intensity after 28 days while the PL intensity of undoped CsPbBr₃ NCs film decreased to 14% during same the time period. Similarly, prior studies show improved stability of excitonic emission during repeated cooling and heating cycles of Mn-doped CsPbBr₃ NCs compared to undoped ones.² Our controlled postsynthesis doping experiments reconfirms that Mn has a vital role in improving stability of host CsPbBr₃ NCs.

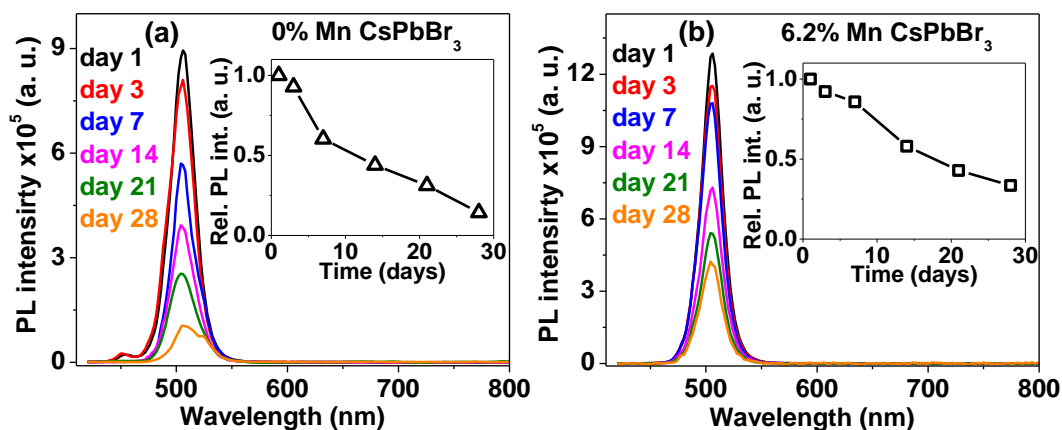


Figure 4.8: PL spectra from day 1 to day 28 for (a) undoped CsPbBr₃ NCs film and (b) 6.2% Mn-doped CsPbBr₃ NCs film under ambient conditions. Inset of (a) and (b) shows their corresponding normalized PL intensity variation with time, symbols denote experimental data and solid line shows trend.

4.4 Conclusions

We show the role of Mn-doping in favorably tuning both the surface and lattice energy to stabilize the black perovskite phase of CsPbI₃ NCs for about a month in ambient conditions. To carry out controlled comparisons of undoped and Mn-doped samples, we employ postsynthesis Mn-doping strategy, where the initial host NCs are obtained from the same synthesis for both doped and undoped samples. Stability and optical properties are studied for both colloidal NCs and their films in ambient conditions. To check the effect of surface energy alone, we treated the undoped CsPbI₃ NCs with OLAI. It is observed that both Mn-doping and treating with OLAI passivate the surface of CsPbI₃ NCs, restricting the growth of colloidal NCs while stored in ambient conditions, compared to their undoped counterparts. This surface passivation improves both the colloidal and phase stability of black CsPbI₃ NCs. But stability studies on NCs films suggest that the surface passivation is not good enough for long term stability of black phase of CsPbI₃, and the lattice contraction upon Mn-doping has a critical role in stabilizing the black phase by about a month. Then we cross check for another composition as well and find that Mn-doped CsPbBr₃ NCs film performed better in terms of retaining original PL intensity with storing time compared to their undoped counterpart.

These insights and overall improvement in the stability of black phase Mn-doped CsPbI₃ and also Mn-doped CsPbBr₃ will be useful for optoelectronic applications in ambient conditions.

4.5 References

1. Kulbak, M.; Gupta, S.; Kedem, N.; Levine, I.; Bendikov, T.; Hodes, G.; Cahen, D. Cesium Enhances Long-Term Stability of Lead Bromide Perovskite-Based Solar Cells. *J. Phys. Chem. Lett.* **2016**, *7*, 167-172.
2. Zou, S., et al. Stabilizing Cesium Lead Halide Perovskite Lattice through Mn(II) Substitution for Air-Stable Light-Emitting Diodes. *J. Am. Chem. Soc.* **2017**, *139*, 11443-11450.
3. Akkerman, Q. A.; Meggiolaro, D.; Dang, Z.; De Angelis, F.; Manna, L. Fluorescent Alloy CsPb_xMn_{1-x}I₃ Perovskite Nanocrystals with High Structural and Optical Stability. *ACS Energy Lett.* **2017**, *2*, 2183-2186.
4. Swarnkar, A.; Mir, W. J.; Nag, A. Can B-Site Doping or Alloying Improve Thermal- and Phase Stability of All-Inorganic CsPbX₃ (X = Cl, Br, I) Perovskites? *ACS Energy Lett.* **2018**, *3*, 286-289.
5. Swarnkar, A.; Marshall, A. R.; Sanehira, E. M.; Chernomordik, B. D.; Moore, D. T.; Christians, J. A.; Chakrabarti, T.; Luther, J. M. Quantum Dot-Induced Phase Stabilization of α -CsPbI₃ Perovskite for High-Efficiency Photovoltaics. *Science* **2016**, *354*, 92-95.
6. Wang, Y.; Zhang, T.; Kan, M.; Zhao, Y. Bifunctional Stabilization of All-Inorganic α -CsPbI₃ Perovskite for 17% Efficiency Photovoltaics. *J. Am. Chem. Soc.* **2018**, *140*, 12345-12348.
7. Wang, K.; Jin, Z.; Liang, L.; Bian, H.; Bai, D.; Wang, H.; Zhang, J.; Wang, Q.; Liu, S. All-Inorganic Cesium Lead Iodide Perovskite Solar Cells with Stabilized Efficiency Beyond 15%. *Nat. Commun.* **2018**, *9*, 4544.
8. Han, B., et al. Stable, Efficient Red Perovskite Light-Emitting Diodes by (α , δ)-CsPbI₃ Phase Engineering. *Adv. Funct. Mater.* **2018**, *28*, 1804285.
9. Pan, J., et al. Bidentate Ligand-Passivated CsPbI₃ Perovskite Nanocrystals for Stable near-Unity Photoluminescence Quantum Yield and Efficient Red Light-Emitting Diodes. *J. Am. Chem. Soc.* **2018**, *140*, 562-565.
10. Sim, K. M.; Swarnkar, A.; Nag, A.; Chung, D. S. Phase Stabilized α -CsPbI₃ Perovskite Nanocrystals for Photodiode Applications. *Laser Photonics Rev.* **2018**, *12*, 1700209.
11. Mir, W. J., et al. Strategy to Overcome Recombination Limited Photocurrent Generation in CsPbX₃ Nanocrystal Arrays. *Appl. Phys. Lett.* **2018**, *112*, 113503.

12. Lin, K., et al. Perovskite Light-Emitting Diodes with External Quantum Efficiency Exceeding 20 Per Cent. *Nature* **2018**, *562*, 245-248.
13. Chiba, T.; Hayashi, Y.; Ebe, H.; Hoshi, K.; Sato, J.; Sato, S.; Pu, Y.-J.; Ohisa, S.; Kido, J. Anion-Exchange Red Perovskite Quantum Dots with Ammonium Iodine Salts for Highly Efficient Light-Emitting Devices. *Nat. Photonics* **2018**, *12*, 681-687.
14. Eperon, G. E.; Paternò, G. M.; Sutton, R. J.; Zampetti, A.; Haghighirad, A. A.; Cacialli, F.; Snaith, H. J. Inorganic Caesium Lead Iodide Perovskite Solar Cells. *J. Mater. Chem. A* **2015**, *3*, 19688-19695.
15. Sun, J.-K., et al. Polar Solvent Induced Lattice Distortion of Cubic CsPbI₃ Nanocubes and Hierarchical Self-Assembly into Orthorhombic Single-Crystalline Nanowires. *J. Am. Chem. Soc.* **2018**, *140*, 11705-11715.
16. Sanehira, E. M.; Marshall, A. R.; Christians, J. A.; Harvey, S. P.; Ciesielski, P. N.; Wheeler, L. M.; Schulz, P.; Lin, L. Y.; Beard, M. C.; Luther, J. M. Enhanced Mobility CsPbI₃ Quantum Dot Arrays for Record-Efficiency, High-Voltage Photovoltaic Cells. *Science Adv.* **2017**, *3*, eaao4204.
17. Liu, F., et al. Highly Luminescent Phase-Stable CsPbI₃ Perovskite Quantum Dots Achieving near 100% Absolute Photoluminescence Quantum Yield. *ACS Nano* **2017**, *11*, 10373-10383.
18. Sutton, R. J.; Filip, M. R.; Haghighirad, A. A.; Sakai, N.; Wenger, B.; Giustino, F.; Snaith, H. J. Cubic or Orthorhombic? Revealing the Crystal Structure of Metastable Black-Phase CsPbI₃ by Theory and Experiment. *ACS Energy Lett.* **2018**, *3*, 1787-1794.
19. Marronnier, A.; Roma, G.; Boyer-Richard, S.; Pedesseau, L.; Jancu, J.-M.; Bonnassieux, Y.; Katan, C.; Stoumpos, C. C.; Kanatzidis, M. G.; Even, J. Anharmonicity and Disorder in the Black Phases of Cesium Lead Iodide Used for Stable Inorganic Perovskite Solar Cells. *ACS Nano* **2018**, *12*, 3477-3486.
20. Zhao, B., et al., Thermodynamically Stable Orthorhombic γ -CsPbI₃ Thin Films for High-Performance Photovoltaics. *J. Am. Chem. Soc.* **2018**, *140*, 11716-11725.
21. Raja, S. N.; Bekenstein, Y.; Koc, M. A.; Fischer, S.; Zhang, D.; Lin, L.; Ritchie, R. O.; Yang, P.; Alivisatos, A. P. Encapsulation of Perovskite Nanocrystals into Macroscale Polymer Matrices: Enhanced Stability and Polarization. *ACS Appl. Mater. Interfaces* **2016**, *8*, 35523-35533.

22. Sun, C.; Zhang, Y.; Ruan, C.; Yin, C.; Wang, X.; Wang, Y.; Yu, W. W. Efficient and Stable White Leds with Silica-Coated Inorganic Perovskite Quantum Dots. *Adv. Mater.* **2016**, *28*, 10088-10094.
23. Gomez, L.; de Weerd, C.; Hueso, J. L.; Gregorkiewicz, T. Color-Stable Water-Dispersed Cesium Lead Halide Perovskite Nanocrystals. *Nanoscale* **2017**, *9*, 631-636.
24. Huang, H.; Bodnarchuk, M. I.; Kershaw, S. V.; Kovalenko, M. V.; Rogach, A. L. Lead Halide Perovskite Nanocrystals in the Research Spotlight: Stability and Defect Tolerance. *ACS Energy Lett.* **2017**, *2*, 2071-2083.
25. Leijtens, T.; Bush, K.; Cheacharoen, R.; Beal, R.; Bowring, A.; McGehee, M. D. Towards Enabling Stable Lead Halide Perovskite Solar Cells; Interplay between Structural, Environmental, and Thermal Stability. *J. Mater. Chem. A* **2017**, *5*, 11483-11500.
26. Chen, D.; Yuan, S.; Chen, J.; Zhong, J.; Xu, X., Robust CsPbX₃ (X = Cl, Br, and I) Perovskite Quantum Dot Embedded Glasses: Nanocrystallization, Improved Stability and Visible Full-Spectral Tunable Emissions. *J. Mater. Chem. C* **2018**.
27. Kong, Z. C.; Liao, J. F.; Dong, Y. J.; Xu, Y. F.; Chen, H. Y.; Kuang, D. B.; Su, C. Y. Core@Shell CsPbBr₃@Zeolitic Imidazolate Framework Nanocomposite for Efficient Photocatalytic CO₂ Reduction. *ACS Energy Lett.* **2018**, *3*, 2656-2662.
28. Krieg, F., et al. Colloidal CsPbX₃ (X = Cl, Br, I) Nanocrystals 2.0: Zwitterionic Capping Ligands for Improved Durability and Stability. *ACS Energy Lett.* **2018**, *3*, 641-646.
29. Li, B.; Zhang, Y.; Fu, L.; Yu, T.; Zhou, S.; Zhang, L.; Yin, L. Surface Passivation Engineering Strategy to Fully-Inorganic Cubic CsPbI₃ Perovskites for High-Performance Solar Cells. *Nat. Commun.* **2018**, *9*, 1076.
30. Li, H.; Qian, Y.; Xing, X.; Zhu, J.; Huang, X.; Jing, Q.; Zhang, W.; Zhang, C.; Lu, Z. Enhancing Luminescence and Photostability of CsPbBr₃ Nanocrystals Via Surface Passivation with Silver Complex. *J. Phys. Chem. C* **2018**, *122*, 12994-13000.
31. Liu, Y.; Li, F.; Liu, Q.; Xia, Z. Synergetic Effect of Postsynthetic Water Treatment on the Enhanced Photoluminescence and Stability of CsPbX₃ (X = Cl, Br, I) Perovskite Nanocrystals. *Chem. Mater.* **2018**, *30*, 6922-6929.
32. Li, Z.; Yang, M.; Park, J. S.; Wei, S. H.; Berry, J. J.; Zhu, K. Stabilizing Perovskite Structures by Tuning Tolerance Factor: Formation of Formamidinium and Cesium Lead Iodide Solid-State Alloys. *Chem. Mater.* **2016**, *28*, 284-292.
33. Ghosh, D.; Walsh Atkins, P.; Islam, M. S.; Walker, A. B.; Eames, C. Good Vibrations: Locking of Octahedral Tilting in Mixed-Cation Iodide Perovskites for Solar Cells. *ACS Energy Lett.* **2017**, *2*, 2424-2429.

34. Liang, J.; Liu, Z.; Qiu, L.; Hawash, Z.; Meng, L.; Wu, Z.; Jiang, Y.; Ono, L. K.; Qi, Y. Enhancing Optical, Electronic, Crystalline, and Morphological Properties of Cesium Lead Halide by Mn Substitution For high-Stability All-Inorganic Perovskite Solar Cells With carbon Electrodes. *Adv. Energy Mater.* **2018**, *8*, 1800504.
35. Dastidar, S.; Egger, D. A.; Tan, L. Z.; Cromer, S. B.; Dillon, A. D.; Liu, S.; Kronik, L.; Rappe, A. M.; Fafarman, A. T. High Chloride Doping Levels Stabilize the Perovskite Phase of Cesium Lead Iodide. *Nano Lett.* **2016**, *16*, 3563-3570.
36. Wang, H.; Bian, H.; Jin, Z.; Liang, L.; Bai, D.; Wang, Q.; Liu, S. F. Synergy of Hydrophobic Surface Capping and Lattice Contraction for Stable and High-Efficiency Inorganic CsPbI₂Br Perovskite Solar Cells. *Sol. RRL*, *2*, 1800216.
37. Parobek, D.; Roman, B. J.; Dong, Y.; Jin, H.; Lee, E.; Sheldon, M.; Son, D. H. Exciton-to-Dopant Energy Transfer in Mn-Doped Cesium Lead Halide Perovskite Nanocrystals. *Nano Lett.* **2016**, *16*, 7376-7380.
38. Liu, W.; Lin, Q.; Li, H.; Wu, K.; Robel, I.; Pietryga, J. M.; Klimov, V. I. Mn²⁺-Doped Lead Halide Perovskite Nanocrystals with Dual-Color Emission Controlled by Halide Content. *J. Am. Chem. Soc.* **2016**, *138*, 14954-14961.
39. Mir, W. J.; Jagadeeswararao, M.; Das, S.; Nag, A. Colloidal Mn-Doped Cesium Lead Halide Perovskite Nanoplatelets. *ACS Energy Lett.* **2017**, *2*, 537-543.
40. Chen, D.; Fang, G.; Chen, X.; Lei, L.; Zhong, J.; Mao, Q.; Zhou, S.; Li, J. Mn-Doped CsPbCl₃ Perovskite Nanocrystals: Solvothermal Synthesis, Dual-Color Luminescence and Improved Stability. *J. Mater. Chem. C* **2018**, *6*, 8990-8998.
41. Liu, F., et al. Colloidal Synthesis of Air-Stable Alloyed CsSn_{1-x}Pb_xI₃ Perovskite Nanocrystals for Use in Solar Cells. *J. Am. Chem. Soc.* **2017**, *139*, 16708-16719.
42. Yang, F.; Hirotsu, D.; Kapil, G.; Kamarudin, M. A.; Ng, C. H.; Zhang, Y.; Shen, Q.; Hayase, S. All-Inorganic CsPb_{1-x}Ge_xI₂Br Perovskite with Enhanced Phase Stability and Photovoltaic Performance. *Angew. Chem., Int. Ed.* **2018**, *57*, 12745-12749.
43. Hu, Y.; Bai, F.; Liu, X.; Ji, Q.; Miao, X.; Qiu, T.; Zhang, S. Bismuth Incorporation Stabilized α -CsPbI₃ for Fully Inorganic Perovskite Solar Cells. *ACS Energy Lett.* **2017**, *2*, 2219-2227.
44. Lau, C. F. J., et al. Strontium-Doped Low-Temperature-Processed CsPbI₂Br Perovskite Solar Cells. *ACS Energy Lett.* **2017**, *2*, 2319-2325.

45. Jena, A. K.; Kulkarni, A.; Sanehira, Y.; Ikegami, M.; Miyasaka, T. Stabilization of α -CsPbI₃ in Ambient Room Temperature Conditions by Incorporating Eu into CsPbI₃. *Chem. Mater.* **2018**, *30*, 6668-6674.
46. Das Adhikari, S.; Dutta, A.; Dutta, S. K.; Pradhan, N. Layered Perovskites L₂(Pb_{1-x}Mn_x)Cl₄ to Mn-Doped CsPbCl₃ Perovskite Platelets. *ACS Energy Lett.* **2018**, *3*, 1247-1253.
47. Protesescu, L.; Yakunin, S.; Bodnarchuk, M. I.; Krieg, F.; Caputo, R.; Hendon, C. H.; Yang, R. X.; Walsh, A.; Kovalenko, M. V. Nanocrystals of Cesium Lead Halide Perovskites (CsPbX₃, X = Cl, Br, and I): Novel Optoelectronic Materials Showing Bright Emission with Wide Color Gamut. *Nano Lett.* **2015**, *15*, 3692-3696.
48. Mir, W. J.; Mahor, Y.; Lohar, A.; Jagadeeswararao, M.; Das, S.; Mahamuni, S.; Nag, A. Postsynthesis Doping of Mn and Yb into CsPbX₃ (X = Cl, Br, or I) Perovskite Nanocrystals for Downconversion Emission. *Chem. Mater.* **2018**, *30*, 8170-8178.
49. Nedelcu, G.; Protesescu, L.; Yakunin, S.; Bodnarchuk, M. I.; Grotevent, M. J.; Kovalenko, M. V. Fast Anion-Exchange in Highly Luminescent Nanocrystals of Cesium Lead Halide Perovskites (CsPbX₃, X = Cl, Br, I). *Nano Lett.* **2015**, *15*, 5635-5640.
50. Swarnkar, A.; Chulliyil, R.; Ravi, V. K.; Irfanullah, M.; Chowdhury, A.; Nag, A. Colloidal CsPbBr₃ Perovskite Nanocrystals: Luminescence Beyond Traditional Quantum Dots. *Angew. Chem., Int. Ed.* **2015**, *54*, 15424-15428.
51. Murray, C. B.; Kagan, C. R.; Bawendi, M. G. Synthesis and Characterization of Monodisperse Nanocrystals and Close-Packed Nanocrystal Assemblies. *Annu. Rev. Mater. Science* **2000**, *30*, 545-610.
52. Tandon, B.; Yadav, A.; Khurana, D.; Reddy, P.; Santra, P. K.; Nag, A. Size-Induced Enhancement of Carrier Density, LSPR Quality Factor, and Carrier Mobility in Cr-Sn Doped In₂O₃ Nanocrystals. *Chem. Mater.* **2017**, *29*, 9360-9368.
53. Kumar, G. S.; Pradhan, B.; Kamilya, T.; Acharya, S. Enhancing Performances of Hybrid Perovskite Light Emitting Diodes with Thickness Controlled PMMA Interlayer. *Bull. Chem. Soc. Jpn.* **2018**, *91*, 1241-1248.
54. Bohn, B. J., et al. Boosting Tunable Blue Luminescence of Halide Perovskite Nanoplatelets through Postsynthetic Surface Trap Repair. *Nano Lett.* **2018**, *18*, 5231-5238.
55. Li, F.; Liu, Y.; Wang, H.; Zhan, Q.; Liu, Q.; Xia, Z. Postsynthetic Surface Trap Removal of CsPbX₃ (X = Cl, Br, or I) Quantum Dots Via a ZnX₂/Hexane Solution toward an Enhanced Luminescence Quantum Yield. *Chem. Mater.* **2018**, *30*, 8546-8554.

56. Mondal, N.; De, A.; Samanta, A. Achieving near-Unity Photoluminescence Efficiency for Blue-Violet-Emitting Perovskite Nanocrystals. *ACS Energy Lett.* **2018**, 32-39.
57. Beaulac, R.; Archer, P. I.; Ochsenein, S. T.; Gamelin, D. R. Mn²⁺-Doped CdSe Quantum Dots: New Inorganic Materials for Spin-Electronics and Spin-Photonics. *Adv. Funct. Mater.* **2008**, 18, 3873-3891.
58. Pradhan, N.; Sarma, D. D. Advances in Light-Emitting Doped Semiconductor Nanocrystals. *J. Phys. Chem. Lett.* **2011**, 2, 2818-2826.
59. Guria, A. K.; Dutta, S. K.; Adhikari, S. D.; Pradhan, N. Doping Mn²⁺ in Lead Halide Perovskite Nanocrystals: Successes and Challenges. *ACS Energy Lett.* **2017**, 2, 1014-1021.
60. Yu-Ran Luo. *Bond Dissociation Energies in Diatomic Molecules*. <https://notendur.hi.is/agust/rannsoknir/papers/2010-91-CRC-BDEs-Tables.pdf>, (accessed January 2019).

Chapter 5

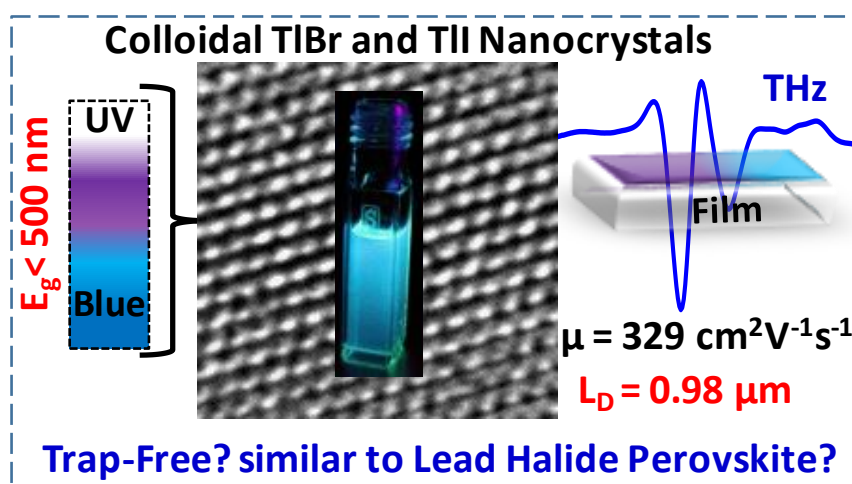
Colloidal Thallium Halide Nanocrystals Analogous to CsPbX₃ Perovskites and their Defect Tolerance

.....
The work presented in this chapter is published under following details. Mir, J. W.; Warankar, A.; Acharya, A.; Das, S.; Mandal, M.; Nag A. *Chem. Sci.*, **2017**, 8, 4602-4611. This is an open access article by the Royal Society of Chemistry publishing group.

Terahertz (THz) spectroscopy (Figure 5.7) study was carried out by Avinash Waranker in Dr. Pankaj Mandal lab at IISER Pune.

Abstract

Colloidal lead halide based perovskites nanocrystals (NCs) have been recently established as an interesting class of defect-tolerant NCs with potential for superior optoelectronic applications. Electronic band structure of thallium halides (TlX, where X = Br, I) show a strong resemblance to lead halide perovskites, where both Pb^{2+} and Tl^+ exhibit $6s^2$ inert pair of electrons and strong spin-orbit coupling. Though the crystal structure of TlX is not perovskite, but the similarities of its electronic structure with lead halide perovskites have motivated us to prepare colloidal TlX NCs. These TlX NCs exhibit a wider band gap (>2.5 eV or < 500 nm) along with a potential to exhibit reduced density of deep defect states. THz probe spectroscopy revealed high effective carrier mobility (~ 220 to $329 \text{ cm}^2\text{V}^{-1}\text{s}^{-1}$), and long diffusion length (~ 0.77 to $0.98 \mu\text{m}$). Moreover TlX NCs show reasonably high photoluminescence efficiency ($\sim 10\%$) for TlBr NCs. This combination of properties is remarkable compared to other wide band gap (>2.5 eV) semiconductor NCs, suggesting the reduction of deep-defect states in our TlX NCs. Furthermore, temperature-dependent reversible structural phase transition along with its influence on optical properties of TlX NCs has been studied.

Graphical abstract

5.1 Introduction

Defect tolerance signifies the tendency of a semiconductor to retain its electronic, optical and optoelectronic properties even in the presence of defects. One of the major problem of colloidal semiconductor nanocrystals (NCs) like CdSe is surface defects, which trap charge carriers, severely limiting their electronic, optical, and optoelectronic properties.¹ This problem of charge trapping becomes more severe for NCs with high optical band gap in the visible spectral region of 400 to 500 nm (3.1 to 2.5 eV). Here, we present a new variety of colloidal semiconductor NCs in the form of TlX (X = I and Br), with optical band gap < 500 nm (>2.5 eV), exhibiting photoconductivity with high effective carrier mobilities ($\sim 330 \text{ cm}^2\text{V}^{-1}\text{s}^{-1}$), long ($\sim 1 \text{ }\mu\text{m}$) diffusion lengths, and reasonably high photoluminescence (PL) efficiency ($\sim 10\%$). These results suggest suppression of defect mediated charge trapping in TlX NCs, compared to many other semiconductors with band gap >2.5 eV.

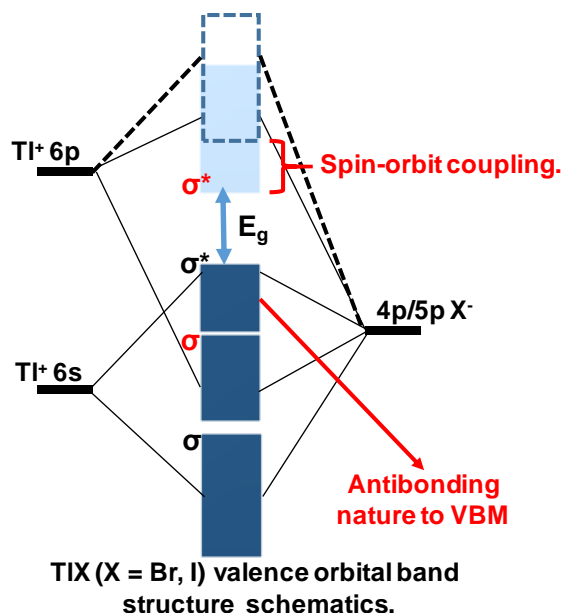


Figure 5.1: Schematic representation of valence orbital band structure of TlX (X = Br, I), depicting bonding and antibonding orbitals forming energy bands of the TlX solid relative to isolated p and s atomic orbitals of Tl^+ and X^- . The non-bonding Tl 6p states mainly constitutes conduction band minimum (light-blue band), which gets stabilized by strong spin-orbit coupling. Anti-bonding interaction of Tl 6s and X np constitute valence band (dark-blue) maximum. The figure has been made following ref.²⁴

In the beginning of 2015, Protesescu *et al*² reported CsPbX₃ (X = Cl, Br, I) perovskite NCs with exceptionally high ($\sim 90\%$ for X = Br) PL efficiency. Subsequently, our group and collaborators showed suppression of PL blinking and terahertz (THz) conductivity with high carrier mobility ($\sim 4500 \text{ cm}^2\text{V}^{-1}\text{s}^{-1}$) within a CsPbBr₃ NC.^{3,4} These results suggest that CsPbBr₃ NCs do not exhibit mid-gap deep trap states, in spite of having high surface-to-volume ratio. Therefore, CsPbX₃ NCs provide a hope for a new kind of nearly trap-free NCs

with superior optical and optoelectronic properties,⁵ as has been already reported in terms of achieving high-efficiency light emitting diodes (LED),⁶⁻⁷ solar cell,⁸ low threshold for lasing,⁹ strong nonlinear absorption along with multi-photon pumped lasing,¹⁰⁻¹¹ and single photon emission¹². There has been significant progress in designing and exploring properties of CsPbX₃ and MAPbX₃ (MA = methylamine) NCs with various shape, size and compositions.^{13-21,22,23} In chapter 2-4 of this thesis, we have shown low doping Mn and Yb in CsPbX₃ NCs can tailor optical properties and improve structural stability of NCs.

This success of CsPbX₃ perovskite NCs has motivated us to search for other kinds of trap-free colloidal semiconductor NCs, particularly with high optical gap corresponding to UV - blue region, where probability of formation deep-trap states increases. In this regard, TlX NC is a potential system, since it share a number of common features with Pb²⁺ based perovskite, such as Tl⁺ is isoelectronic with Pb²⁺ and both possess a lone pair of outermost s-electrons. Anti-bonding interactions of this filled 6s orbital of Tl⁺ with halide 4p/5p orbital forms the valence band maximum (VBM) as shown in Figure 5.1.²⁴ On the other hand, Tl⁺ 6p orbitals mainly contribute to the conduction band minimum (CBM). Another anticipated common feature between Tl⁺ and Pb²⁺ is strong spin-orbit coupling in 6p band.²⁵⁻²⁷ Thus both 6s² electrons and spin-orbit coupling yield the desired electronic band structure for both TlX and CsPbX₃, where anti-bonding states form VBM and spin-orbit coupling stabilize the CBM as depicted in Figure 5.1.²⁸ Such electronic band structure is expected to reduce deep-trap states in a semiconductor nanocrystal. Therefore, metal halides with different composition and structures, but with a valence orbital band structure similar to Figure 5.1 are now being explored.^{28,29,30,31}

At room temperature, TlI exhibits orthorhombic structure with band gap of 2.86 eV (434 nm),³² whereas, TlBr exhibits cubic structure with band gap of 3.05 eV (407 nm).³³ Crystal structure of both TlI and TlBr are different from ABX₃ perovskite (A: monovalent metal/organic ion, B: divalent metal ion), but TlX are analogous to CsPbX₃ perovskite in terms of valence orbital band structure. Bulk and thin films of TlX and their derivatives have already been explored as potential candidates for room temperature X-ray and gamma-ray detection.³⁴⁻³⁶ We report here colloidal TlX NCs. Optical properties including ultrafast optical pump THz probe (OPTP) spectroscopy suggest suppression of deep-defect mediated charge trapping in TlX NCs. Furthermore, temperature dependent structural phase transition was observed using variable-temperature X-ray diffraction (XRD) and differential scanning calorimetry (DSC). To the best of our knowledge, this is the first report on colloidal TlX

NCs, showing interesting properties suitable for optoelectronic applications in the UV-blue region. However, toxicity of Tl based compounds is well known,³⁷⁻³⁸ which will be major hindrance for many real life applications of TlX NCs.

5.2 Experimental Section

5.2.1 TII NCs

0.5 mmol of TlNO₃, 15 mL 1-octadecene, 1 mL oleic acid and 1 mL oleylamine were taken in a three-neck round bottom flask and degassed at 100 °C for about 1 hour. The temperature of reaction mixture was then raised to 300 °C under N₂ atmosphere till solution became clear. The temperature of solution was then lowered to 200 °C (or 170 °C). Simultaneously, in another round bottom flask, 1 mmol of tetra butyl ammonium iodide (TBAI) was mixed with 5 mL 1-octadecene and 5 mL oleylamine and degassed at 140 °C for about 90 minutes. The temperature of the iodide mixture was then raised to 200 °C under N₂ atmosphere, till the solution became clear. The temperature was then lowered to 60 °C. TII NCs were finally obtained by swiftly injecting this iodide solution to the thallium solution maintained at 170 °C for 8.4 nm NCs (or at 200 °C for 4 nm NCs). The reaction was quenched immediately using a bath containing dry ice in acetone. The obtained reaction product was centrifuged at 3000 rpm for 1 minute and the supernatant was taken up for further washing after discarding the precipitate. Small amount (1-2 mL) of tert-butanol (or acetonitrile) anti-solvent was added to the supernatant solution to precipitate out the NCs, along with centrifugation at ~6000 rpm. The obtained precipitate was dispersed in hexane and placed in refrigerator for half an hour, following by decanting the supernatant solution after discarding any precipitate that might have formed. This colloidal NC was used for optical studies in solution phase. Excess amount of the anti-solvent starts degrading the NCs. Sometimes, the washing method was repeated for a second time to get rid of any remaining oily residue, but further repetition of washing process destabilize the colloidal NCs. It must be noted that thallium and its salts, similar to lead salts, are toxic in nature. Hence, necessary precautions need to be taken while using any thallium containing substance.

5.2.2 TlBr NCs

TlBr NCs were synthesized using a protocol similar to that of TII NCs, but with some differences, which are mentioned here. 1 mmol of TlNO₃ and 2 mmol of tetra butyl ammonium bromide were used, and the final reaction was carried out at 300 °C. The washing of colloidal TlBr NCs were carried similar to the case of TII NCs.

5.2.3 Characterization methods

Transmission electron microscopy (TEM) and high resolution TEM (HRTEM) images were captured on a UHR FEG-TEM, JEOL JEM-2100F electron microscope using a 200 kV electron source. Powder XRD data were recorded using Bruker D8 Advance X-ray diffractometer equipped with Cu K α (1.54 Å) radiation. Powder XRD data at different temperatures were recorded using program controller setup in the range of 303 K to 543 K for both heating and cooling cycle. For such measurements, powder sample was placed on a platinum foil and heated (or cooled) with a rate of 0.5 °C/min along with a stabilization time of 5 minutes at each temperature. Throughout the experiment, the sample chamber was kept under vacuum of 10⁻³ mbar. UV-visible absorption spectra were collected using Perkin Elmer Lambda-45 UV/vis spectrometer. PL spectra and PL decay dynamics were measured using Edinburg FLS980 spectrophotometer. The PL decay dynamics were recorded using 340 nm and 400 nm nanosecond pulse LED lasers as excitation sources. DSC curve was obtained by using TA Q20 DSC instrument. PL quantum yield (PL QY) of TIX NCs were obtained using sodium salt of fluorescein dye in water as reference (PL QY = 0.92 in water), whereas PL QY of 4 nm TII NCs was obtained using quinine sulphate in 0.5 M HCl as reference (PL QY = 0.55).

5.3 Results and Discussions

5.3.1 Synthesis

We have employed a hot-injection route for colloidal synthesis of TIX NCs. Colloidal synthesis of TIX NCs is tricky due to highly reactive ionic nature of reaction between TI⁺ and X⁻ ions. Fast growth of NCs makes it difficult to isolate smaller NCs and study the growth kinetics. Another intrinsic behaviour of TII is that the crystal phase transition occurs around the reaction temperatures (170 – 300 °C). Therefore, controlling the crystal structure of TII NCs becomes more challenging. Growth of TIX NCs in our synthesis was stopped immediately after injecting the precursors by applying a bath containing dry ice in acetone. This lowering of reaction temperature is helpful to achieve both homogeneity of crystal structure of TIX product NCs, and suppression of NC growth. Product NCs exhibit colloidal stability for about a week under ambient conditions. Further modification of reaction methodology is required to achieve a better separation of nucleation and growth processes, in order to control the size and shape of NCs over a wider range. In this regard, exploring various surface ligands and washing procedure might help to achieve better quality NCs with improved colloidal stability and optical properties.

5.3.2 Morphology and structure of TII NCs

TEM image shown in Figure 5.2a and corresponding size distribution histogram (Figure 5.2b) show that TII NCs prepared at 170 °C exhibit an average diameter of 8.4 ± 1.2 nm. Inset of Figure 5.2a shows HRTEM image of 8.4 nm TII NC displaying (111) lattice fringes with an interplanar distance of 3.33 Å. Powder XRD pattern (Figure 5.2c) confirms the orthorhombic phase of TII NCs at room temperature, similar to bulk³⁹ TII. Inset of Figure 5.2c shows an orthorhombic unit cell of TII lattice with coordination polyhedra of seven ions around each TI⁺ and I ion. Thus coordination environment of TII is different from that in CsPbI₃ cubic perovskite.² Samara *et al* reported polymorphism in bulk TII with ~1% difference in lattice energy between cubic and orthorhombic phase.³⁹ This has prompted us to study the possible crystal phase transition in our organic capped colloidal NCs, where surface energy can play a crucial role unlike their bulk counterpart.

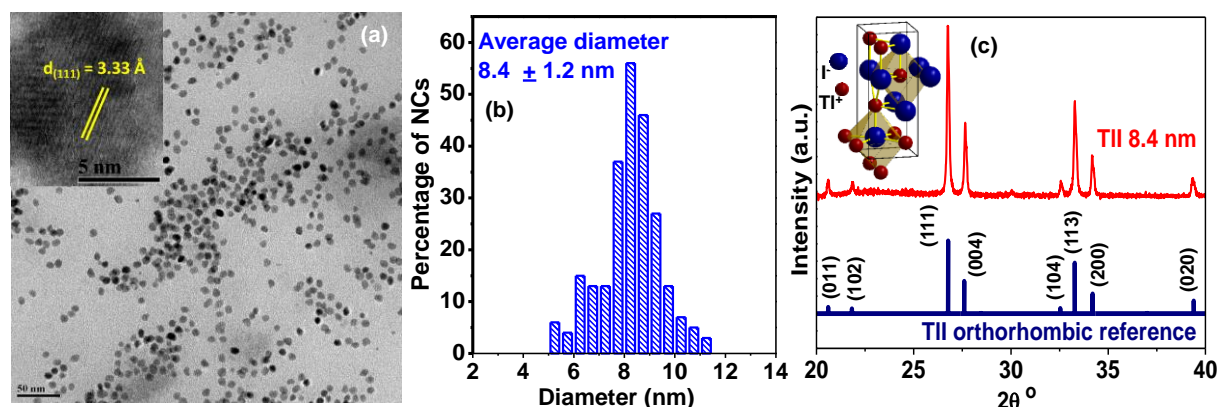


Figure 5.2: (a) TEM image of TII NCs and the inset shows HRTEM image of single NC. (b) Size distribution histogram of TII NCs obtained from image (a) and shows an average size of 8.4 nm. (c) Comparison between powder XRD diffraction patterns of TII NCs (red, upper) and orthorhombic bulk TII reference (blue, lower). The inset shows TII orthorhombic unit cell with coordination network of seven ions around each ion.

5.3.3 Temperature dependent phase transition in TII NCs

Figure 5.3a shows that TII NCs (8.4 nm) initially exhibit orthorhombic structure at 303 K, and remain so when temperature is raised till 423 K (150 °C). At 433 K, TII NCs predominantly exhibit orthorhombic phase but have a minor contribution from cubic phase at $2\theta = 30^\circ$. With further increase in temperature to 443 K, the crystal structure of the NCs transforms to a predominant cubic phase, along with minor peaks from orthorhombic phase. A pure cubic phase, without any contribution from orthorhombic TII, is observed at 483 K, and this cubic phase remains intact on further increase in temperature till 543 K (maximum temperature used in this study).

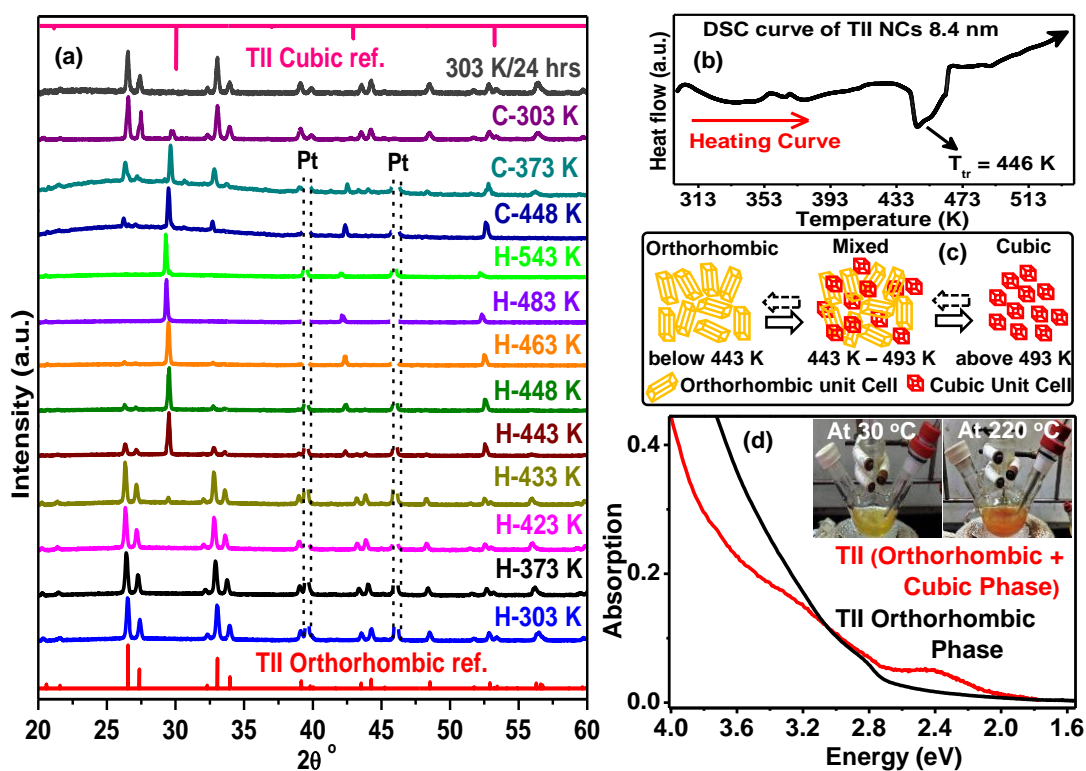


Figure 5.3: (a) Temperature dependent powder XRD patterns of TII NCs from 303 K to 543 K recorded both in forward (heating represented as H-xyz K) and reverse (cooling represented as C-xyz K) direction. (b) DSC plot showing broad endotherm dip at 446 K for orthorhombic to cubic phase transition, which is in agreement with temperature dependent XRD data. (c) Schematics depicting structural phase changes of TII NCs in the given temperature range. Dashed arrows in reverse direction indicate relatively slower reverse phase transition. (d) Optical absorption spectra of TII NCs at 30 °C and after heating to 220 °C but spectra were recorded immediately at room temperature.

Then the NCs are cooled and the transition is monitored in the reverse direction from cubic to orthorhombic phase. But this reverse phase-transition has been observed to be a slow process with cubic phase dominating even after cooling the sample to 373 K. Surprisingly, the sample exhibits a minor contribution from cubic phase along with predominant orthorhombic phase, even after cooling the sample back to 303 K. It takes many hours at 303 K, before the sample completely converts back to a pure orthorhombic phase as shown by the XRD patterns in Figure 5.3a. One should note here that the full width at half maxima (FWHM) of XRD peaks and the lattice parameters remain unchanged before and after the reversible phase transition of orthorhombic TII NCs, suggesting that the average crystallite size remains intact during the temperature dependent phase transition study. Phase transition in TII NCs was further probed using DSC. Figure 5.3b shows a broad endotherm dip at ~446 K, corresponding to phase transition from orthorhombic to cubic phase in TII NCs, and thus, commensurate with temperature dependent powder XRD results. This temperature dependent structural phase

transition of TII NCs has been schematically summarized in Figure 5.3c. TII NCs exhibit orthorhombic structure at room temperature below 443 K, but transforms to cubic phase at 443 K, similar to their bulk³⁹ counterpart. A mixed phase is observed in the temperature range of 443-493 K. Above 493 K only cubic phase is observed in TII NCs. Interestingly, Optical gap of TII NCs are known to change from 2.86 eV for orthorhombic phase to 2.0 eV for cubic phase.²⁶ Our colloidal TII NCs also show a similar change in optical gap (Figure 5.3d) and colour (photographs in the inset of Figure 5.3d) for orthorhombic NCs at 30 °C to cubic phase of NCs at 220 °C. Photographs in the inset of Figure 5.3d show colour of colloidal TII NCs is pale yellow at 30 °C (303 K, and remains so till temperature is as high as ~423 K), but turns into reddish-orange at 220 °C (493 K). For the sample at 220 °C, the hot colloidal dispersion was quickly transferred to a cuvette and the spectrum was collected within a minute at room temperature. In this process there is a small drop in temperature, which might be the reason for seeing some contribution from orthorhombic phase as well in the absorption spectrum after heating the sample at 220 °C. Furthermore, temperature dependent linear fit of unit cell volume (V) as a function of temperature (T) for TII NCs results into similar coefficient of volume expansion (α_V) in both the phases of TII NCs. For orthorhombic phase, $\alpha_V = 1.47 \times 10^{-4} \text{ K}^{-1}$ and for cubic phase $\alpha_V = 1.5 \times 10^{-4} \text{ K}^{-1}$. These values of α_V are in accordance with previously suggested values for bulk³⁹ TII.

5.3.4 Optical properties of TII NCs

UV-visible absorption spectrum (Figure 5.4a) of 8.4 nm TII NCs (prepared at 170 °C) dispersed in hexane shows an excitonic absorption peak at 438 nm (2.83 eV) which is similar to the optical gap of bulk (2.86 eV)²⁹ orthorhombic TII. According to prior reports, Bohr excitonic diameter of TII NCs is expected to be in the range of 9 – 12 nm for orthorhombic phase.⁴⁰ Therefore, a weak confinement of charge carriers is expected for 8.4 nm TII NCs, exhibiting optical gap similar to that of bulk TII. When TII NCs were prepared at 200 °C, smaller NCs with an average diameter of 4 nm were obtained (TEM data not shown here). UV-visible absorption spectrum (Figure 5.4a) of 4 nm TII exhibits a sharper excitonic feature at 365 nm (3.44 eV). This is a significant blue-shift compared to the optical gap of bulk TII, showing the signature of quantum confinement in these NCs. Furthermore, unlike bulk or thin films of TII, our colloidal TII NCs exhibit excitonic features at room temperature, suggesting an increase in excitonic binding energy in these NCs because of quantum confinement of electron and hole wavefunctions. We note here that, because of the fast growth rate, it is difficult to isolate the smaller sizes of TII NCs, so the continuous tuning of

optical gap in the range of 365 nm (3.44 eV) to 438 nm (2.83 eV) is difficult to achieve with reproducibility.

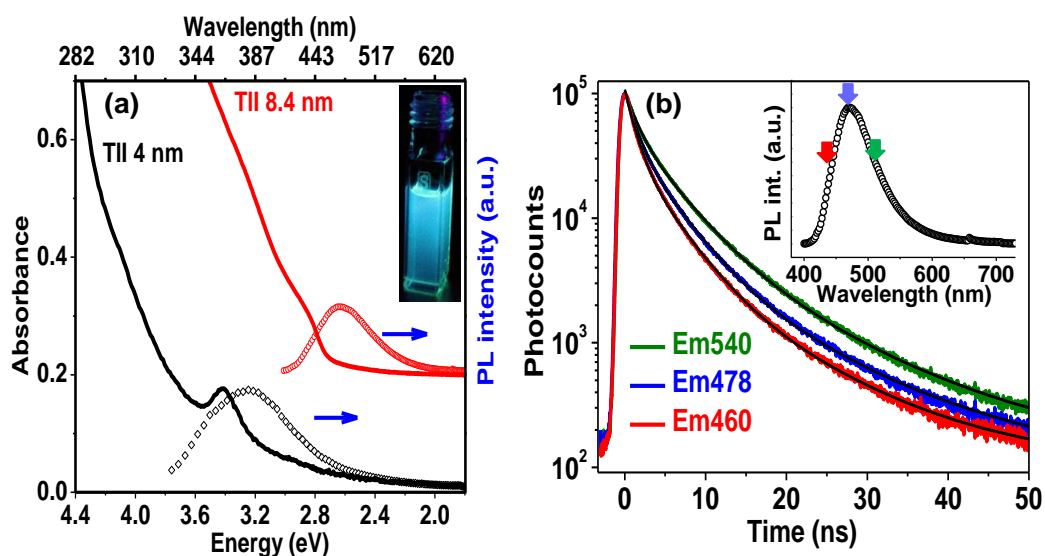


Figure 5.4: (a) UV-visible absorption and PL spectra of TII NCs with an average size of 8.4 nm (red spectrum) and 4 nm (black spectrum). The absorption and PL spectra of 8.4 nm sized NCs are vertically offset (by a constant 0.2) for clarity of presentation. Inset shows photograph of luminescence from colloidal dispersion of 8.4 nm TII NCs after irradiating with 365 nm UV light. (b) PL decay profiles of colloidal TII NCs (8.4 nm) at three different emission wavelengths, after excitation at 400 nm, inset shows corresponding PL plot and arrows depict emission wavelength probed in time resolved PL decay scan.

PL peaks (Figure 5.4a) centred at 382 nm and 480 nm corresponds to 4 and 8.4 nm TII NCs respectively. Inset of Figure 5.4a shows photograph of PL from colloidal TII NCs (8.4 nm) dispersed in hexane under UV illumination (365 nm). The PLQY $\sim 6\%$ was obtained for 8.4 nm TII NCs and $\sim 4\%$ for 4 nm TII NCs. To the best of our knowledge, prior literature on bulk and thin films of TII NCs did not show PL at room temperature. Agekyan *et al*⁴¹ reported similar PL at 80 K from microcrystals of TII embedded in a porous matrix. Probably, the smaller size of our NCs increases overlap between electron and hole wavefunction thus increasing the transition probability for PL. Broadening of PL in our TII NCs suggests the possible contribution from both exciton and shallow defect states in the PL.

To understand the mechanism, PL decay dynamics of TII NCs shown in Figure 5.4b were fitted with tri-exponential decay function and best-fit parameters are summarised in Table 5.1. A non-radiative lifetime $\tau_1 \sim 1$ ns, and two radiative lifetimes $\tau_2 \sim 4$ ns and $\tau_3 \sim 12$ ns are obtained at all three wavelengths of emissions. Such short radiative lifetimes indicate transitions involving delocalized states and might arise from both band edges (or excitonic) and shallow defect states.⁴² Unlike deep trap states in mid-gap, shallow defects are nearly delocalized and optically active. Absence of long (~ 100 ns) lifetime shows the absence of

to bulk⁴³ TlBr at room temperature. Inset of Figure 5.5a shows schematic of cubic unit cell of TlBr lattice with coordination polyhedra of 8 ions around each Tl⁺ and Br⁻ ion in cubic symmetry. Furthermore, the cubic phase of TlBr NCs is stable in the temperature range of 303 K to 573 K with no evident phase transition. TEM image in Figure 5.5b shows nearly spherical morphology of TlBr particles and inset of Figure 5.5b shows an average diameter of 28.7 ± 3.2 nm for TlBr NCs. HRTEM image of TlBr NC shown in Figure 5.5c-d and the corresponding fast Fourier transform (FFT) pattern shown in Figure 5.5e confirm single crystalline nature of TlBr NC.

5.3.6 Optical properties of TlBr NCs

UV-visible absorption spectrum of TlBr NCs in Figure 5.6a shows excitonic feature at 400 nm (3.1 eV), which is in accordance with optical gap of 3.05 eV for bulk³⁰ TlBr. The diameter (28.7 nm) of our TlBr NCs is more than the estimated values of Bohr excitonic diameter (9.7 to 24.6 nm) for TlBr, and therefore, these NCs experience very weak or no quantum confinement effect. PL spectrum (Figure 5.6a) of TlBr NCs shows a peak at 435 nm with QY ~10% at room temperature. Photograph in the inset of Figure 5.6a shows PL of TlBr NCs dispersed in hexane after illuminating with UV light (365 nm). PL decay profiles of colloidal TlBr NCs are qualitatively similar to that of TlI NCs and are shown in Figure 5.6b.

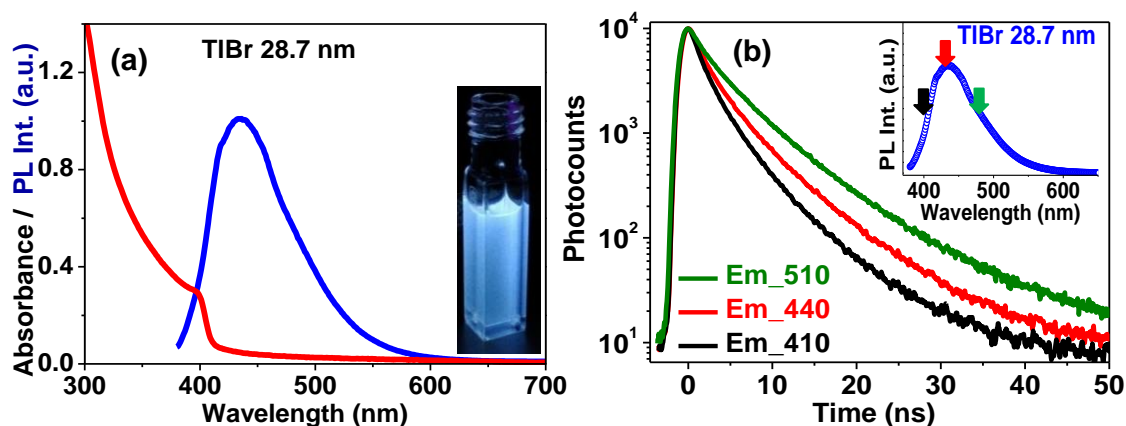


Figure 5.6: (a) UV-visible absorption and PL spectra of colloidal dispersion of TlBr NCs, inset shows photoluminescence from TlBr NCs dispersed in hexane under 365 nm UV radiation. (b) PL decay profiles of TlBr NCs at different emission wavelengths see inset for guidance, after excitation at 340 nm.

5.3.7 Mobility and diffusion length

Effective mobility values ($\phi\mu$) and diffusion length (L_D) were obtained by employing THz spectroscopy on TlX NCs films. The exact experimental details and calculations are not part of my PhD thesis, but available in the published paper Mir et al. *Chem. Sci.*, 2017, 8, 4602-4611. In this thesis, I am just mentioning the major findings of the THz spectroscopic study

to complete the story line of defect tolerant TII NCs. The effective mobilities ($\phi\mu$) (see Figure 5.7) obtained from THz spectroscopy study vary from 220 to 329 $\text{cm}^2\text{V}^{-1}\text{s}^{-1}$ in case of TlBr NCs film and from 90 to 220 $\text{cm}^2\text{V}^{-1}\text{s}^{-1}$ in case of TII NCs film at different fluences in the range of $0.85\text{-}5.86 \times 10^{13}$ photons/ cm^2 . However, $\phi\mu$ values are quite similar at lower pump intensities. The mobility values obtained here are reasonably high compared to many other NC systems, as discussed later. These high effective carrier mobilities further suggest the defect tolerant nature of TIX NCs.

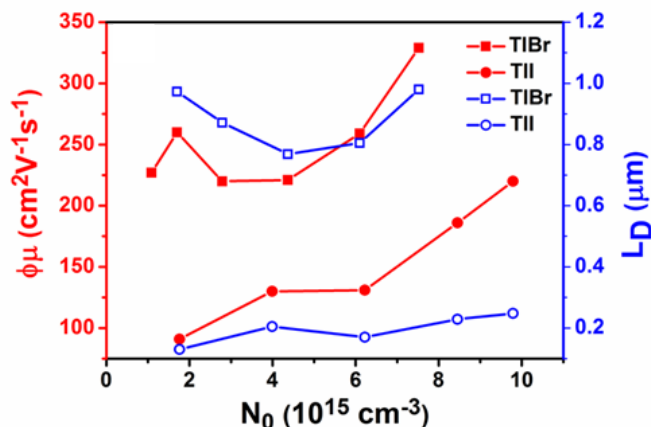


Figure 5.7: Effective carrier mobility ($\phi\mu$, red symbols) and carrier diffusion length (L_D , blue symbols) for (28.7 nm) TlBr and (8.4 nm) TII NCs, as a function of initial carrier density (fluence). Total effective mobility ($\phi\mu$) becomes actual mobility when each absorbed photon generates two free carriers i.e. electron and hole. The symbols denote experimental data and lines for observed trends.

Next, the calculated highest carrier diffusion length (L_D) in TlBr NCs film are $\sim 0.98 \mu\text{m}$ while in TII NCs film a highest value $\sim 0.248 \mu\text{m}$ is reported. As expected, the mobility and the diffusion length have very similar dependence on carrier density (fluence) for a particular sample see Figure 5.7. However, the trends are quite different for TlBr and TII NCs. At a particular carrier density the mobility for TlBr NCs is roughly twice than the mobility for TII NCs. On contrary the diffusion lengths in TlBr NCs are almost an order of magnitude longer than that of TII NCs since the average lifetimes in TlBr NCs are an order of magnitude higher. At certain fluences the L_D values in TlBr NCs are in microns with mobilities of $\sim 300 \text{ cm}^2\text{V}^{-1}\text{s}^{-1}$, which will be good for various optoelectronic properties such as UV, X-ray, gamma-ray detectors. However, one should be careful in interpreting the mobility and diffusion length values obtained from this study and should not expect them to be same in a real device made of these NCs. THz probes the local AC photoconductivity and hence does not reflect any long range disorder in the system. Also THz probe responds only to free carriers leaving excitons unperturbed since $1 \text{ THz} = 4.13 \text{ meV}$.

5.3.8 Comparison of TIX NCs with other semiconductor NCs with optical band gap > 2.5 eV (< 500 nm)

As the optical band gap increases, the probability of finding a defect state deep within the gap increases. For NCs, the problem becomes more acute because of the abundance of surface defects owing to large surface-to-volume ratio. Thereby, developing semiconductor NCs with reduced deep-defect related trap-states for optoelectronic properties in the UV to blue region of electromagnetic spectrum is highly challenging. This vexing problem of deep trap-states is often reflected in the poor luminescence efficiency, low carrier mobility and small diffusion lengths of charge carriers.

Table 5.2: Comparison of PL QY, carrier mobility and carrier diffusion length of our TIX NCs with various well-studied semiconductor NCs exhibiting optical gap < 500 nm.

Sample	optical gap (eV), (nm)	PL QY (%)	mobility ($\text{cm}^2\text{V}^{-1}\text{s}^{-1}$)	diffusion length (μm)	method adapted to measure mobility
TlBr NCs (this work)	3.1, 400	10	329	0.98	THz
TlI NCs (this work)	2.8, 436	6	220	0.25	THz
TlBr bulk ⁴⁴⁻⁴⁵	--	--	$\mu_e = 40.2$ $\mu_h = 11.8$		conductivity, drift-mobility
CsPbCl ₃ NCs ⁴⁶	3.02, 410	3, 1*	--	--	
Carbon-dots QDs ⁴⁷⁻⁴⁹	2.69, 460	4-10, 57*	* $\mu_e = 8.5 \times 10^{-5}$ * $\mu_h = 3.8 \times 10^{-5}$	--	FET
CdS nanorod ⁵⁰⁻⁵¹	3.2, 383	10	32	--	I-V
CdS NCs ⁵²⁻⁵³	2.58, 480	6.4	--	--	
CdS thin film bulk ⁵⁴	--	--	17	--	TFT
CdSe NCs ⁵⁵⁻⁵⁶	2.4 -2.7, 450 – 500	1 - 10	1 – 100	--	THz
ZnSe NCs ⁵⁷	3.3- 2.8, 370-430	10 - 50	--	--	
ZnSe single Crystal ⁵⁸⁻⁵⁹			267, 40*, 0.017*		THz, I-V
CdSe/ZnS Core shell ⁶⁰	2.53, 490	30	--	--	

Asterisk (*) denotes data obtained from film

Table 5.2 suggests that 10% PL QY of our TIX NCs is indeed a reasonably high number in the UV-blue region. Further improvement of PL QY might occur by making core/shell NCs with type-I band alignment at the interface,⁶¹ but such a structure is often detrimental for

charge transport. It is to be noted here that bulk TIX is known to have higher dielectric constants (ϵ_r) ($\epsilon_r = 30.6$ for TlBr and $\epsilon_r = 21.6$ for TlI at 20 °C),⁶² compared to materials such as CdS ($\epsilon_r = 8.9$), CdSe ($\epsilon_r = 10.2$), and ZnSe ($\epsilon_r = 9.2$). This high dielectric constant in TIX is expected to promote excitonic dissociation which is undesirable for PL, but desirable for photoconductivity. High dielectric constant not only reinforces decoupling of photo-generated exciton, but also screens charge carriers from ionic trap-states thereby improving charge transport.²⁸

We measured effective carrier mobility and diffusion length using contact-less THz AC photoconductivity with excitation fluence in the range of 0.85 - 5.86×10^{13} photons/cm², similar to ref. 40. In the absence of available surface engineering methodologies for TIX NCs, this contact-less method is perhaps the only way to measure carrier mobility. A variety of other techniques are also used for measuring carrier mobility and diffusion length in NC solids, and there will be differences in the obtained numbers using different methodologies. In fact, even within THz spectroscopy, the numbers may be different based on whether the NC is measured in colloidal dispersion or in film. Our measurements are done on NC films, which are closer to the architecture of an optoelectronic devices. In spite of the involved uncertainties, Table 5.2 clearly shows that the carrier mobility and diffusion lengths of our TIX NC films are one of the highest. Such a combination of high PL efficiency, high carrier mobility and long diffusion lengths in a wide band gap semiconductor, suggest a minimal density of deep-trap states in our TIX NCs. As discussed earlier, electron band structure in Figure 5.1 indeed suggested the possibility of achieving nearly deep-trap-free TIX NCs, and our experimental results indirectly agree with the prediction. However, more direct experimental and theoretical studies are required to measure the density of deep-defect states in a TIX NC, before confirming defect-tolerant NC. These optical properties suggest TIX NCs can be a potential candidate for a new solution processed semiconductor for optoelectronic application in the UV-blue region. Furthermore, TIX NCs can be considered for solution processed materials for X-ray and gamma-ray detection. But toxicity of Tl is a concern for any real life applications.

5.4 Conclusions

We proposed here colloidal TlBr (28.7 nm diameter) and TlI NCs (8.4 nm and 4 nm diameter), as new wide band gap materials with interesting optical properties in the near-UV to blue spectral region. TlI NCs show orthorhombic structure at room temperature, and then undergo a reversible structural phase transition at 443 K (170 °C). On the other hand, TlBr

NCs exhibit a stable cubic phase in the studied temperature range of 303 K to 573 K. Both kinds of NCs exhibit excitonic absorption feature and PL with a reasonably high QY of 6-10% at room temperature in the violet-blue region, unlike their bulk counterpart. Ultrafast THz spectroscopy was employed to study the carrier dynamics of TIX NC films at different pump fluences. Subsequently, THz photoconductivity revealed high effective carrier mobilities of 329 and 220 $\text{cm}^2\text{V}^{-1}\text{s}^{-1}$, and long diffusion lengths of 0.98 and 0.25 μm for TIBr and TII NCs, respectively. In general, a wide band gap (UV-blue region) semiconductor NC often exhibit a high density of deep-defect states trapping the charge carriers. In the contrary, combination of reasonably high PL QY, high carrier mobility and long diffusion lengths suggest decrease of deep-defect states in our TIX NCs. These results suggest a possibility of defect-tolerant nature of TIX NCs, owing to the interesting valence electronic band structure (Figure 5.1), similar to lead halide perovskite NCs. But further improvement in NC synthesis, optical properties, and also computation studies are required to verify the defect-tolerant nature in TIX NCs.

5.5 References

1. Talapin, D. V.; Lee, J. S.; Kovalenko, M. V.; Shevchenko, E. V. Prospects of Colloidal Nanocrystals for Electronic and Optoelectronic Applications. *Chem. Rev.* **2010**, *110*, 389-458.
2. Protesescu, L.; Yakunin, S.; Bodnarchuk, M. I.; Krieg, F.; Caputo, R.; Hendon, C. H.; Yang, R. X.; Walsh, A.; Kovalenko, M. V. Nanocrystals of Cesium Lead Halide Perovskites (CsPbX_3 , X = Cl, Br, and I): Novel Optoelectronic Materials Showing Bright Emission with Wide Color Gamut. *Nano Lett.* **2015**, *15*, 3692-3696.
3. Swarnkar, A.; Chulliyil, R.; Ravi, V. K.; Irfanullah, M.; Chowdhury, A.; Nag, A. Colloidal CsPbBr_3 Perovskite Nanocrystals: Luminescence Beyond Traditional Quantum Dots. *Angew. Chem., Int. Ed.* **2015**, *54*, 15424-15428.
4. Yettapu, G. R.; Talukdar, D.; Sarkar, S.; Swarnkar, A.; Nag, A.; Ghosh, P.; Mandal, P. Terahertz Conductivity within Colloidal CsPbBr_3 Perovskite Nanocrystals: Remarkably High Carrier Mobilities and Large Diffusion Lengths. *Nano Lett.* **2016**, *16*, 4838-4848.
5. Manser, J. S.; Christians J. A.; Kamat, P. V. Intriguing Optoelectronic Properties of Metal Halide Perovskites. *Chem. Rev.*, **2016**, *116*, 12956-13008.
6. Song, J. Z.; Li, J. H.; Li, X. M.; Xu, L. M.; Dong, Y. H.; Zeng, H. B. Quantum Dot Light-Emitting Diodes Based on Inorganic Perovskite Cesium Lead Halides (CsPbX_3). *Adv. Mater.* **2015**, *27*, 7162_±.

7. Zhang, X. Y.; Lin, H.; Huang, H.; Reckmeier, C.; Zhang, Y.; Choy, W. C. H.; Rogach, A. L. Enhancing the Brightness of Cesium Lead Halide Perovskite Nanocrystal Based Green Light-Emitting Devices through the Interface Engineering with Perfluorinated Lonomer. *Nano Lett.* **2016**, *16*, 1415-1420.
8. Swarnkar, A.; Marshall, A. R.; Sanehira, E. M.; Chernomordik, B. D.; Moore, D. T.; Christians, J. A.; Chakrabarti, T.; Luther, J. M. Quantum Dot-Induced Phase Stabilization of α -CsPbI₃ Perovskite for High-Efficiency Photovoltaics. *Science*, **2016**, *354*, 92-95.
9. Yakunin, S.; Protesescu, L.; Krieg, F.; Bodnarchuk, M. I.; Nedelcu, G.; Humer, M.; De Luca, G.; Fiebig, M.; Heiss, W.; Kovalenko, M. V. Low-Threshold Amplified Spontaneous Emission and Lasing from Colloidal Nanocrystals of Caesium Lead Halide Perovskites. *Nat. Commun.* **2015**, *6*.
10. Wang, Y.; Li, X. M.; Zhao, X.; Xiao, L.; Zeng, H. B.; Sun, H. D. Nonlinear Absorption and Low-Threshold Multiphoton Pumped Stimulated Emission from All-Inorganic Perovskite Nanocrystals. *Nano Lett.* **2016**, *16*, 448-453.
11. Xu, Y. Q., et al. Two-Photon-Pumped Perovskite Semiconductor Nanocrystal Lasers. *J. Am. Chem. Soc.* **2016**, *138*, 3761-3768.
12. Park, Y. S.; Guo, S. J.; Makarov, N. S.; Klimov, V. I. Room Temperature Single-Photon Emission from Individual Perovskite Quantum Dots. *ACS Nano* **2015**, *9*, 10386-10393.
13. Schmidt, L. C.; Pertegas, A.; Gonzalez-Carrero, S.; Malinkiewicz, O.; Agouram, S.; Espallargas, G. M.; Bolink, H. J.; Galian, R. E.; Perez-Prieto, J. Nontemplate Synthesis of CH₃NH₃PbBr₃ Perovskite Nanoparticles. *J. Am. Chem. Soc.* **2014**, *136*, 850-853.
14. Akkerman, Q. A.; D'Innocenzo, V.; Accornero, S.; Scarpellini, A.; Petrozza, A.; Prato, M.; Manna, L. Tuning the Optical Properties of Cesium Lead Halide Perovskite Nanocrystals by Anion Exchange Reactions. *J. Am. Chem. Soc.* **2015**, *137*, 10276-10281.
15. Bekenstein, Y.; Koscher, B. A.; Eaton, S. W.; Yang, P. D.; Alivisatos, A. P. Highly Luminescent Colloidal Nanoplates of Perovskite Cesium Lead Halide and Their Oriented Assemblies. *J. Am. Chem. Soc.* **2015**, *137*, 16008-16011.
16. Zhang, D. D., et al. Synthesis of Composition Tunable and Highly Luminescent Cesium Lead Halide Nanowires through Anion-Exchange Reactions. *J. Am. Chem. Soc.* **2016**, *138*, 7236-7239.
17. Shamsi, J.; Dang, Z. Y.; Bianchini, P.; Canale, C.; Di Stasio, F.; Brescia, R.; Prato, M.; Manna, L. Colloidal Synthesis of Quantum Confined Single Crystal CsPbBr₃ Nanosheets

with Lateral Size Control up to the Micrometer Range. *J. Am. Chem. Soc.* **2016**, *138*, 7240-7243.

18. Ramasamy, P.; Lim, D. H.; Kim, B.; Lee, S. H.; Lee, M. S.; Lee, J. S. All-Inorganic Cesium Lead Halide Perovskite Nanocrystals for Photodetector Applications. *Chem. Commun.* **2016**, *52*, 2067-2070.

19. Hoffman, J. B.; Schleper, A. L.; Kamat, P. V. Transformation of Sintered CsPbBr₃ Nanocrystals to Cubic CsPbI₃ and Gradient CsPbBr_xI_{3-x} through Halide Exchange. *J. Am. Chem. Soc.* **2016**, *138*, 8603-8611.

20. Sichert, J. A., et al. Quantum Size Effect in Organometal Halide Perovskite Nanoplatelets. *Nano Lett.* **2015**, *15*, 6521-6527.

21. Hassan, Y.; Song, Y.; Pensack, R. D.; Abdelrahman, A. I.; Kobayashi, Y.; Winnik, M. A.; Scholes, G. D., Structure-Tuned Lead Halide Perovskite Nanocrystals. *Adv. Mater.* **2016**, *28*, 566±.

22. Tong, Y.; Ehrat, F.; Vanderlinden, W.; Cardenas-Daw, C.; Stolarczyk, J. K.; Polavarapu, L.; Urban, A. S. Dilution-Induced Formation of Hybrid Perovskite Nanoplatelets. *ACS Nano*, **2016**, *10*, 10936-10944.

23. Vikash Kumar, R.; Abhishek, S.; Rayan, C.; Angshuman, N. Excellent Green but Less Impressive Blue Luminescence from CsPbBr₃ Perovskite Nanocubes and Nanoplatelets. *Nanotechnology* **2016**, *27*, 325708.

24. Mudring, A. V. Thallium Halides – New Aspects of the Stereochemical Activity of Electron Lone Pairs of Heavier Main-Group Elements. *Eur. J. Inorg. Chem.* **2007**, *2007*, 882-890.

25. Bachrach, R. Z.; Brown, F. C. Exciton-Optical Properties of TlBr and TlCl. *Phys. Rev. B* **1970**, *1*, 818-831.

26. Heidrich, K.; Staude, W.; Treusch, J.; Overhof, H. Optical Properties and Electronic Structure of Simple Cubic and F.C.C. TlI. *Solid State Commun.* **1975**, *16*, 1043-1045.

27. Treusch, J. Electronic Band Structure, Bonding, and Ionicities of Polymorphous Thallous Halides. *Phys. Rev. Lett.* **1975**, *34*, 1343-1346.

28. Brandt, R. E.; Stevanović, V.; Ginley, D. S.; Buonassisi, T. Identifying Defect-Tolerant Semiconductors with High Minority-Carrier Lifetimes: Beyond Hybrid Lead Halide Perovskites. *MRS Commun.* **2015**, *5*, 265-275.

29. Hamdeh, U. H.; Nelson, R. D.; Ryan, B. J.; Bhattacharjee, U.; Petrich, J. W.; Panthani, M. G. Bismuth Based Hybrid Perovskites A₃Bi₂I₉ (A: Methylammonium or Cesium) for Solar Cell Application. *Chem. Mater.* **2016**, *28*, 6567-6574.
30. Ganose, A. M.; Savory, C. N.; Scanlon, D. O. Beyond Methylammonium Lead Iodide: Prospects for the Emergent Field of nS² Containing Solar Absorbers. *Chem. Commun.* **2017**, *53*, 20-44.
31. Swarnkar, A.; Ravi, V. K.; Nag, A. Beyond Colloidal Cesium Lead Halide Perovskite Nanocrystals: Analogous Metal Halides and Doping. *ACS Energy Lett.*, **2017**, *2*, 1089–1098.
32. Bachrach, R. Z. The Optical Absorption of Orthorhombic Thallous Iodide. *Solid State Commun.* **1969**, *7*, 1023-1025.
33. Heidrich, K.; Staude, W.; Treusch, J.; Overhof, H. Optical Properties and Electronic Structure of Polymorphous Tici and Tibr. *Phys. Rev. Lett.s* **1974**, *33*, 1220-1223.
34. Ijaz ur, R.; Hofstadter, R. Thallium Halide Radiation Detectors. *Phys. Rev. B* **1984**, *29*, 3500-3507.
35. Johnsen, S.; Liu, Z.; Peters, J. A.; Song, J.-H.; Nguyen, S.; Malliakas, C. D.; Jin, H.; Freeman, A. J.; Wessels, B. W.; Kanatzidis, M. G. Thallium Chalcogenides for X-Ray and Γ -Ray Detection. *J. Am. Chem. Soc.* **2011**, *133*, 10030-10033.
36. Wibowo, A. C.; Malliakas, C. D.; Chung, D. Y.; Im, J.; Freeman, A. J.; Kanatzidis, M. G. Thallium Mercury Chalcobromides, TlHg₆Q₄Br₅ (Q = S, Se). *Inorg. Chem.* **2013**, *52*, 11875-11880.
37. Galvan-Arzate, S.; Santamaria, A. Thallium Toxicity. *Toxicol. Lett.* **1998**, *99*, 1-13.
38. Lennartson, A. Toxic Thallium. *Nat. Chem.* **2015**, *7*, 610-610.
39. Samara, G. A.; Walters, L. C.; Northrop, D. A. Polymorphism, Compressibility and Thermal Expansion of Thallous Iodide. *J. Phys. Chem. Solids* **1967**, *28*, 1875-1883.
40. Agekyan, V. F.; Akai, I.; Karasawa, T. Morphology and Optical Spectra of Metal Iodate Microcrystals in Porous Matrices. *Phys. Solid State* **2003**, *45*, 1170-1176.
41. Agekyan, V. F.; Stepanov, Y. A., Optical and Structural Properties of Thallium Halide Microcrystals in a Porous Matrix. *Phys. Solid State* **2001**, *43*, 763-765.
42. Rao, M. J.; Shibata, T.; Chattopadhyay, S.; Nag, A. Origin of Photoluminescence and XAFS Study of (ZnS)_(1-x)(AgInS₂)_(x) Nanocrystals. *J. Phys. Chem. Lett.* **2014**, *5*, 167-173.
43. Smith, H. M.; Zhou, Y.; Ciampi, G.; Kim, H.; Cirignano, L. J.; Shah, K. S.; Haller, E. E.; Chrzan, D. C. First Principles and Experimental Study of the Electronic Structure and Phase Stability of Bulk Thallium Bromide. *Appl. Phys. Lett.* **2013**, *103*, 091901.

44. Leão, C. R.; Lordi, V. Simultaneous Control of Ionic and Electronic Conductivity in Materials: Thallium Bromide Case Study. *Phys. Rev. Lett.* **2012**, *108*, 246604.
45. Hitomi, K.; Matsumoto, M.; Muroi, O.; Shoji, T.; Hiratate, Y. Thallium Bromide Optical and Radiation Detectors for X-Ray and Gamma-Ray Spectroscopy. *IEEE Trans. Nucl. Sci.* **2002**, *49*, 2526-2529.
46. Kim, Y.; Yassitepe, E.; Voznyy, O.; Comin, R.; Walters, G.; Gong, X.; Kanjanaboos, P.; Nogueira, A. F.; Sargent, E. H. Efficient Luminescence from Perovskite Quantum Dot Solids. *ACS Appl. Mater. Interfaces* **2015**, *7*, 25007-25013.
47. Liu, W.; Xu, S.; Li, Z.; Liang, R.; Wei, M.; Evans, D. G.; Duan, X. Layer-by-Layer Assembly of Carbon Dots-Based Ultrathin Films with Enhanced Quantum Yield and Temperature Sensing Performance. *Chem. Mater.* **2016**, *28*, 5426-5431.
48. Sun, Y.-P., et al. Quantum-Sized Carbon Dots for Bright and Colorful Photoluminescence. *J. Am. Chem. Soc.* **2006**, *128*, 7756-7757.
49. Kwon, W.; Do, S.; Won, D. C.; Rhee, S.-W., Carbon Quantum Dot-Based Field-Effect Transistors and Their Ligand Length-Dependent Carrier Mobility. *ACS Appl. Mater. Interfaces* **2013**, *5*, 822-827.
50. Son, J. S.; Park, K.; Kwon, S. G.; Yang, J.; Choi, M. K.; Kim, J.; Yu, J. H.; Joo, J.; Hyeon, T. Dimension-Controlled Synthesis of CdS Nanocrystals: From 0D Quantum Dots to 2D Nanoplates. *Small* **2012**, *8*, 2394-2402.
51. Zhang, Z. Y.; Jin, C. H.; Liang, X. L.; Chen, Q.; Peng, L.-M. Current-Voltage Characteristics and Parameter Retrieval of Semiconducting Nanowires. *Appl. Phys. Lett.* **2006**, *88*, 073102.
52. Saunders, A. E.; Ghezelbash, A.; Sood, P.; Korgel, B. A. Synthesis of High Aspect Ratio Quantum-Size CdS Nanorods and Their Surface-Dependent Photoluminescence. *Langmuir* **2008**, *24*, 9043-9049.
53. Spanhel, L.; Haase, M.; Weller, H.; Henglein, A. Photochemistry of Colloidal Semiconductors. 20. Surface Modification and Stability of Strong Luminescing CdS Particles. *J. Am. Chem. Soc.* **1987**, *109*, 5649-5655.
54. Conde, J.; Mejia, I.; Aguirre-Tostado, F. S.; Young, C.; Quevedo-Lopez, M. A. Design Considerations for II–VI Multi-Gate Transistors: The Case of Cadmium Sulfide. *Semicond. Sci. Technol.* **2014**, *29*, 045006.
55. Qu, L.; Peng, X. Control of Photoluminescence Properties of CdSe Nanocrystals in Growth. *J. Am. Chem. Soc.* **2002**, *124*, 2049-2055.

56. Beard, M. C.; Turner, G. M.; Schmittenmaer, C. A. Size-Dependent Photoconductivity in CdSe Nanoparticles as Measured by Time-Resolved Terahertz Spectroscopy. *Nano Lett.* **2002**, *2*, 983-987.
57. Li, L. S.; Pradhan, N.; Wang, Y.; Peng, X. High Quality ZnSe and ZnS Nanocrystals Formed by Activating Zinc Carboxylate Precursors. *Nano Lett.* **2004**, *4*, 2261-2264.
58. Ropagnol, X.; Morandotti, R.; Ozaki, T.; Reid, M. Toward High-Power Terahertz Emitters Using Large Aperture ZnSe Photoconductive Antennas. *IEEE Photon. J.* **2011**, *3*, 174-186.
59. Venkatachalam, S.; Jeyachandran, Y. L.; Sureshkumar, P.; Dhayalraj, A.; Mangalaraj, D.; Narayandass, S. K.; Velumani, S. Characterization of Vacuum-Evaporated ZnSe Thin Films. *Mater. Charact.* **2007**, *58*, 794-799.
60. Lee, J.; Sundar, V. C.; Heine, J. R.; Bawendi, M. G.; Jensen, K. F. Full Color Emission from II–VI Semiconductor Quantum Dot–Polymer Composites. *Adv. Mater.* **2000**, *12*, 1102-1105.
61. Hines, M. A.; Guyot-Sionnest, P. Synthesis and Characterization of Strongly Luminescing ZnS-Capped CdSe Nanocrystals. *J. Phys. Chem.* **1996**, *100*, 468-471.
62. Samara, G. A. Temperature and Pressure Dependence of the Dielectric Constants of the Thallous Halides. *Phys. Rev.* **1968**, *165*, 959-969.

Appendix A

Strategy to Overcome Recombination Limited Photocurrent in CsPb(Br_{0.65}I_{0.35})₃ Nanocrystal Arrays

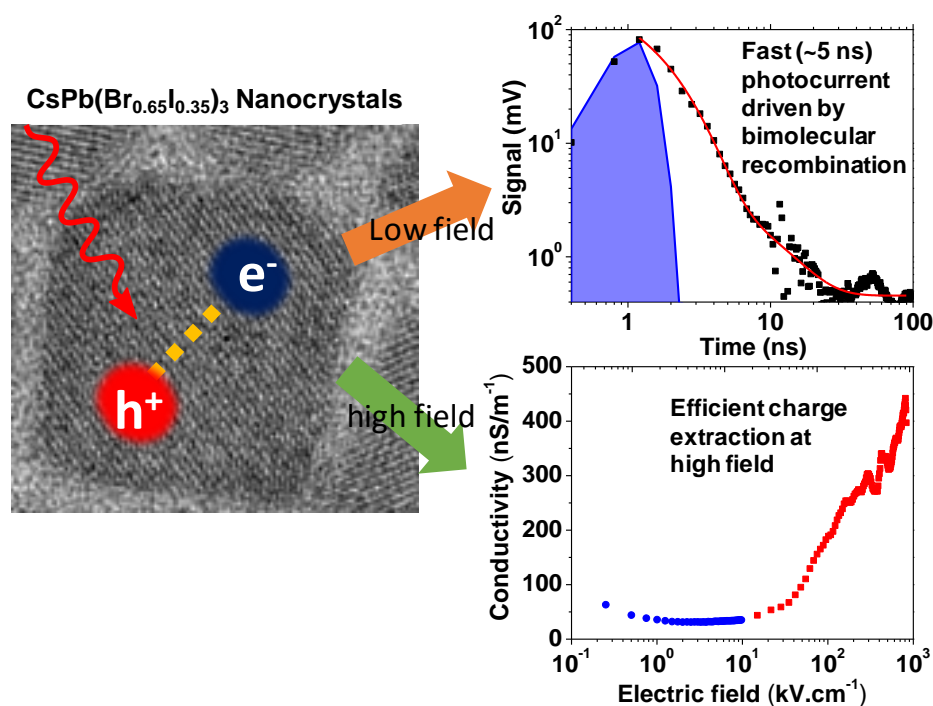
.....
The work presented in this appendix is published under following details. Mir, J. W.; Livache, C.; Goubet, N.; Martinez, B.; Jagtap, A.; Chu, A.; Coutard, N.; Cruguel, H.; Barisien, T.; Ithurria, S.; Nag, A.; Dubertret, B.; Ouerghi, A.; Silly, G. M.; Lhuillier E. *App. Phys. Lett.*, **2018**, *112*, 113503. Permission is taken for the whole article. Copyright 2018 American Institute of Physics.

The work was carried out at INSP (UPMC), Paris, where I worked for 6 months under supervision of Dr. Emmanuel Lhuillier.

Abstract

We investigated the transport properties of CsPb(Br_{0.65}I_{0.35})₃ perovskite nanocrystals (NCs) and is discussed as the representative case of CsPbX₃ perovskite NCs. While this material is very promising for the design of light emitting diodes, lasers, and solar cells. Very little work has been devoted to the basic understanding of their (photo)conductive properties in an ensemble system. By combining DC and time-resolved photocurrent measurements, we demonstrate fast photodetection with time response below ~2 ns. The photocurrent generation in perovskite NCs based arrays is limited by fast bimolecular recombination of the material, which limits the lifetime of the photogenerated electron-hole pairs. We then use nanotrench electrodes to ensure that the device size fits within the obtained diffusion length of the material in order to boost the transport efficiency. By using this strategy we observed an enhancement of the photoresponse by a factor of 1,000.

Graphical abstract



A.1 Introduction

Lead halide based perovskite materials have raised significant scientific and technological interests in the field of solar cells because of their defect-tolerant band structure.¹ These materials lead to large open-circuit voltages (>1 V) and thus high power conversion efficiencies.² Improved solar cell efficiencies ~23% for hybrid perovskites³ and above 16% for perovskite nanocrystals (NCs) based devices have been reported so far.⁴⁻⁵ The idea of using these defect-tolerant lead halide based perovskite NCs for designing high-efficiency light emitting materials was proposed by the Kovalenko group.⁶ A paradigm shift was proposed: instead of preventing the wave function from encountering surface traps by building a shell around the nanocrystal, a defect-tolerant material ensures that no surface traps are generated in the mid-gap region. As a result, CsPbX₃ (with X a halide anion) NCs are able to generate high photoluminescence (PL) efficiency (~90 % based on core only objects) and are obtained through straightforward and reliable synthesis.⁶ Their exceptional light emitting properties have been used to demonstrate low thresholds for lasing,⁷ single photon emission,⁸⁻⁹ and light emitting diodes with narrow emission linewidth.¹⁰⁻¹² As a result, both high light emitting efficiency and defect tolerant nature make them promising candidates for new generation NCs based optoelectronic devices.^{13,14}

As a new class of colloidal nanomaterials, lead halide based perovskite NCs show unique properties, yet reveals some new challenges. In particular, these materials present some stability issues: perovskite NCs degrade under electron beam¹⁵ and undergo structural phase changes or ligand-induced stoichiometry change.¹⁶ As a result, perovskite NCs need to be handled with great care and the conventional method to build conductive NCs based films need to be revised. For example, a phase transfer ligand exchange toward S²⁻ capping, although quite successful for metal chalcogenide NCs,¹⁷⁻¹⁸ cannot be applied to perovskite NCs. Indeed, such a ligand exchange performed on CsPbBr₃ NCs leads to the formation of a conductive and photoresponsive film of PbS NCs. Similarly, ion gel gating¹⁹⁻²⁰ cannot be straight forwardly applied because the ion gel dissolves CsPbX₃ perovskite NCs. As a consequence, the whole surface chemistry toolbox used to tune the tunnelling barrier associated with the capping ligands to make a film photoconductive needs to be revisited.

The recent report of CsPbI₃ NCs based solar cell⁴ with relatively high photon conversion efficiency (13 %) has demanded for a deeper investigation of the charge transport properties of NCs arrays. However currently transport experiments of lead halide perovskite NCs based devices have been mostly explored on diode structures.²¹⁻²³ In such device geometries, the

transport of the NCs layer is blurred with effects coming from the electron and hole extraction layers. This makes the basic understanding of the transport more complex.

In this appendix, we studied transport measurements to highlight the limitations of the photocurrent generation in CsPbX₃ perovskite NCs arrays. We provide evidence that the fast bimolecular recombination of NCs is the main limitation and is responsible for the short photocarrier lifetime. We then propose use of nanotrench device geometry to boost the carrier injection at a given high field and enhance photocurrent generation by a factor of 1,000.

A.2 Experimental Section

A.2.1 Cesium oleate

In a three neck 100 mL flask, 0.8 g of Cs₂CO₃ is mixed with 2.5 mL of oleic acid (OA) and 30 mL of octadecene (ODE). The flask is degassed under vacuum for next 30 minutes at 110 °C. The atmosphere is then switched to Ar and the temperature is raised to 200 °C for 10 min. At this point the cesium salt is fully dissolved. The temperature is cooled down below 110 °C and the flask is further degassed for 10 min. The obtained gel is used as stock solution.

A.2.2 CsPb(Br,I)₃ NCs

In a 25 mL three neck flask, we introduced 101.8 mg of PbBr₂ along with 59.9 mg of PbI₂ in 10 mL of ODE. The flask is degassed first at room temperature until the brisk bubbling of the solution slowed down and then at 110 °C for the next 30 minutes. We then inject 0.5 mL of OA and 0.5 mL of oleylamine (OLA) in this reaction mixture. The atmosphere is switched to Ar and the temperature is set at 180 °C. Meanwhile the stock solution of cesium oleate is warmed up at 60°C. We then quickly inject 0.8 mL of cesium oleate stock solution. The reaction is conducted for 30 sec. The heating mantle is removed and the flask is cooled down using fresh air flux from outside. The obtained solution is centrifuged at 6000 rpm for 5 minutes. The supernatant is discarded and the obtained pellet is redispersed in fresh hexane. For device purpose we carried out 2nd washing using methyl acetate as non-solvent. Typically, methyl acetate is added twice the volume of NCs dispersion and again centrifuged at 6000 rpm for 5 minutes. The obtained pellet is redispersed in hexane and used for device fabrication.

A.2.3 Characterization methods

UV-visible absorption spectra are acquired using a Shimadzu UV-3600 spectrometer. PL spectra (excitation at 420 nm) are obtained from Edinburgh FLS 980 spectrophotometer.

Transmission electron microscopy (TEM) images were captured using JEOL 2010 instrument. The grids are prepared by drop casting dilute solution of NCs dispersed in hexane and degassed overnight under secondary vacuum. PL dynamics were measured through classical gated photon counting using a SR400 unit (from Stanford Research Systems) associated to a high efficiency single photon module working in the visible spectrum (SPCM-AQRH-13-FC from Excelitas Technologies'). The excitation is made by a picosecond laser diode (from Alphas) providing pulses of 60 ps at $\lambda = 407$ nm and great attention was paid to maintain low enough pump fluence and prevent any degradation of the sample during the experiment.

A.2.4 DC transport

DC transport is conducted in air and the sample is connected to Keithley 2634 bi-channel sourcemeter. Two types of electrodes are used; 1) interdigitated gold coated electrodes over Si/SiO₂ substrate in which the interdigits are 2.5 mm long and spaced by 20 μ m, and 2) nanotrench gold coated electrodes over Si/SiO₂ substrate where the two electrodes lie 60 nm apart with high aspect ratio (length \sim 15 μ m). For temperature dependence, the sample is put on the cold finger of cryofree cryostat. For illumination we use a 532 nm DPSS laser diode.

A.2.5 Time resolved transport

For time resolved measurement the sample is biased using a Keithley 2634 sourcemeter. Illumination is ensured by a 0.9 ns CrysLas laser with a high energy density (70 μ J/pulse) at 355 nm. The signal is acquired on a Rohde & Schwarz GHz oscilloscope (RTE 1102).

A.3 Results and discussion

We carried out transport measurements on a series of CsPb(Br_{1-x}I_x)₃ NCs. This appendix will focus on one particular composition of CsPb(Br_{0.65}I_{0.35})₃ NCs. The choice of CsPb(Br_{0.65}I_{0.35})₃ was initially driven by a trade-off between the material stability (higher for Br-rich samples) and the optimal value of the band gap for solar cell application (better suited with iodine). These CsPb(Br_{0.65}I_{0.35})₃ NCs were grown using previously described methods^{4,6} and present a band edge energy of 2.29 eV see Figure A.1A.1a, which is close to the bulk band gap of the material having same halide composition and also consistent with their weak confinement. TEM imaging in Figure A.11b reveals a particle size in the range of 12 ± 2 nm, which is larger than the excitonic Bohr diameter of this material.⁶ The PL decay dynamics in Figure A.1c is fitted with a biexponential decay function with two time constants, 5 ns and 25 ns, which will be discussed later in the this appendix.

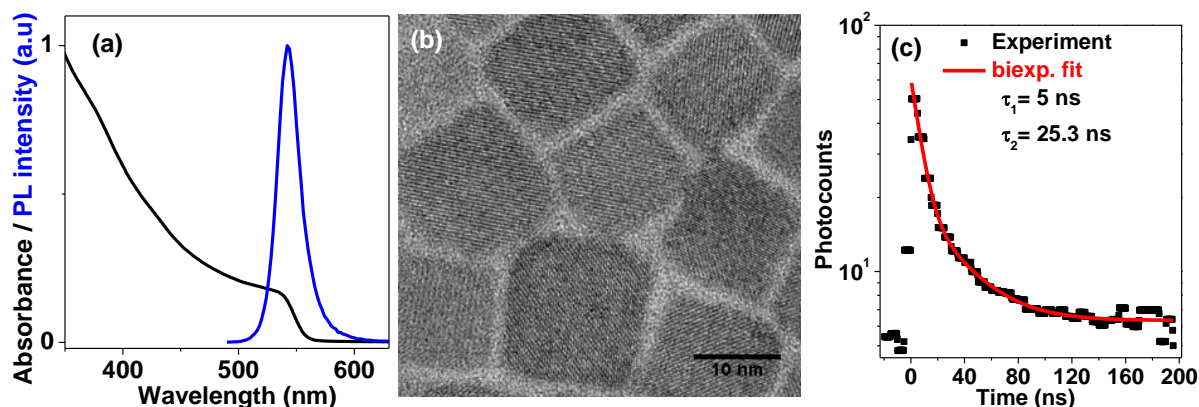


Figure A.1: (a) Absorbance and PL spectra of $\text{CsPb}(\text{Br}_{0.65},\text{I}_{0.35})_3$ NCs. (b) TEM image of $\text{CsPb}(\text{Br}_{0.65},\text{I}_{0.35})_3$ NCs. (c) Room temperature time resolved PL decay dynamics for a film of $\text{CsPb}(\text{Br}_{0.65},\text{I}_{0.35})_3$ NCs. PL decay measurements were carried out on thin films treated with saturated lead acetate in methylacetate.

After synthesis of desired CsPbX_3 NCs composition, colloidal dispersion of NCs was drop-casted over pre-designed electrodes (see the methodology section A.2.4 for electrode details). The insulating long chain oleylammonium capping ligands were then removed by following a previously reported multistep procedure and mild annealing.⁴ The multistep procedure ensures less pin holes or cracks generated by the volume reduction resulting from the removal of long chain organic ligands and annealing steps. Also, higher annealing temperature (~ 200 °C) or longer annealing time leads to strong inter NCs sintering, resulting in a loss of their nano-crystalline aspect. On the other hand, ligand exchange followed by a short mild annealing at 100 °C preserves the NC aspect.

Once the thin film is deposited on metallic electrodes, $\text{CsPb}(\text{Br}_{0.65},\text{I}_{0.35})_3$ NCs presents a conductive ohmic behaviour in Figure A.2a. The inset of Figure A.2b shows the schematics of the device used. Under 532 nm irradiation ($2 \text{ W}\cdot\text{cm}^{-2}$), a significant rise in the conductance is observed, typically by four orders of magnitude see Figure A.2a. The typical responsivity of the film spans from $200 \mu\text{A}\cdot\text{W}^{-1}$ to $1 \text{ mA}\cdot\text{W}^{-1}$ depending on the incident power. The scaling of the photocurrent with the incident light power follows a power law with a 0.64 exponent in Figure A.2b.²⁴ This value is closer to 0.5 expected for bimolecular recombination (electron-hole recombination through radiative and non-radiative paths) than to the value of 1 which often results from a monomolecular process (trapping) usually observed for metal chalcogenide NCs.²⁵ This supports the hypothesis of lower role of surface trapping in these NCs, as expected for a defect-tolerant material in which trap states are away from the band gap. We then investigated the temperature dependence of the current see Figure A.2c. Close to room temperature, the current follows an Arrhenius law, which suggests that transport

occurs through a hopping process to the nearest neighbour. The associated activation energy (240 meV) is smaller than half the band gap expected for an intrinsic semiconductor and could be due to n-type character of our CsPb(Br_{0.65},I_{0.35})₃ NCs arrays.

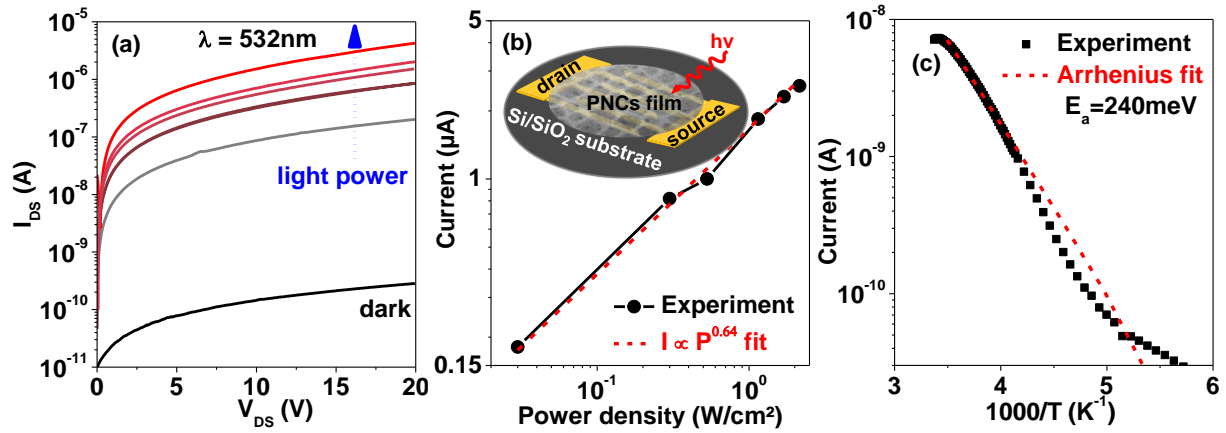


Figure A.2: (a) IV curves of CsPb(Br_{0.65},I_{0.35})₃ NCs film under dark conditions and under illumination at different light irradiance ($\lambda = 532$ nm), under ambient atmosphere and at room temperature over 20 μ m spaced interdigitated Au electrodes. (b) Current as a function of the light irradiance ($\lambda = 532$ nm) for the same film shown in panel (a). The inset shows schematics of the device used. (c) Current as a function of temperature for a film of CsPb(Br_{0.65},I_{0.35})₃ NCs under a voltage of 20 V measured under vacuum and in dark conditions.

We then investigated time-resolved carrier dynamics at the device scale. This is especially challenging because of the insulating character of the film. Under dark conditions, film resistance is typically in the 10 G Ω range and this is the crucial difference with respect to narrower band gap NCs (PbSe NCs) previously probed using a high bandwidth transient photocurrent setup.²⁶⁻²⁷ Measuring fast dynamics in the GHz range requires a special design where both sample stimulation (pulsed ns laser) and acquisition stage have to be compatible with the targeted GHz bandwidth of the setup. The experiments are conducted on transparent electrodes made of ITO so as to avoid any heating effects of the substrate which may lead to an artificial bolometric photoresponse of the device.

The transient photocurrent in CsPb(Br_{0.65},I_{0.35})₃ NCs is extremely fast with a main decay time of 1.2 ns. Typically, two time constants can be extracted from the decay curve in Figure A.3a, a fast component of ~ 1.2 ns and a slower component around 7.3 ns. No long-lived tail is observed, which is consistent with a limited role of deep surface trap states, contrary to what has been observed on metal chalcogenide NCs see ref.²⁸ These transient photocurrent dynamics have to be correlated with the PL dynamics shown in Figure A.1c. In such PL measurements, electron-hole pairs are generated by the laser pulse and the intra NC decay of the exciton population is followed. This PL decay is a good probe for the excited state carrier

density. The fact that similar dynamics are observed using photocurrent experiments suggests that the current magnitude is actually driven by the photogenerated carrier population of NCs.²⁶ This observation is also consistent with the flux dependence of the photocurrent in Figure A.2b which implies that the photocurrent generation is limited by bimolecular recombination. In the current device, the diffusion length can be estimated using an Einstein diffusion equation: we found $L_D = \sqrt{D\tau} = \sqrt{\frac{\mu k_b T}{e} \tau} \approx 58 \text{ nm}$, assuming a mobility of 0.26 cm²V⁻¹s⁻¹ recently reported from field effect transistor measurements²⁹ and $\tau = 5 \text{ ns}$ from our photocurrent decay measurements. This is much smaller than the electrode spacing (20 μm). As a result, only the carriers in the closest vicinity of the electrodes can be collected as all the other carriers undergo recombination before reaching the electrodes. On the other hand, the obtained diffusion length value $\sim 60 \text{ nm}$ is very close to the length of a perovskite NCs layer used for solar cells ($\sim 200 \text{ nm}$) which explain the recently obtained high power conversion efficiency.

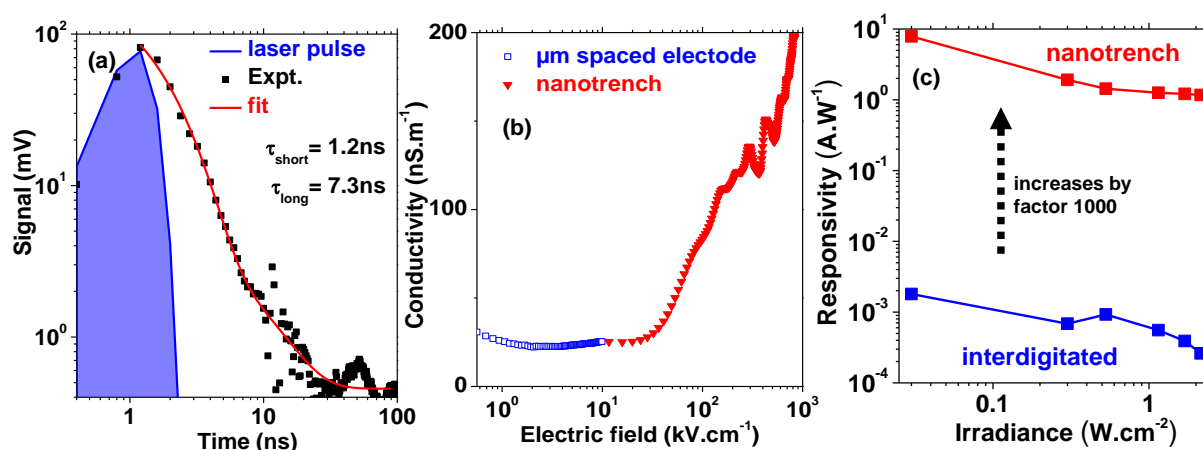


Figure A.3: (a) Transient photocurrent signal obtained in a film of CsPb(Br_{0.65},I_{0.35})₃ NCs at room temperature. The film is deposited on interdigitated electrodes made of ITO/PET. (b) Conductivity as a function of the applied electric field under dark condition in the case of CsPb(Br_{0.65},I_{0.35})₃ NCs. The data have been obtained from interdigitated electrodes at low electric field and from the nanotrench electrodes at high field regime. (c) Responsivity of a film of CsPb(Br_{0.65},I_{0.35})₃ NCs over μm spaced interdigitated electrodes and over nanotrench electrodes.

We finally investigated the effect of electric field on transport, in particular in the high field regime. To do so, we use nanotrench electrodes where the two electrodes lie 60 nm apart and have a high aspect ratio (length of 15 μm). Moreover, they present the key advantage of being built with a high fabrication success ratio ($>80\%$) using only two optical lithography steps in spite of the sub-wavelength size of the trench.^{25, 30} To follow the electric field dependence of the conductance over almost four orders of magnitude, we used μm spaced

interdigitated electrodes for the low field range and nanotrench electrodes for the high field range. The fact that the conductivity curves resulting from the two types of electrodes overlap in Figure A.3b which suggests that the transport mechanism is unchanged. The latter remains dominated by the nearest neighbour hopping mechanism, which is consistent with the fact that 4-5 NCs can fit within the nanotrench gap (60 nm). In the low field range, the conductance of the NCs film is field-independent. On the other hand, above 50 kV.cm^{-1} , we observe a significant rise in the conductance with the applied bias. This threshold corresponds to an energy drop per NC of $\sim 50 \text{ meV}$, which likely results from the charging energy of the NC. By applying a large electric field, we are able to inject charges in perovskite NCs more efficiently and the effect of the electrode structure on photocurrent is quite dramatic. The responsivity of the film is enhanced by more than a factor 1,000 as we switch from μm spaced electrodes to nanoscale devices see Figure A.3c. This increase arises from a combination of (i) an easier charge injection into NCs and (ii) an increase of gain due to the short inter-electrode spacing. In a photoconductor, the gain is the ratio of the photocarrier lifetime ($\sim 5 \text{ ns}$) over the transit time (the time to go from one electrode to the other). In this nanotrench geometry, the transit time is reduced by a factor of 300 as compared to μm spaced electrodes.^{25, 31} Because of the n-type nature of these perovskite NCs, the electron will recirculate several times during the hole carrier lifetime, leading to photogating,³² and the observed enhanced photocurrent.³³

A.4 Conclusions

By using a combination of DC and time resolved transport measurements, we provide evidence that the photocurrent of $\text{CsPb}(\text{Br}_{0.65}\text{I}_{0.35})_3$ NCs is limited by the fast bimolecular recombination of the material. This leads to fast recombination of the photogenerated electron-hole pair which allows for high bandwidth photodetection with time response as short as 1.2 ns but limits the absolute photoresponse of the film. We then propose to use nanotrench electrodes to achieve better charge injection at high electric fields and enhanced the photoresponse by a factor of 1,000.

A.5 References

1. Huang, H.; Bodnarchuk, M. I.; Kershaw, S. V.; Kovalenko, M. V.; Rogach, A. L. Lead Halide Perovskite Nanocrystals in the Research Spotlight: Stability and Defect Tolerance. *ACS Energy Lett.* **2017**, *2*, 2071-2083.
2. Hao, F.; Stoumpos, C. C.; Cao, D. H.; Chang, R. P. H.; Kanatzidis, M. G. Lead-Free Solid-State Organic-Inorganic Halide Perovskite Solar Cells. *Nat. Photonics* **2014**, *8*, 489.

3. NREL Best Research Solar Cell Efficiencies (<https://www.nrel.gov/pv/assets/pdfs/pv-efficiencies-07-17-2018.pdf>), (accessed, 30 January 2019).
4. Swarnkar, A.; Marshall, A. R.; Sanehira, E. M.; Chernomordik, B. D.; Moore, D. T.; Christians, J. A.; Chakrabarti, T.; Luther, J. M. Quantum Dot–Induced Phase Stabilization of α -CsPbI₃ Perovskite for High-Efficiency Photovoltaics. *Science* **2016**, *354*, 92-95.
5. Han, J.; Luo, S.; Yin, X.; Zhou, Y.; Nan, H.; Li, J.; Li, X.; Oron, D.; Shen, H.; Lin, H. Hybrid PbS Quantum-Dot-in-Perovskite for High-Efficiency Perovskite Solar Cell. *Small* **2018**, *14*, 1801016.
6. Protesescu, L.; Yakunin, S.; Bodnarchuk, M. I.; Krieg, F.; Caputo, R.; Hendon, C. H.; Yang, R. X.; Walsh, A.; Kovalenko, M. V. Nanocrystals of Cesium Lead Halide Perovskites (CsPbX₃, X = Cl, Br, and I): Novel Optoelectronic Materials Showing Bright Emission with Wide Color Gamut. *Nano Lett.* **2015**, *15*, 3692-3696.
7. Yakunin, S.; Protesescu, L.; Krieg, F.; Bodnarchuk, M. I.; Nedelcu, G.; Humer, M.; De Luca, G.; Fiebig, M.; Heiss, W.; Kovalenko, M. V. Low-Threshold Amplified Spontaneous Emission and Lasing from Colloidal Nanocrystals of Caesium Lead Halide Perovskites. *Nat. Commun.* **2015**, *6*, 8056.
8. Park, Y.-S.; Guo, S.; Makarov, N. S.; Klimov, V. I. Room Temperature Single-Photon Emission from Individual Perovskite Quantum Dots. *ACS Nano* **2015**, *9*, 10386-10393.
9. Rainò, G.; Nedelcu, G.; Protesescu, L.; Bodnarchuk, M. I.; Kovalenko, M. V.; Mahrt, R. F.; Stöferle, T. Single Cesium Lead Halide Perovskite Nanocrystals at Low Temperature: Fast Single-Photon Emission, Reduced Blinking, and Exciton Fine Structure. *ACS Nano* **2016**, *10*, 2485-2490.
10. Song, J.; Li, J.; Li, X.; Xu, L.; Dong, Y.; Zeng, H. Quantum Dot Light-Emitting Diodes Based on Inorganic Perovskite Cesium Lead Halides (CsPbX₃). *Adv. Mater.* **2015**, *27*, 7162-7167.
11. Yassitepe, E., et al. Amine-Free Synthesis of Cesium Lead Halide Perovskite Quantum Dots for Efficient Light-Emitting Diodes. *Adv. Funct. Mater.* **2016**, *26*, 8757-8763.
12. Staude, I.; Schilling, J. Metamaterial-Inspired Silicon Nanophotonics. *Nat. Photonics* **2017**, *11*, 274.
13. Konstantatos, G.; Sargent, E. H. *Colloidal Quantum Dot Optoelectronics and Photovoltaics* (Cambridge University Press, Cambridge, 2013).

14. Talapin, D. V.; Lee, J. S.; Kovalenko, M. V.; Shevchenko, E. V. Prospects of Colloidal Nanocrystals for Electronic and Optoelectronic Applications. *Chem. Rev.* **2010**, *110*, 389-458.
15. Dang, Z.; Shamsi, J.; Palazon, F.; Imran, M.; Akkerman, Q. A.; Park, S.; Bertoni, G.; Prato, M.; Brescia, R.; Manna, L. In Situ Transmission Electron Microscopy Study of Electron Beam-Induced Transformations in Colloidal Cesium Lead Halide Perovskite Nanocrystals. *ACS Nano* **2017**, *11*, 2124-2132.
16. Liu, Z.; Bekenstein, Y.; Ye, X.; Nguyen, S. C.; Swabeck, J.; Zhang, D.; Lee, S.-T.; Yang, P.; Ma, W.; Alivisatos, A. P. Ligand Mediated Transformation of Cesium Lead Bromide Perovskite Nanocrystals to Lead Depleted Cs_4PbBr_6 Nanocrystals. *J. Am. Chem. Soc.* **2017**, *139*, 5309-5312.
17. Nag, A.; Kovalenko, M. V.; Lee, J.-S.; Liu, W.; Spokoyny, B.; Talapin, D. V. Metal-Free Inorganic Ligands for Colloidal Nanocrystals: S^{2-} , $\text{H}^{\text{s-}}$, Se^{2-} , HSe^- , Te^{2-} , HTe^- , TeS_3^{2-} , OH^- , and NH_2^- as Surface Ligands. *J. Am. Chem. Soc.* **2011**, *133*, 10612-10620.
18. Wang, H.; Lhuillier, E.; Yu, Q.; Mottaghizadeh, A.; Ulysse, C.; Zimmers, A.; Descamps-Mandine, A.; Dubertret, B.; Aubin, H. Effects of Electron-Phonon Interactions on the Electron Tunneling Spectrum of PbS Quantum Dots. *Phys. Rev. B* **2015**, *92*, 041403.
19. Lhuillier, E.; Ithurria, S.; Descamps-Mandine, A.; Douillard, T.; Castaing, R.; Xu, X. Z.; Taberna, P.-L.; Simon, P.; Aubin, H.; Dubertret, B. Investigating the N- and P-Type Electrolytic Charging of Colloidal Nanoplatelets. *J. Phys. Chem. C* **2015**, *119*, 21795-21799.
20. Lhuillier, E.; Robin, A.; Ithurria, S.; Aubin, H.; Dubertret, B. Electrolyte-Gated Colloidal Nanoplatelets-Based Phototransistor and its Use for Bicolor Detection. *Nano Lett.* **2014**, *14*, 2715-2719.
21. Kwak, D.-H.; Lim, D.-H.; Ra, H.-S.; Ramasamy, P.; Lee, J.-S. High Performance Hybrid Graphene-CsPbBr_{3-x}I_x Perovskite Nanocrystal Photodetector. *RSC Adv.* **2016**, *6*, 65252-65256.
22. Palazon, F.; Di Stasio, F.; Lauciello, S.; Krahne, R.; Prato, M.; Manna, L. Evolution of CsPbBr₃ Nanocrystals Upon Post-Synthesis Annealing under an Inert Atmosphere. *J. Mater. Chem. C* **2016**, *4*, 9179-9182.
23. Palazon, F.; Dogan, S.; Marras, S.; Locardi, F.; Nelli, I.; Rastogi, P.; Ferretti, M.; Prato, M.; Krahne, R.; Manna, L. From CsPbBr₃ Nano-Inks to Sintered CsPbBr₃-CsPb₂Br₅ Films Via Thermal Annealing: Implications on Optoelectronic Properties. *J. Phys. Chem. C* **2017**, *121*, 11956-11961.

24. Willis, L. J.; Fairfield, J. A.; Dadosh, T.; Fischbein, M. D.; Drndic, M. Controlling Nanogap Quantum Dot Photoconductivity through Optoelectronic Trap Manipulation. *Nano Lett.* **2009**, *9*, 4191-4197.
25. Lhuillier, E.; Dayen, J.-F.; Thomas, D. O.; Robin, A.; Doudin, B.; Dubertret, B. Nanoplatelets Bridging a Nanotrench: A New Architecture for Photodetectors with Increased Sensitivity. *Nano Lett.* **2015**, *15*, 1736-1742.
26. Gao, J.; Fidler, A. F.; Klimov, V. I. Carrier Multiplication Detected through Transient Photocurrent in Device-Grade Films of Lead Selenide Quantum Dots. *Nat. Commun.* **2015**, *6*, 8185.
27. Fidler, A. F.; Gao, J.; Klimov, V. I. Electron–Hole Exchange Blockade and Memory-Less Recombination in Photoexcited films of Colloidal Quantum Dots. *Nat. Phys.* **2017**, *13*, 604.
28. Martinez, B.; Livache, C.; Goubet, N.; Jagtap, A.; Cruguel, H.; Ouerghi, A.; Lacaze, E.; Silly, M. G.; Lhuillier, E. Probing Charge Carrier Dynamics to Unveil the Role of Surface Ligands in HgTe Narrow Band Gap Nanocrystals. *J. Phys. Chem. C* **2018**, *122*, 859-865.
29. Hu, X., et al. Direct Vapor Growth of Perovskite CsPbBr₃ Nanoplate Electroluminescence Devices. *ACS Nano* **2017**, *11*, 9869-9876.
30. Dayen, J. F.; Faramarzi, V.; Pauly, M.; Kemp, N. T.; Barbero, M.; Pichon, B. P.; Majjad, H.; Begin-Colin, S.; Doudin, B. Nanotrench for Nano and Microparticle Electrical Interconnects. *Nanotechnology* **2010**, *21*, 335303.
31. Wang, H.; Lhuillier, E.; Yu, Q.; Zimmers, A.; Dubertret, B.; Ulysse, C.; Aubin, H. Transport in a Single Self-Doped Nanocrystal. *ACS Nano* **2017**, *11*, 1222-1229.
32. Konstantatos, G.; Sargent, E. H. PbS Colloidal Quantum Dot Photoconductive Photodetectors: Transport, Traps, and Gain. *Appl. Phys. Lett.* **2007**, *91*, 173505.
33. Prins, F., et al. Fast and Efficient Photodetection in Nanoscale Quantum-Dot Junctions. *Nano Lett.* **2012**, *12*, 5740-5743.

Appendix B

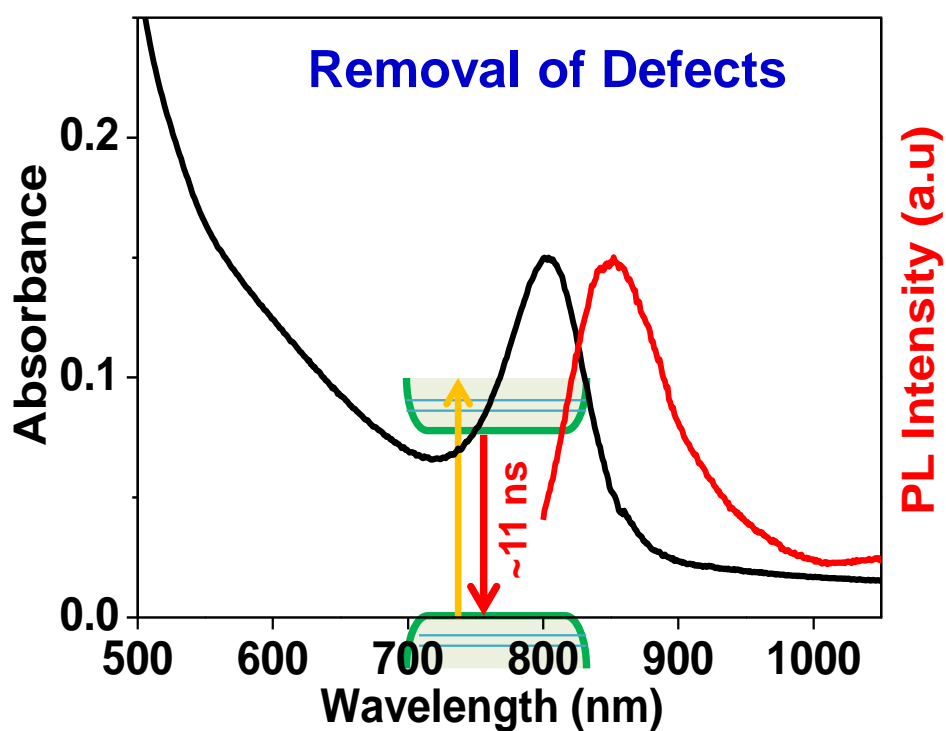
Origin of Excitonic Absorption and Emission from Colloidal Ag₂S Nanocrystals

.....
The work presented in this appendix is published under following details. Mir, J. W.; Swarnkar, A.; Sharma, R.; Katti, A.; Adarsh, V. K.; Nag, A. *J. Phys. Chem. Lett.*, **2015**, *6*, 3915–3922. Permission is taken for the whole article. Copyright 2015 American Chemical Society.

Abstract

Colloidal Ag₂S nanocrystals (NCs) typically do not exhibit sharp excitonic absorption and emission. We first elucidate the reason behind this problem by preparing Ag₂S NCs from nearly mono-disperse CdS NCs employing cation exchange reaction. It was found that the defect-related mid-gap transitions overlap with excitonic transition blurring the absorption spectrum. Based on this observation, we prepared nearly defect-free Ag₂S NCs starting from molecular precursors. The defect-free Ag₂S NCs exhibit sharp excitonic absorption and emission (quantum yield 20%) in near-infrared (853 nm) region.

Graphical abstract



B. 1 Introduction

Monoclinic bulk Ag₂S with a direct bandgap 1170 nm (1.06 eV) has been used as infrared photodetectors, thermo power cells, and luminescence based applications.¹ Recently, colloidal Ag₂S nanocrystals (NCs) have been synthesized and used as biocompatible near infrared (NIR) fluorescent probe.²⁻⁷ Ag₂S NCs are non-toxic, and therefore, unlike Cd, In and As based NCs, a polymer coating is not required for Ag₂S NCs to mitigate the toxicity.⁸ However, Ag₂S NCs typically do not exhibit sharp excitonic absorption and emission unlike other systems such as CdSe, CdS, InP, and PbS NCs.^{2, 5, 7, 9-14} Early studies of Brelle et al suggested Ag₂S NCs exhibits indirect bandgap, therefore, do not exhibit excitonic absorption features.¹⁵ Recently, Wang and coworkers¹⁴ mentioned “special electronic property” is responsible for the absence of excitonic transitions in Ag₂S NCs. Neither the details of this special behavior nor the origin of formation of unexpected (since monoclinic bulk Ag₂S is a direct bandgap semiconductor) indirect bandgap semiconductor was proposed. In a rare occasion, Jiang et al¹⁶ showed both excitonic absorption and emission from Ag₂S NCs without explaining its origin.

There can be many possible reasons for not observing excitonic features in absorption spectrum, for example, (i) small excitonic binding energy, (ii) the ensemble spectrum may get broadened because of polydispersity in NC size, and (iii) sub-bandgap transitions involving defect states or capping molecules or impurity phase overlapping with the excitonic transition. All these possibilities are detrimental for various applications including NIR luminescence for biological applications, and optical limiters. Other less explored applications such as photovoltaics and photodetectors using Ag₂S NCs also require defect-free NCs with narrow size distribution. Therefore, understanding the reason behind absence of both excitonic absorption and emission in Ag₂S NCs is important for both fundamental studies and applications.

In order to address the problem, we prepared Ag₂S NCs using two different pathways. First, Ag₂S NCs were prepared from CdS NCs employing postsynthesis cation exchange reaction. These cation-exchanged Ag₂S NCs exhibit quantum confinement effect and narrow size-distribution, but still do not exhibit sharp excitonic absorption because of overlapping defect-related mid-gap absorption. Based on this learning, we employed a second pathway of directly preparing Ag₂S NCs free from mid-gap defect related absorption, and thereby, observed sharp excitonic absorption and emission from Ag₂S NCs.

B.2 Experimental Section

B.2.1 Cation exchange of CdS NCs to Ag₂S NCs

CdS NCs with average diameters in the range of 1.6 nm to 4.1 nm were prepared following ref.²⁸ Cation exchange reactions (CdS NCs to Ag₂S NCs) were carried out by treating dilute dispersion of CdS NCs in toluene with concentrated methanolic solution of AgNO₃ (keeping Cd²⁺:Ag⁺ ratio of 1:4) at room temperature, following ref.¹⁷ Whereas, reverse cation exchange from Ag₂S to CdS NCs was done at elevated temperature around 80-90 °C. A dilute dispersion of Ag₂S NCs in toluene and 0.2 mL trioctylphosphine (TOP) was heated to 80 °C under inert atmosphere, followed by injection of excess Cd((NO)₃)₂ in acetonitrile.

B.2.2 Direct colloidal synthesis of Ag₂S NCs from molecular precursors

Direct synthesis of 3-mercaptopropionic acid (3-MPA) capped Ag₂S NCs were carried out after modifying the synthesis reported in ref.¹⁶ 0.05 mmol AgNO₃ and 10 mL ethylene glycol (EG) were taken in a three-necked round-bottom flask and subjected to vacuum and inert atmosphere alternatively two to three times along with stirring at room temperature. The flask was then heated to 100 °C under inert atmosphere with continuous stirring followed by injection of 1 mL of 3-MPA. A white precipitate was observed, which subsequently become a clear solution. The reaction temperature was set to different temperatures and time, and the optimized reaction condition was found to be 145 °C for a reaction time of 10 min exhibiting sharp excitonic absorption and emission. The product NCs were precipitated and washed using methanol/ethanol and redispersed in a polar solvent such as DMSO.

B.2.3 Characterization methods

PL and PL decay dynamics using time correlated single photon counting (TCSPC) technique were recorded using Edinburgh FLS980 instrument employed with liquid nitrogen cooled NIR PMT detector. PL quantum yield (PLQY) were measured using Indocyanine green as a reference dye (PLQY in DMSO 12%). UV-visible-NIR absorption spectra of NCs were recorded using a Perkin Elmer, Lambda-45 UV/Vis/NIR spectrometer. Bruker D8 Advance X-ray diffractometer equipped with copper K_α (1.54 Å) radiation was employed to obtain powder XRD data.

B.3 Results and discussions

B.3.1 Ag₂S NCs from CdS NCs employing cation exchange

In order to understand the effect of size distribution and quantum confinement effect on the excitonic transitions of Ag₂S NCs, we employed cation exchange reaction (schematically

represented in Figure B.1a) to synthesize Ag_2S NCs from CdS NCs following ref.¹⁷ Such cation exchange reactions are known to retain almost the same size of original NCs with minor adjustment.¹⁷⁻¹⁸

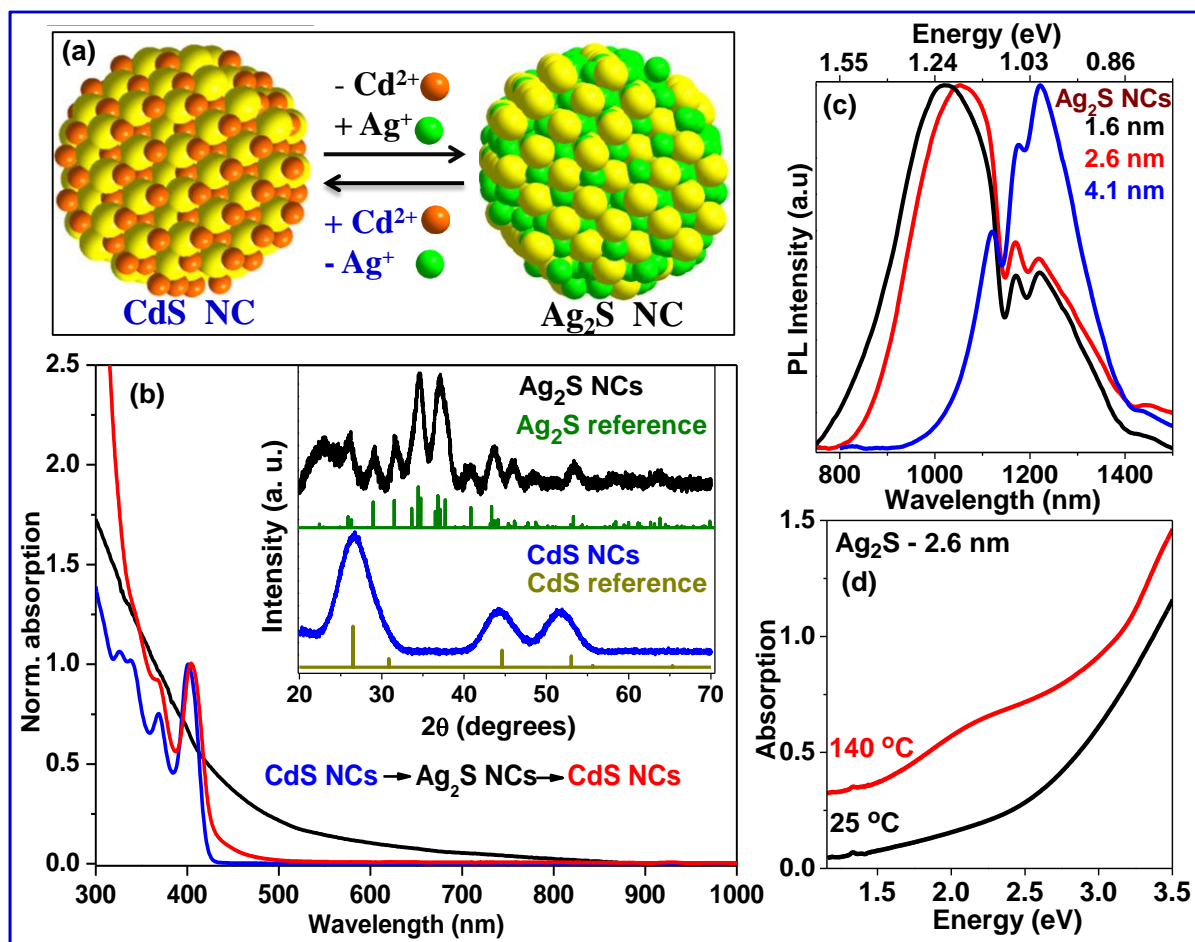


Figure B.1: (a) Schematic illustration of reversible cation exchange process, CdS to Ag_2S and back to CdS NCs. (b) UV-visible-NIR absorption spectra of initial CdS NCs (blue), Ag_2S NC (black) obtained after forward cation exchange and regenerated CdS NCs (red) obtained after reverse cation exchange. Blue and red spectra were normalized at the peak of lowest energy excitonic transitions. Inset shows XRD patterns of initial CdS NCs and Ag_2S NCs synthesized via cation exchange. (c) PL spectra of Ag_2S NCs showing size dependent change in emission wavelength. (d) Optical absorption spectra of Ag_2S -2.6 NCs (synthesized via cation exchange of 2.6 nm CdS NCs) and subjected to annealing under inert atmosphere using 1-octadecene as solvent. Spectrum for 140 °C annealing (red color) was shifted vertically upward for clarity.

Figure B.1b shows a UV-visible-NIR absorption spectrum of CdS NCs exhibiting four sharp excitonic features confirming narrow size distribution. However, Ag_2S NCs obtained after cation exchange of these CdS NCs exhibit a broad absorption spectrum, without any excitonic feature. Powder X-ray diffraction (XRD) patterns in the inset of Figure B.1b confirm the success of this cation exchange reaction. Interestingly, the Ag_2S NCs formed can be reversibly cation exchanged back to CdS, and the final CdS NCs obtained also exhibit

sharp excitonic features in the absorption spectrum, as shown by the red colored spectrum in Figure B.1b. This reversible cation exchange (CdS to Ag₂S to CdS) experiment confirms that the size and size distribution of NCs remained intact throughout the cation exchange processes. But, Ag₂S NCs obtained through cation exchange of CdS NCs did not exhibit any excitonic feature, inspite of having narrow size distribution. Therefore, ruling out broad size-distribution as the possible cause for the absence of excitonic absorption features, let us study the effect of quantum confinement of charge carriers in Ag₂S NCs. For this purpose, different sizes (1.6, 2.6 and 4.1 nm) of CdS NCs were prepared followed by cation exchange reactions forming different sizes of Ag₂S NCs, termed as Ag₂S-1.6, Ag₂S-2.6 and Ag₂S-4.1 in remaining part of this appendix. Absorption spectra for Ag₂S NCs obtained after cation exchange reactions for all sizes of CdS NCs were broad and featureless similar to that in Figure B.1b (black spectrum). PL spectra of different sized CdS NCs (data not shown here) and Ag₂S NCs (see Figure B.1c) exhibit the systematic quantum confinement effect with change in NCs size. All cation exchanged Ag₂S NC samples exhibit broad defect-related peak in the NIR region with PL efficiency < 0.5%.

Cation-exchanged Ag₂S NCs exhibits both quantum confinement effect and narrow size-distribution. So it is unclear why excitonic transition is not observed in absorption spectrum. There may be other transitions that overlap with excitonic transition. In an attempt to remove any such non-crystalline defects contributing to the absorption spectrum, we annealed the colloidal Ag₂S NCs dispersed in 1-octadecene (ODE) under inert atmosphere. Interestingly, Figure B.1d shows that the excitonic peak starts appearing at ~2 eV after annealing at 140 °C. This mild annealing is neither expected to improve the size distribution nor should it increase the excitonic binding energy. Therefore, excitonic feature after this mild annealing is because of improvement in crystallinity through removal of defects.¹⁹⁻²⁰ Further increase in annealing temperature to 200 °C leads to the segregation of Ag impurity phase, similar to earlier report.²¹ Results of cation exchange reaction infer that unwanted defect-related broad absorption blurs the features of excitonic absorption, and quenches the excitonic emission. Therefore, a model synthesis of high quality Ag₂S NCs should mainly target to remove such defects.

B.3.2 High quality Ag₂S NCs with sharp excitonic absorption and emission

There are some inherent differences of Ag₂S NC system compared to well-known II-VI NCs such as CdS NCs. For example, (i) Ag₂S has very low solubility product (6×10^{-51}) compared

to CdS (8×10^{-28}) and therefore nucleation of Ag₂S NCs can become uncontrollably favorable even at lower temperature, (ii) Ag⁺ ion in Ag₂S crystal has high ionic mobility unlike Cd²⁺ in CdS,²² and (iii) Ag⁺ precursors in the reaction mixture have a propensity to form Ag metal (standard reduction potential, $E^{\circ}_{\text{Ag}^+/\text{Ag}} = + 0.80 \text{ V}$), whereas, synthesis of CdS NCs is not known to suffer from such impurity phase ($E^{\circ}_{\text{Cd}^{2+}/\text{Cd}} = - 0.40 \text{ V}$).²³ All these factors can lead to the formation of detrimental defects in Ag₂S NCs. Keeping in mind the highly reactive formation of Ag₂S, and high mobility of Ag⁺, a lower reaction temperature and less reactive precursors for both Ag⁺ and S²⁻ appears to be a rational design for improving the crystallinity of Ag₂S NCs. These are probably the reasons why the popular “hot injection”²⁴ synthesis of colloidal NCs at temperatures $\sim 300 \text{ }^\circ\text{C}$, has largely failed to produce high quality Ag₂S NCs. Additionally, since there is possibility of formation of Ag metal, excess of sulfur precursor will help in the formation of Ag₂S NCs. We employed these reaction conditions for the direct synthesis of Ag₂S NCs.

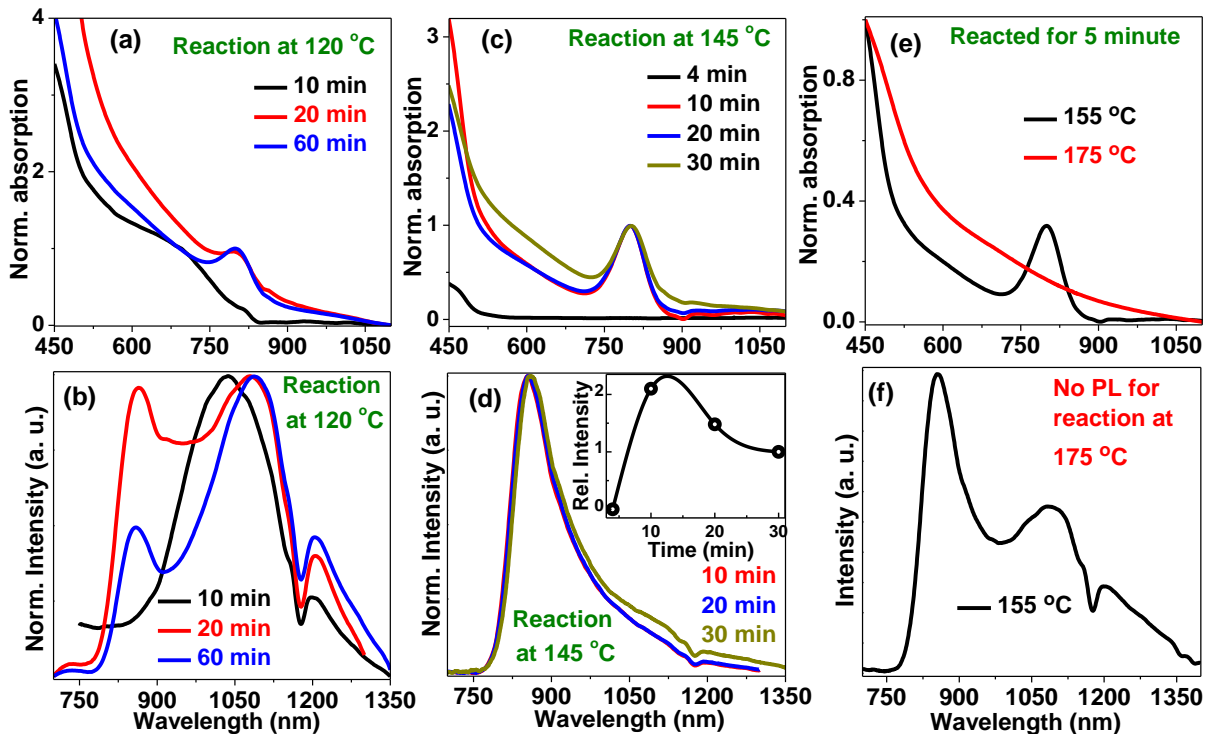


Figure B.2: Temporal evolution of UV-visible-NIR absorption and corresponding PL spectra of Ag₂S NCs synthesized directly from molecular precursors at different reaction temperatures. (a-b) For reaction carried out at 120 °C, (c-d) reaction carried out at 145 °C, and (e-f) reaction carried out at 155 to 175 °C.

Figure B.2a shows UV-visible-NIR absorption spectra for Ag₂S NCs prepared at 120 °C at different reaction times. A broad absorption shoulder appears at $\sim 650 \text{ nm}$ after 10 minutes of reaction, followed by emergence of excitonic peak at 800 nm after 20 minutes. Importantly, significant absorption is observed at wavelengths longer than 850 nm, i.e., at energies lower

than the optical band gap. This low-energy absorption may arise from defect-related mid-gap transitions.²⁵ Corresponding PL data in Figure B.2b shows defect-related broad emissions after 10 min of reaction. Excitonic PL at 858 nm is observed only after 20 minutes of reaction, along with a more intense defect-related emission at 1088 nm (Figure B.2b). After 60 min, relative intensity of excitonic emission increased compared to defect-related emission. PL excitation (PLE) spectra (data not shown here) for both 850 and 1088 nm emission suggest that both emissions originate via excitation of Ag₂S NCs, without involving any separate impurity phase. These results suggest that, the reaction was slow at 120 °C, where mid-gap defects dominates the absorption and PL data till 20 minutes of reaction, after which excitonic peak starts appearing but the mid-gap defect states are present even after 60 minutes of reaction.

Consequently, we increased the reaction temperature to 145 °C. Figure B.2c-d shows that the excitonic absorption at 800 nm and emission at 853 nm appears as early as 10 min for reaction carried out at 145 °C. Importantly, defect-related absorption tail at longer wavelength (>850 nm) is absent, which leads to the rare observation of sharp excitonic absorption and emission from Ag₂S NCs. A high PL efficiency ~20% is also observed for this optimized sample. Please note that, it is more difficult to achieve high PL efficiency in NIR region than in visible region. As the reaction time increases, the PL efficiency decreases as shown in the inset of Figure B.2d. A reaction temperature higher than 145 °C is not suitable for both excitonic absorption and emission as shown in Figure B.2e-f. Therefore, 145 °C is the optimized reaction temperature for the synthesis of these colloidal Ag₂S NCs. Please note that, Figure B.1d also suggested optimum temperature ~140 °C is helping to anneal out defects from cation-exchanged Ag₂S NCs. Higher temperatures may lead to the starting of partial segregation of Ag phase.²¹

We also note that a very high molar ratio of 3-MPA with respect to Ag⁺ concentration is maintained to obtain high quality Ag₂S NCs. 3-MPA acts both as S-precursor and capping ligand. A higher concentration of 3-MPA inhibits formation of Ag⁰ impurities. Another important chemical used in the synthesis is EG. When reaction was carried out in the absence of EG by mixing AgNO₃ and 3-MPA in dimethyl sulphoxide (DMSO), the formation of Ag₂S NCs was too fast even at a low temperature of 70 °C (data not shown here). Such fast and low-temperature reaction conditions leads to Ag₂S NCs with a high density of mid-gap defects. Compared to 70°C, reaction at 145 °C give high quality sample with minimum number of defects in our optimized reaction.

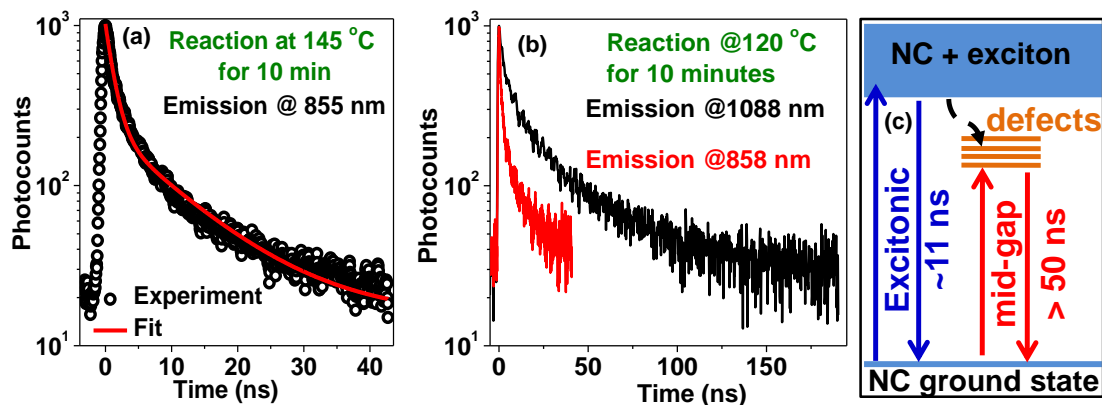


Figure B.3: PL decay dynamics of Ag₂S NCs, (a) reaction at 145 °C for 10 minutes, (b) reaction at 120 °C or 10 minutes. (c) Schematic illustration of possible electronic absorption and emission pathways in Ag₂S NCs. Mid-gap defects in Ag₂S blurs excitonic absorption and quenches excitonic emission. Removal, of such mid-gap defects resulted into excitonic absorption and emission for our optimized Ag₂S NCs.

Figure B.3a shows that the PL decay dynamics of optimized Ag₂S NCs (reaction temperature = 145 °C, reaction time = 10 min). The decay can be fitted with bi-exponential decay with lifetimes ~1 ns and 11 ns. The shorter lifetime (~1 ns or less) is typically attributed to non-radiative decay, and we attribute the lifetime ~11 ns to radiative excitonic recombination. This is a unique observation, since all prior reports of Ag₂S NCs showed decay with a significant contribution from longer lifetime component > 50 ns, and which can even extend up to hundreds of ns.^{12, 14} This faster decay of our Ag₂S NCs is the characteristic of excitonic emission, whereas, prior reports measured lifetime of defect-related emission. In Figure B.3b, we present lifetime data of one of our sample that exhibit both excitonic emission and defect-related emission in Ag₂S NCs for reaction at 120 °C, 10 minutes time. Clearly, defect-related emission has the longer lifetime component, whereas, PL decay of excitonic emission of the same sample is significantly faster.

Figure B.3c schematically summarizes the discussion regarding excitonic transition and defects in Ag₂S NCs. Unlike II-VI semiconductor NCs, mid-gap defects in Ag₂S NCs exhibit significant absorption. The exact nature of these defect states that obliterate excitonic feature from absorption spectrum of Ag₂S NCs is not yet known. Surface capping of our Ag₂S NCs remains same for all samples, but some optimized samples do not exhibit defect-related absorption, whereas, other samples show significant defect-related absorption. These results suggest that defects exhibiting mid-gap absorption might be located inside the lattice itself. Compared to surface-defects, a lattice-defect is expected to have a better spatial overlap with the delocalized valence and conduction band electronic wavefunctions, therefore, can exhibit a higher transition probability involving localized lattice-defect and delocalized valence

and/or conduction band.^{19-20, 29} Point defects in the lattice of Ag₂S NCs can arise from Ag⁺ vacancy/interstitial, because of high ionic diffusion capability of Ag⁺.^{26, 27} Possibility of any other kinds of crystal defects cannot be ignored at present. So, we speculate that the lattice defect is the primary cause of not observing excitonic absorption and emission in Ag₂S NCs and our optimized reaction conditions leads to better crystallinity of Ag₂S NCs removing unwanted lattice-defects, which in turn exhibit sharp excitonic absorption and emission.

B.4 Conclusions

Apart from narrow size distribution, removal of mid-gap defects is an important criterion for observing sharp excitonic absorption in colloidal Ag₂S NCs, which are more prone to form lattice defects compared to other semiconductors NCs such as CdS, CdSe, and PbS. These defects in Ag₂S NCs lead to broad absorption that overlap with excitonic transitions blurring the excitonic absorption, and quenches the excitonic PL. After realizing that the mid-gap states arising from lattice-defects are the major problem, defect-free colloidal Ag₂S NCs (4.5 nm diameter) were prepared starting from molecular precursors. These defect-free Ag₂S NCs exhibit sharp NIR excitonic absorption at 800 nm and excitonic PL at 858 nm. High PL efficiency (~20%) was observed for the NIR emission along with fastest PL decay (two lifetimes, nonradiative ~1 ns and radiative 11 ns) is reported so far in case of Ag₂S NCs.

B.5 References

1. Huxter, V. M.; Mirkovic, T.; Nair, P. S.; Scholes, G. D. Demonstration of Bulk Semiconductor Optical Properties in Processable Ag₂S and EuS Nanocrystalline Systems. *Adv. Mater.* **2008**, *20*, 2439-2443.
2. Du, Y. P.; Xu, B.; Fu, T.; Cai, M.; Li, F.; Zhang, Y.; Wang, Q. B. Near-Infrared Photoluminescent Ag₂S Quantum Dots from a Single Source Precursor. *J. Am. Chem. Soc.* **2010**, *132*, 1470-1471.
3. Zhang, Y.; Hong, G. S.; Zhang, Y. J.; Chen, G. C.; Li, F.; Dai, H. J.; Wang, Q. B. Ag₂S Quantum Dot: A Bright and Biocompatible Fluorescent Nanoprobe in the Second Near-Infrared Window. *ACS Nano* **2012**, *6*, 3695-3702.
4. Hong, G. S.; Robinson, J. T.; Zhang, Y. J.; Diao, S.; Antaris, A. L.; Wang, Q. B.; Dai, H. J. In Vivo Fluorescence Imaging with Ag₂S Quantum Dots in the Second Near-Infrared Region. *Angew. Chem., Int. Ed.* **2012**, *51*, 9818-9821.
5. Wang, Y.; Yan, X. P. Fabrication of Vascular Endothelial Growth Factor Antibody Bioconjugated Ultrasmall Near-Infrared Fluorescent Ag₂S Quantum Dots for Targeted Cancer Imaging in Vivo. *Chem. Commun.* **2013**, *49*, 3324-3326.

6. Wang, C. X.; Wang, Y.; Xu, L.; Zhang, D.; Liu, M. X.; Li, X. W.; Sun, H. C.; Lin, Q.; Yang, B. Facile Aqueous-Phase Synthesis of Biocompatible and Fluorescent Ag₂S Nanoclusters for Bioimaging: Tunable Photoluminescence from Red to Near Infrared. *Small* **2012**, 83137-3142.
7. Hocaoglu, I.; Cizmeciyan, M. N.; Erdem, R.; Ozen, C.; Kurt, A.; Sennaroglu, A.; Acar, H. Y. Development of Highly Luminescent and Cytocompatible Near-IR-Emitting Aqueous Ag₂S Quantum Dots. *J. Mater. Chem.* **2012**, 22, 14674-14681.
8. Tang, R.; Xue, J. P.; Xu, B. G.; Shen, D. W.; Sudlow, G. P.; Achilefu, S. Tunable Ultrasmall Visible-to-Extended Near-Infrared Emitting Silver Sulfide Quantum Dots for Integrin-Targeted Cancer Imaging. *ACS Nano* **2015**, 9, 220-230.
9. Sewall, S. L.; Cooney, R. R.; Anderson, K. E. H.; Dias, E. A.; Kambhampati, P. State-To-State Exciton Dynamics in Semiconductor Quantum Dots. *Phys. Rev. B* **2006**, 74, 235328.
10. Sahu, A.; Qi, L. J.; Kang, M. S.; Deng, D. N.; Norris, D. J. Facile Synthesis of Silver Chalcogenide (Ag₂E; E = Se, S, Te) Semiconductor Nanocrystals. *J. Am. Chem. Soc.* **2011**, 133, 6509-6512.
11. Jasieniak, J.; Califano, M.; Watkins, S. E. Size-Dependent Valence and Conduction Band-Edge Energies of Semiconductor Nanocrystals. *ACS Nano* **2011**, 5, 5888-5902.
12. Jiang, P.; Tian, Z. Q.; Zhu, C. N.; Zhang, Z. L.; Pang, D. W. Emission-Tunable Near-Infrared Ag₂S Quantum Dots. *Chem. Mater.* **2012**, 24, 3-5.
13. Gui, R. J.; Wan, A. J.; Liu, X. F.; Yuan, W.; Jin, H. Water-Soluble Multidentate Polymers Compactly Coating Ag₂S Quantum Dots with Minimized Hydrodynamic Size and Bright Emission Tunable from Red to Second Near-Infrared Region. *Nanoscale* **2014**, 6, 5467-5473.
14. Zhang, Y. J.; Liu, Y. S.; Li, C. Y.; Chen, X. Y.; Wang, Q. B. Controlled Synthesis of Ag₂S Quantum Dots and Experimental Determination of the Exciton Bohr Radius. *J. Phys. Chem. C* **2014**, 118, 4918-4923.
15. Brelle, M. C.; Zhang, J. Z.; Nguyen, L.; Mehra, R. K. Synthesis and Ultrafast Study of Cysteine- and Glutathione-Capped Ag₂S Semiconductor Colloidal nanoparticles. *J. Phys. Chem. A* **1999**, 103, 10194-10201.
16. Jiang, P.; Zhu, C. N.; Zhang, Z. L.; Tian, Z. Q.; Pang, D. W. Water-Soluble Ag₂S Quantum Dots for Near-Infrared Fluorescence Imaging In Vivo. *Biomaterials* **2012**, 33, 5130-5135.
17. Son, D. H.; Hughes, S. M.; Yin, Y. D.; Alivisatos, A. P. Cation Exchange Reactions-in Ionic Nanocrystals. *Science* **2004**, 306, 1009-1012.

18. Beberwyck, B. J.; Surendranath, Y.; Alivisatos, A. P. Cation Exchange: A Versatile Tool for Nanomaterials Synthesis. *J. Phys. Chem. C* **2013**, *117*, 19759-19770.
19. Torimoto, T.; Ogawa, S.; Adachi, T.; Kameyama, T.; Okazaki, K. I.; Shibayama, T.; Kudo, A.; Kuwabata, S. Remarkable Photoluminescence Enhancement of ZnS-AgInS₂ Solid Solution Nanoparticles by Post-Synthesis Treatment. *Chem. Commun.* **2010**, *46*, 2082-2084.
20. Kadlag, K. P.; Patil, P.; Rao, M. J.; Datta, S.; Nag, A. Luminescence and Solar Cell from Ligand-Free Colloidal AgInS₂ Nanocrystals. *Crystengcomm* **2014**, *16*, 3605-3612.
21. Aleali, H.; Sarkhosh, L.; Karimzadeh, R.; Mansour, N. Optical Limiting Response of Ag₂S Nanoparticles Synthesized by Laser Ablation of Silver Target in DMSO. *Phys. Status Solidi B-Basic Solid State Phys.* **2011**, *248*, 680-685.
22. Allen, R. L.; Moore, W. J. Diffusion of Silver in Silver Sulfide *J. Phys. Chem.* **1959**, *63*, 223-226.
23. Barrow, G. N., *Physical Chemistry 5th edition*, Tata McGraw-Hill Publishing Co. Ltd., New Delhi, 2007.
24. Murray, C. B.; Norris, D. J.; Bawendi, M. G. Synthesis and Characterization of Nearly Monodisperse CdE (E = S, Se, Te) Semiconductor Nanocrystallites. *J. Am. Chem. Soc.* **1993**, *115*, 8706-8715.
25. Superior Colloidal Stability of NCs After Rigorous Centrifugation Suggest NCs are not Agglomerated. So Significant Scattering of Incident Light Because of Agglomeration of NCs can be Ruled Out.
26. Xu, Z.; Bando, Y.; Wang, W. L.; Bai, X. D.; Golberg, D. Real-Time In Situ HRTEM-Resolved Resistance Switching of Ag₂S Nanoscale Ionic Conductor. *ACS Nano* **2010**, *4*, 2515-2522.
27. Shen, H. P.; Jiao, X. J.; Oron, D.; Li, J. B.; Lin, H. Efficient Electron Injection in Non-Toxic Silver Sulfide (Ag₂S) Sensitized Solar Cells. *J. Power Sources* **2013**, *240*, 8-13.
28. Yu, W. W.; Peng, X. G. Formation of High-Quality CdS and other II-VI Semiconductor Nanocrystals in Noncoordinating Solvents: Tunable Reactivity of Monomers. *Angew. Chem., Int. Ed.* **2002**, *41*, 2368-2371.
29. Rao, M. J.; Shibata, T.; Chattopadhyay, S.; Nag, A. Origin of Photoluminescence and XAFS Study of (ZnS)_(1-x)(AgInS₂)_(x) Nanocrystals. *J. Phys. Chem. Lett.* **2014**, *5*, 167-173.

**Thesis Outlook and
Future Directions**

Doping in novel defect tolerant CsPbX₃ (X = Cl, Br, I) perovskite Nanocrystals (NCs)

CsPbX₃ perovskite nanocrystals (NCs) recently emerged as the solution processed semiconductors showing impressive optoelectronic properties. In 2015, the first report suggested significant defect tolerant character in optical properties of CsPbX₃ NCs despite having high surface to volume ratio.¹ For example, 90% PL quantum yield (PLQY) of CsPbX₃ perovskite NCs without making core-shell type surface passivation is remarkable.¹ The defect tolerant character in these CsPbX₃ perovskite NCs is a newer direction to design novel semiconductors for optoelectronic applications. On the other hand, doping is an established strategy to tailor optical and electronic properties of semiconductor NCs.² We, therefore, doped Mn²⁺ and Yb³⁺ in defect tolerant CsPbX₃ NCs to tailor optical functionality. Apart from introducing new optical functionality, another aspect of doping has been explored where Mn-doping in CsPbX₃ NCs improves structural stability.³⁻⁴

In prior literature, trivalent lanthanide (Ln³⁺) doping is mostly explored in wide band gap insulators such as oxides and fluorides.⁵ This is because Ln³⁺ prefers octahedral or higher coordination and semiconductors like Si, II-III, and III-V typically have tetrahedral coordination. Therefore successful incorporation of Ln³⁺ into the lattice of a semiconductor remained challenging. Interestingly, the octahedral coordination of Pb²⁺ cation in CsPbX₃ perovskite NCs is unique unlike tetrahedral coordination environment in other semiconductors. This aspect makes CsPbX₃ perovskite NCs as the novel semiconductor hosts for lanthanide (Ln³⁺) dopants.

Therefore, the thesis addresses synthesis challenge and optical properties of Mn- and Yb-doped CsPbX₃ perovskite NCs. The idea was to combine the impressive properties of defect tolerant CsPbX₃ perovskite NCs with dopant properties. Mn- and Yb-doping in CsPbX₃ perovskite NCs introduces new luminescence channel at ~586 nm and ~990 nm respectively. Both the dopant emissions are significantly red shifted from absorption spectra of host NCs. This red shifted Mn- and Yb-emission are free from radiative losses such as self-absorption or non-radiative losses like Forster resonance energy transfer (FRET). The losses become critical when NCs are closely packed in films close to device geometry and therefore cannot be afforded in a real optoelectronic device. Thus, the Mn- and Yb- emission have tremendous scope in light emitting diodes (LEDs),⁶ luminescent solar concentrators (LSCs),⁷ and to boost external quantum efficiency of Si solar cells below 450 nm.⁸ Also both Mn²⁺ and Yb³⁺ ions have magnetic moments and can introduce magnetic character in the doped CsPbX₃ NCs due to exchange interactions of dopant with the carrier of host. The strength of

this dopant-carrier interaction increases as the quantum confinement increases. This aspect makes doping more desirable in NCs under strong quantum confinement regime, but this aspect is not much explored in this thesis.

One important problem is that, optoelectronically active black phase of CsPbI₃ NCs has limited stability in ambient conditions at room temperature. In chapter 4, we show that postsynthesis Mn-doping in CsPbI₃ NCs improves the stability of black phase at room temperature in ambient atmosphere (relative humidity ~30%) for about a month. Consequently, Mn-doped CsPbI₃ NCs with improved stability can be explored in solar cells and LEDs in ambient conditions. More importantly the role of Mn-doping in stabilizing both surface and lattice energies has been understood.

Pb-free TlX (X = Br, I) NCs

The defect tolerance in CsPbX₃ perovskite NCs gave rise to the curiosity to search for Pb-free defect tolerant metal halide NCs. Tl⁺ is isoelectronic to Pb²⁺. Also the valence electronic structure of TlX is similar to that of CsPbX₃. Therefore, we got motivated to prepare TlX NCs and studied their optoelectronic properties. Overall, TlX is found to be a good optoelectronic material in UV-blue region of electromagnetic spectrum, but toxicity of Tl is a concern for real life application.

Methodology development

In order to address the doping challenge in CsPbX₃ (X = Cl, Br, I) perovskite NCs, we have designed one pot synthesis strategy in chapter 2 to dope Mn²⁺ in CsPbCl₃ nanoplatelets (NPLs). But the same one pot synthesis failed to dope Mn in narrower band gap CsPbBr₃ perovskite NCs. Therefore, in chapter 3 we designed novel postsynthesis strategy to dope Mn and Yb in all compositions of CsPbX₃ (X = Cl, Br, I) NCs. Although Mn-doping in CsPbI₃ NCs is not expected to introduce new optical functionality but our target was to stabilize the black phase of CsPbI₃ NCs. The controlled experimental studies on stability of black phase CsPbI₃ NCs upon doping Mn is addressed in chapter 4. Finally, synthesis challenge of TlX NCs is addressed in chapter 5 to design Pb-free defect tolerant NCs.

Relevance of the results

We reported first time Mn²⁺ doping in CsPbCl₃ NPLs. The thickness of NPLs is about 2.3 nm, exhibiting strong quantum confinement effect. This quantum confinement is expected to significantly enhance dopant-carrier interaction, compared to two prior reports,⁹⁻¹⁰ where Mn²⁺ is doped in CsPbCl₃ nanocubes with edge length longer than excitonic Bohr diameter.

Our report on Mn-doped CsPbCl₃ NPLs opens up new opportunity to explore dopant-carrier interaction such as light or electrical bias induced magnetization in Mn-doped CsPbCl₃ perovskite NPLs. Our present finding show that Mn-doping in CsPbCl₃ NPLs introduces Mn-emission at ~586 nm with maximum PLQY ~20% for 0.8% Mn-dopant concentration and longer lifetime of 1.6 ms.

On the other hand one pot synthesis of Mn-doped CsPbBr₃ NCs is challenging. To address this challenge we introduced novel postsynthesis strategy in chapter 3 to dope Mn in CsPbBr₃ NCs. Different shapes of CsPbBr₃ NCs were doped with Mn²⁺, mainly to study the effect of quantum confinement changing the band gap on dopant emission. Our present findings show that changing optical band gap upon tuning quantum confinement affects the Mn-emission of Mn-doped CsPbBr₃ NCs. Mn-doped CsPbBr₃ NCs with band gap ≥ 490 nm or ≤ 2.53 eV resulted in absence of Mn-emission at room temperature. This is due to thermally activated back energy transfer from dopant to host which quenches the Mn-emission at room temperature. The back energy transfer can be suppressed leading to Mn-emission by increasing optical gap through quantum confinement effect or measuring PL at lower temperature (≤ 225 K). On the other hand, Yb-doping introduce near-infrared (NIR) emission ~990 nm (1.25 eV) in all composition of CsPbX₃ (X = Cl, Br, I) perovskite NCs including different shapes. These Yb-doped CsPbX₃ NCs have potential scope in NIR LEDs, sensors and lasing.

Apart from introducing new optical functionality, chapter 4 shows that Mn-doping in CsPbI₃ NCs can improve stability of desired black phase for about a month at room temperature with relative humidity ~30%. The results were obtained based on our postsynthesis doping strategy which is beyond experimental uncertainties unlike prior reports.³⁻⁴ This postsynthesis doping in CsPbI₃ NCs allowed us to study the role of both surface and lattice contribution, improving the stability of black phase of CsPbI₃ NCs. The improved stability of black phase Mn-doped CsPbI₃ NCs can be directly explored for solar cell or LED performance. Such solar cells or LEDs should mainly target stability aspect of device under continuous operation.

Another perspective addressed is complete substitution of Pb²⁺ with different metal ion and design of new defect tolerant semiconductor NCs. For this purpose, Pb-free TIX NCs are synthesized for the first time in chapter 5. Our TIX NCs show PL at room temperature unlike bulk TIX with a short PL decay lifetime in the range of 4 - 12 ns. Reasonable good PLQY

numbers in the range of 4 - 10% in UV-blue region of electromagnetic spectrum are observed. Interestingly, terahertz (THz) carrier dynamics revealed high carrier mobilities and diffusion lengths suggesting defect tolerant nature of our TIX NCs. These TIX NCs can be explored for lasing in UV-blue region of electromagnetic spectrum. High toxicity of Tl must be considered before handling these TIX NCs.

Future directions

Magneto-optical properties of Ln^{3+} ($\text{Ln}^{3+} = \text{Tb}^{3+}, \text{Dy}^{3+}, \text{Ho}^{3+}, \text{Er}^{3+}$) doped CsPbX_3 perovskite NCs

So far, magneto-optical properties have been explored in transition metal ion doped semiconductor NCs.¹¹⁻¹³ For example Mn^{2+} doped CdSe NCs show Zeeman splitting of excitonic PL at low temperatures ~ 4 K at zero external magnetic fields due to dopant-carrier exchange interactions.¹⁴ Mn^{2+} ion with net magnetic moment corresponding to five unpaired electrons splits excitonic PL of CdSe NC (see Figure 1.4a-b in the introduction chapter), but poor signal to noise ratio signifies weaker exchange interactions.¹⁴ Similarly, light or electrical bias induced magnetization in Mn-doped CdSe or CdSe/CdS core/shell NCs respectively were pronounced at low temperature upto 50 K.¹²⁻¹³ These observations suggest weaker dopant-carrier exchange interactions which become pronounced at only lower temperatures.

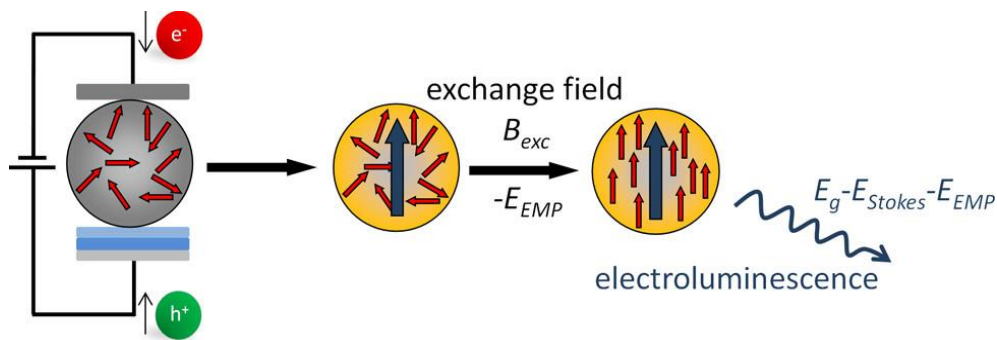


Figure 1: (a) Schematics showing principle of exciton-magnetic polaron (EMP) formation through electrical biasing in a single NC doped with magnetic ions. Initially magnetic moments are randomly organized and upon injecting electron and hole in NC across two ends, exciton formation takes place. Exchange interaction (B_{exc}) of excitons and magnetic moments of dopant ions result into net overall magnetic moment in absence of external magnetic field. Photon emission during or after EMP formation is red shifted compared to excitonic emission by energy difference of (E_{EMP}) and increases with decrease in temperature. This emission (electroluminescence in above case) can be used as probe to see this EMP formation. The figure has been reprinted with permission from ref. 12. Copyright 2017 American Chemical Society.

One way to enhance these dopant-carrier interactions is choosing magnetic dopant with higher magnetic moment than that of Mn^{2+} ion. Ln^{3+} based dopants, where $\text{Ln}^{3+} = \text{Tb}^{3+}, \text{Dy}^{3+},$

Ho^{3+} , and Er^{3+} are ideal choices which have magnetic moment per ion nearly double than transition metal based Mn^{2+} ion. But tetrahedral coordination environment in semiconductor host such as CdSe, GaAs, and Si makes Ln^{3+} doping challenging in these hosts. Interestingly, the octahedral coordination requirement of Ln^{3+} is well satisfied by CsPbX_3 perovskite semiconductors. Therefore, one direct future outlook is to examine the magneto-optical properties of Ln^{3+} doped CsPbX_3 perovskite semiconductor NCs with scope of stronger exchange interaction compared to Mn-doped CdSe NCs. For example, Figure 1 schematically shows the principle of electrical bias induced magnetization in magnetic ion doped NC. Initially magnetic moments of dopant ion are aligned in random direction with zero net moment of magnetization. Injecting electron and hole across two electrodes leads to formation of excitons see middle schematics in Figure 1. Light can also be used rather than electrical bias to generate the excitons. Exchange interaction (B_{exc}) of excitons with magnetic dopants then aligns magnetic moments of all dopants in one direction resulting into non-zero net magnetic moment in NC (see right schematics in Figure 1). This interaction between exciton and magnetic dopant leads to the exciton magnetic polaron (EMP) formation. During or after EMP formation takes place, photon emission (electroluminescence in case of electrical biasing) can occur. Emission involving formation of EMP is red shifted in energy compared to excitonic emission by a difference of EMP formation energy (E_{EMP}). Also, the red shift increases by decreasing temperature. Thus, electroluminescence emission energy as a function of temperature can be used as the probe to examine this EMP formation. It has been observed in Mn^{2+} doped CdSe/CdS core/shell NCs that maximum energy gained in completely aligning all ensemble Mn^{2+} moments with exchange fields ($E_{\text{EMP}}^{\text{sat}}$) is 14 meV and is less than room temperature ~ 25 meV.¹² This $E_{\text{EMP}}^{\text{sat}}$ energy is expected to be higher with the combination of Ln^{3+} based magnetic dopants and CsPbX_3 perovskite NCs based host. Strong quantum confinement in Ln^{3+} doped CsPbX_3 NCs will be desired to further increase the dopant-carrier exchange interactions. Overall, CsPbX_3 perovskite NCs doped with Ln^{3+} based magnetic dopants have scope of exhibiting stronger dopant-carrier exchange interactions and need to be explored. One can quickly realize the efficacy of Ln^{3+} based magnetic ion interaction with charge carrier of doped CsPbX_3 perovskite NCs and their practical implication in spintronics or solotronics devices.¹¹

Yb-doped CsPbX_3 perovskite for future NIR laser, sensors

Yb^{3+} doping in CsPbX_3 perovskite NC host has seen tremendous success in terms of high PLQY observed for NIR Yb-emission. Prior report on Yb^{3+} doping in CsPbCl_3 perovskite

NCs and another recent report on CsPb(Cl_{1-x}Br_x)₃ perovskite thin films suggest Yb-emission PLQY in the range of 135-190% in NIR region (~990 nm) through quantum cutting phenomenon.¹⁵ Thus, one can explore these Yb-doped CsPbX₃ perovskite/NCs for near-infrared LEDs and proximity or ON/OFF sensors benefitting from this quantum cutting phenomenon.

References:

1. Protesescu, L.; Yakunin, S.; Bodnarchuk, M. I.; Krieg, F.; Caputo, R.; Hendon, C. H.; Yang, R. X.; Walsh, A.; Kovalenko, M. V. Nanocrystals of Cesium Lead Halide Perovskites (CsPbX₃, X = Cl, Br, and I): Novel Optoelectronic Materials Showing Bright Emission with Wide Color Gamut. *Nano Lett.* **2015**, *15*, 3692-3696.
2. Pradhan, N.; Das Adhikari, S.; Nag, A.; Sarma, D. D. Luminescence, Plasmonic, and Magnetic Properties of Doped Semiconductor Nanocrystals. *Angew. Chem., Int. Ed.* **2017**, *56*, 7038-7054.
3. Zou, S., et al. Stabilizing Cesium Lead Halide Perovskite Lattice through Mn(II) Substitution for Air-Stable Light-Emitting Diodes. *J. Am. Chem. Soc.* **2017**, *139*, 11443-11450.
4. Akkerman, Q. A.; Meggiolaro, D.; Dang, Z.; De Angelis, F.; Manna, L. Fluorescent Alloy CsPb_xMn_{1-x}I₃ Perovskite Nanocrystals with High Structural and Optical Stability. *ACS Energy Lett.* **2017**, *2*, 2183-2186.
5. Wang, F.; Liu, X. Recent Advances in the Chemistry of Lanthanide-Doped Upconversion Nanocrystals. *Chem. Soc. Rev.* **2009**, *38*, 976-989.
6. Rath, A. K.; Bhaumik, S.; Pal, A. J. Mn-Doped Nanocrystals in Light-Emitting Diodes: Energy-Transfer to Obtain Electroluminescence from Quantum Dots. *App. Phys. Lett.* **2010**, *97*, 113502.
7. Meinardi, F.; Akkerman, Q. A.; Bruni, F.; Park, S.; Mauri, M.; Dang, Z.; Manna, L.; Brovelli, S. Doped Halide Perovskite Nanocrystals for Reabsorption-Free Luminescent Solar Concentrators. *ACS Energy Lett.* **2017**, *2*, 2368-2377.
8. Wang, Q.; Zhang, X.; Jin, Z.; Zhang, J.; Gao, Z.; Li, Y.; Liu, S. F. Energy-Down-Shift CsPbCl₃:Mn Quantum Dots for Boosting the Efficiency and Stability of Perovskite Solar Cells. *ACS Energy Lett.* **2017**, *2*, 1479-1486.
9. Parobek, D.; Roman, B. J.; Dong, Y.; Jin, H.; Lee, E.; Sheldon, M.; Son, D. H. Exciton-to-Dopant Energy Transfer in Mn-Doped Cesium Lead Halide Perovskite Nanocrystals. *Nano Lett.* **2016**, *16*, 7376-7380.

10. Liu, W.; Lin, Q.; Li, H.; Wu, K.; Robel, I.; Pietryga, J. M.; Klimov, V. I. Mn²⁺-Doped Lead Halide Perovskite Nanocrystals with Dual-Color Emission Controlled by Halide Content. *J. Am. Chem. Soc.* **2016**, *138*, 14954-14961.
11. Beaulac, R.; Archer, P. I.; Ochsenein, S. T.; Gamelin, D. R. Mn²⁺-Doped CdSe Quantum Dots: New Inorganic Materials for Spin-Electronics and Spin-Photonics. *Adv. Funct. Mater.* **2008**, *18*, 3873-3891.
12. Muckel, F.; Barrows, C. J.; Graf, A.; Schmitz, A.; Erickson, C. S.; Gamelin, D. R.; Bacher, G. Current-Induced Magnetic Polarons in a Colloidal Quantum-Dot Device. *Nano Lett.* **2017**, *17*, 4768-4773.
13. Beaulac, R.; Schneider, L.; Archer, P. I.; Bacher, G.; Gamelin, D. R. Light-Induced Spontaneous Magnetization in Doped Colloidal Quantum Dots. *Science* **2009**, *325*, 973-976.
14. Fainblat, R.; Barrows, C. J.; Hopmann, E.; Siebeneicher, S.; Vlaskin, V. A.; Gamelin, D. R.; Bacher, G. Giant Excitonic Exchange Splittings at Zero Field in Single Colloidal CdSe Quantum Dots Doped with Individual Mn²⁺ Impurities. *Nano Lett.* **2016**, *16*, 6371-6377.
15. Milstein, T. J.; Kroupa, D. M.; Gamelin, D. R. Picosecond Quantum Cutting Generates Photoluminescence Quantum Yields over 100% in Ytterbium-Doped CsPbCl₃ Nanocrystals. *Nano Lett.* **2018**, *18*, 3792-3799.

List of Publications

Included in Thesis

- 1) **Wasim J. Mir**, Abhishek Swarnkar, Rituraj Sharma, Aditya Katti, K. V. Adarsh, Angshuman Nag. Origin of Unusual Excitonic Absorption and Emission from Colloidal Ag₂S Nanocrystals: Ultrafast Photophysics and Solar Cell. *J. Phys. Chem. Lett.* **2015**, *6*, 3915–3922.
- 2) **Wasim J. Mir**, Metikoti Jagadeeswararao, Shyamashis Das, and Angshuman Nag. Colloidal Mn-Doped Cesium Lead Halide Perovskite Nanoplatelets. *ACS Energy Lett.* **2017**, *2*, 537–543.
- 3) **Wasim J. Mir**, Avinash Warankar, Ashutosh Acharya, Shyamashis Das, Pankaj Mandal, Angshuman Nag. Colloidal Thallium Halide Nanocrystals with Reasonable Luminescence, Carrier Mobility and Diffusion Length. *Chem. Sci.* **2017**, *8*, 4602-4611.
- 4) **Wasim J. Mir**, Yogesh Mahor, Amruta Lohar, Metikoti Jagadeeswararao, Shyamashis Das, Shailaja Mahamuni, Angshuman Nag. Postsynthesis Doping of Mn and Yb into CsPbX₃ (X = Cl, Br, or I) Perovskite Nanocrystals for Downconversion Emission. *Chem. Mater.* **2018**, *30*, 8170–8178.
- 5) **Wasim J. Mir**, Clément Livache, Nicolas Goubet, Bertille Martinez, Amardeep Jagtap, Audrey Chu, Nathan Coutard, Hervé Cruguel, Thierry Barisien, Sandrine Ithurria, Angshuman Nag, Benoit Dubertret, Abdelkarim Ouerghi, Mathieu G. Silly, Emmanuel Lhuillier. Strategy to Overcome Recombination Limited Photocurrent Generation in CsPbX₃ Nanocrystal Arrays *App. Phys. Lett.* **2018**, *112*, 113503.
- 6) **Wasim J. Mir**, Abhishek Swarnkar, Angshuman Nag. Postsynthesis Mn-Doping in CsPbI₃ Nanocrystals to Stabilize Black Perovskite Phase *Nanoscale* **2019**, *11*, 4278-4286.

Not included in Thesis

- 1) **Wasim J. Mir**, Alexandre Assouline, Clément Livache, Bertille Martinez, Nicolas Goubet, Xiang Zhen Xu, Gilles Patriarche, Sandrine Ithurria, Hervé Aubin, Emmanuel Lhuillier. Electronic Properties of (Sb;Bi)₂Te₃ Colloidal Heterostructured Nanoplates Down to the Single Particle Level. *Sci. Rep.* **2017**, *7*, 9647.
- 2) Abhishek Swarnkar, **Wasim J. Mir**, Angshuman Nag. Can B-Site Doping or Alloying Improve Thermal- and Phase-Stability of All-Inorganic CsPbX₃ (X = Cl, Br, I) Perovskites? *ACS Energy Lett.* **2018**, *3*, 286–289.

- 3) Anirban Mondal, J. Aneesh, Vikash Kumar Ravi, Rituraj Sharma, **Wasim J. Mir**, Mathew C Beard, Angshuman Nag, and K. V. Adarsh. Ultrafast Exciton Many-Body Interactions and Hot-Phonon Bottleneck in Colloidal Cesium Lead Halide Perovskite Nanocrystals. *Phy. Rev. B.* **2018**, *98*, 115418.
- 4) Shrreya Krishnamurthy, Rounak Naphade, **Wasim J. Mir**, Suresh Gosavi, Sudip Chakraborty, Ramanathan Vaidhyanathan, Satishchandra Ogale. Molecular and Self-Trapped Excitonic Contributions to the Broadband Luminescence in Diamine-Based Low-Dimensional Hybrid Perovskite Systems. *Adv. Opt. Mater.* **2018**, *6*, 1800751.
- 5) Abhishek Swarnkar, **Wasim J. Mir**, Rayan Chakraborty, Metikoti Jagadeeswararao, Tariq Sheikh, Angshuman Nag. Are Chalcogenide Perovskites an Emerging Class of Semiconductors for Optoelectronic Properties and Solar Cell? *Chem. Mater.* **2019**, *31*, 565–575.



RightsLink®

[Home](#)[Create Account](#)[Help](#)

ACS Publications Title:
Most Trusted. Most Cited. Most Read.

Origin of Unusual Excitonic Absorption and Emission from Colloidal Ag₂S Nanocrystals: Ultrafast Photophysics and Solar Cell

Author: Wasim J. Mir, Abhishek Swarnkar, Rituraj Sharma, et al

Publication: Journal of Physical Chemistry Letters

Publisher: American Chemical Society

Date: Oct 1, 2015

Copyright © 2015, American Chemical Society

LOGIN

If you're a **copyright.com user**, you can login to RightsLink using your copyright.com credentials.

Already a **RightsLink user** or want to [learn more?](#)

PERMISSION/LICENSE IS GRANTED FOR YOUR ORDER AT NO CHARGE

This type of permission/license, instead of the standard Terms & Conditions, is sent to you because no fee is being charged for your order. Please note the following:

- Permission is granted for your request in both print and electronic formats, and translations.
- If figures and/or tables were requested, they may be adapted or used in part.
- Please print this page for your records and send a copy of it to your publisher/graduate school.
- Appropriate credit for the requested material should be given as follows: "Reprinted (adapted) with permission from (COMPLETE REFERENCE CITATION). Copyright (YEAR) American Chemical Society." Insert appropriate information in place of the capitalized words.
- One-time permission is granted only for the use specified in your request. No additional uses are granted (such as derivative works or other editions). For any other uses, please submit a new request.

If credit is given to another source for the material you requested, permission must be obtained from that source.

[BACK](#)[CLOSE WINDOW](#)

Copyright © 2019 [Copyright Clearance Center, Inc.](#) All Rights Reserved. [Privacy statement](#). [Terms and Conditions](#). Comments? We would like to hear from you. E-mail us at customercare@copyright.com

[Back to view orders](#)

[Copy order](#)



Print this page
Print terms & conditions
Print citation information
([What's this?](#))

Confirmation Number: 11788236
Order Date: 02/03/2019

Customer Information

Customer: Wasim Mir
Account Number: 3001391601
Organization: Wasim Mir
Email:
wasimjeelani.mir@students.iiserpune.ac.in
Phone: +91 7006031347

Search order details by:

Go


This is not an invoice

Order Details

Chemical Society reviews

Billing Status:
N/A

Order detail ID: 71794433
ISSN: 1460-4744
Publication Type: e-Journal
Volume:
Issue:
Start page:
Publisher: ROYAL SOCIETY OF CHEMISTRY
Author/Editor: Royal Society of Chemistry (Great Britain)

Permission Status:  **Granted**
Permission type: Republish or display content
Type of use: Thesis/Dissertation
Order License Id: 4521470544600

[Hide details](#)

Requestor type	Publisher, not-for-profit
Format	Print, Electronic
Portion	chart/graph/table/figure
Number of charts/graphs/tables/figures	1
The requesting person/organization	Wasim Jeelani Mir
Title or numeric reference of the portion(s)	Chapter 1
Title of the article or chapter the portion is from	surface to volume ratio
Editor of portion(s)	N/A
Author of portion(s)	Wasim Jeelani Mir
Volume of serial or monograph	N/A
Page range of portion	9-10
Publication date of portion	May 2019
Rights for	Main product

Duration of use	Life of current edition
Creation of copies for the disabled	no
With minor editing privileges	no
For distribution to	Worldwide
In the following language(s)	Original language of publication
With incidental promotional use	no
Lifetime unit quantity of new product	More than 2,000,000
Title	Synthesis and Photophysics of Mn- and Yb-doped Colloidal CsPbX ₃ (X= Cl, Br, I) Perovskite and Analogous TlX Nanocrystals
Institution name	n/a
Expected presentation date	Feb 2019

Note: This item was invoiced separately through our **RightsLink service**. [More info](#)

\$ 0.00

Total order items: 1

Order Total: \$0.00



Title: Giant Excitonic Exchange Splittings at Zero Field in Single Colloidal CdSe Quantum Dots Doped with Individual Mn²⁺ Impurities

Author: Rachel Fainblat, Charles J. Barrows, Eric Hopmann, et al

Publication: Nano Letters

Publisher: American Chemical Society

Date: Oct 1, 2016

Copyright © 2016, American Chemical Society

LOGIN

If you're a **copyright.com user**, you can login to RightsLink using your copyright.com credentials.

Already a **RightsLink user** or want to [learn more?](#)

PERMISSION/LICENSE IS GRANTED FOR YOUR ORDER AT NO CHARGE

This type of permission/license, instead of the standard Terms & Conditions, is sent to you because no fee is being charged for your order. Please note the following:

- Permission is granted for your request in both print and electronic formats, and translations.
- If figures and/or tables were requested, they may be adapted or used in part.
- Please print this page for your records and send a copy of it to your publisher/graduate school.
- Appropriate credit for the requested material should be given as follows: "Reprinted (adapted) with permission from (COMPLETE REFERENCE CITATION). Copyright (YEAR) American Chemical Society." Insert appropriate information in place of the capitalized words.
- One-time permission is granted only for the use specified in your request. No additional uses are granted (such as derivative works or other editions). For any other uses, please submit a new request.

If credit is given to another source for the material you requested, permission must be obtained from that source.

[BACK](#)[CLOSE WINDOW](#)



RightsLink®

[Home](#)[Account Info](#)[Help](#)

Title: Interface Engineering of Mn-Doped ZnSe-Based Core/Shell Nanowires for Tunable Host-Dopant Coupling

Logged in as:
Wasim Mir
Account #:
3001391601

Author: Zhi-Jun Li, Elan Hofman, Amanda Blaker, et al

[LOGOUT](#)

Publication: ACS Nano

Publisher: American Chemical Society

Date: Dec 1, 2017

Copyright © 2017, American Chemical Society

PERMISSION/LICENSE IS GRANTED FOR YOUR ORDER AT NO CHARGE

This type of permission/license, instead of the standard Terms & Conditions, is sent to you because no fee is being charged for your order. Please note the following:

- Permission is granted for your request in both print and electronic formats, and translations.
- If figures and/or tables were requested, they may be adapted or used in part.
- Please print this page for your records and send a copy of it to your publisher/graduate school.
- Appropriate credit for the requested material should be given as follows: "Reprinted (adapted) with permission from (COMPLETE REFERENCE CITATION). Copyright (YEAR) American Chemical Society." Insert appropriate information in place of the capitalized words.
- One-time permission is granted only for the use specified in your request. No additional uses are granted (such as derivative works or other editions). For any other uses, please submit a new request.

If credit is given to another source for the material you requested, permission must be obtained from that source.

[BACK](#)[CLOSE WINDOW](#)

Copyright © 2019 [Copyright Clearance Center, Inc.](#) All Rights Reserved. [Privacy statement.](#) [Terms and Conditions.](#) Comments? We would like to hear from you. E-mail us at customercare@copyright.com



RightsLink®

[Home](#)[Account Info](#)[Help](#)

Title: Doped Halide Perovskite Nanocrystals for Reabsorption-Free Luminescent Solar Concentrators

Logged in as:

Wasim Mir

Account #:
3001391601

Author: Francesco Meinardi, Quinten A. Akkerman, Francesco Bruni, et al

[LOGOUT](#)

Publication: ACS Energy Letters

Publisher: American Chemical Society

Date: Oct 1, 2017

Copyright © 2017, American Chemical Society

PERMISSION/LICENSE IS GRANTED FOR YOUR ORDER AT NO CHARGE

This type of permission/license, instead of the standard Terms & Conditions, is sent to you because no fee is being charged for your order. Please note the following:

- Permission is granted for your request in both print and electronic formats, and translations.
- If figures and/or tables were requested, they may be adapted or used in part.
- Please print this page for your records and send a copy of it to your publisher/graduate school.
- Appropriate credit for the requested material should be given as follows: "Reprinted (adapted) with permission from (COMPLETE REFERENCE CITATION). Copyright (YEAR) American Chemical Society." Insert appropriate information in place of the capitalized words.
- One-time permission is granted only for the use specified in your request. No additional uses are granted (such as derivative works or other editions). For any other uses, please submit a new request.

If credit is given to another source for the material you requested, permission must be obtained from that source.

[BACK](#)[CLOSE WINDOW](#)

Copyright © 2019 [Copyright Clearance Center, Inc.](#) All Rights Reserved. [Privacy statement.](#) [Terms and Conditions.](#) Comments? We would like to hear from you. E-mail us at customercare@copyright.com



RightsLink®

[Home](#)
[Account Info](#)
[Help](#)


Title: Highly efficient luminescent solar concentrators based on earth-abundant indirect-bandgap silicon quantum dots

Author: Francesco Meinardi, Samantha Ehrenberg, Lorena Dharmo, Francesco Carulli, Michele Mauri et al.

Publication: Nature Photonics

Publisher: Springer Nature

Date: Feb 20, 2017

Copyright © 2017, Springer Nature

Logged in as:
Wasim Mir
Account #:
3001391601

[LOGOUT](#)

Order Completed

Thank you for your order.

This Agreement between Wasim J. Mir ("You") and Springer Nature ("Springer Nature") consists of your license details and the terms and conditions provided by Springer Nature and Copyright Clearance Center.

Your confirmation email will contain your order number for future reference.

[printable details](#)

License Number	4521460924590
License date	Feb 03, 2019
Licensed Content Publisher	Springer Nature
Licensed Content Publication	Nature Photonics
Licensed Content Title	Highly efficient luminescent solar concentrators based on earth-abundant indirect-bandgap silicon quantum dots
Licensed Content Author	Francesco Meinardi, Samantha Ehrenberg, Lorena Dharmo, Francesco Carulli, Michele Mauri et al.
Licensed Content Date	Feb 20, 2017
Licensed Content Volume	11
Licensed Content Issue	3
Type of Use	Thesis/Dissertation
Requestor type	academic/university or research institute
Format	print and electronic
Portion	figures/tables/illustrations
Number of figures/tables/illustrations	1
High-res required	no
Will you be translating?	no
Circulation/distribution	10,001 to 20,000
Author of this Springer Nature content	no
Title	Synthesis and Photophysics of Mn- and Yb-doped Colloidal CsPbX ₃ (X= Cl, Br, I) Perovskite and Analogous TIX Nanocrystals
Institution name	n/a
Expected presentation date	Feb 2019
Portions	Figure 1a
Requestor Location	Wasim J. Mir Hostel 2, IISER Pune campus, Pashan Near Dr. Hommi Bha bha road

2/3/2019

Rightslink® by Copyright Clearance Center

Pune, Maharashtra, Maharashtra 411008
India
Attn: Hostel 2, IISER Pune campus, Pashan

Billing Type

Invoice

Billing address

Hostel 2, IISER Pune campus, Pashan
IISER Pune, Department of Chemistry,
Main Building, Lab 125B
Dr. Homi Bhabha Road, Pashan
PUNE, India 411008
Attn: Wasim Jeelani Mir

Total

0.00 USD

[ORDER MORE](#)

[CLOSE WINDOW](#)

Copyright © 2019 [Copyright Clearance Center, Inc.](#) All Rights Reserved. [Privacy statement.](#) [Terms and Conditions.](#)
Comments? We would like to hear from you. E-mail us at customercare@copyright.com



RightsLink®

[Home](#)[Account Info](#)[Help](#)

Title: Spin-Polarizable Excitonic Luminescence in Colloidal Mn²⁺-Doped CdSe Quantum Dots

Author: Rémi Beaulac, Paul I. Archer, Xinyu Liu, et al

Publication: Nano Letters

Publisher: American Chemical Society

Date: Apr 1, 2008

Copyright © 2008, American Chemical Society

Logged in as:

Wasim Mir

Account #:
3001391601

[LOGOUT](#)

PERMISSION/LICENSE IS GRANTED FOR YOUR ORDER AT NO CHARGE

This type of permission/license, instead of the standard Terms & Conditions, is sent to you because no fee is being charged for your order. Please note the following:

- Permission is granted for your request in both print and electronic formats, and translations.
- If figures and/or tables were requested, they may be adapted or used in part.
- Please print this page for your records and send a copy of it to your publisher/graduate school.
- Appropriate credit for the requested material should be given as follows: "Reprinted (adapted) with permission from (COMPLETE REFERENCE CITATION). Copyright (YEAR) American Chemical Society." Insert appropriate information in place of the capitalized words.
- One-time permission is granted only for the use specified in your request. No additional uses are granted (such as derivative works or other editions). For any other uses, please submit a new request.

If credit is given to another source for the material you requested, permission must be obtained from that source.

[BACK](#)[CLOSE WINDOW](#)

Copyright © 2019 [Copyright Clearance Center, Inc.](#) All Rights Reserved. [Privacy statement](#). [Terms and Conditions](#). Comments? We would like to hear from you. E-mail us at customercare@copyright.com



RightsLink®

[Home](#)
[Account Info](#)
[Help](#)


Title: Mn²⁺-Doped CdSe Quantum Dots: New Inorganic Materials for Spin-Electronics and Spin-Photonics

Author: Rémi Beaulac, Paul I. Archer, Stefan T. Ochsenbein, et al

Publication: Advanced Functional Materials

Publisher: John Wiley and Sons

Date: Dec 15, 2008

Copyright © 2008, John Wiley and Sons

Logged in as:

Wasim Mir

Account #:
3001391601

[LOGOUT](#)

Order Completed

Thank you for your order.

This Agreement between Wasim J. Mir ("You") and John Wiley and Sons ("John Wiley and Sons") consists of your license details and the terms and conditions provided by John Wiley and Sons and Copyright Clearance Center.

Your confirmation email will contain your order number for future reference.

[printable details](#)

License Number	4521420527368
License date	Feb 03, 2019
Licensed Content Publisher	John Wiley and Sons
Licensed Content Publication	Advanced Functional Materials
Licensed Content Title	Mn ²⁺ -Doped CdSe Quantum Dots: New Inorganic Materials for Spin-Electronics and Spin-Photonics
Licensed Content Author	Rémi Beaulac, Paul I. Archer, Stefan T. Ochsenbein, et al
Licensed Content Date	Dec 15, 2008
Licensed Content Volume	18
Licensed Content Issue	24
Licensed Content Pages	19
Type of use	Dissertation/Thesis
Requestor type	University/Academic
Format	Print and electronic
Portion	Figure/table
Number of figures/tables	2
Original Wiley figure/table number(s)	Figure1b, Figure 2
Will you be translating?	No
Title of your thesis / dissertation	Synthesis and Photophysics of Mn ⁻ and Yb-doped Colloidal CsPbX ₃ (X= Cl, Br, I) Perovskite and Analogous TIX Nanocrystals
Expected completion date	Feb 2019
Expected size (number of pages)	200
Requestor Location	Wasim J. Mir Hostel 2, IISER Pune campus, Pashan Near Dr. Hommi Bha bha road Pune, Maharashtra, Maharashtra 411008 India Attn: Hostel 2, IISER Pune campus, Pashan

Publisher Tax ID EU826007151

Total 0.00 USD

Would you like to purchase the full text of this article? If so, please continue on to the content ordering system located here: [Purchase PDF](#)

If you click on the buttons below or close this window, you will not be able to return to the content ordering system.

ORDER MORE

CLOSE WINDOW

Copyright © 2019 [Copyright Clearance Center, Inc.](#) All Rights Reserved. [Privacy statement.](#) [Terms and Conditions.](#)
Comments? We would like to hear from you. E-mail us at customercare@copyright.com



RightsLink®

[Home](#)[Account Info](#)[Help](#)

Title: Doping Lanthanide into Perovskite Nanocrystals: Highly Improved and Expanded Optical Properties

Logged in as:

Wasim Mir

Account #:
3001391601

Author: Gencai Pan, Xue Bai, Dongwen Yang, et al

[LOGOUT](#)

Publication: Nano Letters

Publisher: American Chemical Society

Date: Dec 1, 2017

Copyright © 2017, American Chemical Society

PERMISSION/LICENSE IS GRANTED FOR YOUR ORDER AT NO CHARGE

This type of permission/license, instead of the standard Terms & Conditions, is sent to you because no fee is being charged for your order. Please note the following:

- Permission is granted for your request in both print and electronic formats, and translations.
- If figures and/or tables were requested, they may be adapted or used in part.
- Please print this page for your records and send a copy of it to your publisher/graduate school.
- Appropriate credit for the requested material should be given as follows: "Reprinted (adapted) with permission from (COMPLETE REFERENCE CITATION). Copyright (YEAR) American Chemical Society." Insert appropriate information in place of the capitalized words.
- One-time permission is granted only for the use specified in your request. No additional uses are granted (such as derivative works or other editions). For any other uses, please submit a new request.

If credit is given to another source for the material you requested, permission must be obtained from that source.

[BACK](#)[CLOSE WINDOW](#)

Copyright © 2019 [Copyright Clearance Center, Inc.](#) All Rights Reserved. [Privacy statement.](#) [Terms and Conditions.](#) Comments? We would like to hear from you. E-mail us at customercare@copyright.com



RightsLink®

[Home](#)[Account Info](#)[Help](#)

Title: Picosecond Quantum Cutting Generates Photoluminescence Quantum Yields Over 100% in Ytterbium-Doped CsPbCl₃ Nanocrystals

Logged in as:
Wasim Mir
Account #:
3001391601

[LOGOUT](#)

Author: Tyler J. Milstein, Daniel M. Kroupa, Daniel R. Gamelin

Publication: Nano Letters

Publisher: American Chemical Society

Date: Jun 1, 2018

Copyright © 2018, American Chemical Society

PERMISSION/LICENSE IS GRANTED FOR YOUR ORDER AT NO CHARGE

This type of permission/license, instead of the standard Terms & Conditions, is sent to you because no fee is being charged for your order. Please note the following:

- Permission is granted for your request in both print and electronic formats, and translations.
- If figures and/or tables were requested, they may be adapted or used in part.
- Please print this page for your records and send a copy of it to your publisher/graduate school.
- Appropriate credit for the requested material should be given as follows: "Reprinted (adapted) with permission from (COMPLETE REFERENCE CITATION). Copyright (YEAR) American Chemical Society." Insert appropriate information in place of the capitalized words.
- One-time permission is granted only for the use specified in your request. No additional uses are granted (such as derivative works or other editions). For any other uses, please submit a new request.

If credit is given to another source for the material you requested, permission must be obtained from that source.

[BACK](#)[CLOSE WINDOW](#)

Copyright © 2019 [Copyright Clearance Center, Inc.](#) All Rights Reserved. [Privacy statement](#). [Terms and Conditions](#).
Comments? We would like to hear from you. E-mail us at customercare@copyright.com



RightsLink®

[Home](#)[Account Info](#)[Help](#)

ACS Publications
Most Trusted. Most Cited. Most Read.

Title: Effect of Yb³⁺ on the Crystal Structural Modification and Photoluminescence Properties of GGAG:Ce³⁺

Logged in as:

Wasim Mir

Account #:
3001391601

Author: Zhao-Hua Luo, Yong-Fu Liu, Chang-Hua Zhang, et al

[LOGOUT](#)

Publication: Inorganic Chemistry

Publisher: American Chemical Society

Date: Mar 1, 2016

Copyright © 2016, American Chemical Society

PERMISSION/LICENSE IS GRANTED FOR YOUR ORDER AT NO CHARGE

This type of permission/license, instead of the standard Terms & Conditions, is sent to you because no fee is being charged for your order. Please note the following:

- Permission is granted for your request in both print and electronic formats, and translations.
- If figures and/or tables were requested, they may be adapted or used in part.
- Please print this page for your records and send a copy of it to your publisher/graduate school.
- Appropriate credit for the requested material should be given as follows: "Reprinted (adapted) with permission from (COMPLETE REFERENCE CITATION). Copyright (YEAR) American Chemical Society." Insert appropriate information in place of the capitalized words.
- One-time permission is granted only for the use specified in your request. No additional uses are granted (such as derivative works or other editions). For any other uses, please submit a new request.

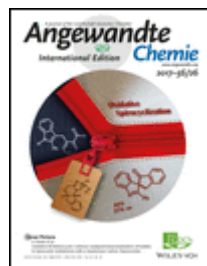
If credit is given to another source for the material you requested, permission must be obtained from that source.

[BACK](#)[CLOSE WINDOW](#)

Copyright © 2019 [Copyright Clearance Center, Inc.](#) All Rights Reserved. [Privacy statement.](#) [Terms and Conditions.](#) Comments? We would like to hear from you. E-mail us at customercare@copyright.com



RightsLink®

[Home](#)
[Account Info](#)
[Help](#)


Title: Colloidal CsPbBr₃ Perovskite Nanocrystals: Luminescence beyond Traditional Quantum Dots

Author: Abhishek Swarnkar, Ramya Chulliyil, Vikash Kumar Ravi, et al

Publication: Angewandte Chemie International Edition

Publisher: John Wiley and Sons

Date: Nov 6, 2015

Copyright © 2015, John Wiley and Sons

Logged in as:
Wasim Mir
Account #:
3001391601

[LOGOUT](#)

Order Completed

Thank you for your order.

This Agreement between Wasim J. Mir ("You") and John Wiley and Sons ("John Wiley and Sons") consists of your license details and the terms and conditions provided by John Wiley and Sons and Copyright Clearance Center.

Your confirmation email will contain your order number for future reference.

[printable details](#)

License Number	4521421091918
License date	Feb 03, 2019
Licensed Content Publisher	John Wiley and Sons
Licensed Content Publication	Angewandte Chemie International Edition
Licensed Content Title	Colloidal CsPbBr ₃ Perovskite Nanocrystals: Luminescence beyond Traditional Quantum Dots
Licensed Content Author	Abhishek Swarnkar, Ramya Chulliyil, Vikash Kumar Ravi, et al
Licensed Content Date	Nov 6, 2015
Licensed Content Volume	54
Licensed Content Issue	51
Licensed Content Pages	5
Type of use	Dissertation/Thesis
Requestor type	University/Academic
Format	Print and electronic
Portion	Figure/table
Number of figures/tables	1
Original Wiley figure/table number(s)	Figure 2a
Will you be translating?	No
Title of your thesis / dissertation	Synthesis and Photophysics of Mn- and Yb-doped Colloidal CsPbX ₃ (X= Cl, Br, I) Perovskite and Analogous TIX Nanocrystals
Expected completion date	Feb 2019
Expected size (number of pages)	200
Requestor Location	Wasim J. Mir Hostel 2, IISER Pune campus, Pashan Near Dr. Hommi Bha bha road Pune, Maharashtra, Maharashtra 411008

	India
	Attn: Hostel 2, IISER Pune campus, Pashan
Publisher Tax ID	EU826007151
Total	0.00 USD

Would you like to purchase the full text of this article? If so, please continue on to the content ordering system located here: [Purchase PDF](#)

If you click on the buttons below or close this window, you will not be able to return to the content ordering system.

ORDER MORE

CLOSE WINDOW

Copyright © 2019 [Copyright Clearance Center, Inc.](#) All Rights Reserved. [Privacy statement.](#) [Terms and Conditions.](#)
Comments? We would like to hear from you. E-mail us at customercare@copyright.com



RightsLink®

[Home](#)
[Account Info](#)
[Help](#)


Title: Genesis, challenges and opportunities for colloidal lead halide perovskite nanocrystals
Author: Quinten A. Akkerman et al
Publication: Nature Materials
Publisher: Springer Nature
Date: Feb 19, 2018
 Copyright © 2018, Springer Nature

Logged in as:
 Wasim Mir
 Account #:
 3001391601

[LOGOUT](#)

Order Completed

Thank you for your order.

This Agreement between Wasim J. Mir ("You") and Springer Nature ("Springer Nature") consists of your license details and the terms and conditions provided by Springer Nature and Copyright Clearance Center.

Your confirmation email will contain your order number for future reference.

[printable details](#)

License Number	4521430173071
License date	Feb 03, 2019
Licensed Content Publisher	Springer Nature
Licensed Content Publication	Nature Materials
Licensed Content Title	Genesis, challenges and opportunities for colloidal lead halide perovskite nanocrystals
Licensed Content Author	Quinten A. Akkerman et al
Licensed Content Date	Feb 19, 2018
Type of Use	Thesis/Dissertation
Requestor type	academic/university or research institute
Format	print and electronic
Portion	figures/tables/illustrations
Number of figures/tables/illustrations	1
High-res required	no
Will you be translating?	no
Circulation/distribution	10,001 to 20,000
Author of this Springer Nature content	no
Title	Synthesis and Photophysics of Mn- and Yb-doped Colloidal CsPbX ₃ (X= Cl, Br, I) Perovskite and Analogous TIX Nanocrystals
Institution name	n/a
Expected presentation date	Feb 2019
Portions	Figure 2b
Requestor Location	Wasim J. Mir Hostel 2, IISER Pune campus, Pashan Near Dr. Hommi Bha bha road Pune, Maharashtra, Maharashtra 411008 India Attn: Hostel 2, IISER Pune campus, Pashan
Billing Type	Invoice
Billing address	Hostel 2, IISER Pune campus, Pashan IISER Pune, Department of Chemistry, Main Building, Lab 125B Dr. Homi Bhabha Road, Pashan

2/3/2019

Rightslink® by Copyright Clearance Center

PUNE, India 411008
Attn: Wasim Jeelani Mir

Total

0.00 USD

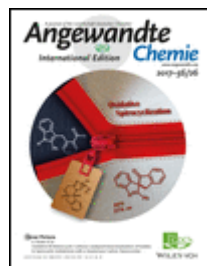
ORDER MORE

CLOSE WINDOW

Copyright © 2019 [Copyright Clearance Center, Inc.](#) All Rights Reserved. [Privacy statement](#). [Terms and Conditions](#).
Comments? We would like to hear from you. E-mail us at customer care@copyright.com



RightsLink®

[Home](#)
[Account Info](#)
[Help](#)


Title: Luminescence, Plasmonic, and Magnetic Properties of Doped Semiconductor Nanocrystals

Author: Narayan Pradhan, Samrat Das Adhikari, Angshuman Nag, et al

Publication: Angewandte Chemie International Edition

Publisher: John Wiley and Sons

Date: May 23, 2017

Copyright © 2017, John Wiley and Sons

Logged in as:
Wasim Mir
Account #:
3001391601

[LOGOUT](#)

Order Completed

Thank you for your order.

This Agreement between Wasim J. Mir ("You") and John Wiley and Sons ("John Wiley and Sons") consists of your license details and the terms and conditions provided by John Wiley and Sons and Copyright Clearance Center.

Your confirmation email will contain your order number for future reference.

[printable details](#)

License Number	4521471074934
License date	Feb 03, 2019
Licensed Content Publisher	John Wiley and Sons
Licensed Content Publication	Angewandte Chemie International Edition
Licensed Content Title	Luminescence, Plasmonic, and Magnetic Properties of Doped Semiconductor Nanocrystals
Licensed Content Author	Narayan Pradhan, Samrat Das Adhikari, Angshuman Nag, et al
Licensed Content Date	May 23, 2017
Licensed Content Volume	56
Licensed Content Issue	25
Licensed Content Pages	17
Type of use	Dissertation/Thesis
Requestor type	University/Academic
Format	Print and electronic
Portion	Figure/table
Number of figures/tables	1
Original Wiley figure/table number(s)	Figure 1
Will you be translating?	No
Title of your thesis / dissertation	Synthesis and Photophysics of Mn- and Yb-doped Colloidal CsPbX ₃ (X= Cl, Br, I) Perovskite and Analogous TIX Nanocrystals
Expected completion date	Feb 2019
Expected size (number of pages)	200
Requestor Location	Wasim J. Mir Hostel 2, IISER Pune campus, Pashan Near Dr. Hommi Bha bha road Pune, Maharashtra, Maharashtra 411008 India Attn: Hostel 2, IISER Pune campus, Pashan
Publisher Tax ID	EU826007151

Total

0.00 USD

Would you like to purchase the full text of this article? If so, please continue on to the content ordering system located here: [Purchase PDF](#)

If you click on the buttons below or close this window, you will not be able to return to the content ordering system.

ORDER MORE

CLOSE WINDOW

Copyright © 2019 [Copyright Clearance Center, Inc.](#) All Rights Reserved. [Privacy statement](#). [Terms and Conditions](#).
Comments? We would like to hear from you. E-mail us at customercare@copyright.com



RightsLink®

[Home](#)[Account Info](#)[Help](#)

Title: Design of Lead-Free Inorganic Halide Perovskites for Solar Cells via Cation-Transmutation

Author: Xin-Gang Zhao, Ji-Hui Yang, Yuhao Fu, et al

Publication: Journal of the American Chemical Society

Publisher: American Chemical Society

Date: Feb 1, 2017

Copyright © 2017, American Chemical Society

Logged in as:

Wasim Mir

Account #:
3001391601

[LOGOUT](#)

PERMISSION/LICENSE IS GRANTED FOR YOUR ORDER AT NO CHARGE

This type of permission/license, instead of the standard Terms & Conditions, is sent to you because no fee is being charged for your order. Please note the following:

- Permission is granted for your request in both print and electronic formats, and translations.
- If figures and/or tables were requested, they may be adapted or used in part.
- Please print this page for your records and send a copy of it to your publisher/graduate school.
- Appropriate credit for the requested material should be given as follows: "Reprinted (adapted) with permission from (COMPLETE REFERENCE CITATION). Copyright (YEAR) American Chemical Society." Insert appropriate information in place of the capitalized words.
- One-time permission is granted only for the use specified in your request. No additional uses are granted (such as derivative works or other editions). For any other uses, please submit a new request.

If credit is given to another source for the material you requested, permission must be obtained from that source.

[BACK](#)[CLOSE WINDOW](#)

Copyright © 2019 [Copyright Clearance Center, Inc.](#) All Rights Reserved. [Privacy statement.](#) [Terms and Conditions.](#) Comments? We would like to hear from you. E-mail us at customercare@copyright.com



RightsLink®

[Home](#)[Create Account](#)[Help](#)

ACS Publications
Most Trusted. Most Cited. Most Read.

Title: Postsynthesis Doping of Mn and Yb into CsPbX₃ (X = Cl, Br, or I) Perovskite Nanocrystals for Downconversion Emission

Author: Wasim J. Mir, Yogesh Mahor, Amruta Lohar, et al

Publication: Chemistry of Materials

Publisher: American Chemical Society

Date: Nov 1, 2018

Copyright © 2018, American Chemical Society

LOGIN

If you're a **copyright.com user**, you can login to RightsLink using your copyright.com credentials. Already a **RightsLink user** or want to [learn more?](#)

PERMISSION/LICENSE IS GRANTED FOR YOUR ORDER AT NO CHARGE

This type of permission/license, instead of the standard Terms & Conditions, is sent to you because no fee is being charged for your order. Please note the following:

- Permission is granted for your request in both print and electronic formats, and translations.
- If figures and/or tables were requested, they may be adapted or used in part.
- Please print this page for your records and send a copy of it to your publisher/graduate school.
- Appropriate credit for the requested material should be given as follows: "Reprinted (adapted) with permission from (COMPLETE REFERENCE CITATION). Copyright (YEAR) American Chemical Society." Insert appropriate information in place of the capitalized words.
- One-time permission is granted only for the use specified in your request. No additional uses are granted (such as derivative works or other editions). For any other uses, please submit a new request.

[BACK](#)[CLOSE WINDOW](#)

Copyright © 2019 [Copyright Clearance Center, Inc.](#) All Rights Reserved. [Privacy statement.](#) [Terms and Conditions.](#) Comments? We would like to hear from you. E-mail us at customercare@copyright.com



RightsLink®

[Home](#)[Account Info](#)[Help](#)

Title: Current-Induced Magnetic Polarons in a Colloidal Quantum-Dot Device

Author: Franziska Muckel, Charles J. Barrows, Arthur Graf, et al

Publication: Nano Letters

Publisher: American Chemical Society

Date: Aug 1, 2017

Copyright © 2017, American Chemical Society

Logged in as:

Wasim Mir

Account #:
3001391601

[LOGOUT](#)

PERMISSION/LICENSE IS GRANTED FOR YOUR ORDER AT NO CHARGE

This type of permission/license, instead of the standard Terms & Conditions, is sent to you because no fee is being charged for your order. Please note the following:

- Permission is granted for your request in both print and electronic formats, and translations.
- If figures and/or tables were requested, they may be adapted or used in part.
- Please print this page for your records and send a copy of it to your publisher/graduate school.
- Appropriate credit for the requested material should be given as follows: "Reprinted (adapted) with permission from (COMPLETE REFERENCE CITATION). Copyright (YEAR) American Chemical Society." Insert appropriate information in place of the capitalized words.
- One-time permission is granted only for the use specified in your request. No additional uses are granted (such as derivative works or other editions). For any other uses, please submit a new request.

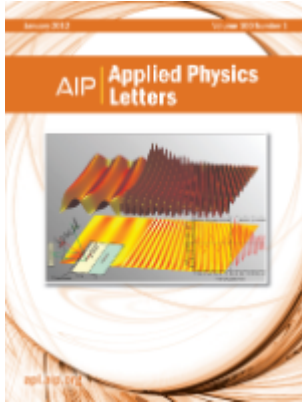
If credit is given to another source for the material you requested, permission must be obtained from that source.

[BACK](#)[CLOSE WINDOW](#)

Copyright © 2019 [Copyright Clearance Center, Inc.](#) All Rights Reserved. [Privacy statement.](#) [Terms and Conditions.](#) Comments? We would like to hear from you. E-mail us at customercare@copyright.com



RightsLink®

[Home](#)
[Account Info](#)
[Help](#)


Title: Strategy to overcome recombination limited photocurrent generation in CsPbX₃ nanocrystal arrays

Author: Wasim J. Mir, Clément Livache, Nicolas Goubet, et al

Publication: Applied Physics Letters

Volume/Issue: 112/11

Publisher: AIP Publishing

Date: Mar 12, 2018

Page Count: 5

Rights managed by AIP Publishing.

Logged in as:
Wasim Mir
Account #:
3001391601

[LOGOUT](#)

Order Completed

Thank you for your order.

This Agreement between Wasim J. Mir ("You") and AIP Publishing ("AIP Publishing") consists of your license details and the terms and conditions provided by AIP Publishing and Copyright Clearance Center.

Your confirmation email will contain your order number for future reference.

[printable details](#)

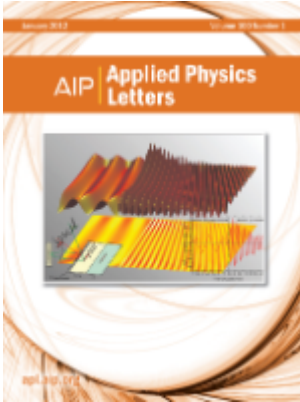
License Number	4521411436034
License date	Feb 03, 2019
Licensed Content Publisher	AIP Publishing
Licensed Content Publication	Applied Physics Letters
Licensed Content Title	Strategy to overcome recombination limited photocurrent generation in CsPbX ₃ nanocrystal arrays
Licensed Content Author	Wasim J. Mir, Clément Livache, Nicolas Goubet, et al
Licensed Content Date	Mar 12, 2018
Licensed Content Volume	112
Licensed Content Issue	11
Requestor type	Author (original article)
Format	Print and electronic
Portion	Excerpt (> 800 words)
Requestor Location	Wasim J. Mir Hostel 2, IISER Pune campus, Pashan Near Dr. Hommi Bha bha road Pune, Maharashtra, Maharashtra 411008 India Attn: Hostel 2, IISER Pune campus, Pashan
Billing Type	Invoice
Billing address	Hostel 2, IISER Pune campus, Pashan IISER Pune, Department of Chemistry, Main Building, Lab 125B Dr. Homi Bhabha Road, Pashan PUNE, India 411008 Attn: Wasim Jeelani Mir
Total	0.00 USD

[ORDER MORE](#)
[CLOSE WINDOW](#)

Copyright © 2019 [Copyright Clearance Center, Inc.](#) All Rights Reserved. [Privacy statement.](#) [Terms and Conditions.](#)
Comments? We would like to hear from you. E-mail us at customercare@copyright.com



RightsLink®

[Home](#)
[Account Info](#)
[Help](#)


Title: Strategy to overcome recombination limited photocurrent generation in CsPbX₃ nanocrystal arrays

Author: Wasim J. Mir, Clément Livache, Nicolas Goubet, et al

Publication: Applied Physics Letters

Volume/Issue: 112/11

Publisher: AIP Publishing

Date: Mar 12, 2018

Page Count: 5

Rights managed by AIP Publishing.

Logged in as:
Wasim Mir
Account #:
3001391601

[LOGOUT](#)

Order Completed

Thank you for your order.

This Agreement between Wasim J. Mir ("You") and AIP Publishing ("AIP Publishing") consists of your license details and the terms and conditions provided by AIP Publishing and Copyright Clearance Center.

Your confirmation email will contain your order number for future reference.

[printable details](#)

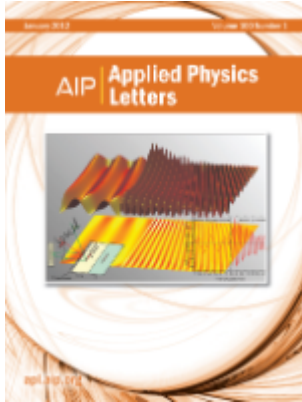
License Number	4521420142295
License date	Feb 03, 2019
Licensed Content Publisher	AIP Publishing
Licensed Content Publication	Applied Physics Letters
Licensed Content Title	Strategy to overcome recombination limited photocurrent generation in CsPbX ₃ nanocrystal arrays
Licensed Content Author	Wasim J. Mir, Clément Livache, Nicolas Goubet, et al
Licensed Content Date	Mar 12, 2018
Licensed Content Volume	112
Licensed Content Issue	11
Requestor type	Author (original article)
Format	Print and electronic
Portion	Figure/Table
Number of figures/tables	3
Requestor Location	Wasim J. Mir Hostel 2, IISER Pune campus, Pashan Near Dr. Hommi Bha bha road Pune, Maharashtra, Maharashtra 411008 India Attn: Hostel 2, IISER Pune campus, Pashan
Billing Type	Invoice
Billing address	Hostel 2, IISER Pune campus, Pashan IISER Pune, Department of Chemistry, Main Building, Lab 125B Dr. Homi Bhabha Road, Pashan PUNE, India 411008 Attn: Wasim Jeelani Mir
Total	0.00 USD

[ORDER MORE](#)
[CLOSE WINDOW](#)

Copyright © 2019 [Copyright Clearance Center, Inc.](#) All Rights Reserved. [Privacy statement.](#) [Terms and Conditions.](#)
Comments? We would like to hear from you. E-mail us at customercare@copyright.com



RightsLink®

[Home](#)
[Account Info](#)
[Help](#)


Title: Strategy to overcome recombination limited photocurrent generation in CsPbX₃ nanocrystal arrays

Author: Wasim J. Mir, Clément Livache, Nicolas Goubet, et al

Publication: Applied Physics Letters

Volume/Issue: 112/11

Publisher: AIP Publishing

Date: Mar 12, 2018

Page Count: 5

Logged in as:
Wasim Mir
Account #:
3001391601

[LOGOUT](#)

Rights managed by AIP Publishing.

Order Completed

Thank you for your order.

This Agreement between Wasim J. Mir ("You") and AIP Publishing ("AIP Publishing") consists of your license details and the terms and conditions provided by AIP Publishing and Copyright Clearance Center.

Your confirmation email will contain your order number for future reference.

[printable details](#)

License Number	4521420262530
License date	Feb 03, 2019
Licensed Content Publisher	AIP Publishing
Licensed Content Publication	Applied Physics Letters
Licensed Content Title	Strategy to overcome recombination limited photocurrent generation in CsPbX ₃ nanocrystal arrays
Licensed Content Author	Wasim J. Mir, Clément Livache, Nicolas Goubet, et al
Licensed Content Date	Mar 12, 2018
Licensed Content Volume	112
Licensed Content Issue	11
Requestor type	Author (original article)
Format	Print and electronic
Portion	Abstract
Requestor Location	Wasim J. Mir Hostel 2, IISER Pune campus, Pashan Near Dr. Hommi Bha bha road Pune, Maharashtra, Maharashtra 411008 India Attn: Hostel 2, IISER Pune campus, Pashan
Billing Type	Invoice
Billing address	Hostel 2, IISER Pune campus, Pashan IISER Pune, Department of Chemistry, Main Building, Lab 125B Dr. Homi Bhabha Road, Pashan PUNE, India 411008 Attn: Wasim Jeelani Mir
Total	0.00 USD

[ORDER MORE](#)
[CLOSE WINDOW](#)

Copyright © 2019 [Copyright Clearance Center, Inc.](#) All Rights Reserved. [Privacy statement.](#) [Terms and Conditions.](#)
Comments? We would like to hear from you. E-mail us at customercare@copyright.com



RightsLink®

[Home](#)[Create Account](#)[Help](#)

ACS Publications Title:
Most Trusted. Most Cited. Most Read.

Origin of Unusual Excitonic Absorption and Emission from Colloidal Ag₂S Nanocrystals: Ultrafast Photophysics and Solar Cell

Author: Wasim J. Mir, Abhishek Swarnkar, Rituraj Sharma, et al

Publication: Journal of Physical Chemistry Letters

Publisher: American Chemical Society

Date: Oct 1, 2015

Copyright © 2015, American Chemical Society

LOGIN

If you're a **copyright.com user**, you can login to RightsLink using your copyright.com credentials.

Already a **RightsLink user** or want to [learn more?](#)

PERMISSION/LICENSE IS GRANTED FOR YOUR ORDER AT NO CHARGE

This type of permission/license, instead of the standard Terms & Conditions, is sent to you because no fee is being charged for your order. Please note the following:

- Permission is granted for your request in both print and electronic formats, and translations.
- If figures and/or tables were requested, they may be adapted or used in part.
- Please print this page for your records and send a copy of it to your publisher/graduate school.
- Appropriate credit for the requested material should be given as follows: "Reprinted (adapted) with permission from (COMPLETE REFERENCE CITATION). Copyright (YEAR) American Chemical Society." Insert appropriate information in place of the capitalized words.
- One-time permission is granted only for the use specified in your request. No additional uses are granted (such as derivative works or other editions). For any other uses, please submit a new request.

[BACK](#)[CLOSE WINDOW](#)

Copyright © 2019 [Copyright Clearance Center, Inc.](#) All Rights Reserved. [Privacy statement.](#) [Terms and Conditions.](#) Comments? We would like to hear from you. E-mail us at customercare@copyright.com